UNIVERSITÉ DU LUXEMBOURG

PhD-FSTM-2022-126
The Faculty of Science, Technology and Medicine

DISSERTATION

Defence held on 30/09/2022 in Luxembourg

to obtain the degree of

DOCTEUR DE L'UNIVERSITÉ DU LUXEMBOURG

EN SCIENCES DE L'INGÉNIEUR

by

ARNAUD MAZIER
Born on 3rd November 1995 in Cannes (France)

DATA-DRIVEN PATIENT-SPECIFIC BREAST MODELING: A SIMPLE, AUTOMATIZED, AND ROBUST COMPUTATIONAL PIPELINE

Dissertation defence committee

Dr Stéphane Bordas, dissertation supervisor
Professor, Université du Luxembourg

Dr Benjamin Gilles
Scientific director, AnatoScope SA

Dr Andreas Zilian, Chairman
Professor, Université du Luxembourg

Dr Yohan Payan
Professor, Université de Grenoble

Dr Stéphane Cotin, Vice Chairman
Professor, Research Director, INRIA

Dr Thiranja Prasad Babarenda Gamage
Research Fellow, University of Auckland

Data-driven patient-specific breast modeling: a simple, automatized and robust computational pipeline

Arnaud Mazier

October 26, 2022

Abstract

Background Breast-conserving surgery is the most acceptable option for breast cancer removal from an invasive and psychological point of view. During the surgical procedure, the imaging acquisition using Magnetic Image Resonance is performed in the prone configuration, while the surgery is achieved in the supine stance. Thus, a considerable movement of the breast between the two poses drives the tumor to move, complicating the surgeon's task. Therefore, to keep track of the lesion, the surgeon employs ultrasound imaging to mark the tumor with a metallic harpoon or radioactive tags. This procedure, in addition to an invasive characteristic, is a supplemental source of uncertainty. Consequently, developing a numerical method to predict the tumor movement between the imaging and intra-operative configuration is of significant interest.

Methods In this work, a simulation pipeline allowing the prediction of patient-specific breast tumor movement was put forward, including personalized preoperative surgical drawings. Through image segmentation, a subject-specific finite element biomechanical model is obtained. By first computing an undeformed state of the breast (equivalent to a nullified gravity), the estimated intra-operative configuration is then evaluated using our developed registration methods. Finally, the model is calibrated using a surface acquisition in the intra-operative stance to minimize the prediction error.

Findings The capabilities of our breast biomechanical model to reproduce real breast deformations were evaluated. To this extent, the estimated geometry of the supine breast configuration was computed using a corotational elastic material model formulation. The subject-specific mechanical properties of the breast and skin were assessed, to get the best estimates of the prone configuration. The final results are a Mean Absolute Error of 4.00 mm for the mechanical parameters $E_{\text{breast}} = 0.32$ kPa and $E_{\text{skin}} = 22.72$ kPa. The optimized mechanical parameters are congruent with the recent state-of-the-art. The simulation (including finding the undeformed and prone configuration) takes less than 20 s. The Covariance Matrix Adaptation Evolution Strategy optimizer converges on average between 15 to 100 iterations depending on the initial parameters for a total time comprised between 5 to 30 mins. To our knowledge, our model offers one of the best compromises between accuracy and speed. The model could be effortlessly enriched through our recent work to facilitate the use of complex material models by only describing the strain density energy function of the material. In a second study, we developed a second breast model aiming at mapping a generic model embedding breast-conserving surgical drawing to any patient. We demonstrated the clinical applications of such a model in a real-case scenario, offering a relevant education tool for an inexperienced surgeon.

Conclusion Satisfactory results were obtained for the estimation of breast deformation under gravity, as well as the mapping of breast-conserving surgical drawings with clinical data validation. In addition to a suitable accuracy, we have demonstrated the feasibility of such applications using a simulation framework that perturbates the least the current surgical pipeline.

Keywords: Biomechanical model, breast simulation, patient-specific, registration, undeformed configuration, inverse problems

I dedicate this thesis to Sophie Ribes, who guided me on this difficult road and taught me the meaning of scientific rigor.

Acknowledgments

First of all, I would like to thank my thesis supervisor, Stéphane Bordas, who allowed me to achieve this thesis project and also allowed me to integrate and work with an outstanding team. Thank you Stéphane for your support and guidance, the freedom of exploring and collaborating without any limits was the best present you could have given me.

I would also like to express my gratitude to the members of my thesis committee. Benjamin Gilles introduced me to the AnatoScope company and Stéphane Bordas; your incredible previous works deeply inspired me. Andreas Zilian for his expertise in mechanics and finite-element, to have my thesis reviewed by such an expert was a blessing. Yohan Payan, your previous work with Anna Mira was the inspiration for this study, and presenting my work to such an expert was an honor. Stéphane Cotin, your projects to connect real-time simulations with the clinical pipeline admiringly motivated this project, and having the chance to collaborate with you and your team was a delightful experience. Finally, it was a pleasure to present my work to Thiranja Prasad Babarenda Gamage and have my work assessed by such an expert in breast simulations. I am grateful to all of you.

This thesis was funded through the RAINBOW project, gathering 15 Ph.D. students. Hence, I would like to thank Faezeh Moshfeghifar, Thomas Alscher, Torkan Gholamalizadeh, José Tascon, Hamed Shayestehpour, Christos Koutras, Kate Kardash, Patricia Alcañiz, Zhongyun He, Antoine Perney, Ehsan Mikaeili, and Vasileios Krokos. We always shared good moments during the training and it was a pleasure sharing with all of you. Similarly, the PIs of this project have always been keen and eager to help us. Special thanks to Miguel Otaduy, Pierre Kerfriden, Kenny Erleben, and Christine Andersen for making this experience incredible.

This project is the result of a collaboration with several institutes. Firstly, the company AnatoScope. Spending almost one year with them in Montpellier was a blessing. They taught me the darkest secrets of SOFA while giving me proper guidance and an extraordinary mood, without them, this project would not have been possible. Hence, I would like to acknowledge the whole company but more specifically, the people in Montpellier that made me part of a bigger family: Marc Legendre, Benjamin Gilles, Christopher Masri, Maxime Tournier, Adrien Debord, Olivia Le Goff, Robin Deroze, Alex Lalaque, Anne-Kim Banchereau, Christina Phung, Dyana Doukhan, Guillaume Duponchel, François Faure, Hèlene Perrier, Jean-David Génevaux, Kévin Pavy, Frédérick Van Meer, Romain Testylier, and Clément Darche.

Secondly, the Hopital Arnaud de Villeneuve. The hospital provided the medical images used in this study at the Département de Gynécologie Obstétrique. Big thanks to Dr. Gauthier Rathat and Prof. Guillaume Captier, that often took the time to illustrate the breast anatomy and the clinical challenges of this project.

Lastly, the fourth floor of the Maison du Nombre at the University of Luxembourg. Spending 4 years in a foreign country is a tough experience but meeting this wonderful team made this time feels like a glimpse. Therefore, I would like to start those acknowledgments by my office mates (the so-called squeezers office): Saurabh Deshpande (it was nice

to meet all your diverse (not so diverse) collaborators), Milad Zeraatpisheh (I wish you the best in your future endeavors and passionate chess games), and Aflah Elouneg (I wish you the best for increasing your s-index). Then I cannot forget all the other members starting from those that left before me: Marco Magliulo (thank you for your incredible atmosphere and crazy stories), Raphael Bulle (I wish you the best in Canada), Hugues Meyer (exemplary Ph.D. student, I wish you a bright future), Davide Baroli (for all the contacts, papers, and codes), Hussein Rappel, Soumianarayanan Vijayaraghavan, Thibault Jacquemin, and Paul Hausseux (for our incredible tennis games). Finally the current team: Jack Hale (I cannot thank you enough for your teaching about FEniCS), Lars Beex (thank you for your honesty in every exchanges we had), Jakub Lengiewicz (thank you for creating this Machine Learning that bounded us together), Anas Obeidat (thank you for every pizza and nights at your place), Olivier Francis (thank you for your daily jokes, even though they were much funnier in French), Anina Glumac (a devoted scientist mother), Stéphane Urcun (I admired your work and hope that we will one day collaborate by any means, I enjoyed every conversations we had (scientific or not)), Juan Aguilar, Vu Chau (the old buffalo), Sofia Farina (starting and finishing at the same time, congrats doctor), Michal Habera (for our lovely FEniCS discussions), Diego Hurtado (thank you for those 4 years of Spanish), Onkar Jadhav, Chintan (Vipulbai) Jansari (I hope our collaboration will be fruitful, no doubts that you will crush your PhD), Aravind Kadhambariyil (I wish you all the success in your thesis and music, I will continue listening your songs), Zhaoxiang Shen (at least I didn't forget you gym buddy), Jiajia Wang, Lee Chen, Natasha Kuhlmann, Chrysovalantou Kalaitzidou, Eleni Koronaki, Diego Kozlowski, Damian Mingo, Raquel Navarro, Paris Papavasileiou (I hope we will meet again for a famous pétanque), Sona Salehian, Renaldo Sauveur, Jinyuan Wang (thank you for introducing me to the Luxembourger volleyball experience, long live ULVB), Lan Shang, Pratik Schude, Vikram Sundara, Sajad Tabibi, Daniel Louw, Thomas Lavigne (best trainee ever, I wish you all the best for your upcoming project), and Meryem Abbad. This experience in Luxembourg would not have been the same without the excellent administrative support from Odile Marois (thank you for your kindness and constant support through those years), Ruken Bulut (Brrrrrrttttt), and Paula Souza.

During this Ph.D. project, I mainly used two open-source simulation software: SOFA and FEniCS. I would like to thank both communities for their excellent support and willingness to create efficient and public simulation tools. Special thanks to Hugo Talbot for being my entry point in the SOFA family and Sidaty El Hadramy for our collaboration in the SOniCS plugin. I wish both communities a bright future and additional contributions to those wonderful projects.

Lastly, I would like to acknowledge my family for their constant support in continuing my studies until the end. Even though it meant leaving the family nest, they always supported me, and coming back home was permanently the best moment of the year. Merci Papa, Maman, Clément, et le reste de la famille pour votre soutien, je vous aime du plus profond de mon coeur. Among my family, I would like to thank one last person, my partner Marie, without whom this thesis would have not been as enjoyable. Thank you for your patience, your encouragement, and your unconditional support. We form an exceptional team, and

each day I realize a little more how lucky I am to have you by my side. I wish you all the best in your future, hoping to still be by your side to provide you the support you were to me.

Scientific contributions

Journal articles

- Arnaud Mazier, Sophie Ribes, Benjamin Gilles, Stéphane P.A. Bordas, A rigged model of the breast for preoperative surgical planning, Journal of Biomechanics, Volume 128, 2021, 110645, ISSN 0021-9290, https://doi.org/10.1016/j.jbiomech.2021.110645.

- Arnaud Mazier, Alexandre Bilger, Antonio E. Forte, Igor Peterlik, Jack S. Hale, Stéphane P.A. Bordas, Inverse deformation analysis: an experimental and numerical assessment using the FEniCS Project, Engineering with Computers, https://doi.org/10.1007/s00366-021-01597-z.

- Thomas Lavigne, Arnaud Mazier, Antoine Perney, Stéphane P.A. Bordas, François Hild, Jakub Lengiewicz, Digital Volume Correlation for large deformations of soft tissues: Pipeline and proof of concept for the application to breast *ex vivo* deformations, Journal of the Mechanical Behavior of Biomedical Materials, https://doi.org/10.1016/j.jmbbm.2022.105490.

Preprints

- Arnaud Mazier, Sidaty El Hadramy, Jean-Nicolas Brunet, Jack S. Hale, Stéphane Cotin, Stéphane P.A. Bordas, SOniCS: Develop intuition on biomechanical systems through interactive error controlled simulations, https://doi.org/10.48550/arXiv.2208.11676.

- Arnaud Mazier, Stéphane P.A. Bordas, Breast simulation pipeline: from medical imaging to patient-specific simulations.

Conference presentations

- Arnaud Mazier, Alexandre Bilger, Antonio E. Forte, Igor Peterlik, Jack S. Hale, Stéphane P.A. Bordas, Inverse simulation for retrieving the undeformed position for hyperelastic materials: application to breast simulation, World Congress of Computational Mechanics (WCCM ECCOMAS Congress 2020) 2020, Paris, 2020, https://orbilu.uni.lu/handle/10993/42678.

- Arnaud Mazier, Thomas Lavigne, Jakub Lengiewicz, Saurabh Deshpande, Stéphane Urcun, Stéphane P.A. Bordas, Towards real-time patient-specific breast simulations: from full-field information to surrogate model, 9th World Congress of Biomechanics (WCB 2022), Taipei, 2022, https://orbilu.uni.lu/handle/10993/51163.

- Arnaud Mazier, Sidaty El Hadramy, Jean-Nicolas Brunet, Jack S. Hale, Stéphane Cotin, Stéphane P.A. Bordas, SOniCS, Interfacing SOFA and FEniCS for advanced

constitutive models, FEniCS conference 2022, San Diego, 2022, https://158.64.79.159/handle/10993/51743. Award of the best presentation by a PhD student.

Seminars

- Arnaud Mazier, Digital twinning for real-time simulation, EIB tech fair 2019, Luxembourg, 2019.
- Arnaud Mazier, An introduction to patient-specific simulation with SOFA framework, Legato team seminar, Luxembourg, 2020.
- Arnaud Mazier, Decision Trees methods, an overview of the white-boxes, Legato machine learning seminar, Luxembourg, 2020.
- Arnaud Mazier, Sidaty El Hadramy, Jean-Nicolas Brunet, Jack S. Hale, Stéphane Cotin, Stéphane P.A. Bordas, SOniCS, Interfacing SOFA and FEniCS for advanced constitutive models, SOFA Week 2021.

Software

- Arnaud Mazier, Sidaty El Hadramy, Jean-Nicolas Brunet, SOniCS, SOFA plugin for using FEniCSx automatic differentiation features for advanced constitutive models (LGPLv3). Github repository: https://github.com/mimesis-inria/caribou/tree/FeniCS-features.
- Arnaud Mazier, Alexandre Bilger, Antonio E. Forte, Igor Peterlik, Jack S. Hale, Stéphane P.A. Bordas, fenics-inverseFEM, FEniCS code for inverse FEM hyper-elasticity (LGPLv3). Github repository: https://github.com/Ziemnono/fenics-inverseFEM. Figshare containing all the examples of the associated paper https://doi.org/10.6084/m9.figshare.14035793.v1.

Contents

List of Tables

List of Figures

Introduction

Most technical engineering tools that require a high level of precision are performed by machines which even completely replace humans in the new generation of industry, Industry 4.0 [107]. However, when it comes to health, the situation is more nuanced. Medical gestures and operations remain the prerogative of humans. Unlike the industrial world where humans assist robots, in surgery, robots may assist humans. This relationship between man and machine has been intensively studied [43] in a world where software in surgery with image processing, surgical planning, and finally intraoperative assistance is growing.

In this thesis, we are interested in a specific medical application: the numerical simulation of soft tissues for patient-specific breast conservative surgeries. This project is part of the European Innovative Training Network (ITN) Rapid Biomechanics Simulation for Personalized Clinical Design (RAINBOW), funded by the European Union's Horizon 2020 Research and Innovation program under a Marie Skłodowska-Curie grant. In this program, 15 Ph.D. students worked jointly to explore and develop new methods in various areas of personalized biomechanical simulations.

The partners of this thesis were AnatoScope and the Centre Hospitalier Universitaire (CHU) of Montpellier Arnaud de Villeneuve. Anatoscope provided their knowledge and numerical tools for patient-specific modeling and simulations. The CHU of Montpellier was in charge of delivering medical images and breast anatomical and surgical expertise.

In this introduction, we first discuss the core problem of this thesis by indicating the different steps of the breast-conserving surgery pipeline. Then, we will state the key requirements of physics-based breast simulations while presenting some of the challenges found in the existing literature and the reasons why they are still the object of ongoing research. Finally, we will conclude with a clear record of the contributions found in this work and a precise outline of the manuscript.

Goal of the thesis

The main objective of breast-conserving surgery is a complete removal with adequate safety margins. A surgical revision is necessary in 10 to 15% of cases because of damage to the margins. This revision remains high, regardless of the type of location. The second is cosmetic and mainly depends on the quantity of tissue removed and is directly related to the spot.

In the context of breast-conserving surgery, the tumors are localized and identified using MRI in the prone position, breast oriented downwards. While for practical reasons, tumor resection is performed in a supine configuration, breast upwards. It requires an additional, complex, invasive procedure to attach physical landmarks to the tumors. Indeed, the two most commonly used techniques of location in France are the metallic harpoon and isotopic localization, called Radioguided Occult Lesion Localization (ROLL). The mutual disadvantage is discomfort, as it is performed on the conscious patient the day before or the morning of the operation. Additionally, the tumor needs to be identified again in another configuration as shown in figure 1. This thesis aims to replace the invasive procedure

with a numerical prediction of tumor location in the supine configuration and to provide the surgeon with per-operative visualization of the tumor. It requires the construction of patient-specific breast models, including personalized rheology (material properties), which cannot be measured directly. The scientific challenge is to produce a novel Inverse Method to compute the parameters based on the breast surface shape in different poses, captured using a depth camera. A Finite Element (FE) model of the breast will be constructed from MRI using segmentation and registration techniques. The method will compute the rheology parameters which produce the observed shape. These will be used during the operation to infer the internal tumor position based on the external breast shape.

Challenges and key requirements

This Ph.D. subject is challenging for several reasons. First, it is at the crossroad between different fields and is strongly multi-disciplinary. Indeed, modeling the breast requires a strong basis in medical imaging, anatomy, or biology. Secondly, achieving efficient and patient-specific numerical simulations requires a deep understanding of continuum mechanics coupled with data-driven methods. Finally, offering intuitive tools to medical staff while accounting for surgical timing required strong informatics skills. Indeed this level of performance can only be achieved through efficient low-level languages such as C++. However, as C++ is a complex language for novices, Python bindings were also used for more user-friendliness.

From a medical point of view, having access to medical data was a challenge. Indeed, MRIs are costly, difficult to set up, can last for 40 mins, require medical staff, and are dangerous for the patient. Additionally, obtaining MRIs in the operative configuration for validation is nearly impossible as the screening is clinically irrelevant. Hence, the surgeons use histologic sampling to confirm the success of the tumor resection. Finally, the COVID situation also negatively impacted our research. As the medical staff prioritized dealing with the complex sanitary situation, reaching out to them was complicated, and less of their work was dedicated to research.

From a scientific perspective, there is still no gold standard of breast models for numerical simulations. While several teams developed their models using in-house software or commercial solutions, no open-source model has been found to experiment with our data. Additionally, breast cancer is a broad discipline where breast models are developed for different endeavors, such as mammogram simulations or tumor segmentation automation. Because of the organ complexity, a wide variety of models were created employing various hypotheses. For example, the material model selection, variability of the boundary conditions, and degree of heterogeneity (number of organs to consider), just to cite a few.

Modeling a complex organ such as the breast presented numerous challenges. The first hurdle is the intra and inter-patient variability. Indeed, as every woman has different anatomy, the breast geometry is highly variable from one person to another. This makes the generalization of a model complex, as, in addition to the external shape of the breast, the inner volume is also relatively variable (mammary gland shape and density, pectoral shape, ligaments' position). Finally, the breast mechanical properties are also remarkably

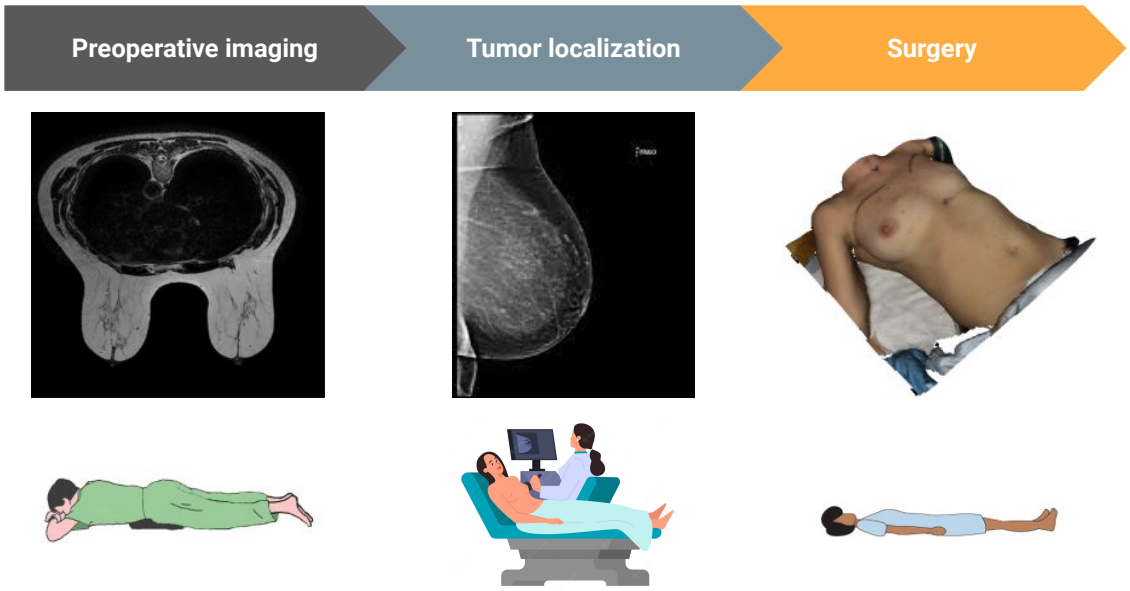

Figure 1: Breast-conserving surgery clinical pipeline. Starting from the left, the identification and evaluation of the tumor occur using an MRI in prone configuration. It allows to naturally expend the breast to evaluate the shape, position, and any relevant information helping the diagnosis. On the right side, the end of the pipeline is represented by a 3D surface acquisition of the patient. In the intra-operative configuration (supine), the surgeon will operate to remove the tumor without any medical imaging guidance. One problem remains, forecasting the tumor position after such a large movement of the breast from the imaging to the surgical configuration. To improve the surgeon's precision, in the middle of the image, an additional step is needed for locating the tumor. The position of the tumor is marked in another new configuration using ultrasound imaging for spotting the tumor and using a Radioguided Occult Lesion Localization (ROLL) or metallic harpoon. The goal of this thesis is to remove this extra step by proposing numerical methods capable of predicting the tumor localization from the imaging to the intra-operative configuration.

variable depending on the woman's age, biological and hormonal condition, genetics, etc...

Developing a breast model is already a challenge by itself, but as we aim at implementing our solution in a clinical pipeline, additional constraints have to be applied to make it a suitable tool for medical staff.

Accuracy

The physical modeling of soft tissues composing an organ aims at predicting its deformations under different constraints. Hence, the realism of a simulation requires choosing a material model that will represent, as closely as possible, the observed behavior of the organ. Additionally, to obtain an accurate deformation of the organ, interactions with the adjacent anatomical structures must also be taken into account. Defining an accuracy criterion can be seen as the degree of realism of the desired deformation that will depend on the final application. For training a surgical procedure, the visual feedback and the effort are, for example, more important than the precision of the deformation. For a simulation more oriented towards surgical planning, it becomes much more important to have a realistic deformation. In the context of predicting tumor localization, an emphasis on accuracy is necessary for two reasons. The first argument is the tumor size. Indeed, depending on the grade of the tumor, ranging from 2 to 8 cm on average (15 in extreme cases), the lesion is small compared with the simulation domain and deformation range. This automatically sets an error threshold which has to reach at least 1 mm for representing less than 10% of the tumor size. Secondly, as the surgeon will perform a tumor resection with security margins of approximately 1 cm, it is necessary to have a millimetric precision of the tumor position estimation. Indeed, if a greater error is obtained it can guide the surgeon to an incorrect solution that can induce a second operation, endangering the patient and leading to supplementary costs. The simulation accuracy can only be assessed by quantifying the error between the prediction of the model and the clinical ground truth, resulting in a data-driven simulation.

Finally, the accuracy is narrowly related to the simulation time. Indeed, most numerical simulations need a certain amount of time to converge due to a significant number of degrees of freedom to represent the domain. Hence an acceptable trade-off needs to be found. The biggest challenge is to find a threshold between the accuracy and the simulation speed.

Timing

One principal point for the simulation is to be compatible with surgical timing. A strong constraint of the breast-conserving surgery pipeline is to go through an MRI in the prone configuration followed by an ultrasound screening a few hours or the previous day of the surgery. In an ideal clinical pipeline, the patient should have the surgery as close as possible in time to the MRI. This will allow the tumor to move less while conserving breast mechanical properties (we recall that breast properties might differ in a few days due to hormonal fluctuation). Hence, the simulation from the imaging configuration to the surgical one has to be fast to stay compatible with the surgical timing (ideally less than 10 to 20

minutes). The problem of obtaining real-time simulations has already multiple solutions, such as machine learning or model order reduction. Unfortunately, most of these techniques require an offline training stage or a deterministic model (same boundary conditions, topology, or mechanical parameters), which is impossible in our case. Secondly, the application is designed for medical staff that will prefer a fluid, rapid, and interactive simulation.

In other words, the simulation should be fast without compromising the deformation prediction.

Utility

For most scientific applications, the end users are knowledgeable or experienced individuals. For our application, the final users are the medical staff who are not experts in physics-based simulations. Hence, extensive discussions have been conducted to understand and comprehend the main expectation of the application. The first element (in addition to the accuracy) includes a fluid, robust (in the sense of rarely crashing and few lags), and easy-to-use application. Indeed, displaying countless options to the user or unadapted visualization would be terrible. For instance, surgeons are not interested in displaying the stress field generated by breast movement. Their principal focus is to have a photo-realistic representation of the model that clearly indicates the tumor position in the patient. Additionally, they want to use the software independently without needing external assistance. A second feature is to disrupt the least possible the existing surgical pipeline. Indeed, imposing additional steps or clinical examinations, such as requiring more MRIs would be irrealistic and drastically change the surgeons' protocols. Finally, the software should be easy to install and not require sophisticated computers, such as HPC (High-Performance Computers). This adds the constraint of using simple models that can run rapidly without extraordinary CPUs (Central Processing Units), GPUs (Graphical Processing Units), or RAM (Random Access Memory).

Contributions

The contributions made in this research project are divided in five parts:

- Contribution 1 Breast cancer clinical background and Finite Element Method (FEM) necessary for the understanding of the manuscript.
- Contribution 2 Software for mapping preoperative breast-conservative surgical pattern on any patient
  - Contribution 2.1 State-of-the art of mathematical models to fit patient-specific breast data.
  - Contribution 2.2 Creation of a new model made of rigging, skinning, and blendshape to create a simple template model embedded with the surgical drawing.
  - Contribution 2.3 Registration method to rapidly deform the model to fit a cohort of 7 patients.

- Contribution 3 Open-source algorithm to recover the undeformed configuration of a object.
  - Contribution 3.1 Historical state-of-the-art of inverse method to recover the undeformed configuration (physics-based and iteratives).
  - Contribution 3.2 Open-source implementation details using the FEniCS software and several numerical test cases.
  - Contribution 3.3 Confrontation of the algorithm with real-data using a highly deformable silicone beam and comparison with other pieces of software.
- Contribution 4 Open-source software allowing SOFA users to create any material models and finite elements kernels using the FEniCS software.
  - Contribution 4.1 State-of-the-art of existing pieces of software and introduction to SOFA and FEniCS.
  - Contribution 4.2 Explanation of the SOniCS plugin and examples of Saint Venant-Kirchhoff material model generation.
  - Contribution 4.3 Numerical validations, benchmark with FEBio, and complex surgical haptic simulation.
- Contribution 5 Creation of new simple, fast, and intuitive finite element breast model.
  - Contribution 5.1 State-of-the-art of breasts numerical models and mechanical properties of the tissues.
  - Contribution 5.2 Creation of a numerical pipeline: from imaging to the finite element model.
  - Contribution 5.3 Data-driven and patient-specific material properties from imaging to surgical configuration.

Outline

The outline of this manuscript directly follows the order of the mentioned contributions. We will begin with an introduction to breast cancer, starting with an anatomical description of the breast, followed by statistics, the different types and grades, imaging procedures, and possible treatments. For a better understanding of the rest of the manuscript, a short introduction to the FEM is given, detailing the kinematics tensors and the strong from that we aim at solving. In chapter 2, we developed a simple model designed to predict patient-specific preoperative surgical drawings using the SOFA software. Indeed, a crucial step preceding any surgical pipeline is drawing surgical patterns to allow the surgeon to plan the operation. We tackled this problem by using rigging, skinning, and blenshapes methods to implement a fast and simple model, mapping information from a template model to any surgical scan patients in any position. In chapter 3, using the FEniCS software, we created an open-source code enabling us to find the undeformed configuration of an object. Indeed,

a necessary step of the breast-conserving surgical pipeline is to reverse the gravity to infer the so-called "undeformed configuration" which could be understood as a 0-gravity state. In chapter 4, we will describe the successful coupling of our two simulations framework, SOFA, and FEniCS, to effortlessly obtain complex material models in SOFA. In chapter 5, we will combine all our previous findings to create a new numerical model of the breast suitable for real-time simulations. Finally, chapter 6 will close this thesis with a conclusion and a summary of the observations made throughout our work and our recommendations for future research.

1 Clinical and mechanical background

Breast cancer results in a disorder of specific cells that multiply and most often form a mass called a tumor inside the breast. There are different types of breast cancer that do not develop in the same way, some can take several months, others even years to develop. Some are "aggressive" and are quickly growing, while others are evolving slower. The cancer cells can stay in the breast or also spread to other organs (called metastasis), which is an even more threatening situation. In this section, we will give brief statistics about breast cancer. Before detailing the different causes, grades, and types of cancer, we will describe the breast anatomy. Finally, we will explain the breast imaging procedures, as well as, the various possible treatments. An extra sub-section will be dedicated to introducing the fundamentals of the finite element method that will be necessary for a better understanding of this manuscript.

1.1 Breast cancer

The estimated number of breast cancer cases in 2020 worldwide for females of all ages is 2 261 419, representing almost 25% of the global number of cancer. Concerning mortality, 684 996 have died from breast cancer, representing 15.5% of the women that died from cancer. It makes it the most prevalent and lethal cancer for women. The average age is 47.8 years old [211]. The disease is constantly growing and is estimated to reach 3.19 million cases in 2040.

The major problem of breast cancer is the discreteness of the symptoms. Indeed, most of the time, the women will only feel a lump or mass in a breast which is the most common sign of breast cancer. The bump is usually painless, stiff, presents an irregular shape, and appears to be "fixed" to the breast. One or more hard lumps in the armpit could suggest that the breast cancer has spread to the axillary nodes (part of the lymph nodes) but frequently remain painless. Another discrete factor could be the change in the skin: retraction, redness, swelling, or orange peel appearance. The same symptoms can be observed in the nipples or areolas (the area around the nipple): retraction, change in color, oozing or discharge. Similarly, local changes in the shape of the breasts, such as redness, swelling, and warmth may be a sign of inflammatory breast cancer. A problematic point is if the cancer is not diagnosed early, the tumor may grow and spread to other parts of the body, causing more severe symptoms like bone pain, nausea, loss of appetite, weight loss, jaundice, shortness of breath, coughing, fluid accumulation around the lungs (pleural effusion), headaches, double vision, and muscle weakness.

Contrary to commonly accepted ideas, only 5 to 10% of diagnosed breast cancers patients are genetically predisposed to breast cancers [229], while non-familial cancers make up the remaining 90-95%. Among the non-familial breast cancers, several factors are known.

- Many cocktails of molecules and known mechanisms seem to be able to trigger or promote breast cancer. For instance, the inhibition of the DNA damage response system may be involved in half of all breast cancers, especially those induced or

facilitated by hormones used in menopausal hormone treatments. Additionally, the protein (Akt1) is over-expressed in 50% of sporadic breast cancers and could, therefore, predispose to breast cancer or be involved in other processes (environmental and non-genetic). Similarly, another protein, CK2 (an enzyme important for epithelial cell plasticity), appears to be involved in the progression of breast cancers. Indeed, the alteration of the CK2 activity is accompanied by a mutation of epithelial cells into cancer cells (more mobile and a source of metastasis).

- Breast cancer is often hormone-dependent and some factors that increase estrogen levels are therefore at risk. Schematically, the risk of breast cancer increases with the number of menstrual cycles, whether artificial (estrogen-progestin pill) or natural [45]. Similarly, hormonal replacement therapy during menopause significantly increases the risk of breast cancer [26]. Late menopause and early puberty also increase the number of menstrual cycles and thus estrogen levels. Different factors of precocious puberty have been identified. Among those factors, childhood obesity, increased consumption of animal proteins (meat, milk), consumption of sweetened beverages, and exposure to endocrine disruptors seem to increase the estrogen level (increasing breast cancer risk).

- Women who have not had a child or a first late pregnancy have a significantly increased risk of developing breast cancer compared to those who had at least one child before 30 years. In fact, the cycles preceding the first full-term pregnancy seem to be the most dangerous for the breast. Pregnancy protects the breast by changing the breast cells, favoriting more significant cell differentiation. Pregnancy, especially, an early one, acts as a vaccine against estrogens [68, 146]. Breastfeeding acts as a protector against breast cancer [209], notably by putting the ovaries to sleep and reducing the number of cycles. Voluntary interruption of pregnancy does not increase the risk of breast cancer.

- The parallelism between the incidence increase of breast cancer over the last 50 years and the proliferation of endocrine disruptors, synthetic chemicals with estrogenic or carcinogenic action [56]. Molecules such as ES, DDT, bisphenol A, and dioxins from various sources like pesticides, industrial chemicals, plastics and plasticizers, fuels, and other chemicals omnipresent in the environment are major sources of concern for endocrinologists. For example, girls who were heavily exposed in utero in the 1960s to DDT have a fourfold increase in breast cancer risk.

- Obesity increases the risk of breast cancer. For example, when tumor cells (murine or human) are cocultured with mature adipocytes, the latter increase the invasive capacity of cancer. In general, obesity doubles the risk of breast cancer by increasing the amount of fatty tissue, boosting the level of estrogen in the blood through aromatase activation (enzyme). This enzyme transforms androgen-type hormones into estrogen and continues after menopause, increasing the risk of breast cancer in overwieghted postmenopausal women.

- The consumption of animal fats and trans fatty acids (used in several food industry preparations) could be risk factors. This relationship between the level of animal fat intake and breast cancer has been known for a long time, while the influence of polyunsaturated fats is less clear. Risk of breast cancer increases by almost 50% in women with high blood levels of trans fatty acids, which may be present in industrial foods such as industrial bread and cookies, pastries, cakes, chips, and pizza dough.

- Several scientific studies have identified milk as a risk factor for hormone-dependent cancers such as prostate, ovarian, and breast [119]. The increased risk is linked to IGF-1 increase levels in the blood, which is strongly correlated with milk consumption. The link thus appears to be established in the pre-menopausal phase and also seems consistent with the absence of cancer observed in the population with Laron syndrome, which does not produce IGF-1. The concentration of IGF-1 significantly varies depending on the type of milk [44], whether it is low-fat or in the ruminants' environment. However, other studies establish a protective role linked to the vitamin D or calcium content of milk [203].

- Numerous studies have shown that alcohol consumption increases the risk of breast cancer. This risk is increased on average by 30% for three glasses of alcohol per day. Meta-analyses have confirmed the role of alcohol in the genesis or facilitation of breast cancer. The risk increases by about 10% for every 10 g of alcohol (consumed on average per day) depending on genetic sensitivities. There is a correlation between smoking and the occurrence of breast cancer [231]

- Breast cancer is often associated with low vitamin D levels (deficiency or insufficiency in 78% of cases [156]). Vitamin D and its pharmaceutical analogs have antiproliferation and pro-differentiation effects. It is, therefore, essential for the prevention and treatment of cancers in general. In particular, it can limit excessive estrogen production by acting on aromatase.

- New radiological examination modalities, such as coronary CT scans, may lead to sufficient radiation to increase the risk of breast cancer decades after the examination was performed. Night work may increase the risk of breast cancer [115].

Finally, 5-10% of breast cancers diagnosed are genetically predisposed [229]. In 2008, 10 genes were associated with an increased risk of breast cancer, and 9 are related to the DNA damage response system. The tenth encodes a protein that inhibits the action of the AKT1 enzyme (an enzyme whose inhibition also plays a role in non-genetic cancers). Two of these ten genes (called BRCA1 and BRCA2) alone are responsible for half of these genetically predisposed cancers, or 2.5 to 5% of all breast cancers, and frequently appear in women with no particular health problems. Although, very infrequently, the patient has a known genetic disease. Young age, family history, cancers occurring in both breasts successively or simultaneously, the occurrence of second cancer in the ovary, and medullary histological type of cancer are all signs of predisposed breast cancer.

1.2 Breast anatomy

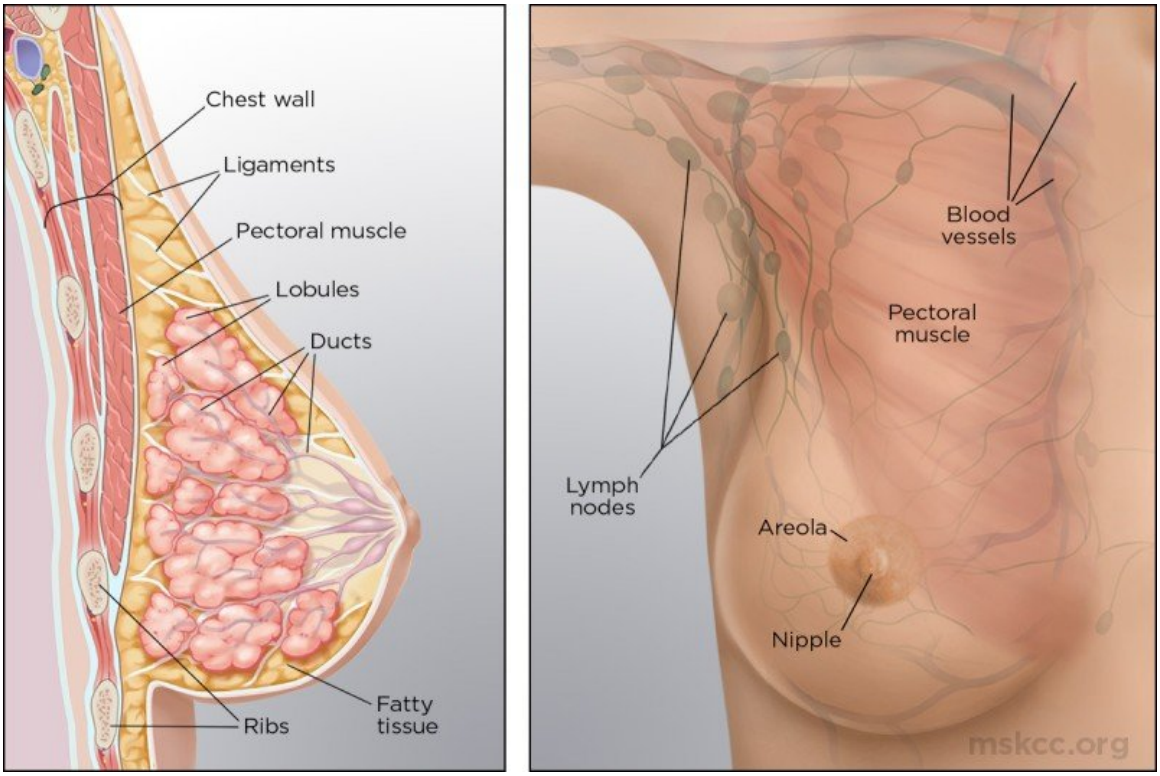

Figure 2: Female breast anatomy. On the left, a sagittal view detailing the different tissues. On the right, a front view of the organ highlighting the blood (in red and blue) and lymph vessels (in green) route.

Breasts are part of the female and male sexual anatomy. For females, the breasts have two principal utilities breastfeeding and sexual pleasure. The breast is made of a surface layer and an internal volume. The visible parts of the breast anatomy include the skin comprised of the nipples and areolae. The areola is the circular dark-colored area of skin surrounding the nipple. They have glands called Montgomery's glands secreting a lubricating oil protecting the nipple and skin from injuries during breastfeeding. The nipple solely corresponds to the areola center and holds nine milk ducts and nerves.

Inside, the breast is made of several tissues, as depicted in figure 2. The fatty tissues (adipose) are the main component of the breast and are responsible for the breast size. Besides the fatty tissues, the breast is made of glandular tissues embedding the lobes. Generally, a breast can be characterized by the ratio between the volume of glandular tissue and adipose. This ratio is especially variable among women. Each breast has between 15 to 20 lobes or sections surrounding the inner nipple. Those lobes also contain tiny bulblike glands called lobules producing milk. Each lobe is linked to the nipple through milk or

lactiferous ducts responsible for carrying the milk from the lobules to the nipples.

In addition to a complex structure, the breast is circulated by blood vessels distributing the blood throughout the breasts, chest, and body. The lymph vessels are part of the lymphatic system transporting lymph, a fluid that supports the immune system fight infection. Lymph vessels connect to lymph nodes, or glands can be found under the armpits or in the chest. Finally, the nipples have hundreds of nerve endings, which makes them extremely sensitive to touch and arousal.

The breasts lie between rib II and VI and predominantly lean on the pectoralis major muscle. The pectoralis major originates from the medial surface of the clavicle and the anterior surface of the sternum and inserts into the lateral lip of the bicipital groove of the humerus. At the axillary margins, the breasts lean on the pectoralis minor, serratus major, external oblique muscles, and the fascia of the thorax.

Similarly to the human body, the breast is a finely balanced system. For females, estrogen, progesterone, and prolactin play a key role in breast development and function. Estrogen stretches milk ducts and supports them in creating side branches to carry more milk. Prolactin promotes the production of progesterone and prepares glands for milk production. Progesterone increases the number and size of lobules in preparation for breastfeeding. This hormone also enlarges blood vessels and breast cells after ovulation.

Meanwhile, male breasts do not have a specific function. During puberty, the male hormone testosterone commonly stops breasts from developing. On the outside, males have nipples and areolae. Internally, they have undeveloped milk ducts and no glandular tissue. Male breast problems can include gynecomastia, a benign condition that causes the breasts to enlarge, and very rarely, breast cancer. Consequently, in this thesis, we will mainly drive our attention on female breast cancer.

1.3 Different types of breast cancer

In order to plan the optimal treatment and increase the chances of success in fighting the disease, it is essential to define the different types of breast cancer, as shown in figure 3. The classification of breast cancers is mainly assessed according to two factors. First, by determining the type of tumor involving the area of the breast affected. Secondly, defining the subtype by discovering the type of mutation that provoked the tumor. The following points are resuming the different type of tumors found in the literature.

- **DCIS (Ductal Carcinoma In Situ)**. The DCIS originates from the epithelial cells lining the milk ducts (in charge of conducting the milk produced by the breast lobules to the nipple). In the initial phase of proliferation, the cancer cells cannot yet spread beyond the duct where they originated. The boundary between the duct and the supporting tissue is the basement membrane. It is the crossing of this basement membrane that distinguishes DCIS from (invasive) breast cancer. Approximately 20% of surgically treated DCIS is found to be invasive on histological analysis. The mode of the proliferation of DCIS depends on the degree of differentiation. Indeed, well-differentiated DCIS tends to spread discontinuously within a single breast quadrant

and multiple discontinuous foci of DCIS separated by areas of healthy tissue are responsible, for 70% of well-differentiated DCIS. The analysis of cancerous foci is done by microscopic examination of the surgical specimen. The lesions are referred to as multifocal (several foci) and monocentric (a single quadrant), while multicentric lesions, i.e., involving several quadrants, are rare.

- **Invasive ductal carcinoma (IDC)**. Like DCIS, IDC affects the milk ducts but is more invasive, meaning that it will spread and extend into the breast tissue. IDC or ductal adenocarcinoma is the most common type of breast cancer. It originates in the cells of the breast ducts and proliferates beyond the ducts by invading the surrounding breast tissue. Cancer then takes the form of a mass or thickening of the mammary gland. This type of cancer can also invade the lymph nodes then, entering a metastatic stage, meaning that the disease has spread outside the breast to form secondary sites in other body parts.

- **Lobular carcinoma in situ (LCIS)**. LCIS is characterized by the development of abnormal cells in the mammary glands and does not spread out of the lobules into the surrounding breast tissue. It frequently occurs in both breasts at the same time and is most often detected during a biopsy to check for a breast lump or to follow up on an abnormal mammogram. LCIS is not a precancerous condition or breast cancer. It is a sign or marker that a woman is at increased risk of developing breast cancer. Several women with LCIS will not get invasive breast cancer and researchers still struggle to determine which women will eventually develop invasive breast cancer. One certainty is that women with LCIS combined with other risk factors such as family history have a higher risk of developing invasive breast cancer than women with LCIS without risk factors. Because of this increased risk, women with LCIS need to be screened for breast cancer.

- **Invasive lobular carcinoma (ILC)**. ILC accounts for approximately 10% of all invasive breast cancers. ILC originates in the lobules of the breast and crosses them, thus invading the surrounding breast tissue. It can also spread (metastasize) to lymph nodes or other body parts. ILC can occur in more than one area of the breast (multifocal, or multicentric disease). Like LCIS, it is more likely to affect both breasts than other types of breast cancer but the cells of ILC do not form a mass. Instead, they form a single band in the fatty tissue, creating a thick zone of breast tissue. There may then be changes in the skin of the breast, such as a different texture or dimpling. ILCs are challenging to detect by mammograms, while MRIs, ultrasounds, or biopsies are a better solution for the diagnosis.

- **Inflammatory breast cancer**. Inflammatory breast cancer is a rare type of breast cancer and accounts for less than 4% of all types of women's breast cancer. Inflammatory breast cancer is an aggressive form of breast cancer that develops rapidly. It is often diagnosed at an advanced stage (when the tumor cells have invaded the lymph nodes of the breast) or when the tumor has secondary locations (metastases). The

rapid development of this form of breast cancer usually results in breast swelling. Due to the blockage of the lymphatic vessels by the cancer cells, the skin tends to become red or purplish in about one-third of the breast. Unlike other forms of breast cancer, there is no lump inside the breast.

- **Mucinous carcinoma**. Mucinous or colloid carcinoma is rare, representing about 2% of all invasive breast cancers. It occurs more often in women between 60 and 70 years old and is formed by cancer cells secreting mucus. Mucinous carcinoma has a better prognosis than other common types of invasive breast cancer.

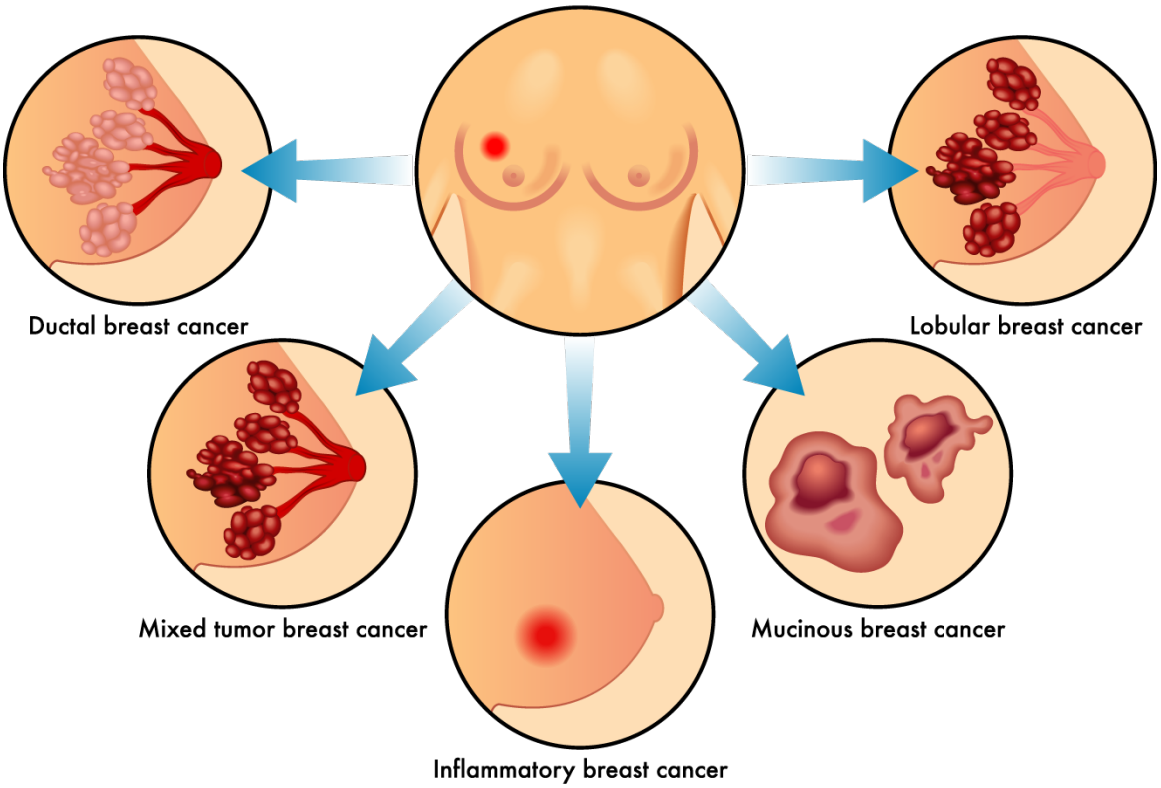

Figure 3: The different breast cancer types. Image extracted from `www.scientia.global.com`

As mentioned previously, breast cancer is also classified accordingly to its subtypes. Indeed, breast cancer is a heterogeneous disease often requiring laboratory tests to discover what type of mutation is causing the tumor development. Several principal types of mutations can be found in the literature.

- **Hormone receptor positive**. Hormone receptors are located on the surface of cells in the body that allow the cells to receive messages from hormones and adapt their

function and behavior. This subtype of cancer accounts for about 60% to 75% of breast cancers. In the breast, there are estrogen (ER) and progesterone (PR) receptors. Laboratory testing will determine if the tumor is due to the hyperactivation of these receptors in response to hormones. The tumor will then be called ER or PR-positive depending on the hormone hyperactivated. Hormone receptor-positive cancers are found most of the time in postmenopausal women.

- **HER2-positive**. This subtype accounts for approximately 15% to 30% of breast cancer cases. HER2 is a receptor located on the surface of cells transmitting a signal to cells when activated by an epidermal growth factor. In this subtype of cancer, the HER2 receptor is found in abnormal amounts on the cell's surface and is usually overactivated. It results in more important signals sent to the cell overgrowing and multiplying abnormally.

- **Triple-negative**. When the laboratory test does not reveal any mutations in the above-mentioned genes (ER, PR, HER2), the term "triple negative" is employed. Triple-negative breast cancer accounts for about 15% of invasive breast cancers and appears to be more common in younger women.

- **BRCA**. Most breast cancers are sporadic, meaning that they are not inherited. However, there is a form of breast cancer that is called hereditary. This form of tumor is less common, representing between 5 to 10% of breast cancer cases, and is caused by a gene called BRCA (which exists in two forms, BRCA1 and BRCA2). Individuals carrying the mutation affecting this gene have a predisposition to developing breast cancer.

As presented, there is not "one" but "many" types and subtypes of breast cancer. Hence, determining the type and subtype of disease allows medical teams to develop a treatment strategy to best treat breast cancer. Therefore, breast cancer is not only qualified depending on the type but also on the grade.

1.4 Different grades

To obtain a standard classification of breast cancer, staging is used to assess the extent of cancer. It is performed with the help of clinical (palpation of the tumor to look for abnormal nodes in the breast), radiological (mammography, ultrasound), and histological (microscope on biopsy samples before or after surgery) examinations. From stage II onwards, other examinations (chest X-ray, ultrasound or CT scan of the abdomen, bone scan, MRI) are carried out to verify the presence or absence of metastases, which are cancer cells that have migrated to distant sites such as the liver, bones, lungs, and brain.

To assess the different stages of breast cancer, the TNM classification is the most frequently used and is based on 3 criteria. "T" for tumor size and infiltration, ranging from Tx (tumor not evaluable) to T4. Then, "N" for the degree of lymph node involvement, ranging from Nx (node involvement not evaluable) to N3. Finally, "M" for the presence or

absence of distant metastases; with Mx (insufficient information to classify metastases), M0 (absence of metastasis), or M1 (presence of metastasis). The TNM classification indicates the stage of breast cancer that is shortly presented (note that it can vary depending on the country).

- **Stage 0**: in situ cancer. The tumor remains localized to the duct where it originated and is non-infiltrative nor spread beyond the basement membrane (T1 N0 M0).
- **Stage I**: tumor measures 2 cm or less. Tumor prior 2 cm without lymph node involvement nor distant metastases (T1 N0 M0).
- **Stage II**
  - **Stage IIA**: Tumor prior 2 cm with invasion of 1 to 3 axillary nodes or involvement of internal mammary sentinel nodes, without metastases (T0/1/2 N1 M0). Or tumor bigger than 2 cm (but less than 5 cm), without lymph node involvement or metastases (T2/3 N0 M0).
  - **Stage IIB**: The tumor is larger than 2 cm but not larger than 5 cm but the cancer has also spread to 1-3 axillary lymph nodes, internal mammary lymph nodes or both (T2/3 N1/2 M0). Or the tumor is bigger than 5 cm (T4 N0 M0).
- **Stage III**
  - **Stage IIIA**: Any tumor, without metastasis, with at least 4 axillary nodes involved or clinical internal mammary invasion or involvement of subclavicular nodes or homolateral supraclavicular nodes (all T N2/3 M0).
  - **Stage IIIB**: Tumor with direct extension to the chest wall or skin, or inflammatory tumor (T4 all N M0).
  - **Stage IIIC**: Tumor has spread to 10 or more axillary lymph nodes or to lymph nodes below the collarbone (infraclavicular nodes). Or the cancer has spread to lymph nodes above the collarbone (supraclavicular nodes).
- **Stage IV**: metastatic cancer. Regardless of the size of the tumor and the degree of lymph node involvement, the presence of distant metastases classifies the cancer as stage IV (all T all N M1).

In addition to the TNM classification relying on medical imaging information, the Bloom-Richardson grading system also evaluates the tumor grades but based on histological examination (biopsy), taking into account:

- the appearance of the cancer cells: the more a cancer cell has changed from normal cells, the more aggressive it is.
- the characteristics of the cell nuclei: the larger the cell nuclei and the more varied their size and shape, the more aggressive the cells are the number of cells in mitosis.

- cell multiplication: the higher this number, the faster the tumor cells divide, and the more aggressive the cancer can spread.

The Bloom Richardson classification compiles a general score based on the 3 sub-scores of each criterion. Each sub-score is ranging from 1 to 3 and the overall score obtained determines the histopronostic grade. An example of such a grading system is given in figure 4. The grade is I or low grade (least aggressive tumors) for a total score of 3, 4, or 5. The grade is II for a score of 6 or 7. Finally, the grade is III or higher (most aggressive tumors) for a score of 8 or 9.

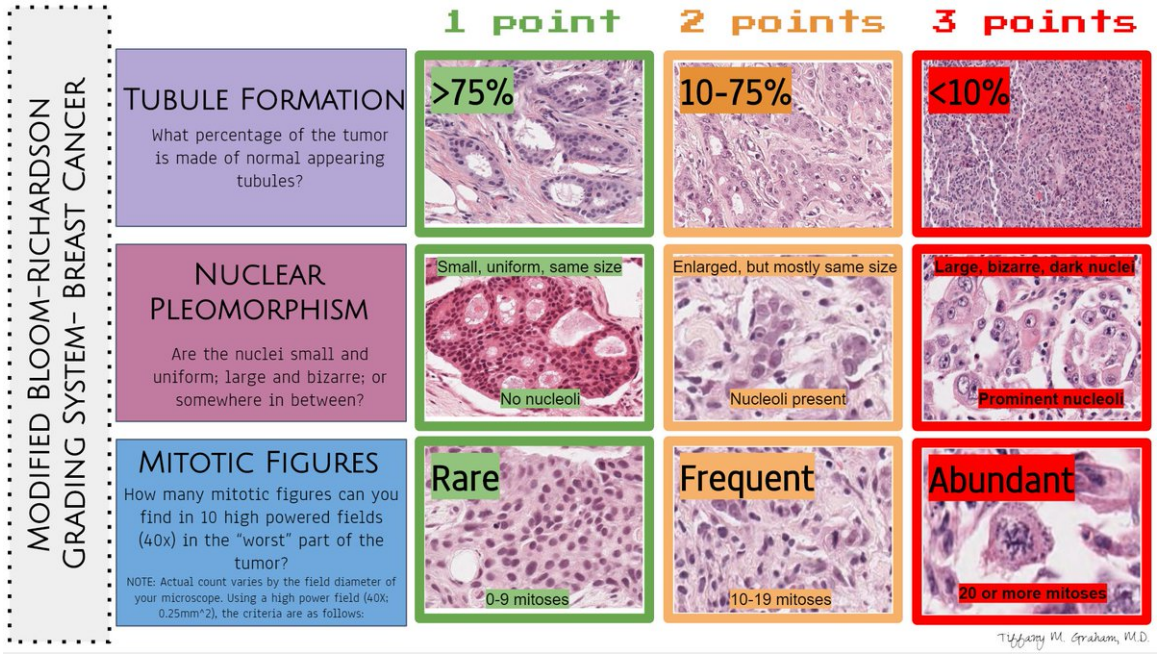

Figure 4: Bloom Richardson classification grading system. For each criterion (tubule formation, nuclear pleomorphism, and mitotic figure) a subscore is evaluated depending on the histological observations. The sub-scores are then summed to obtain a general score allowing to grade the tumor. Image extracted from `www.iheartpathology.net`.

As we have just seen, the grade is determined using different classifications. These classifications allow standardizing the breast tumor identification between the institutes and professions, making medical decisions based on a uniform scale. As explained in this section, the grading can be assessed through medical images or histological observations that we detail in the next section.

1.5 Breast detection and imaging procedures

As mentioned previously, breast imaging procedures are necessary to assess the grade of the breast tumor. In addition to the grade, the symptoms of the disease are especially

discrete, and planning regular checkups can ensure breast detection in the early stages. In this section, we recall the most common imaging procedure and methods in the context of breast cancer.

- **Palpation**. The clinical examination of the breasts is still of great interest for orienting the diagnostic strategy, assessing the prognosis, or guiding the therapeutic decision tree. The palpation has several benefits like the low cost of the clinical examination, it could be self-done or by a clinician, and it holds fundamental data that are not available from imaging data. For example, inflammatory signs, skin involvement by dermal-epidermal nodules, or nipple involvement by Paget's disease. Even after breast cancer treatment, the clinical examination remains useful for early diagnosis of complications related to treatment or possible loco-regional recurrence. Breast palpation and imaging are complementary techniques that must be combined. For the procedure, the woman is undressed to the waist, arms at her sides while sitting, then arms raised while lying down. Good palpation should be done on the hand flat, with the tip of the index and the medius, always on the side to be examined. It is necessary to make small circular movements of the fingertips with pressure of the gland on the costal side. The feel of the touch is crucial information for the medical expert and could already be used as a first diagnosis. For instance, the elastic behavior of a lesion could indicate a fibroadenoma while resistance could indicate the presence of a cyst which could be even firmer under tension. A stiff, protruding, angular tumor suggests cancer or a benign calcified lesion while a colloid or medullary cancer is often soft in consistency.

- **Mammogram**. A mammogram is an X-ray of the breasts. It enables to obtain images of the inside of the breast using X-rays and to detect any abnormalities. Usually, two X-rays are taken of each breast, one frontal and one oblique so that both sides of each breast can be compared. A mammogram can be performed either as part of a breast cancer screening or when symptoms are present. A screening mammogram is a gold standard for breast cancer evaluation, allowing the detection of small early-stage cancers, even before the appearance of symptoms. Meanwhile, a diagnostic mammogram is performed when a patient presents symptoms that may suggest breast cancer and consists of a basic mammogram focusing on suspicious areas. The mammogram is performed in a standing position, with the patient bare-chested. To obtain a good quality analysis and see the breast in its entirety, each breast is successively compressed between two plates to spread out the breast and avoid overlapping images (insufficient compression can prevent the detection of an abnormality). It provokes a sensation of compression usually unpleasant for women. The average standard mammogram takes 10 to 15 minutes. In certain conditions, especially when the breasts are too dense, mammography is less effective (adolescents, young women, breastfeeding). In these cases, a breast ultrasound is used.

- **Tomosynthesis or 3D Mammogram**. Traditional mammography projects the entire volume of the breast on a single plane (2D). Despite the image's high resolution,

over-projection effects can mask lesions or create pathology artifacts. Tomosynthesis, by acquiring multiple images at a very low dose, makes it possible to separate the different depths of the breast and eliminate the effects of lesion masking or over projection. As in mammography, the breast is compressed, but the X-ray tube moves in an arc instead of remaining stationary. This technique was prototyped in 1997 and has only been able to grow thanks to computing power improvements of computers. Initially, several hours were needed to reconstruct an image that is now obtained in a few seconds. The projection image (2D) is still necessary, either to have an overall view of the breast or to keep the possibility of comparing the current situation with the images previously obtained with conventional techniques. If a conventional image is taken in addition to the tomosynthesis, this procedure doubles the dose of exposure to the breast. This double irradiation is within the tolerated limits for breast examinations (e.g., in the FDA recommendations). However, all measurements must be taken to limit the radiation dose as much as possible. The technology of the synthetic 2D image is as reliable (or even more reliable in some cases) than that of traditional mammography. The latest scientific publications demonstrate that this is the right option [206, 239]. Indeed, the most recent studies have shown that this way of examining the breast provides the most information (30% more sensitivity than traditional mammography) with the most accuracy (30% more specificity than traditional mammography) while maintaining a minimal radiation dose (1 to 1.5 mSv), the equivalent of 3 to 4 months of natural radiation (radon, cosmic radiation, and associated terrestrial radiation) [75, 192].

- **Ultrasound**. Breast ultrasound uses ultrasound to produce painless images of the inside of the breast. A breast ultrasound is performed by a radiologist and is often completing a mammogram. It is useful to observe the liquid or solid nature of nodules palpated or discovered on the mammogram. A breast ultrasound can be performed for several reasons. First, following a mammogram when the latter has revealed an abnormality. In this case, the ultrasound allows the radiologist to analyze the anomaly in more detail. Secondly, when the density of the breasts does not allow for a good quality mammogram (usually the case for young women). Then, for pregnant women ultrasound is safe during pregnancy. Finally, it can be used to drive the radiologist when taking a sample (biopsy) of the irregularity, ensuring guidance in real-time. The examination is performed sitten on a chair, a gel is applied to the breasts to ensure good contact between the skin and the ultrasound probe. The radiologist will systematically examine all areas of the breast, taking up to 5 or 10 minutes

- **Magnetic Resonance Imaging**. MRI stands for Magnetic Resonance Imaging. MRI uses a large magnet to produce radio frequency waves to vibrate the numerous hydrogen nuclei that make up the tissues of the breast and thus produce images. This examination is generally proposed following the initial assessment performed by mammography and ultrasound. The patient lies on the stomach, with the breasts falling into a specific antenna. The examination time can last from 15 to 30 minutes

on average while trying to remain perfectly still. The injection of a contrast medium is necessary for this examination (Gadolinium is the most common). Breast MRI allows a better assessment of tumor size and multifocality/multicentricity of the breast tumor and may, therefore, in some situations, be beneficial in the preoperative workup, especially in cases of high breast density or lobular carcinoma. However, each new lesion detected by MRI must be confirmed by a biopsy under ultrasound or MRI before any change in the type of surgery, which leads to an increase in diagnostic procedures and preoperative delay. Furthermore, the use of breast MRI increases the rate of mastectomy, and the benefit on the rate of repeat surgery, recurrence, or survival is not known.

In the breast clinical pipeline, after using medical imaging to assess the tumor grade and shape, a decision concerning the treatment has to be concluded.

1.6 Different treatments

The choice of treatment for breast cancer depends on multiple factors: the age of the patient, menopaused, presence of hormone-sensitive cancers in the family, medical and surgical history, location of the tumor, unifocal or multifocal, histological type of the tumor, grade, hormone-sensitive, HER2 positive, molecular biology data, stage, overall health status, lifestyle choices. All those factors will influence the medical decision, hence, the treatment chosen. Among the different treatments for breast cancer, we find:

- **Surgical treatment**. Two types of surgery are possible: breast conserving surgery and non-conserving surgery.
  - **Breast-conserving surgery (lumpectomy or segmentectomy)** consists of removing the tumor and a limited amount of surrounding tissue. The conservative technique is proposed when the tumor is unique (or possibly when two tumors are close) and small enough compared with the size of the breast to be removed completely with a sufficient margin of healthy tissue around it. Radiation therapy to the breast is sometimes performed in addition to conservative surgery. If the tumor is large, neoadjuvant chemotherapy or hormone therapy (i.e., performed before surgery) may be used to reduce the size of the tumor and allow for conservative surgery. This operation is the most appealing as it is the least traumatic and does not necessitate reconstruction of the breast (or only partial). Unfortunately, it is a precise and delicate operation that requires experienced surgeons.
  - **Non-conservative breast surgery (mastectomy)** involves removing the breast, areola, and nipple. Non-conservative surgery is indicated if the tumor is too massive and neoadjuvant chemotherapy or hormone therapy is not possible. Other reasons could be the shape and location of the tumor that preclude conservative surgery, or if multiple tumors are present in the breast. In all cases, breast

surgery is completed by an axillary lymph node procedure, either sentinel lymph node removal or lymph node dissection. Following a mastectomy, it is possible to have breast reconstruction (either simultaneously or in a second stage). The effectiveness of this operation is undoubtedly and presents many advantages such as not requiring precise surgery, cheap cost (if we are not considering the cost of breast reconstruction), and rapid. Hence, the psychological trauma is enormous for the patient, and recovering from such an operation is demanding.

- **Radiation therapy**. Radiation therapy destroys cancer cells using X-rays. The radiation is directed precisely at the cancer cells to preserve as many healthy tissues and nearby organs. For in situ and invasive breast cancer, radiation therapy is often used in addition to surgery (adjuvant radiation therapy), but it can also be exclusive. It is focused on the breast if it has been preserved or on the chest wall after mastectomy and is extended to the axillary, supra-clavicular, and internal mammary lymph nodes if the first relays are reached.

- **Chemotherapy and targeted therapies**. Chemotherapy and targeted therapies are drug treatments used to treat breast cancer. They are general medical treatments that work on the whole body and reach the cancer cells wherever they are. While chemotherapy works on the mechanisms of cell division, targeted therapies block specific mechanisms of the cancer cells (block the amplification of the HER2 gene). Chemotherapy is not routinely used in the treatment of breast cancer. For "localized" invasive cancers, chemotherapy may be necessary after surgery (adjuvant chemotherapy) when the risk of recurrence is high. In the case of HER2 gene amplification, it is combined with a specific targeted therapy. These medical treatments can be started before surgery (neoadjuvant treatments) in case of progressive and inflammatory tumors and will be continued afterward. For metastatic cancers, the treatment is essentially based on chemotherapy, possibly combined with targeted therapy and/or hormonal therapy, with the aim of stabilizing the evolution of the disease. Several types of drug treatments exist for chemotherapy and targeted therapies. For adjuvant and neoadjuvant, we notably find Anthracyclines (doxorubicin and epirubicin), Taxanes (paclitaxel and docetaxel), 5-fluorouracil or capecitabine, Cyclophosphamide, and Carboplatin. For metastatic cancers, we additionally find Taxanes (paclitaxel, docetaxel, or albumin-bound paclitaxel), Ixabepilone, Eribulin, Anthracyclines (doxorubicin, liposomal doxorubicin, or epirubicin), Platinum agents (cisplatin), Vinorelbine, Capecitabine, and Gemcitabine.

- **Hormone therapy**. Hormone therapy consists of preventing the stimulation of cancer cells by female hormones (estrogen, progesterone) synthesized by the ovaries or fatty tissue after menopause: the methods used consist either in blocking the synthesis of these hormones in the ovaries or in using drugs that compete with these hormones. Hormone therapy is used alone or after chemotherapy and/or radiotherapy. Cancer must be hormone-sensitive, which is defined by the presence of hormone

receptors on tumor biopsies. In the case of "localized" hormone-sensitive invasive cancer, adjuvant hormone therapy is most often proposed after the combination of surgery/radiotherapy and possible chemotherapy: it is prescribed for a long period of at least 5 years. Hormone therapy can also be used before local treatment (neoadjuvant hormone therapy) to reduce the size of the tumor. In the case of metastatic cancer, hormone therapy may be prescribed alone or in combination with other drugs to stabilize the disease. There are several types of hormone therapy drugs such as Tamoxifen, Toremifene, Fulvestrant, or Aromatase inhibitors.

- **Experimental treatments**. Cryosurgery, also called cryoablation, cryosurgical ablation, or cryotherapy. The procedure uses extreme cold (liquid nitrogen or carbon dioxide) to freeze and destroy abnormal cells or tissue. Over the past years, cryosurgery was primarily used to treat tumors located outside the body. Today, it is also being evaluated and used to treat some tumors inside the body, such as breast cancer [216]. Encouraging antibody treatments, such as the Trodelvy combined with chemotherapy, showed acceptable results. At the time of writing, this treatment is available to any triple-negative breast cancer without progress after at least two other attempts at treatment.

Despite a wide variety of treatments, in this thesis, we will focus on breast-conserving surgery, notably on the numerical simulation of the intra-operative configuration knowing the imaging stance. The final aim is to indicate the tumor displacement to the surgeon without requiring supplementary volumic medical imaging in the surgical pose. Among the different methods for mathematically estimating breast displacement, we chose to use the Finite Element Method (FEM) and give a brief introduction in the next section.

1.7 Finite element background

1.7.1 Kinematics

Consider a deformable body $\mathcal{B}$. We denote the undeformed configuration Ω_0. The location of a particle of $\mathcal{B}$ in Ω_0 is denoted $\boldsymbol{X}$. Conversely, the deformed configuration is noted Ω, and the location of a particle of $\mathcal{B}$ in Ω is noted $\mathbf{x}$. A one-to-one mapping $\boldsymbol{\phi}$ maps the position of a particle $\boldsymbol{X}$ in Ω_0 to the position of the same particle $\boldsymbol{x}$ in Ω, i.e $\boldsymbol{x} = \phi(\boldsymbol{X})$. The configuration Ω can be obtained by $\boldsymbol{\phi}(\Omega_0) = \{\boldsymbol{\phi}(\boldsymbol{X}) \mid \boldsymbol{X} \in \Omega_0\}$. These definitions are depicted in figure 5.

Let us introduce the deformation gradient $\boldsymbol{F}$ that maps a line element $\mathrm{d}\boldsymbol{X}$ in Ω_0 to a line element $\mathrm{d}\boldsymbol{x}$ in Ω:

$$d\boldsymbol{x} = \boldsymbol{F} \cdot d\mathbf{X}. \tag{1}$$

We can write the deformation gradient and the Jacobian as

$$\boldsymbol{F} = \frac{\partial \boldsymbol{\phi}}{\partial \boldsymbol{X}}, \tag{2}$$

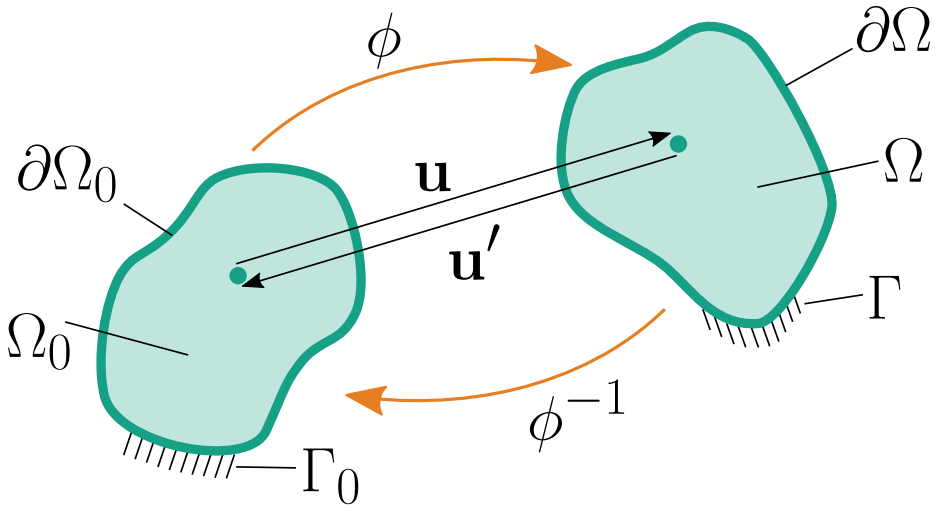

Figure 5: In a standard deformation analysis we compute the displacement vector $\boldsymbol{u}$ from knowledge of the undeformed configuration Ω_0. In the inverse deformation analysis the goal is to compute the displacement vector $\boldsymbol{u}'$ from knowledge of the deformed configuration Ω.

$$J = \det \boldsymbol{F}. \tag{3}$$

As $\boldsymbol{\phi}$ is a one-to-one mapping, $\boldsymbol{F}$ is not singular and can be inverted, resulting in $J \neq 0$. The Jacobian maps a volume element $\mathrm{d}\Omega_0$ in Ω_0 to a volume element $\mathrm{d}\Omega$ in Ω

$$\mathrm{d}\Omega = J \cdot \mathrm{d}\Omega_0. \tag{4}$$

For each point, we introduce the displacement $\boldsymbol{u}$ as the position difference between the deformed and the undeformed configuration

$$\begin{aligned} \boldsymbol{u}(\boldsymbol{X}) &= \boldsymbol{x} - \boldsymbol{X} \\ &= \boldsymbol{\phi}(\boldsymbol{X}) - \boldsymbol{X} \end{aligned} \tag{5}$$

The deformation gradient can also be written as a function of the displacement such as

$$\boldsymbol{F} = \frac{\partial \boldsymbol{\phi}}{\partial \boldsymbol{X}} = \frac{\partial \boldsymbol{u}}{\partial \boldsymbol{X}} + \boldsymbol{I} = \nabla_0 \boldsymbol{u} + \boldsymbol{I}, \tag{6}$$

where $\nabla_0(\bullet)$ is the gradient in Ω_0, with respect to the initial spatial position. The gradient in Ω, with respect to the deformed spatial position, is denoted $\nabla(\bullet)$. $\boldsymbol{I}$ is the usual second-order identity tensor. Similarly to the strain measure $\boldsymbol{F}$, we introduce the right Cauchy-Green strain tensor $\boldsymbol{C}$, its conjugate the left Cauchy-Green strain tensor $\boldsymbol{B}$ and the Green-Lagrange strain tensor $\boldsymbol{E}$

$$\mathbf{C} = \boldsymbol{F}^T \boldsymbol{F}, \tag{7}$$

$$\boldsymbol{B} = \boldsymbol{F}\boldsymbol{F}^T, \tag{8}$$

$$\boldsymbol{E} = \frac{1}{2}(\mathbf{C} - \boldsymbol{I}). \tag{9}$$

The non-linearities in $\boldsymbol{E}$ (Equation 9) are due to the term: $\nabla \boldsymbol{u} \cdot (\nabla \boldsymbol{u})^T$. For infinitesimal strain, the non-linearities are neglected, leading to the following approximation:

$$\boldsymbol{\varepsilon} \approx \frac{1}{2}\left(\nabla \boldsymbol{u} + (\nabla \boldsymbol{u})^T\right) \tag{10}$$

Hyperelastic material laws commonly use invariants of $\boldsymbol{C}$ and $\boldsymbol{B}$ to define their elastic energy

$$\mathrm{I}_{\boldsymbol{C}} = \mathrm{tr}(\mathbf{C}), \tag{11}$$

$$\mathrm{II}_{\boldsymbol{C}} = \frac{1}{2}\left((\mathrm{tr}(\mathbf{C}))^2 - \mathrm{tr}\left(\mathbf{C}^2\right)\right), \tag{12}$$

$$\mathrm{III}_{\boldsymbol{C}} = \det \mathbf{C}. \tag{13}$$

1.7.2 Strong form

At equilibrium in the deformed configuration, the balance of momentum can be written as follows

$$\nabla \cdot \boldsymbol{\sigma} + \rho \boldsymbol{b} = \mathbf{0}, \tag{14}$$

where $\boldsymbol{\sigma}$ is the Cauchy stress tensor, ρ is the density of the material in the deformed configuration and $\boldsymbol{b}$ are the external forces in the deformed configuration. Equation 14 is called the strong form and is written in the deformed configuration Ω. To write the strong form in the initial configuration Ω_0, we introduce the density of the material ρ_0 in the undeformed configuration and the first Piola-Kirchhoff stress tensor $\boldsymbol{P}$

$$\nabla_0 \cdot \boldsymbol{P} + \rho_0 \boldsymbol{b} = \mathbf{0}, \tag{15}$$

where $\boldsymbol{\sigma}$ and $\boldsymbol{P}$ are related by the Piola transform

$$\boldsymbol{\sigma} = \frac{1}{J}\boldsymbol{P}\boldsymbol{F}^T. \tag{16}$$

1.7.3 Weak form

The weak form is obtained by multiplying the strong form by test functions $\boldsymbol{\eta}$ and integrating over the whole domain. Equation 15 is written in the initial configuration and leads to

$$-\int_{\Omega_0} (\nabla_0 \cdot \boldsymbol{P}) \cdot \boldsymbol{\eta} \, \mathrm{d}\Omega_0 = \int_{\Omega_0} (\rho_0 \boldsymbol{b}) \cdot \boldsymbol{\eta} \, \mathrm{d}\Omega_0. \tag{17}$$

By using the divergence theorem we obtain

$$-\int_{\Omega_0} (\nabla_0 \cdot \boldsymbol{P}) \cdot \boldsymbol{\eta} \, \mathrm{d}\Omega_0 = \int_{\Omega_0} \boldsymbol{P} : \nabla_0 \boldsymbol{\eta} \, \mathrm{d}\Omega_0 - \int_{\partial\Omega_0} (\boldsymbol{P} \cdot \boldsymbol{n}) \cdot \boldsymbol{\eta} \, \mathrm{d}\partial\Omega_0, \tag{18}$$

where the colon operator : is the inner product between tensors, $\boldsymbol{n}$ is the outward unit normal at the boundary and $\partial\Omega_0$ the surface boundary of Ω_0. The quantity $\boldsymbol{P}\cdot\boldsymbol{n}$ is the traction boundary condition. We here assume that it is prescribed on a part Γ_0 of the boundary as $\boldsymbol{P}\cdot\boldsymbol{n}=\boldsymbol{t}_0$. On the remaining part of the boundary, we assume that the value of the displacement is given, i.e. a Dirichlet condition. We then obtain the equilibrium in the reference configuration

$$\int_{\Omega_0}\boldsymbol{P}:\nabla_0\boldsymbol{\eta}\,\mathrm{d}\Omega_0=\int_{\Omega_0}\rho_0\boldsymbol{b}_0\cdot\boldsymbol{\eta}\,\mathrm{d}\Omega_0+\int_{\Gamma_0}\boldsymbol{t}_0\cdot\boldsymbol{\eta}\,\mathrm{d}\Gamma_0. \tag{19}$$

Note that the boundary integral on the remaining part $\partial\Omega_0\setminus\Gamma_0$ vanishes due to the Dirichlet condition. By injecting equation 16 in the last equation 19, we obtain the weak form in the deformed configuration

$$\int_{\Omega}\boldsymbol{\sigma}:\nabla\boldsymbol{\eta}\,\mathrm{d}\Omega=\int_{\Omega}\rho\boldsymbol{b}\cdot\boldsymbol{\eta}\,\mathrm{d}\Omega+\int_{\Gamma}\boldsymbol{t}\cdot\boldsymbol{\eta}\,\mathrm{d}\Gamma. \tag{20}$$

1.7.4 Material model

So far, we have introduced the stress tensor and considered the kinematic relations, i.e., the relations between displacements and strains. To complete the field equations, we need a stress-strain relation, constitutive equations, or material model which sets a relationship between the stress and strain tensors. The simplest material model is the isotropic and linear elastic called Hooke's law. It sets the relation between the strain tensor $\boldsymbol{\varepsilon}$ defined in equation 10 and the stress tensor $\boldsymbol{\sigma}$ defined in equation 14 through the fourth-order elastic compliance tensor $\boldsymbol{C^e}$:

$$\boldsymbol{\varepsilon}=\boldsymbol{C^e}:\boldsymbol{\sigma}. \tag{21}$$

Due to the symmetry of the tensors, equation 21 could also be written using Voigt notations as

$$\begin{pmatrix}\varepsilon_{xx}\\ \varepsilon_{yy}\\ \varepsilon_{zz}\\ \varepsilon_{xy}\\ \varepsilon_{yz}\\ \varepsilon_{xz}\end{pmatrix}=\frac{1}{E}\begin{bmatrix}1&-\nu&-\nu&0&0&0\\ -\nu&1&-\nu&0&0&0\\ -\nu&-\nu&1&0&0&0\\ 0&0&0&2(1+\nu)&0&0\\ 0&0&0&0&2(1+\nu)&0\\ 0&0&0&0&0&2(1+\nu)\end{bmatrix}\begin{pmatrix}\sigma_{xx}\\ \sigma_{yy}\\ \sigma_{zz}\\ \sigma_{xy}\\ \sigma_{yz}\\ \sigma_{xz}\end{pmatrix} \tag{22}$$

E is the Young's modulus or the modulus of elasticity and describes the material stiffness in Pa. The higher the modulus, the more stress is needed to create the same amount of strain; an idealized rigid body would have an infinite Young's modulus. Conversely, a very soft material (such as a fluid) would deform without force and would have zero Young's modulus. ν is the Poisson's ratio describing the deformation (expansion or contraction) of material in directions perpendicular to the specific orientation of loading. Most materials

have Poisson's ratio values ranging between 0.0 and 0.5. For soft materials, such as rubber, Poisson's ratio is near 0.5. For open-cell polymer foams, Poisson's ratio is near 0 since the cells tend to collapse in compression. Many typical solids have Poisson's ratios in the range of 0.2–0.3.

The Hooke's law is a suitable material model for isotropic linear materials. Hence, constitutive equations are established depending on the phenomenology of the object (i.e., hyperelastic, anisotropic, plastic, viscoelastic). A description of suitable models for highly deformable objects is described in sections 3.2.2, 4.2.1, 4.3.3, 4.4, and 5.4.

Finally, numerically solving the strong form requires discretizing the integration domain using Galerkin methods for instance. Additionally, to avoid any rigid body motions, boundary conditions have to be prescribed to constrain the problem. These processes are further detailed in section 4.2.2.

Glossary

blendshape	Blendshapes are a deformed version of a template mesh and are stored as a series of vertex positions. These blendshapes constitute an anatomical space of deformation and can be linearly combined to obtain multiple body shapes .
registration	Registration is the process that allows to map the model on the data of the patient. In our study, registration is a method for fitting the model on the 3D scans of the patients.
rigging	Rigging is a computer animation technique in which an articulated object is represented in two parts: a surface representation used to draw the object (called the mesh or skin) and a hierarchical set of interconnected parts (called bones, and collectively forming the skeleton or rig).
skinning	Skinning is the process of binding the surface representation to the rig through a blend weight matrix to adjust the influence of each bone.

Nomenclature

In this paper, $\mathbb{R}$ represents the vector space of real numbers. $\mathbb{R}^n$ is a vector of dimension n, $\mathbb{R}^{n\times m}$ is a matrix of dimension $n \times m$ and $\mathbb{R}^{n\times m\times j}$ is a n-dimensional vector of $m \times j$ matrices.

A	Number of blendshapes	$\in \mathbb{R}$
K	Number of bones	$\in \mathbb{R}$
N	Number of mesh vertices	$\in \mathbb{R}$
V	Matrix of vertices positions of the scan	$\in \mathbb{R}^{N\times 3}$
Blendshape		
B	Matrix of deformed vertices positions after blendshapes application	$\in \mathbb{R}^{N\times 3}$
b	Vector of matrix shape displacement	$\in \mathbb{R}^{A\times N\times 3}$
Optimisation		
E_D	Data-fitting energy	$\in \mathbb{R}$
E_J	Joint regularisation energy	$\in \mathbb{R}$
E_S	Scale regularisation energy	$\in \mathbb{R}$
E_{BS}	Blendshape regularisation energy	$\in \mathbb{R}$
E_L	Landmark-fitting energy	$\in \mathbb{R}$
Model parameters (DOFs)		
α	Vector of blendshape weights	$\in \mathbb{R}^{A}$
$R(q)$	Vector of rotation matrix from the quaternion q	$\in \mathbb{R}^{K\times 3\times 3}$
S	Vector of scale matrix	$\in \mathbb{R}^{K\times 3\times 3}$
T	Vector of offset vector	$\in \mathbb{R}^{K\times 3\times 1}$
v	Matrix of vertices positions of the template mesh	$\in \mathbb{R}^{N\times 3}$
Skinning		
M	Matrix of deformed vertices positions after skinning application	$\in \mathbb{R}^{N\times 3}$

$R(q^*)$	Vector of initial rotation matrix from the quaternion q	$\in \mathbb{R}^{K\times 3\times 3}$
$T(q^*)$	Vector of initial offset vector	$\in \mathbb{R}^{K\times 3\times 1}$
w	Matrix of blend weights	$\in \mathbb{R}^{K\times N}$

2 A rigged model of the breast for preoperative surgical planning [1]

Abstract

In breast surgical practice, drawing is part of the preoperative planning procedure and is essential for a successful operation. In this study, we design a pipeline to assist surgeons with patient-specific breast surgical drawings. We use a deformable torso model containing the surgical patterns to match any breast surface scan. To be compatible with surgical timing, we build an articulated model through a skinning process coupled with shape deformers to enhance a fast registration process. On one hand, the scalable bones of the skinning account for pose and morphological variations of the patients. On the other hand, pre-designed artistic blendshapes create a linear space for guaranteeing anatomical variations. Then, we apply meaningful constraints to the model to find a trade-off between precision and speed. The experiments were conducted on 7 patients, in 2 different poses (prone and supine) with a breast size ranging from 36A and 42C (US/UK bra sizing). The acquisitions were obtained using the depth camera Structure Sensor, and the breast scans were acquired in less than 1 minute. The result is a registration method converging within a few seconds (3 maximum), reaching a Mean Absolute Error of 2.3 mm for mesh registration and 8.0 mm for breast anatomical landmarks. Compared to the existing literature, our model can be personalized and does not require any database. Finally, our registered model can be used to transfer surgical reference patterns onto any patient in any position.

2.1 Introduction

In 2018 breast cancer was the second most prevalent cancer with more than 2 million cases and an increasing incidence rate of 0.3% per year [54]. Surgery remains one of the most common treatments. In 2016, nearly one-half of patients with early-stage (Stage I or II) breast cancer underwent breast-conserving surgery [54].

The least invasive and traumatic operation, lumpectomy, consists of removing the breast tumor, including surrounding tissues [189]. Before surgery, the surgeon draws surgical patterns on the patient in a preoperative position (standing). Then, the surgeon instantly operates in the intra-operative stance (supine) [57]. These patterns, also called surgical drawings, are part of the preoperative planning procedure. Most of the time, they are noticeable anatomical landmarks or a visual map that will guide the surgeon during the surgery [57]. The operation success is highly dependent on the preoperative planning and will influence the final breast shape [177]. However, surgical drawings require experience and accuracy that can be challenging for junior surgeons, especially when no gold standard is established.

In this study, we focus on devices and methods that can satisfy two constraints:

[1] Reproduced from: A. Mazier, S. Ribes, B. Gilles, S.P.A. Bordas, A rigged model of the breast for preoperative surgical planning, Journal of Biomechanics, Volume 128, 2021, 110645, ISSN 0021-9290, `https://doi.org/10.1016/j.jbiomech.2021.110645`.

- an intuitive acquisition device capable of capturing the external shape of the patient as quickly as possible to be compatible with surgical requirements,
- a deformable upper-torso model embedding surgical drawings that can rapidly fit the patient scan.

To satisfy the first constraint, devices like 3D surface scanning can fulfill the surgical timing criteria [37]. Initially, these devices were expensive and limited to applications such as computer graphics. Nowadays, they are affordable and widely used for plastic surgery assistance [219]. To satisfy the second constraint, many techniques have been developed. Among them, non-rigid registration methods allow to reconstruct patients' breasts with high precision, template-free, and markerless by solely using a low-cost depth camera [117, 118]. The major drawback is the execution time ranging between 1 to 2 hours, making the method unpracticable for our application. The finite element method relies on physics-based equations to compute realistic deformations of the model [62] and can be improved with free form deformers for higher precision [19, 122]. This method is computationally expensive and solving partial derivative equations requires information which is difficult to obtain (e.g. mechanical and rheological properties, boundary conditions, loading). Moreover, free form deformers require control points to improve the registration accuracy at the cost of an increased computation time. 3D morphable models (3DMM) used with landmark constraints are fast, accurate, and can support different inputs such as 3D scans or 2D images [110, 194]. Despite a compatible timing, the method requires anatomical landmarks to provide an initial shape and relies on a consequent database that is not compatible with our database size. Learned-models are widely used for their robustness to pose variation, flexibility, speed, and efficiency but require a large dataset to train the model [20, 36]. The Skinned Multi-Person Linear (SMPL) model uses corrective body-shape and pose-dependent shape learned from thousands of 3D body scans to provide a real-time, partially open-source, and realistic articulated model [130]. Despite viable medical applications [97], the model relies on an unadapted learning database made of women wearing bras. It makes it impossible for us to capture anatomical details that are only visible on bare breasts. To the authors' knowledge, there is no open-source database of 3D scans of bare breasts available.

In this paper, we propose a flexible model allowing to fit a set of patients in different surgical positions, without any previous training phase or mesh pre-treatment. To ensure a quasi-instantaneous patient fitting, we developed a simple articulated model made of virtual bones to permit pose modifications, namely skinning [13, 101, 104, 121]. This model is made more adaptive by allowing bone scalability to cater for variations in body morphologies. Moreover, we used a simple linear model of body shapes to account for morphological variations in breast shape, also known as blendshapes [108, 125, 136, 169]. In this work, we assumed that an accurate registration enables a mapping of the model's surgical drawing to any patient scan. Indeed, the model gathers anatomical features and surgical patterns made by a senior surgeon, thus providing a gold standard for inexperienced surgeons. The final aim of this study is to provide a pipeline to assist junior surgeons with

preoperative breast surgical drawings for lumpectomy surgery, including, a patient-specific model ready for biomechanical simulations.

2.2 Method

2.2.1 Participants

The study was performed on 7 women, in preoperative and intra-operative positions. The preoperative configuration corresponds to the stand-up position where the surgeon draws the surgical patterns on the patient. The intra-operative stance corresponds to the supine position (the patient lays on the back) for the surgery. Their ages varied between 47 and 69 years and the surgeon manually measured their breast size from 36A to 42C in US/UK bra sizing [235]. We noticed one notable case of breast asymmetry (one breast had a different size or volume to the other one). All the patients were diagnosed with breast cancer and chose lumpectomy as the most suitable treatment, under medical recommendation. We obtained consent from the 7 patients for the study and a favorable opinion from the "Comité Local d'éthique Recherche". It has been precisely obtained on the 07/16/2017 under the label 2017_CLER-MTP_07-04. The study was declared in the registry of the CNIL (MR003) under the name of the "Centre Hospitalier Universitaire" (CHU) of Montpellier and registered on the ClinicalTrials website `https://www.clinicaltrials.gov/ct2/show/study/NCT03214419`.

2.2.2 Instruments

To obtain a 3D surface mesh of the patient we used the depth camera Structure Sensor 3D Scanning by Occipital. This scanning device suffers from a high noise-sensitivity and the possible creation of spurious gaps within the mesh. However, it satisfies our criteria in terms of rapid acquisition time, a user-friendly interface, and reasonable price.

2.2.3 Procedures

After sketching the preoperative surgical drawing, the surgeon used the device mounted on a digital tablet to scan the upper-body of the patient. To obtain global features of the patient, the surgeon circled around the target at approximately 1 m. Otherwise, to capture more complex shapes like the breast fold, the surgeon should be closer to the target (around 30 cm). The device aimed at the patient for 20 seconds to 1 minute, depending on the desired resolution. The surgeon performed the 14 scans without any previous training. The result was a surface mesh of the patient obtained in less than 1 minute, including the scan and the reconstruction.

2.2.4 Rigging

Each bone of the rig is considered as a rigid-scalable object, meaning that each bone will have 9 absolute degrees of freedom (DOFs) (3 rotations, 3 translations, and 3 for the scale).

The relative motion of the bones is constrained by the joints. We computed local rotations and translations of the joints by computing relative transformations at a rigid point attached to the scalable bones, represented by the spheres in figure 6a. Constraints were then applied through Lagrange multipliers on both local rotations and translations [217]. Quaternions were used to define the axis angle of every bone. From this, we computed a local rotation matrix.

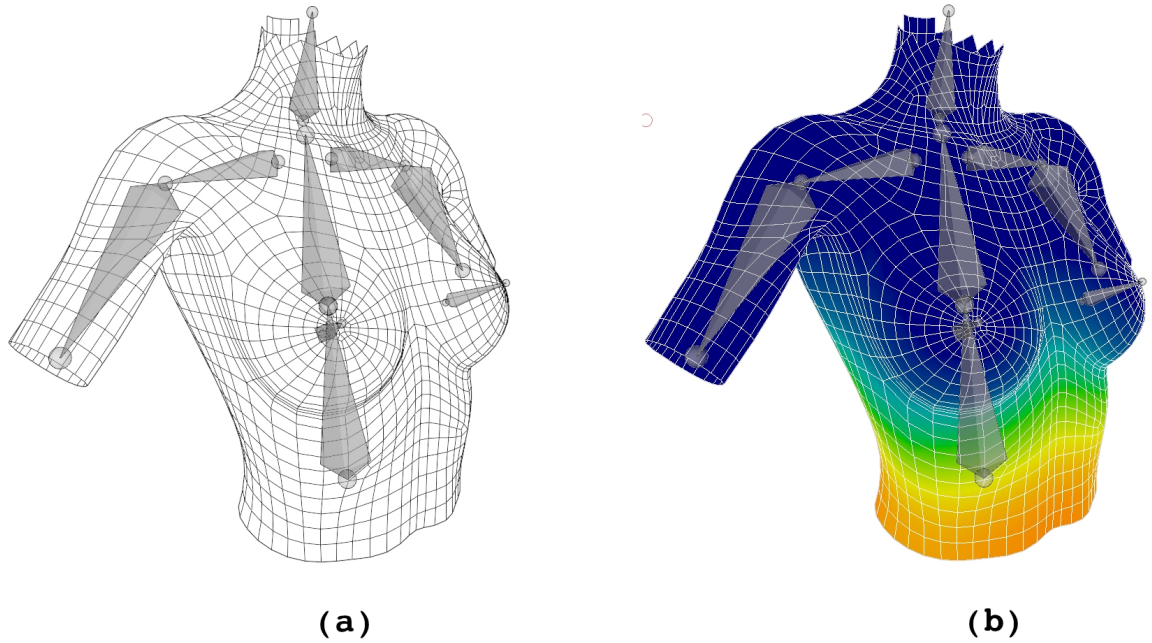

Figure 6: (a) Template mesh skin (in wire-frame) and virtual bones (in grey). (b) Blend weight colormap associated to the lower bone (red for a weight of 1 and blue for a weight of 0).

2.2.5 Skinning

We used blend weights to adjust the influence of each skeletal bone on the skin. In figure 6b, we displayed the colormap of the blend weights associated with the lower bone. The red regions are rigidly attached to the bone and follow the motion of the bone. Conversely, blue areas are not affected by the movements of the bone. The blend weight matrix can be manually given by the user or can be automatically calculated by 3D modeling software such as Blender [2].

In this study, the model was made of $K = 9$ bones and $N = 2200$ vertices as shown in figure 6a. We used the following notations: $R_j(q)$ the rotation matrix of the j-th bone obtained from the quaternion rotation, T_j the associated vector bone offset and S_j the

[2] https://www.blender.org/

scale matrix with a scale coefficient for each direction. As a result, with a given set of K bones, bones rotation $R(q) = [R_1(q), ..., R_K(q)]$, bone offset $T = [T_1, ..., T_K]$, bone scale $S = [S_1, ..., S_K]$. By calling the elements of the blend weight matrix $w_{j,i}$ ($w \in \mathbb{R}^{K \times N}$) and the rest template mesh vertices v_i ($v \in \mathbb{R}^{N \times 1}$). The computed vertices M_i are given by the equation of the Linear Blend Skinning (LBS):

$$M_i(R(q), S, T) = \sum_j^K w_{j,i}(R_j(q) S_j v_i^T + T_j), \tag{23}$$

2.2.6 Blendshapes

For our model, an artist created $A = 55$ blendshapes affecting global features such as shoulders or belly size as well as more local ones establishsuch as nipples and aureole shapes. Let v denotes the vertex positions of the template mesh, B the blendshape function computing the deformed vertex positions and b_k the k-th shape displacement matrix, with $v, B, b_k \in \mathbb{R}^{N \times 3}$. Blendshape displacements provide a set of basis vectors that define a linear space which is used to generate a vector space, onto which the patient's shape is projected.

$$B(\alpha_k) = v + \sum_k^A \alpha_k b_k, \tag{24}$$

where A is the number of blendshapes and $\alpha_k \in \mathbb{R}^A$ the linear blendshape weights affected to each k-th blendshape. To ensure convexity and invariance for rotation and translation, these weights should fulfil the following conditions: $\sum_{i=1}^n \alpha_k = 1$ and $\alpha_k > 0, \forall k \in [1, n]$. These 55 blending weights (α_k) can be used as DOFs for our deformable model, we call α the vector storing the α_k values.

By combining different body shapes, the model can cover a large deformation space to fit several morphologies (figure 7) and can be easily enriched by adding more blendshapes.

2.2.7 Final model

In the final model, we combined the effect of blendshapes mixed with the scalable bones from the skinning. By inserting equation 24 into 23, we obtained:

$$M_i(R(q), S, \alpha, T) = \sum_j^K w_{j,i}(R_j(q) S_j B_i^T(\alpha) + T_j), \tag{25}$$

To avoid distortion of the model and to regularize the energy minimization we defined 3 additional energy terms. A scale energy E_S to penalize the scale matrix of each bone towards its original scale (with $\mathbb{I}_3$ the order 3 identity matrix). A blendshape energy E_{BS} to regularize the blendshape weights towards 0 and a joint energy E_J to regularize the translations and the relative rotations of each joint to their initial configurations, respectively

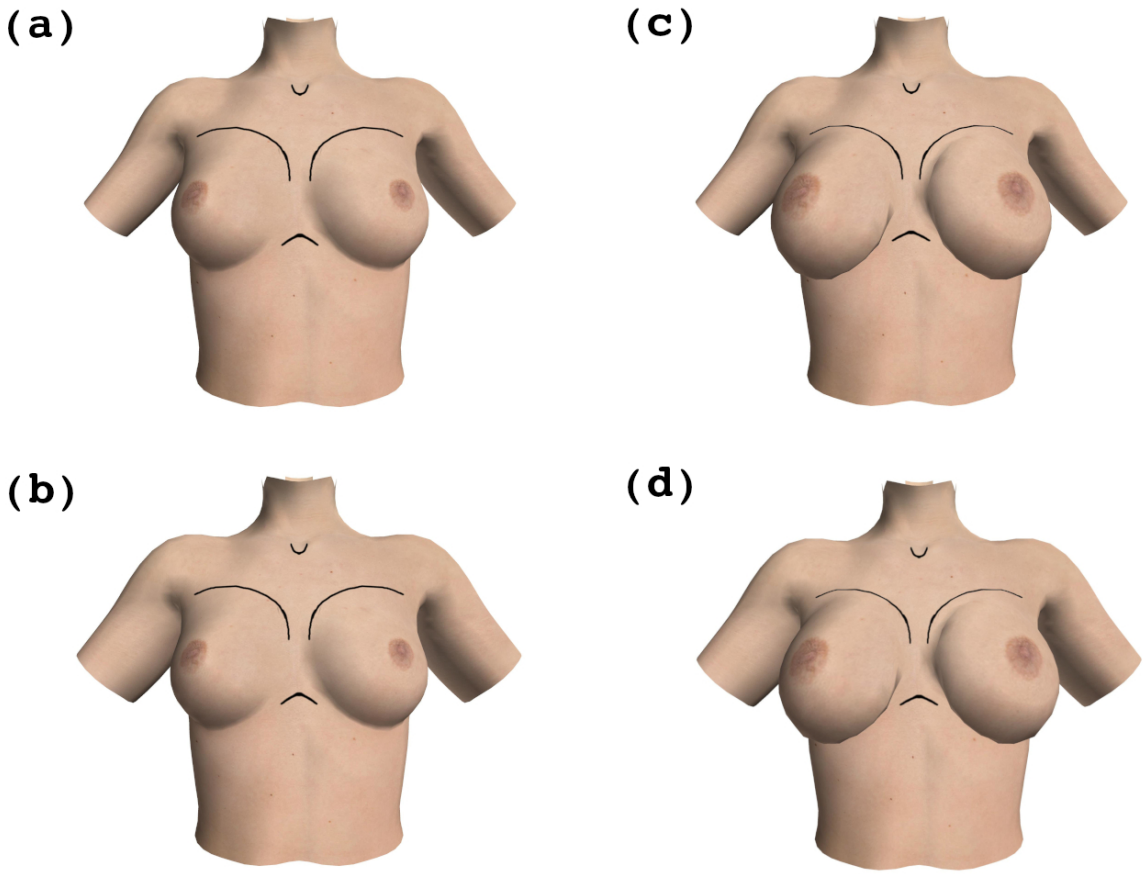

Figure 7: (a) Template mesh. (b) First blendshape affecting the breast size (α0b0 with α0=1). (c) Second blendshape affecting the arm size (α1b1 with α1=1). (d) First and second blendshapes activated (α0b0+α1b1 with α0=α1=1).

T_j^* and $R_j(q^*)$ for the j^{th} bone. With $\| \bullet \|$ the Euclidean norm, we obtained the following equations:

$$E_S(S) = \sum_j^K \| S_j - \mathbb{I}_3 \|^2, \tag{26}$$

$$E_{BS}(\alpha) = \| \alpha \|, \tag{27}$$

$$E_J(R(q), T) = \sum_j^K \| \log(R_j(q^*) R_j^{-1}(q)) \|^2 + \| T_j - T_j^* \|^2 . \tag{28}$$

2.3 Registration

We chose the Simulation Open Framework Architecture (SOFA [69]) to perform the registration of our model to the 7 patients in preoperative and intra-operative stance. To fit the skin of the model to the scan of the patient, we chose to minimize the closest-point distances such as in the Iterative Closest Point (ICP) algorithm [18]. More precisely, we used an octree structure to find the closest vertex on the scan from source vertices. Then, we projected the source point onto the closest primitive (triangle, edge, or point) around each closest vertex. This allows for a more accurate registration rather than using point-to-point distances and differentiating 29 with respect to M_i can be easily done by computing the normal vectors of the triangles of the scan. As the scanning process depends on the surgeon, some scans can be incomplete with only the front view and artifacts, as shown in figure 8a. To improve the robustness of the algorithm against noise and local solutions, filters to reject outliers were added (distance and normal vector threshold).

Based on correspondences established at each iteration, we identified the best set of parameters that minimized the distance from the scan to the deformed model. We defined a data energy term that penalizes the squared Euclidean distance between the model vertices M_i and the target mesh vertices V_j according to the closest point algorithm:

$$E_D(R(q), S, \alpha, T) = \sum_{(i,j)}^{N_{CP}} \parallel d_{CP} \parallel^2 = \sum_{(i,j)}^{N_{CP}} \parallel M_i(R(q), S, \alpha, T) - V_j \parallel^2, \tag{29}$$

where N_{CP} represents the index pairs found by the closest point algorithm and d_{CP} the distance between V_j the closest point from M_i on the set of target mesh triangles. The total energy to minimize is :

$$E_{\text{tot}}(R(q), S, \alpha, T) = \frac{1}{\lambda_D} E_D + \frac{1}{\lambda_S} E_S + \frac{1}{\lambda_{BS}} E_{BS} + \frac{1}{\lambda_J} E_J \tag{30}$$

with $\lambda_D = 10e^{-3}, \lambda_S = 10e^{-2}, \lambda_{BS} = 10e^{-3}, \lambda_J = 10e^{-2}$ set empirically. We used a regularized Newton algorithm and stop the minimization when we reached our convergence threshold based on the distance compared to the last iteration.

As described in [217], we iteratively minimized equation 29 using an implicit integration of Newton's equation, using a compliant formulation to handle both stiff constraints (joint translations and rotations) and elastic terms in a stable manner. The solver finds a compromise between minimizing the distance to the data and the distortion of the reference model.

According to [67], we manually added 12 anatomical landmarks on all scans and on the model in preoperative and intra-operative stance (respectively figure 8a and 8b). Among the 12 landmarks, 2 have no symmetry along the sternum from top to down: the sternal notch and the xiphoid. Then, 6 symmetric landmarks (right and left) from top to bottom: the acromial extremity of the clavicle, the mid-axillary point, the pectoralis the insertion in the arm, the nipple, and the lowest breast point with respect to the vertical body axis.

These landmarks were chosen for their easy reproducibility, as validation criterion for the registration, and to possibly strengthen our registration.

Our registration approach offers the possibility to combine automatic vertex matching (closest-point algorithm) with manual vertex matching (landmarks). By enabling the surgeon to interactively select these landmarks, we can add a landmark energy term to penalize the squared distance between the model landmarks and the scans landmarks. The landmark energy E_L expression is similar to equation 29, but we replaced the closest-points index pairs with the corresponding landmarks index pairs.

$$E_{\text{fin}}(R(q), S, \alpha, T) = E_{\text{tot}} + \frac{1}{\lambda_L} E_L, \tag{31}$$

with $\lambda_L = 10e^{-4}$ also set empirically.

Finally, we drew on the model the surgical drawing of a lumpectomy. They were made of 4 shapes: 2 arrows delineating the upper and lower sternum, 2 curves delimiting the right and left breast (figure 8b).

2.4 Statistics

To assess the quality of the registrations, we used the Python packages NumPy [93] and SciPy [225] to calculate statistical quantities. For each of the 14 registrations, we recorded the time needed to reach the convergence criteria of the solver. Then, we evaluated the surface registration error by calculating the final distances between the vertices of the model and the vertices of the scans (d_{CP}). We did the same for the landmarks registration error by calculating the distances between the landmarks of the model and the landmarks of the scans (d_L). For each distance vector, in order to avoid signed distances, we computed the MAE $= \frac{\sum_{i=1}^{n} |d_i|}{n}$, where $n = N_{CP}$ and $d = d_{CP}$ for the surface MAE, whereas $n = 12$ and $d = d_L$ for the landmarks MAE. Finally, we computed the standard deviation, minimum and maximum values of the absolute distances.

2.5 Results

Table 2 shows the result of the 14 registrations and the figure 8b the visual result of the registration of our model on 2 patients. On average, the registration process took a bit more than 2 seconds. The surface MAE for preoperative and intra-operative were respectively 2.41 and 2.28 mm, while the results were higher for the landmarks MAE, 8.46 and 7.41 mm. In figure 8c, we also display the surface scan of the patient with the prediction of the surgical drawing of our model (in white) compared to the surgeon's drawing (in black).

Furthermore, we demonstrated the impact of the landmarks on the registration process in figure 9. Indeed, without using the landmarks in the registration, we achieved a MAE of 2.01 cm between the landmarks of the model and the scans, which was too large. By taking the 12 landmarks into account, we improved the landmarks MAE to 8.03 mm without increasing the surface MAE.

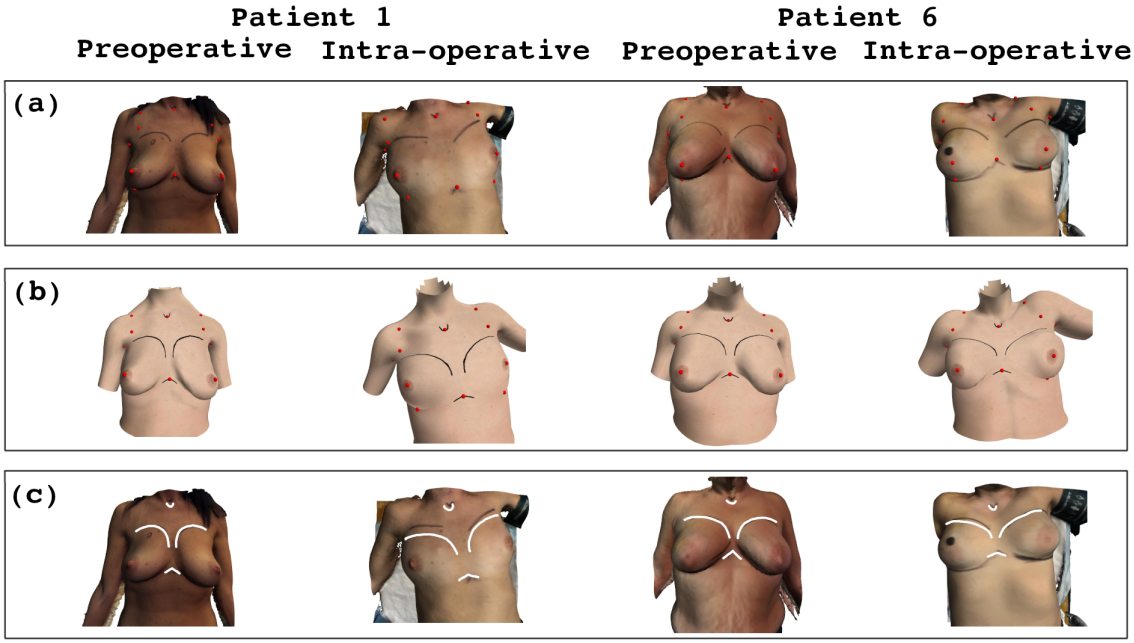

Figure 8: Comparison of surgical pattern drew by the surgeon and guessed pattern by the model. (a) Scan of patients 1 and 6 in preoperative and intra-operative stance. The red spheres represent the 12 landmarks described in [Farinella et al., 2006] and the black shapes are the surgical drawing made by the surgeon on the patient. (b) Model registered on the preoperative and intra-operative patient scan. The red spheres represent the 12 landmarks described in [Farinella et al., 2006] and the black shapes are the surgical drawing made by the surgeon on our model. (c) Superimposition of the surgical drawing made by the surgeon on the patients (black) and our surgical drawing estimation of our model (white).

Moreover, we studied the effect of blendshape numbers on the performances of the model. As shown in figures 10 and 11, for all patients and the 2 configurations, increasing the number of blendshapes decreased the surface MAE. Hence, we observed a non-constant loss that seemed to be triggered after reaching a certain number which was not the same for all patients.

Finally, we conducted a sensitivity analysis of the model parameters in both configurations. As we empirically chose the values of $\lambda_D, \lambda_S, \lambda_{BS}, \lambda_J$ and λ_L, we investigated the impact of these parameters on the surface and landmarks MAE. To that extent, we modified one particular parameter while fixing all other parameters to their original value and calculated the mean MAE for all patients. As mentioned in section 2.3, these parameters represent the impact of specific energies on the entire system (equation 31). The results are displayed in preoperative configuration, in figures 12 and 13, but the curves are similar in intra-operative stance.

Preoperative configuration

Patient	Time (s)	Surface distance error			Landmarks distance error			
		MAE (mm)	SD (mm)	Max (mm)	MAE (mm)	SD (mm)	Max (mm)	Min (mm)
0	1.98	2.31	3.24	23.7	8.24	3.42	13.8	3.74
1	2.17	2.22	4.06	45.6	8.70	4.99	16.2	4.68
2	2.11	2.58	2.94	35.9	11.03	5.88	25.0	2.34
3	1.32	2.23	2.15	14.5	8.98	3.97	16.2	1.61
4	1.38	2.43	2.88	25.0	8.17	6.54	20.7	0.94
5	2.23	2.23	3.39	23.3	7.22	3.46	11.9	1.21
6	1.79	2.87	3.71	51.5	6.89	5.72	22.9	3.53
Mean	**1.85**	**2.41**	**3.19**	**31.4**	**8.46**	**4.85**	**18.1**	**1.98**

Intra-operative configuration

Patient	Time (s)	Surface distance error			Landmarks distance error			
		MAE (mm)	SD (mm)	Max (mm)	MAE (mm)	SD (mm)	Max (mm)	Min (mm)
0	2.01	2.39	3.48	31.9	9.36	3.68	14.9	3.40
1	1.90	2.11	3.00	17.7	7.96	4.13	15.2	1.54
2	1.99	2.14	3.13	20.1	7.23	3.74	14.0	1.02
3	2.54	2.33	2.78	19.6	3.95	3.40	12.3	0.37
4	2.14	1.85	2.78	24.3	7.32	3.44	11.2	0.21
5	3.01	2.44	2.86	20.4	7.03	4.91	15.8	2.84
6	1.80	2.70	3.43	30.6	10.39	4.36	19.6	2.85
Mean	**2.20**	**2.28**	**3.06**	**23.5**	**7.61**	**3.95**	**14.7**	**1.75**

Table 2: Registration statistics errors for preoperative and intra-operative stance.

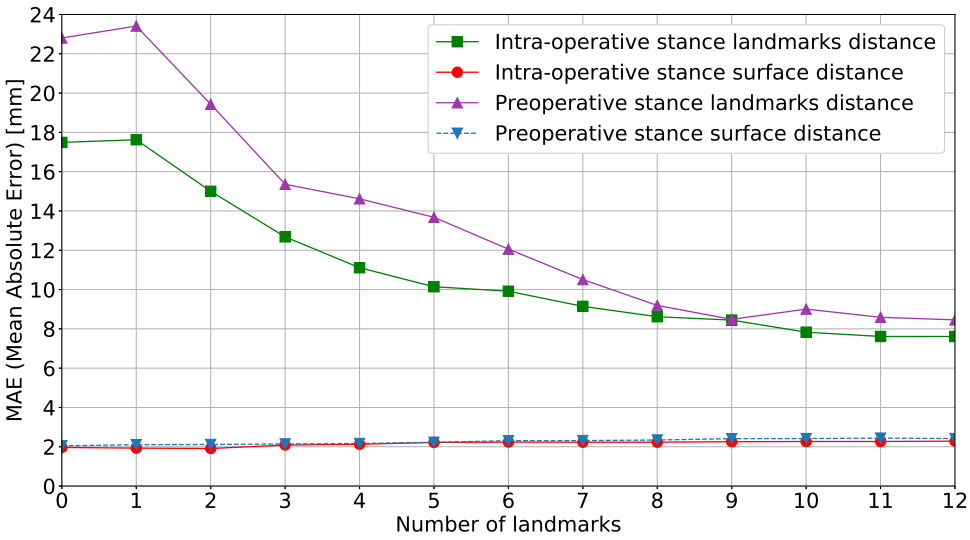

Figure 9: Mean Absolute Error (MAE) by increasing the number of landmarks in equation 9 according to [67].

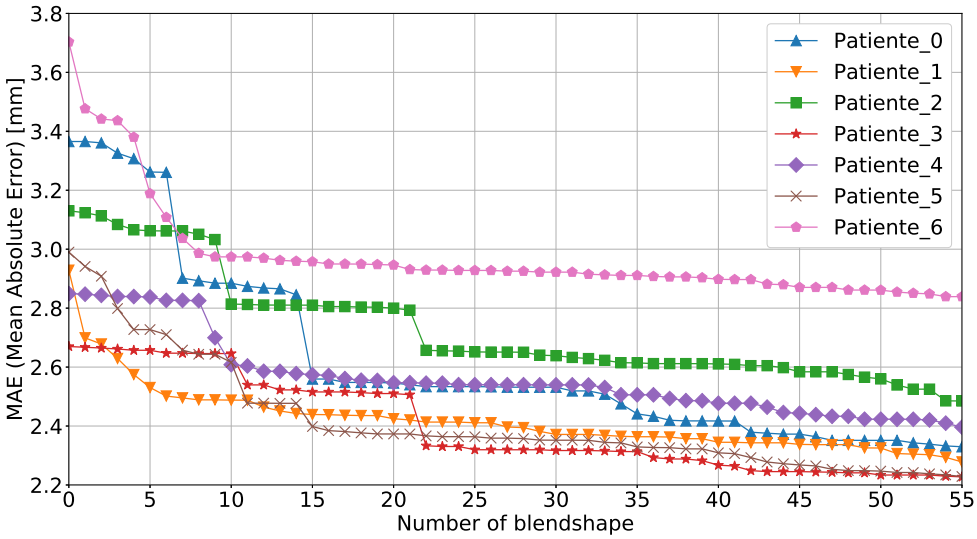

Figure 10: Mean Absolute Error of the surface (surface MAE) by increasing the number of blendshape in preoperative stance.

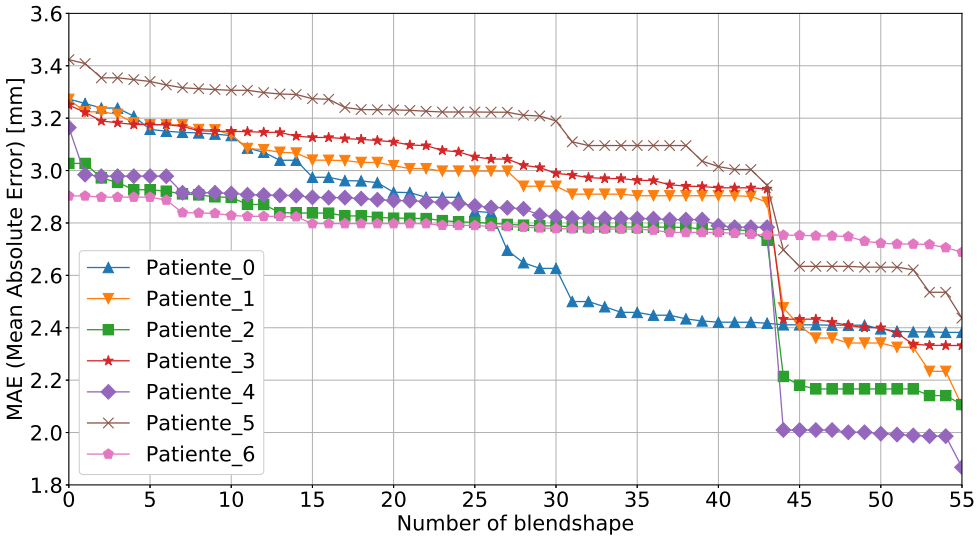

Figure 11: Mean Absolute Error of the surface (surface MAE) by increasing the number of blendshape in intra-operative stance.

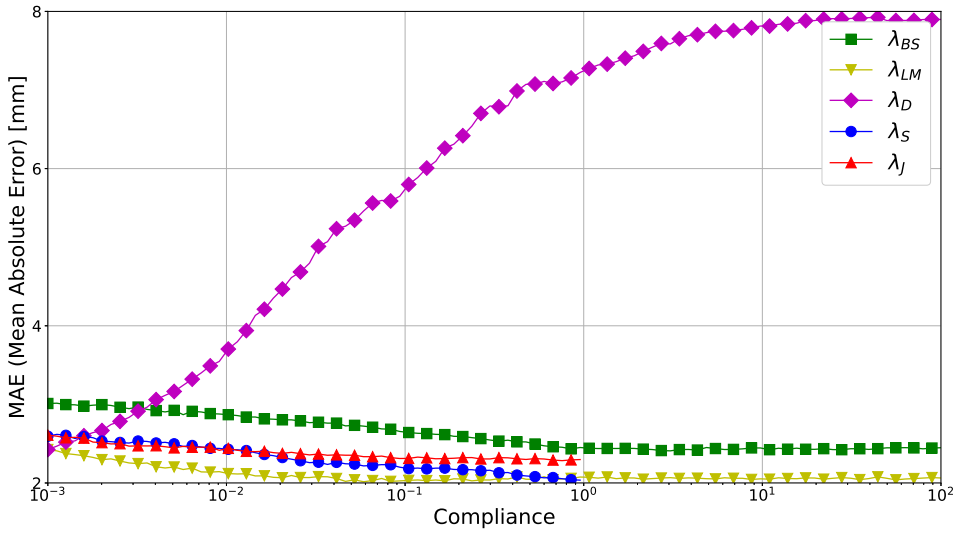

Figure 12: Sensibility analysis of the surface Mean Absolute Error (surface MAE) of the model in preoperative stance.

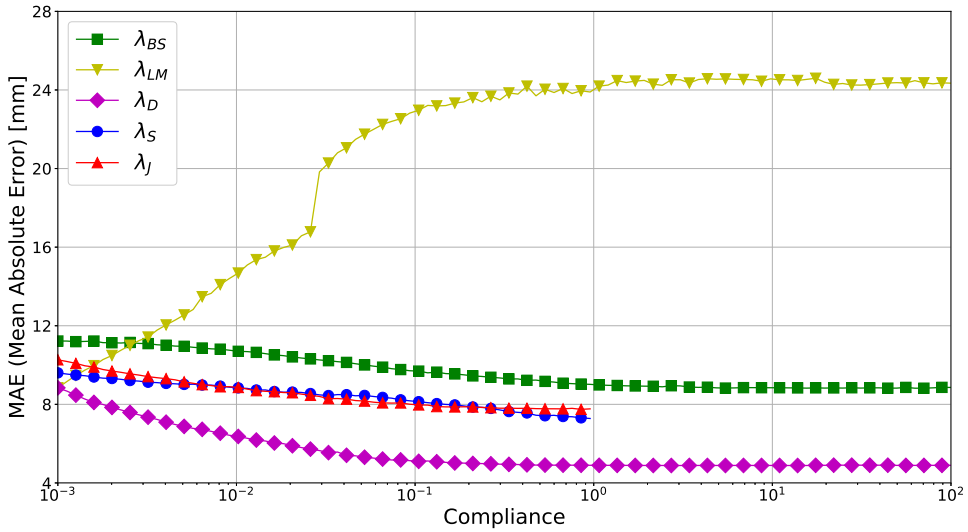

Figure 13: Sensibility analysis of the surface Mean Absolute Error (surface MAE) of the model in preoperative stance.

2.6 Discussion

The research presented shows that the registration is efficient and independent of the pose or the morphology. Indeed, we observed a slight difference in surface and landmarks MAE between the preoperative and the intra-operative position. Indeed, we noticed a fair matching between the surgical patterns drew by the surgeon and the prediction of our model (figure 8c). These results support our hypothesis that an accurate registration (low MAE) leads to an overlapping of the surgical drawings of the model (made by the senior surgeon) and of the scan, becoming a gold standard for inexperienced surgeons. The registration results obtained in this study are congruent with those present in the literature. [194] used 3D Morphable Models of the breast to fit two possible inputs: 2D photos and 3D scans. For 310 3D scans, an average distance error of 2.36 mm in 3.15 s was obtained with a standard deviation of 0.18 mm. While these results are similar in magnitude to those of the present study, [194] produced a lower standard deviation error (probably due to the high number of scans) but did not treat articulated movements of the patients. [19] used Free Form Deformers to register MRI images to surface scan (obtained with the Kinect camera) with a Euclidean error lower than 1 mm a Haussdorf distance of 4.34 mm. Hence, [19] model does not support pose variation and the authors did not communicate about the computational time.

We showed that increasing the number of landmarks decreases the MAE to enhance the registration accuracy. This improvement is expected but highlights, in some cases, an inaccurate matching of the closest point algorithm. Indeed, some landmarks such as the nipples are geometrically significant on the mesh and can be detected by the automatic algorithm; others like the sternum are only textured information and struggle to be detected by the closest point procedure. Manually adding the landmarks takes less than 30 seconds and produces a more accurate registration using less computational time.

By expanding the number of blendshapes, the deformation space of the model is also expanded. As a result, the model can fit more complex body shapes. Hence, determining the right amount of blendshapes can be delicate and a compromise has to be found between accuracy and registration time. On one hand, increasing the number of blendshapes augments the number of DOFs leading to higher registration time. On the other hand, one blendshape can be meaningful for one particular morphology but meaningless for another one. For example, in figure 11, blendshape 44 had a significant impact on the majority of the patients but not for *Patient 0* and *Patient 6*. This result is also highlighted in [130] where they increased the number of blendshapes from 1 to 300 and decreased the mean absolute error from 6.6 mm to 3.1 mm. In our case, for the proposed application, 55 blendshapes are a reasonable balance with a mean accuracy lower than 3 mm for the surface registration and an execution time below to 3 s.

Finally, we demonstrated the robustness of the model through a sensitivity analysis. Hence, we highlighted once again, the inaccurate matching of the closest-point algorithm when we increased the impact of E_D (decreasing the value of λ_D to improve the surface MAE) which resulted in a decrease of the landmark MAE. Furthermore, we showed a weak impact of $\lambda_S, \lambda_{BS}, \lambda_J$ (which prevent model distortion) as reducing their values only force

the model to its initial configuration. Conversely, selecting a value upper than 10 for λ_S and λ_J led to singularities as we did not constrain the scale and the joints rotation and translation of the model. It is well-known that LBS can suffer from the "candy-wrap" effect, i.e., the mesh loses volume when joints rotations are too important. But this effect can be alleviated by using Dual Quaternion Skinning [109] or Implicit Skinning [222]. So far, we did not observe such behaviors in our application. Finally, the model is flexible and can be easily modified by tuning the regularization parameters or by adding new blendshapes, landmarks, and bones.

Several limitations are acknowledged. One major limitation is the low number of participants (7) leading to a weak anatomical variability and a difficult validation. Through the sensitivity analysis, we showed the impact of the parameters (λ) that penalize the different energy terms. Hence, setting these parameters is not simple as they are just penalization terms and it can be hard to find the optimal ones for each model. Furthermore, we manually created our blendshapes to reproduce the soft tissue deformations that require knowledge and experience. Despite overcoming the problem of a database, generating unrepresentative blendshapes can add unnecessary DOFs to the model.

Suggestions for future work include the automatic detection of the landmarks, for instance, by using the scan textures. These are for the moment identified manually by the surgeon which is an advantage for flexibility but a drawback for automation. Thus, to reduce the computational time, we used a coarse mesh. But the refinement of the mesh can lead to better registration with a slight increase of the registration time. Another step forward to improve the validation would be to have access to a larger population in order to create a statistical database. This could be done by adding a Bayesian regularisation term [184] to the energy minimization term. Finally, the registration provides a patient-specific mesh ready for biomechanical simulations. Hence, this work can be the basis for pre to the intra-operative mapping of tumors using the finite element method.

2.7 Conclusion

In the present study, we registered a simplified breast-model on 7 patients in the preoperative and intra-operative configurations. We showed that Linear Blend Skinning was a good approximation of the bones joint motion and allowed the model to fit different poses. Morphological differences as well as soft-tissue deformation induced by different poses, could be modeled by using blendshapes. Our application was mainly focused on lumpectomy but the methodology is general enough to be compatible with other surgical patterns such as mastectomy or mammary reduction. The method could even be generalized to other body parts but would require creating a new rig, mesh, and blendshapes. We showed a concrete clinical application of breast patient-specific modeling for preoperative surgery drawing based on real data. In the end, our model fits a scan in less than 3 seconds, is robust to noise, incomplete data, posture, and morphological variations of patients.

References

[13] Ilya Baran and Jovan Popovi. "Automatic rigging and animation of 3D characters". In: *ACM Transactions on Graphics* 26.3 (2007). DOI: 10.1145/1275808.1276467 (page 32).

[18] Paul J Besl and Neil D Mckay. "A Method for Registration of 3-D Shapes". In: *IEEE Transactions on Pattern Analysis and Machine Intelligence* 14.2 (1992), pp. 239–256. DOI: 10.1109/34.121791 (page 37).

[19] S Bessa, Pedro H Carvalho, and P Oliveira. "Registration of Breast MRI and 3D Scan Data Based on Surface Matching". In: *In Proceedings of the IEEE 16th International Symposium on Biomedical Imaging* (2019). DOI: 10.1109/ISBI.2019.8759306 (pages 32, 43).

[20] Sílvia Bessa et al. "3D digital breast cancer models with multimodal fusion algorithms". In: *The Breast* 49 (2020), pp. 281–290. ISSN: 15323080. DOI: 10.1016/j.breast.2019.12.016 (page 32).

[36] Dan Casas and Miguel A Otaduy. "Learning Nonlinear Soft-Tissue Dynamics for Interactive Avatars". In: *In Proceedings of the ACM on Computer Graphics and Interactive Techniques* (2018). DOI: 10.1145/3203187 (page 32).

[37] Michael P. Chae et al. "Breast volumetric analysis for aesthetic planning in breast reconstruction: A literature review of techniques". In: *Gland Surgery* 5.2 (2016), pp. 212–226. ISSN: 22278575. DOI: 10.3978/j.issn.2227-684X.2015.10.03 (page 32).

[54] Carol E DeSantis et al. "Breast Cancer Statistics , 2019". In: *American Cancer Society Journal* 69.6 (2019), pp. 438–451. DOI: 10.3322/caac.21583 (page 31).

[57] Martha Duraes et al. "Surgery of nonpalpable breast cancer: First step to a virtual per-operative localization? First step to virtual breast cancer localization". In: *The Breast Journal* 25.5 (2019), pp. 874–879. DOI: doi.org/10.1111/tbj.13379. eprint: https://onlinelibrary.wiley.com/doi/pdf/10.1111/tbj.13379. URL: https://onlinelibrary.wiley.com/doi/abs/10.1111/tbj.13379 (page 31).

[62] Björn Eiben et al. "Surface driven biomechanical breast image registration". In: *In Proceedings of SPIE Medical Imaging* (2016). ISSN: 16057422. DOI: 10.1117/12.2216728 (pages 32, 117, 127).

[67] Giovanni Maria Farinella et al. "Objective Outcome Evaluation of Breast Surgery". In: *In Proceedings of Medical Image Computing and Computer-Assisted Intervention – MICCAI 2006: 9th International Conference* (2006). DOI: 10.1007/11866565_95 (pages 37, 40).

[69] François Faure et al. "SOFA: A Multi-Model Framework for Interactive Physical Simulation". In: *Soft Tissue Biomechanical Modeling for Computer Assisted Surgery.* Ed. by Yohan Payan. Berlin, Heidelberg: Springer Berlin Heidelberg, 2012, pp. 283–321. ISBN: 978-3-642-29014-5. DOI: 10.1007/8415_2012_125. URL: https://doi.org/10.1007/8415_2012_125 (pages 37, 64, 130).

[93] Charles R. Harris et al. "Array programming with NumPy". In: *Nature* 585.7825 (Sept. 2020), pp. 357–362. DOI: 10.1038/s41586-020-2649-2. URL: https://doi.org/10.1038/s41586-020-2649-2 (page 38).

[97] Nikolas Hesse et al. "Learning and Tracking the 3D Body Shape of Freely Moving Infants from RGB-D sequences". In: *IEEE Transactions on Pattern Analysis and Machine Intelligence* (2019), pp. 1–12. DOI: 10.1109/TPAMI.2019.2917908 (page 32).

[101] Alec Jacobson and Olga Sorkine. "Stretchable and Twistable Bones for Skeletal Shape Deformation". In: *ACM Transactions on Graphics* 30.6 (2011), pp. 1–8. ISSN: 15577368. DOI: 10.1145/2070781.2024199 (page 32).

[104] Doug L James and Christopher D Twigg. "Skinning Mesh Animations". In: *ACM Transactions on Graphics* 1.212 (2005), pp. 399–407. DOI: 10.1145/1073204.1073206 (page 32).

[108] Pushkar Joshi et al. "Learning controls for blend shape based realistic facial animation". In: *In Proceedings of 2003 ACM SIGGRAPH/Eurographics Symposium on Computer Animation* (2003). DOI: 10.1145/1198555.1198588 (page 32).

[109] Ladislav Kavan et al. "Geometric skinning with approximate dual quaternion blending". In: *ACM Transactions on Graphics* 27.4 (2008), pp. 1–23. ISSN: 07300301. DOI: 10.1145/1409625.1409627 (page 44).

[110] Youngjun Kim, Kunwoo Lee, and Wontae Kim. "3D virtual simulator for breast plastic surgery". In: *Computer Animation and Virtual Worlds* (2008), pp. 33–47. DOI: 10.1002/cav.237 (page 32).

[117] R M Lacher et al. "Nonrigid reconstruction of 3D breast surfaces with a low-cost RGBD camera for surgical planning and aesthetic evaluation". In: *Medical Image Analysis* 53 (2019), pp. 11–25. DOI: 10.1016/j.media.2019.01.003 (page 32).

[118] René M Lacher et al. "A comparative study of breast surface reconstruction for aesthetic outcome assessment". In: *In Proceedings of Medical Image Computing and Computer-Assisted Intervention - MICCAI 2017: 20th International Conference,* (2017). ISSN: 16113349. DOI: 10.1007/978-3-319-66185-8_58 (page 32).

[121] Binh Huy Le and Zhigang Deng. "Robust and accurate skeletal rigging from mesh sequences". In: *ACM Transactions on Graphics* 33.4 (2014). ISSN: 15577333. DOI: 10.1145/2601097.2601161 (page 32).

[122] Angela W. C. Lee et al. "Breast Image Registration by Combining Finite Elements and Free-Form Deformations". In: *Digital Mammography*. Ed. by Joan Martí et al. Berlin, Heidelberg: Springer Berlin Heidelberg, 2010, pp. 736–743. ISBN: 978-3-642-13666-5 (page 32).

[125] J P Lewis et al. "Practice and Theory of Blendshape Facial Models". In: *Proceedings of Eurographics 2014 - State of the Art Reports*. 2014. DOI: 10.2312/egst.20141042 (page 32).

[130] Matthew Loper et al. "SMPL : A Skinned Multi-Person Linear Model". In: *ACM Transactions on Graphics* 34 (2015), 248:1–248:16. DOI: 10.1145/2816795.2818013 (pages 32, 43).

[136] Wan-Chun Ma et al. "A blendshape model that incorporates physical interaction". In: *Computer Animation and Virtual Worlds* 23 (2012), pp. 235–243. DOI: 10.1145/2073304.2073343 (page 32).

[169] Frederick I Parke. "Computer generated animation of faces". In: *Proceedings of the ACM annual conference* (1972), pp. 451–457. DOI: 10.1145/800193.569955 (page 32).

[177] Ganiyu A Rahman. "Breast conserving therapy: A surgical technique where little can mean more". In: *Journal of Surgical Technique and Case Report* 3.1 (2011), pp. 1–4. ISSN: 20068808. DOI: 10.4103/2006-8808.78459 (page 31).

[184] H. Rappel et al. "A Tutorial on Bayesian Inference to Identify Material Parameters in Solid Mechanics". In: *Archives of Computational Methods in Engineering* 27.2 (2020), pp. 361–385. ISSN: 18861784. DOI: 10.1007/s11831-018-09311-x (page 44).

[189] Amy E. Rivere, V. Suzanne Klimberg, and Kirby I. Bland. "32 - Breast Conservation Therapy for Invasive Breast Cancer". In: *The Breast (Fifth Edition)*. Ed. by Kirby I. Bland et al. Fifth Edition. Elsevier, 2018, 462–476.e4. ISBN: 978-0-323-35955-9. DOI: doi.org/10.1016/B978-0-323-35955-9.00032-5. URL: https://www.sciencedirect.com/science/article/pii/B9780323359559000325 (page 31).

[194] Guillermo Ruiz et al. "Weighted regularized statistical shape space projection for breast 3D model reconstruction". In: *Medical Image Analysis* 47 (2018), pp. 164–179. DOI: 10.1016/j.media.2018.04.007 (pages 32, 43).

[217] Maxime Tournier et al. "Stable Constrained Dynamics". In: *ACM Transactions on Graphics, Association for Computing Machinery, in Proceedings of SIGGRAPH* 34.4 (2015), 132:1–132:10. DOI: 10.1145/2766969 (pages 34, 37, 130).

[219] Chieh Han John Tzou et al. "Comparison of three-dimensional surface-imaging systems". In: *Journal of Plastic, Reconstructive and Aesthetic Surgery* 67.4 (2014), pp. 489–497. ISSN: 18780539. DOI: 10.1016/j.bjps.2014.01.003 (page 32).

[222] Rodolphe Vaillant et al. "Implicit skinning: Real-time skin deformation with contact modeling". In: *ACM Transactions on Graphics* 32.4 (2013). ISSN: 07300301. DOI: 10.1145/2461912.2461960 (page 44).

[225] Pauli Virtanen et al. "SciPy 1.0: Fundamental Algorithms for Scientific Computing in Python". In: *Nature Methods* 17 (2020), pp. 261–272. DOI: 10.1038/s41592-019-0686-2 (page 38).

[235] R Zheng, W Yu, and J Fan. "2 - Breast measurement and sizing". In: *Innovation and Technology of Women's Intimate Apparel*. Ed. by W. Yu et al. Woodhead Publishing Series in Textiles. Woodhead Publishing, 2006, pp. 28–58. ISBN: 978-1-84569-046-5. DOI: doi.org/10.1016/B978-1-84569-046-5.50002-1. URL: https://www.sciencedirect.com/science/article/pii/B9781845690465500021 (pages 33, 120).

3 Inverse deformation analysis: an experimental and numerical assessment using the FEniCS Project [3]

Abstract

In this paper we develop a framework for solving inverse deformation problems using the FEniCS Project finite element software. We validate our approach with experimental imaging data acquired from a soft silicone beam under gravity. In contrast with inverse iterative algorithms that require multiple solutions of a standard elasticity problem, the proposed method can compute the undeformed configuration by solving only one modified elasticity problem. This modified problem has a complexity comparable to the standard one. The framework is implemented within an open-source pipeline enabling the direct and inverse deformation simulation directly from imaging data. We use the high-level Unified Form Language (UFL) of the FEniCS Project to express the finite element model in variational form and to automatically derive the consistent Jacobian. Consequently, the design of the pipeline is flexible: for example, it allows the modification of the constitutive models by changing a single line of code. We include a complete working example showing the inverse deformation of a beam deformed by gravity as supplementary material.

3.1 Introduction

Motivation. The organization of a standard biomechanical *deformation analysis* pipeline typically proceeds as follows. First, by using imaging techniques such as Magnetic Resonance Imaging (MRI) a segmented image of the region of interest is obtained. This segmented image is then meshed so that it can be used as input for a finite element simulation. The mesh is considered as the initial, undeformed or reference configuration of an elastic body. Then, by applying external forces to this elastic body we can find its deformed (or current) equilibrium configuration.

Conversely, an *inverse deformation analysis* allows us to find the undeformed configuration of a body knowing its deformed configuration. In the case of an object subject to gravity, the undeformed configuration can be seen as a theoretical *gravity-free* configuration. Consequently, determining the rest-position of an organ is of interest in many (bio)mechanical problems, as explained in figure 14. For example, in abdominal aortic aneurysms to compute the residual stresses [133, 176]or open-configuration [237] or in breast cancer as an intermedial configuration between the imaging and surgical stance [152]. Besides, this approach can also be used in problems of industrial interest such as tire or turbine blade design [65, 114].

Problem statement. The objective of inverse deformation analysis is to determine the undeformed configuration of an object such that it attains a known deformed configuration under the action of a known loading. It is important to note the distinction between inverse

[3]Reproduced from: A. Mazier, A. Bilger, A.E. Forte, I. Peterlik, J.S. Hale, S.P.A. Bordas, Inverse deformation analysis: an experimental and numerical assessment using the FEniCS Project, Engineering with Computers, `https://doi.org/10.1007/s00366-021-01597-z`.

deformation analysis and common inverse problems. In a typical inverse problem, we might assume we know the applied forces, the initial and deformed configuration, and the goal is to determine the model parameters that minimize some distance (metric) between initial and deformed configurations. In an inverse deformation analysis, we assume we know the applied forces, boundary conditions, model parameters, and the deformed configuration. The objective is to determine the undeformed configuration that would lead to the deformed configuration if the external forces were to be applied.

Background. Several authors have tackled the problem of inverse deformation analysis using a variety of strategies. To the best of our knowledge, Adkins [1] was the first to propose exchanging the role of the deformed and undeformed configurations, i.e. to express the displacement of the body as a function of the deformed state. The study was limited to plane strain deformations and uniform extension. Schield [199] applied the same formalism to a homogeneous elastic material, without body force. He showed the equivalence of the equilibrium equations if the initial and deformed configurations are interchanged as well as the volumetric strain energies. The results provided by this approach are shown to be commensurate with those of Adkins [1] but are based on dual relations between the initial configuration and the deformed configuration. Carlson [32] used a variational principle to achieve the same as Schield [199] and showed the validity of the approach for different elastic materials. More recently, Carroll [33] mathematically analyzed the Schield transformation and the proven inverse deformation theorem. The theorem states that if a particular deformation is supported without body force for a specific strain energy W, then the inverse deformation is another energy W^*, derived from the first: $W^*(\boldsymbol{F}) = \det(\boldsymbol{F})W\left(\boldsymbol{F}^{-1}\right)$, where $\boldsymbol{F}$ is the deformation gradient.

Govindjee [85, 86] introduced the reparameterization of the weak form of the forward problem of finite elasticity as a solution method for the inverse problem. This approach only requires C_0 continuity and has a direct physical connection to the problem. Additionally, the procedure eliminates boundary condition difficulties, can be straightforwardly implemented using standard forward numerical methods, and can deal with both compressible or incompressible materials.

Inspired by Govindjee [85] (Eulerian model) and Yamada [232] (Arbitrary Lagrangian-Eulerian (ALE)), Fachinotti [64] rewrote the constitutive equations in terms of Lagrangian variables. In contrast to Eulerian and ALE variables, the Lagrangian formulation requires only a few modifications from the direct to the inverse analysis code (i.e., the computations of the finite element residual vector and the Jacobian matrix). The formulation is convenient and allows to solve *inverse design problems* such as finding the unloaded shape of a turbine blade under known loading. But few drawbacks arise such as the difficulty of deriving and implementing the consistent Jacobian of the finite element formulation. Despite the usefulness of the approach, to our knowledge, this type of analysis is still not available in any widely used commercial simulation software.

Iterative methods identify the undeformed configuration based on several forward calculations. The algorithm is introduced by Sellier [202] with a fixed-point method for elastostatic problems and then generalizes as the *backward displacement method* by Bols [22] for

patient-specific blood vessel simulations. The iterative algorithm of Sellier has been widely applied to many image-based biomechanical simulations, mainly thanks to its algorithmic simplicity and its ability to use a standard non-linear elasticity simulation software [152]. However, when applied to strongly non-linear problems resulting from material or geometric non-linearity, the algorithm lacks robustness. Furthermore, iterative methods usually require at least one non-linear elasticity problem solution, resulting in higher costs compared with the approach of Fachinotti [64].

In the computer graphics community, Chen [40] used Asymptotic Numerical Methods (ANM) to compute the rest-shape of elastic objects with a neo-Hookean material model. The ANM considers a parametrized version of the static equilibrium: $f(x, X) + \lambda g = 0$, where g is gravity, λ a loading parameter and f are the internal forces with the given deformed configuration x and the unknown rest-configuration X. Then, the algorithm incrementally computes the asymptotic expansion of the curve in (X, λ) space until $\lambda = 1$, which corresponds to the rest-position. In this study, ANM offers superior performance, robustness, and convergence speed over traditional Newton-type methods for highly nonlinear material models. But the major drawback of the method is the complexity of changing the model formulation. Indeed, using a different material model implies to establish a different quadratic relationship between Cauchy stresses and the rest-position, then deriving the asymptotic local expansion. More recently, Ly [134] developed an inversion algorithm applicable to geometrically non-linear thin shells, including the effects of contact and dry friction with an external body.

Contribution. In this paper we propose to use the Lagrangian formulation of Fachinotti [64] coupled with automatic code generation tools provided by the FEniCS Project finite element software [135] to compute the rest or undeformed configuration of an object knowing the deformed configuration, the external loads and the material properties. We show experimental validation that the methodology is effective at recovering the undeformed configuration from imaging data. The formulation requires only a few minor modifications of the direct simulations, making it easy to implement. The automated differentiation tools from FEniCS Project provide a great deal of flexibility, for example, permitting users to quickly and easily modify the material model to suit their own problem.

Outline. This paper is organized as follows; first, we explain the inverse deformation analysis methods as well as the near-incompressible hyperelastic model used for the study. We test our formulation on some simple analytical cases described in [123, 149]. Then, we show in a numerical example how our variational formulation can surpass the iterative algorithm proposed by Sellier [202]. Finally, we demonstrate a relevant real-world application by retrieving the undeformed configuration of a Polydimethylsiloxone (PDMS) beam under the action of gravity from imaging data.

3.2 Inverse finite strain elasticity

This section presents two methods to compute the undeformed configuration knowing the deformed configuration under known loading. We first introduce our methodology derived from Fachinotti [64], then we briefly outline a simple iterative geometric algorithm described

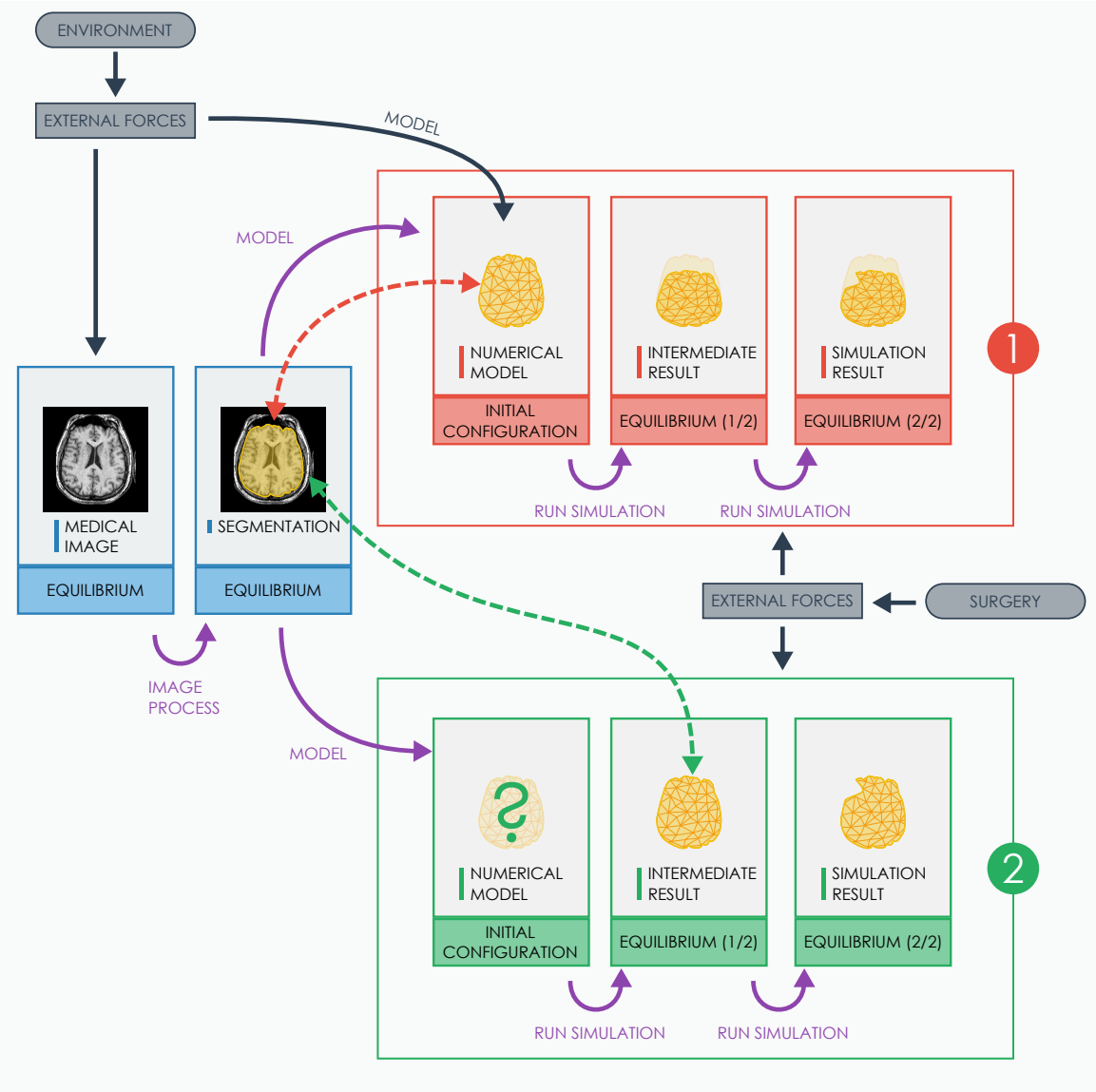

Figure 14: Our pipeline starts with the acquisition of a medical image, in which the organ can be segmented. The organ is observed at equilibrium under the effect of external forces due to its environment (e.g. gravity). In the usual pipeline (1, in red), the segmented geometry is considered as the initial geometry. Then, the external forces are applied until equilibrium to obtain the intermediate geometry used for simulating the procedure. We propose an alternative approach (2, in green), where we constrain the intermediate geometry to be identical to the segmented geometry. It involves the computation of a new geometry (represented by the question mark symbol), which is the organ geometry such that it would deform to the segmented/imaged configuration if external forces were applied. Here, the final result takes into account the undeformed geometry of the organ.

in [202].

3.2.1 Inverse FEM method

Mathematical operators. In this paper, we define the colon operator (:) as the inner product between tensors (summed pairwise product of all elements). Let $\boldsymbol{A}$ and $\boldsymbol{B}$ be rank-2 tensors, the inner product is then defined as $\boldsymbol{A} : \boldsymbol{B} = \mathrm{tr}(\boldsymbol{A}^T\boldsymbol{B}) = A_{ij}B_{ij}$ using the Einstein notation. In a same way, we define the dot product between vectors as $\boldsymbol{u} \cdot \boldsymbol{v} = u_i v_i$. Finally, $\nabla(\bullet)$ denotes the vector differential operator such that $\nabla \boldsymbol{v} = \frac{\partial v_j}{\partial x_i}$.

Consider a deformable body $\mathcal{B}$. We denote the undeformed configuration Ω_0. The location of a particle of $\mathcal{B}$ in Ω_0 is denoted $\boldsymbol{X}$. Conversely, the deformed configuration is noted Ω, and the location of a particle of $\mathcal{B}$ in Ω is noted $\mathbf{x}$. A one-to-one mapping $\boldsymbol{\phi}$ maps the position of a particle $\boldsymbol{X}$ in Ω_0 to the position of the same particle $\boldsymbol{x}$ in Ω, i.e $\boldsymbol{x} = \phi(\boldsymbol{X})$. The configuration Ω can be obtained by $\boldsymbol{\phi}(\Omega_0) = \{\boldsymbol{\phi}(\boldsymbol{X}) \mid \boldsymbol{X} \in \Omega_0\}$.

The weak form of the static equilibrium of the inverse deformation is expressed in the deformed configuration:

$$\int_\Omega \boldsymbol{\sigma} : \nabla \boldsymbol{\eta} \, \mathrm{d}\Omega = \int_\Omega \rho \boldsymbol{b} \cdot \boldsymbol{\eta} d\Omega + \int_\Gamma \boldsymbol{t} \cdot \boldsymbol{\eta} \, \mathrm{d}\Gamma, \tag{32}$$

where $\boldsymbol{\sigma}$ is the Cauchy stress tensor and $\nabla(\bullet)$ the gradient in Ω with respect to the deformed spatial position of the test function $\boldsymbol{\eta}$. ρ is the density of the material in the deformed configuration and $\boldsymbol{b}$ are the external forces in the deformed configuration. Finally, a traction boundary condition prescribed on a part Γ of the boundary as $\boldsymbol{\sigma} \cdot \boldsymbol{n} = \boldsymbol{t}$ with $\boldsymbol{n}$ the outward unit normal at the boundary . On the remaining part of the boundary, we assume that the value of the displacement is given, i.e. a Dirichlet condition.

This approach has the advantage of being based on classical mechanical principles. However, mechanical quantities such as strains or stresses are defined depending on $\boldsymbol{X}$. Whereas, in the inverse approach, the initial geometry is replaced by the deformed geometry $\boldsymbol{x}$. We redefine the classical displacement $\boldsymbol{u}(\boldsymbol{X}) = \boldsymbol{x} - \boldsymbol{X} = \boldsymbol{\phi}(\boldsymbol{X}) - \boldsymbol{X}$ as

$$\boldsymbol{u}'(\boldsymbol{x}) = \boldsymbol{X} - \boldsymbol{x}. \tag{33}$$

Note that trivially

$$\boldsymbol{u}' \circ \boldsymbol{\phi} + \boldsymbol{u} = 0. \tag{34}$$

This redefinition does not modify the classical finite element pipeline: the unknown position is still the first term in which the known position is subtracted. In addition, as we compute gradients in the deformed configuration, this necessitates the redefinition of the deformation gradient as well:

$$\boldsymbol{F} = \frac{\partial \boldsymbol{\phi}(\boldsymbol{X})}{\partial \boldsymbol{X}} = \left(\frac{\partial \boldsymbol{X}}{\partial \boldsymbol{x}}\right)^{-1} = \left(\frac{\partial \boldsymbol{u}'(\boldsymbol{x})}{\partial \boldsymbol{x}} + \boldsymbol{I}\right)^{-1} = \left(\nabla \boldsymbol{u}' + \boldsymbol{I}\right)^{-1}. \tag{35}$$

Henceforth, when performing an inverse deformation analysis, $\boldsymbol{F}$ and all derived quantities (strain measures, invariants, energy densities, stress measures etc.) are always computed using the above redefinition in terms of $\boldsymbol{u}'$.

This new formulation requires us to only make one change compared to the classical direct finite element pipeline; rewrite $\boldsymbol{F}$ in terms of $\boldsymbol{u}'$. This formulation can find the undeformed configuration of an object, knowing only the deformed configuration and the applied forces. The process is not iterative (we perform several Newton-Raphson iterations but only one simulation) and based on the equation of continuum mechanics.

3.2.2 Nearly-incompressible constitutive model

For many materials, simple elastic models such as the St. Venant Kirchhoff model are not sufficient to describe the observed behavior. More complex hyperelastic models provide a mechanism of modeling the stress-strain behavior of complex materials such as elastomers or biological tissues. They can be assumed compressible, i.e. the volume may change during deformation or nearly-incompressible or even completely incompressible, i.e. the volume is preserved during deformation $\det \boldsymbol{F} \sim 1$.

For a hyperelastic material, the strain energy density function describes the stored energy as a function of the isochoric deformation, i.e. shape deformations without volume change. But using the standard displacement-based finite element method to describe incompressible material behavior may cause numerical problems typically referred to as *locking*. Simply put, locking occurs when too many constraints are imposed on the discrete formulation and its overall approximation power is destroyed.

To overcome these difficulties, mixed formulations have been developed. In these formulations, the variational principle is modified by writing the potential energy functional. The strain energy is expressed in terms of the deviatoric component only and the incompressibility constraint is explicitly enforced using a Lagrange multiplier with physical meaning akin to pressure (p). It turns out that the Lagrange multipliers can be expressed as a function of the hydrostatic pressure values $f(p)$ [52].

$$\psi(\boldsymbol{C}, p) = \psi_{\text{deviatoric}}(\boldsymbol{C}) + f(p), \tag{36}$$

$$f(p) = \psi_{\text{hydrostatic}}(J), \text{ with } p = \sigma_{\text{hydro}} = \frac{1}{3}\operatorname{tr}(\boldsymbol{\sigma}) = \frac{\partial \psi_{\text{hydrostatic}}(J)}{\partial J}, \tag{37}$$

where J is the Jacobian defined as $J = \det \boldsymbol{F}$ and $\boldsymbol{C}$ is the right Cauchy-Green deformation tensor. Among the hyperelastic materials, we chose to use neo-Hooke [166] and Mooney-Rivlin [154, 190] models, often used for modeling soft object deformations.

Neo-Hookean By calculating $f(p)$, we can deduce the mixed displacement-pressure formulation of a nearly-incompressible neo-Hookean material

$$\psi_{\text{NH}}(\boldsymbol{C}, p) = \frac{\mu}{2}(\mathrm{I}_B - 3) - \mu \ln(J) + p \ln(J) - \frac{1}{2\lambda}p^2, \tag{38}$$

with

$$\psi_{\text{deviatoric}}(\boldsymbol{C}) = \frac{\mu}{2}(\mathrm{I}_B - 3) - \mu \ln(J), \tag{39}$$

and

$$\psi_{\text{hydrostatic}}(J) = \frac{\lambda}{2} \ln(J)^2, \tag{40}$$

where λ and μ are material constants called the Lamé parameters.

Mooney-Rivlin By calculating $f(p)$, we can deduce the mixed displacement-pressure formulation of a nearly-incompressible Mooney-Rivlin material

$$\psi_{\text{MR}}(\boldsymbol{C}, p) = C_1 \left(\overline{\mathrm{I}_C} - 3\right) + C_2 \left(\overline{\mathrm{II}_C} - 3\right) + p(J-1) - \frac{1}{4D_1} p^2, \tag{41}$$

with C_1, C_2, D_1 material constants, in addition of

$$\psi_{\text{deviatoric}}(\boldsymbol{C}) = C_1 \left(\overline{\mathrm{I}_C} - 3\right) + C_2 \left(\overline{\mathrm{II}_C} - 3\right), \tag{42}$$

and

$$\psi_{\text{hydrostatic}}(J) = D_1 (J-1)^2, \tag{43}$$

with the modified invariants $\overline{\mathrm{I}_C} = J^{-\frac{2}{3}}\, \mathrm{I}_C$, $\overline{\mathrm{II}_C} = J^{-\frac{4}{3}}\, \mathrm{II}_C$ and classic invariants $\mathrm{I}_{\boldsymbol{C}} = \mathrm{tr}(\mathbf{C})$, $\mathrm{II}_{\boldsymbol{C}} = \frac{1}{2}\left((\mathrm{tr}(\mathbf{C}))^2 - \mathrm{tr}\left(\mathbf{C}^2\right)\right)$. These nearly-incompressible energy densities are used to generate the results from the FEniCS Project presented in this paper.

Finally, the strain energy density can be related to the second Piola-Kirchhoff $\boldsymbol{S}$ and then to the Cauchy stress tensor by recalling the relation $\frac{\partial J}{\partial \boldsymbol{C}} = \frac{1}{2} J \boldsymbol{C}^{-1}$

$$\boldsymbol{S} = 2\frac{\partial \psi}{\partial \boldsymbol{C}} = 2(f\prime(p)\frac{\partial J}{\partial \boldsymbol{C}} + \frac{\psi_{\text{deviatoric}}}{\partial \boldsymbol{C}}), \tag{44}$$

$$\boldsymbol{\sigma} = J^{-1} \boldsymbol{F} \boldsymbol{S} \boldsymbol{F}^T J = f\prime(p) + 2J^{-1} \boldsymbol{F} \frac{\psi_{\text{deviatoric}}}{\partial \boldsymbol{C}} \boldsymbol{F}^T, \tag{45}$$

where $f\prime$ denotes the differentiation of $f(p)$ with respect to p.

3.2.3 Finite element solver

We use the FEniCS Project finite element software [135] to discretise both the standard finite strain elasticity problem and the inverse finite strain elasticity problem that we will outline in the next section. We use a mixed displacement-pressure finite element formulation with second-order continuous Lagrangian finite elements for displacement $\mathbf{u}$ and first-order continuous Lagrangian finite elements for pressure p. This pairing is well-known to be inf-sup stable [74] and relatively robust with respect to numerical locking.

The variational form of the residual equation 32 is defined in the Unified Form Language (UFL) [5] and symbolically differentiated to derive an expression for consistent Jacobian. The FEniCS Form Compiler (FFC) [128] is used to automatically generate low-level C++

code from the high-level UFL description that can calculate the Jacobian and residual cell tensors. The overall solution process is driven by the DOLFIN finite element library [129]. We use a standard Newton-Raphson algorithm with continuation in the loading parameter. The linear system within the Newton-Raphson algorithm is solved using the direct solver MUMPS via PETSc [12]. To be more precise, inside PETSc we use the direct sparse MUMPS solver as a preconditioner to a single iteration of a Krylov method, leading to convergence in one iteration. The relative tolerance of the solve is in the order of $1e^{-12}$. The complete implementation of the standard or inverse problem is around 100 lines of Python code that closely follows the mathematical structure of the problem. We refer the reader to the supplementary material [143] for further details.

3.2.4 Iterative geometric algorithm

Sellier [202] proposed an Iterative Geometric Algorithm (IGA, not to be confused with Isogeometric Analysis). The algorithm is simple to implement and only requires an existing (standard) forward deformation solver. The algorithm starts with an initial guess for the undeformed configuration (usually chosen, for lack of a better choice, the deformed one) and applies successive displacement fields to it until a convergence criterion is reached. The sequence of displacement fields is obtained from the direct simulations of the current rest-configuration undergoing external forces. The shape of the object after the direct simulation provides an error compared to the exact rest-configuration by measuring the distance to the initial configuration. An updated estimate of the undeformed configuration is calculated by correcting the previous guess with the difference between the computed and deformed configuration. The algorithm stops when the error (computed using the l^2-norm) is below a defined threshold ϵ or a maximum number of iterations $NB^{\max}$ has been reached. The process is outlined in algorithm 1

Algorithm 1 Iterative geometric algorithm from Sellier [202].

$X^0 \leftarrow X^{\text{ini}}$
run direct simulation 0 with X^0 the initial configuration
$u^0 \leftarrow x^0 - X^0$
err $\leftarrow$ error between x^0 and X^{ini}
$j \leftarrow 1$
while err $> \epsilon$ **and** $j < NB^{\max}$ **do**
    $X^j \leftarrow X^{(j-1)} - u^{(j-1)}$
    run direct simulation j with $X^{(j-1)}$ the initial configuration
    $u^j \leftarrow x^j - X^j$
    err $\leftarrow$ error between x^j and X^{ini}
    $j \leftarrow j + 1$
end while

3.3 Numerical results

The inverse deformation framework is very similar to the traditional direct framework. To assess the numerical precision of the inverse method, we first applied a serie of tests to verify the soundness of the direct and inverse approaches in which an analytical solution is known. We tested our formulation on some simple analytical cases described in [123, 149] such as simple and generalized shears. Due to the triviality of the tests, they are detailed in the Appendix section 3.6 and can be found in the supplementary material [143].

3.3.1 Single unit tetrahedron

Part I: Let us consider a mesh with a single unit tetrahedron with a linear Lagrangian finite element space. Its domain is denoted Ω_0^T. The nodal coordinates are $[0,0,0]^T$, $[1,0,0]^T$, $[0,1,0]^T$ and $[0,0,1]^T$. The nodes with $y=0$ are fixed, leaving only one free node. A uniform force $\boldsymbol{f}$ is applied along the y-axis. The tetrahedron is deformed so that the free node moves along the y-axis.

In a first step, we compute the deformation $\boldsymbol{\phi}$ with the direct method. A displacement $\boldsymbol{u}$ is computed for the free node. The deformed domain is $\Omega^T = \boldsymbol{\phi}(\Omega_0^T)$. In a second step, the initial geometry is the deformed geometry Ω^T, i.e. a unit tetrahedron with the nodes $y=0$ fixed, and the remaining node displaced from $\boldsymbol{u}$. The same uniform force $\boldsymbol{f'} = \boldsymbol{f}$ is applied. An inverse simulation is computed so that the displacement of the free node is $\boldsymbol{u'}$. This example is depicted in figure 15a.

Part II: We consider the same unit tetrahedron, with the same boundary conditions. A uniform force $\boldsymbol{f'}$ is applied along the y-axis.

In the first step, an inverse simulation is computed, leading to a displacement of $\boldsymbol{u'}$. In the second step, the resulting geometry is deformed with a direct simulation leading to a displacement of $\boldsymbol{u}$. This part of the example is depicted in 15b.

The difference with the first part of the test is the order of the successive simulations. In **part I**, the inverse simulation is performed after the direct simulation. In **part II**, it is the opposite. In both parts of the test, the goal is to verify that the following relationship: $\boldsymbol{u'} = -\boldsymbol{u}$.

Furthermore, the inverse simulation is computed with IGA to compare the results and performance with our method. In this test, the error measure is defined as: $\|\boldsymbol{u'} + \boldsymbol{u}\|_{l^2}$. We measured this error with different constitutive equations and varying their associated mechanical parameters. In total, we performed 153 tests and provided a statistical analysis in table 3.

We observe that the accuracy of the iterative algorithm depends on the number of iterations, but it also increases the computational cost because each iteration calls a direct simulation. Our method provides high accuracy while requiring only the solution of a problem with similar complexity to a single iteration of IGA. Beyond the numerical results, one point is that in 7 tests over the 153 of the **part II**, the iterative algorithm was not able to reach the accuracy of our method within 50 iterations.

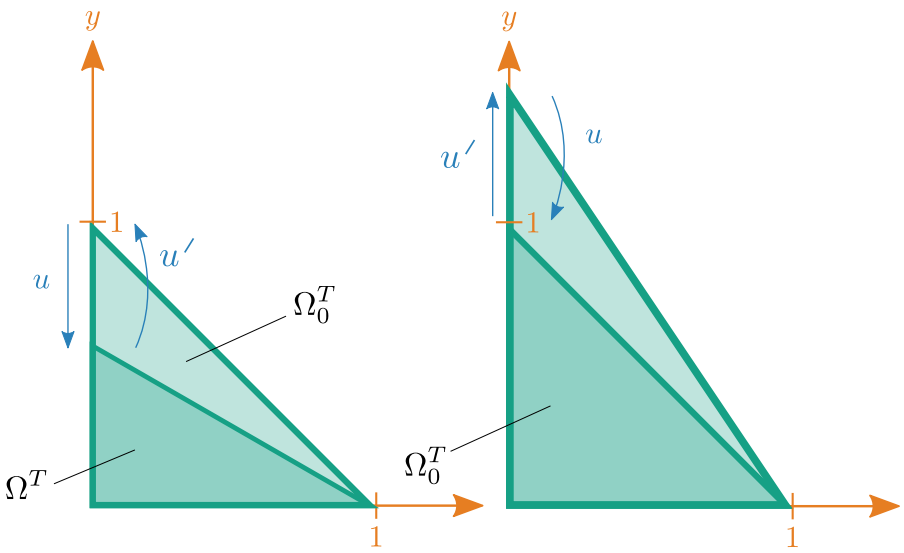

(a) Part I (b) Part II

Figure 15: Single tetrahedron test, plane view. The two bottom nodes are fixed ($\boldsymbol{u} = (0,0,0)^T$ for $y = 0$). In part I, a force $\boldsymbol{f}$ is applied on the "free node" ($y = 1$) generating a displacement $\boldsymbol{u}$. Then a second force $\boldsymbol{f'} = \boldsymbol{f}$ (generating $\boldsymbol{u'}$)is applied on the same node to retrieve the initial configuration. In Part II, we reiterate the same procedure as Part I except that we first apply $\boldsymbol{f'}$ and then $\boldsymbol{f}$ on the "free node".

	Part I			Part II		
	FEM	IGA (1)	IGA (2)	FEM	IGA (1)	IGA (2)
average error	4.49E-12	2.12E-6	2.28E-12	5.22E-12	1.98E-6	2.28E-12
SD	1.07E-11	1.09E-6	6.69E-12	1.25E-11	1.05E-6	2.41E-12
minimum	9.26E-22	5.44E-8	4.15E-35	1.04E-21	5.47E-8	6.76E-12
maximum	5.52E-11	4.48E-6	5.11E-11	7.26E-11	3.99E-6	5.04E-11
avg #simulations	1	4.70	11.2	1	4.84	13.4
avg time (ms)	34	162	387	33	162	387
avg time ratio	1	4.75	11.35	1	4.70	11.70

Table 3: Benchmark results on a single tetrahedron simulation. We compare our inverse FEM deformation algorithm (FEM), with the iterative geometric algorithm (IGA (1)) with the arbitrary convergence criterion 10^{-6}, and with the IGA at the same accuracy than PB (IGA (2)). We compute statistical indicators such as the average error, the standard deviation (SD) of the error, the minimum and maximum errors. In addition, we calculate the average number of simulations (avg #simulations), the average time needed to reach the convergence criterion (avg time) and the average time ratio (avg time ratio) obtained with $\frac{\text{avg time}}{\text{FEM avg time}}$.

3.3.2 Sagging block

In section 3.6, we applied different displacements on a cube using simple and generalized shears. For the sagging block case, we use the same pipeline as mentioned in section 3.3.1. Namely, we deform and object by applying a force and recover its initial shape by exercising the opposite force on the deformed object. The geometry is a 3-dimensional unit cube of 1 m length, fixed at the bottom (Dirichlet condition $\boldsymbol{u} = (0, 0, 0)^T$ when $y = 0$) with gravity as a body force applied to the entire object. For the material model, we used the incompressible Neo-Hookean defined in equation 38. We performed several Monte Carlo (MC) simulations which to study the error of the recovered initial shape using different material parameters. For the sake of simplicity, we assumed that λ and μ were both following an uniform distribution between an acceptable range of values.

$$\mu \sim U(2.0 \times 10^3, 2.0 \times 10^5),$$
$$\lambda \sim U(8.0 \times 10^4, 8.0 \times 10^6).$$

We empirically chose those values as lower and upper limits because we could observe large visible deformations within these bounds. We draw 100 samples of each parameters and make all possible combinations leading to $100^2 = 10000$ simulations. To study the error, we calculated the Mean Absolute Error (MAE) between the initial shape and the initial shape predicted by our inverse deformation algorithm. The MAE is defined as $\text{MAE} = \frac{\sum_i^N |e|}{N}$, where $e = x_{prediction} - x_{initial}$ and N the number of points of the cube.

The result of the MC simulations are shown in the 3D plot in figure 16. We observe a small error when the material parameters are on the upper limit of our distribution e.g. a MAE $= 1.21 \times 10^{-9}$ m for $\mu = 175 \times 10^3$ Pa and $\lambda = 50 \times 10^5$ Pa. On the contrary, when moving to smaller values e.g. $\mu = 20 \times 10^3$ Pa and $\lambda = 30 \times 10^5$ Pa, the MAE is increasing to 1.21×10^{-5} m. This behavior is expected as choosing smaller values of λ and μ induce larger displacements increasing the MAE. Hence, the obtained MAE are more than acceptable and choosing lower values of the material parameters will surely increase the MAE but also create convergence issues for such large deformations. Furthermore, we performed a mesh convergence analysis shown in figure 17 proving that refining the mesh leads to a smaller MAE.

3.4 Experimental results

In this section, we will demonstrate that our inverse simulation method can match the outcome of a real experiment and therefore has value as a predictive modelling tool.

We fixed one extremity of a beam made from Polydimethylsiloxane (PDMS) to a vertical support and allowed it to deform under gravity, slowly accompanied to the equilibrium position by hand and released in that position. The deformed steady state was reached in about 1 min (after vibrations were completely damped) resulting in the configuration displayed in figure 18. To conduct the experiment, the room environmental temperature

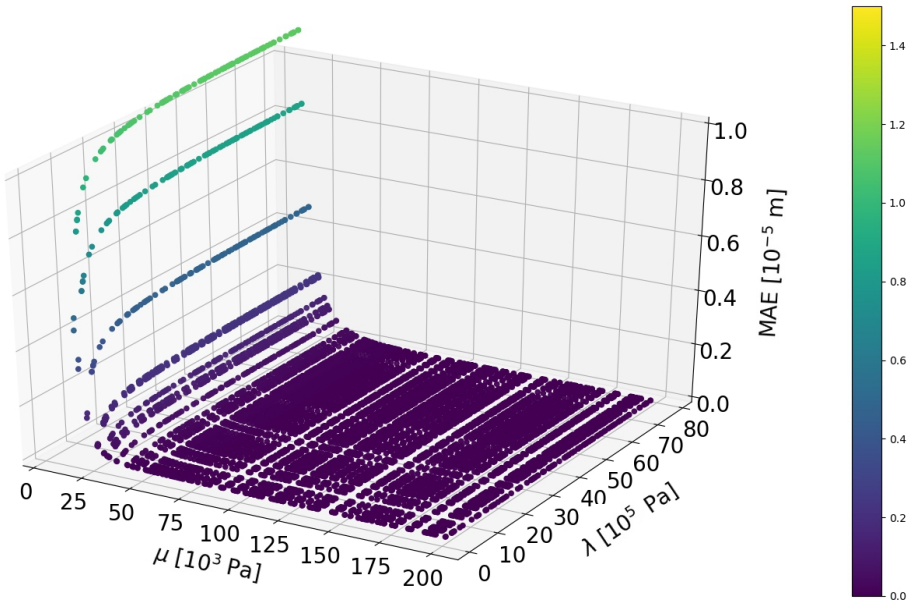

Figure 16: Sagging block Monte Carlo simulations using a uniform distribution of Neo-Hookean material parameters. The Mean Absolute Error (MAE) between the initial shape and the predicted shape of the inverse deformation algorithm is calculated for 10000 simulations.

was recorded to 19°C and the humidity at around 50% (the metrology lab is set to keep these temperatures and humidities). It is known that the mechanical properties of the PDMS material are very sensitive to its curing temperature. On the contrary, the material is very stable once it is fully cured and the mechanical properties are constant for a large range of temperatures centered around the 19°C used for testing. This is obviously not the case if the sample is heated up to temperatures in the range of 80-90°C, but these are not biological values and are out of the scope of the study. Note that the humidity effects are negligible since the material is quite hydrophobic. To extract the mesh of the deformed configuration from the image, we used the software Blender[4] and contoured the beam on 2D images by hand, as shown in figure 19. From Blender, we exported a quadrilateral surface mesh as an .obj file. Then, by using the CGAL library, we generated tetrahedrons from the surface mesh. A custom code converted the tetrahedra data structure to a dolfin-compatible .xml file. This code is available as a submodule on our Github page [143]. This mesh will be called the "reference" and used as ground-truth for this section.

To run the inverse deformation algorithm, we need three input parameters: the applied force field, the deformed configuration, and the mechanical properties. In this section, the force field is gravity and the deformed configuration was obtained by manual processing. A separate experiment was performed to obtain the mechanical properties and will be detailed

[4]https://www.blender.org/

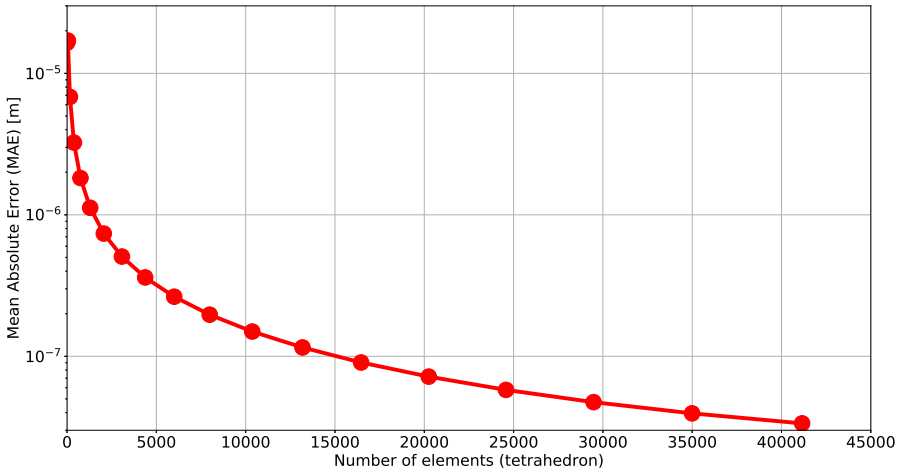

Figure 17: Semilog plot of the mesh convergence analysis of the sagging block simulation. The Mean Absolute Error (MAE) between the initial shape and the predicted shape of the inverse deformation algorithm is calculated for different mesh refinement with fixed parameters ($\lambda = 80 \times 10^4$ Pa and $\mu = 25 \times 10^3$).

in the following section.

3.4.1 Material

We used a PDMS (Sylgard 184, Ellsworth Adhesives) cylinder of density 965 kg/m^3 of undeformed dimensions 182 mm and 8.5 mm for length and diameter, respectively.

For the sample preparation the elastomeric part and curing agent were mixed in a 10 : 1 ratio and cured at room temperature for 24 h before being tested [73]. A surgical knife was used for cutting cylindrical shapes from the second cylinder of PDMS, for compression tests samples (diameter 11 mm, height 7 ± 1 mm).

To characterize the material properties, we used the Mach-1™ mechanical testing system (Biomomentum, Canada) as a testing rig for the unconfined compression tests. We used the following protocol:

- A 1.5 mm single-axis load cell with a resolution of 75 µN was used to measure the vertical force.
- The vertical displacement was measured by the moving stage of the rig with a resolution of 0.1 µN.
- To minimize friction, paraffin oil was used between the sample and the compression platens.

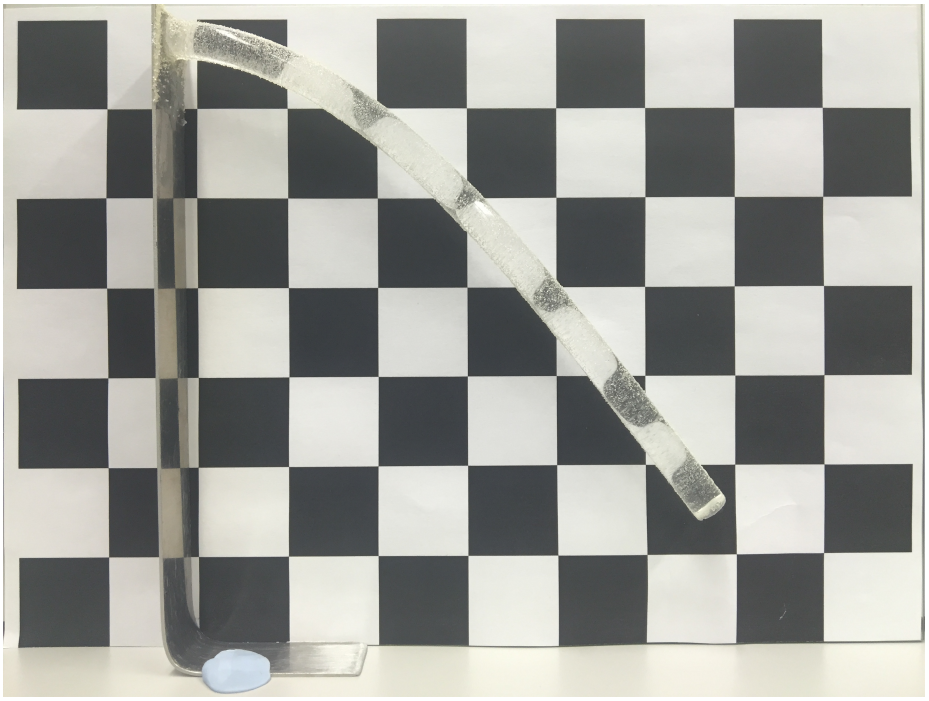

Figure 18: Experimental set-up: Initially a straight PDMS cylindrical beam of 182 mm length and 8.5 mm diameter, clamped on the left side and deformed by gravity.

- One loading cycle was executed on each specimen. To detect the response of the material at large strains, the samples were compressed at a constant speed of 0.083 mm/s until a displacement corresponding to 30% of the measured height was achieved. Particular attention was used to monitor the samples that had uniformly expanded in the radial direction and that their upper and lower faces remained adhered to the moving platen and the fixed platform for the entire duration of the test.
- The Abaqus evaluation routine was used to fit the true stress - true strain experimental curves with a Mooney-Rivlin model. Abaqus employs a linear least-squares fit for the Mooney-Rivlin form to find the optimal model parameters.

In our case the optimal parameters are: $D_1 = 7.965 \times 10^{-8}$ Pa, $C_{10} = 101.709$ kPa, $C_{01} = 151.065$ kPa. The value of D_1 is close to 0 which validates our incompressibility hypothesis. The two obtained values of C_{10} and C_{01} are the optimal values to describe the behavior of the PDMS using a Mooney-Rivlin material formulation.

3.4.2 Direct simulation

We run three simulations with identical geometry, material properties, boundary conditions, and material model to verify that these commonly used softwares produce quantitatively

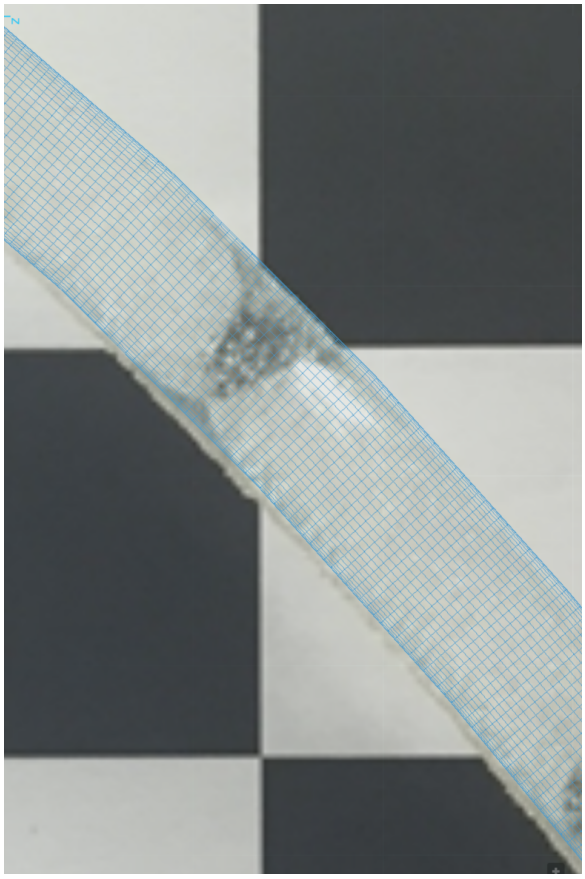

Figure 19: Manual process in Blender to delineate the contours and extract the 3D mesh of the deformed configuration.

similar results. For each software, we used an incompressible Mooney-Rivlin model and boundary conditions imitating the setup shown in figure 18. Namely, a Dirichlet boundary condition of $\boldsymbol{u} = 0$ on the left side of the beam (to imitate the clamping of the beam to the support) and the gravity is applied as a body force on the entire object.)

FEniCS: We use the same model as described in section 3.2.2.

Abaqus: We use a static step with a gravity load to solve the beam deformation in Abaqus. Abaqus/Standard uses Newton's method as a numerical technique for solving the nonlinear equilibrium equations. We employed C3D8RH elements, an 8-node linear brick, hybrid/mixed, constant pressure, reduced integration with hourglass control. Hybrid elements are usually used in Abaqus when the material definition is close to incompressibility to avoid locking. The reduced integration is used to speed up computational time and avoid numerical locking.

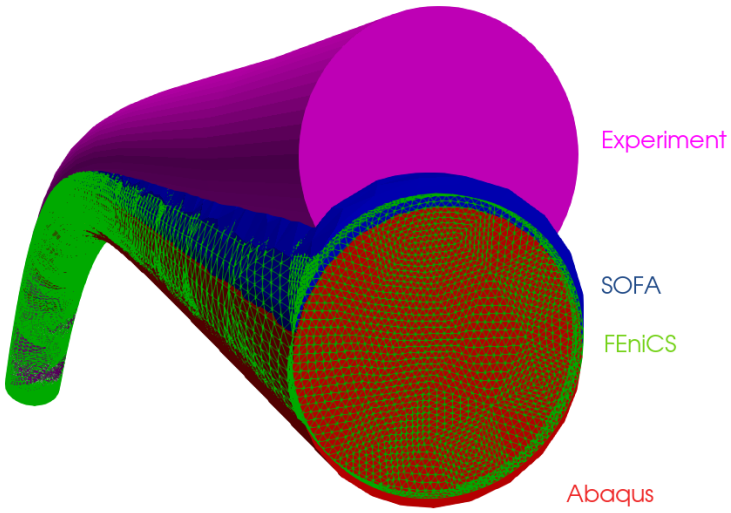

Figure 20: Comparison of the deformation of the beam for the direct simulation of 3 different softwares. The 3 simulations have the same geometry, boundary conditions, material model, and mechanical parameters corresponding to the experiment's material (PDMS) found in section 3.4.1. From top to down, in magenta: the experimental data, in blue: the SOFA simulation, in wire-frame green: the FEniCS simulation and in red: the Abaqus simulation.

SOFA: We employ the *Multiplicative Jacobian Energy Decomposition* method (MJED) which is an optimized algorithm for building the stiffness and tangent stiffness matrices of non-linear hyperelastic materials [139]. An MJED implementation is available in SOFA [69] for finite element formulation using linear tetrahedral elements. The linear system of equations is solved in every step of quasi-static simulation using a fast in-house linear equation solver based on the Cholesky [116] decomposition.

The visual result of the forward simulations using the 3 softwares are shown in figure 20. For each model, we perform a mesh convergence analysis shown in figure 21 where we plot the maximum deformation of the beam (located at the tip) for different mesh resolutions.

We observe that the tip displacement for the three software converges to similar solutions (FEniCS: 132.52 mm, Abaqus: 132.71 mm, SOFA: 130.31 mm) while the experimental value is 127.68 mm. We observe a small difference between the numerical solutions and the experiment.

FEniCS and Abaqus give similar results while SOFA is 2 mm off, compared to the 2 others softwares. We observe in figure 21 that FEniCS and Abaqus converged with 60,000 points while SOFA is still not converged with 160,000 points (due to computational

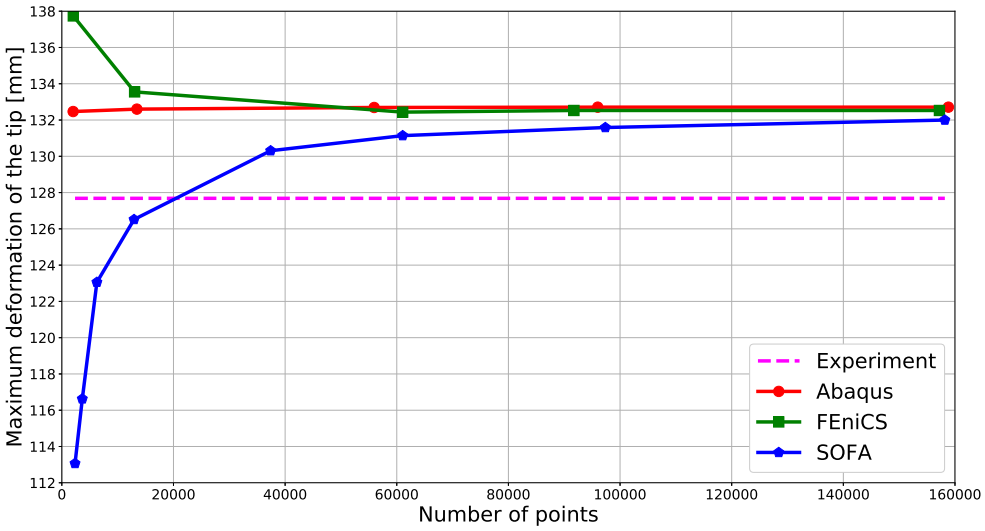

Figure 21: Mesh convergence analysis of the forward simulation. We calculate the maximum deformation of the tip of beam for several level of refinement of the mesh.

resources limitations). One reason is that SOFA is usually designed for real-time simulation and only uses dynamic solvers which can lead to inaccuracy compared with static solvers from FEniCS and Abaqus. Furthermore, the differences between numerical solutions can be explained by the use of three slightly different formulations of the Mooney-Rivlin law as well as different solvers for solving the equation. Finally, one can note that the ABAQUS simulation converges very quickly. Possibly because ABAQUS is using a hexahedral cell shape with quadratic polynomial interpolation of the displacement field, against tetrahedron cells in FEniCS and SOFA. It is well known, at least in the Engineering community, that finite elements based on hexahedral cells often perform better in practice.

Some factors can explain the difference between the numerical solutions and the experimental value. For instance, the variation may be explained by inadequate constitutive equations or boundary conditions. Then, uncertainties in the mechanical properties measures may also be a factor, especially because the PDMS might exhibit slightly asymmetric behaviour under compression and tension. Finally, we obtained the reference mesh of the undeformed configuration manually based on 2D imaging data where inaccuracies can be introduced.

3.4.3 Inverse simulation

In the previous section, we compared the forward simulations of three different software with our experimental solution. In this section, we want to verify the possibility of retrieving

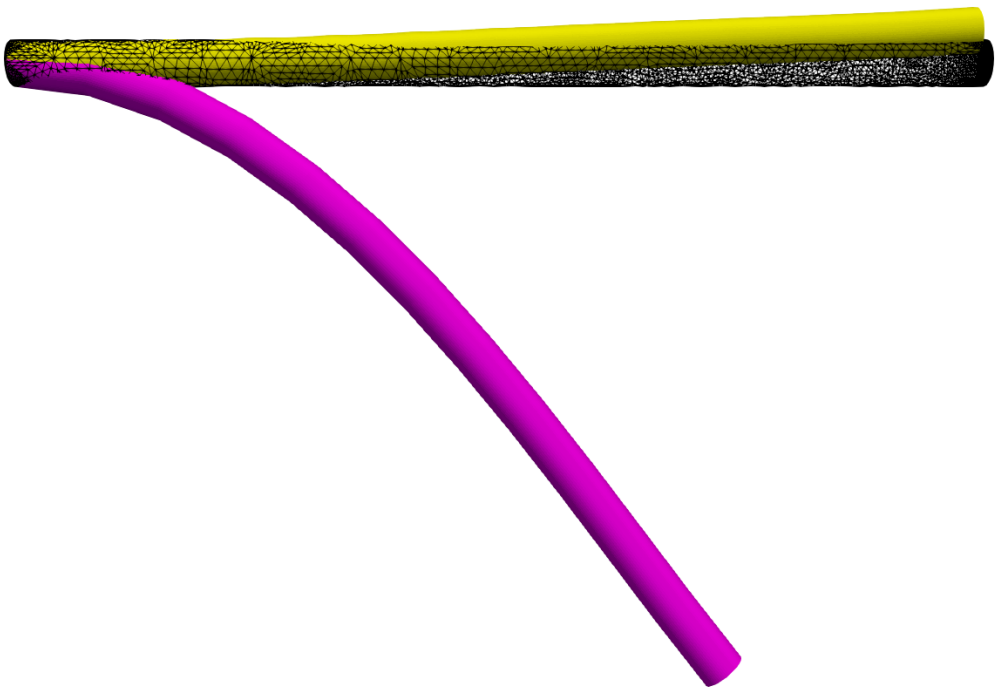

Figure 22: 3D plot of the inverse simulation. From down to top, in magenta: the experimental data we wish to retrieve the undeformed configuration, in wire-frame black: the theoretical straight beam , in yellow: the result of the FEniCS inverse simulation.

the undeformed configuration of our experimental solution knowing only the surface of the deformed configuration, the known applied loads and the material properties.

For this, we converted our experimental surface mesh of the deformed configuration into a volumetric mesh and applied our inverse deformation algorithm implemented using FEniCS. We previously showed a deformation difference of 4.84 mm for the forward simulation in FEniCS. Of course, we do not expect to obtain a perfectly straight beam (the ideal undeformed configuration), but rather an error on the same order as in the forward simulation (i.e. 4.84 mm).

We show in figure 22 the result of the inverse deformation algorithm. As expected, the inverse simulation (in yellow) applied to the experimental data (deformed configuration in magenta) is slightly different from the theoretical straight beam that we should obtain (in black). To be more precise, we achieve an error of 5.36 mm compared with the idealized straight beam. As mentioned previously, we expect an error on the order of that for the standard deformation problem (4.84 mm) due to the inherent parametric and modeling uncertainties (material model, material properties, boundary conditions, geometry) already discussed. We therefore judge that the proposed methodology has strong potential for prediction of the undeformed configuration of a soft body.

3.5 Conclusions

In the present paper we performed two physical experiments and one numerical experiment to address the *inverse deformation problem*. First an unconfined experiment to find the material properties, and then the cantilever beam problem to find the deformed configuration. The inverse deformation was a computational exercise to see if the undeformed configuration could be recovered.

Our study used the Lagrangian formulation of [64] as a basis for implementing the inverse algorithm in the FEniCS Project finite element software. We took advantage of the automatic differentiation and code generation capabilities to bypass the difficulties of deriving and implementing the consistent Jacobian. The user must then supply the deformed configuration, the mechanical properties, boundary conditions and the applied forces. The user can easily modify the input mesh, run the code efficiently in parallel, change the constitutive model or change the boundary conditions according to their needs. We have made the code and data available in the supplementary material.

We applied the approach to simple academic examples where we considered two different incompressible hyperelastic models (neo-Hookean and Mooney-Rivlin) and different boundary conditions. We demonstrated on a simple test case that our method is more efficient in terms of robustness and accuracy than the IGA method of [202]. We have only compared with the classical IGA method of Sellier but other works like [187] have improved on this algorithm. However, we can say that unless an iterative approach requires only one forward model solution, in most circumstances the mechanics-based approach detailed here is likely to be faster and more robust.

Finally we applied the method to an experiment with a PDMS beam deformed under gravity. We verified and quantified the performance of the direct simulations of three different widely-used software (Abaqus, FEniCS, SOFA). Using the inverse deformation algorithm we achieve an error of 5.36 mm for the tip displacement compared to the idealised straight beam.

Despite our progress in providing a flexible inverse deformation algorithm, some work remains to assess its robustness. Our experiments were only focused on using homogeneous nearly-incompressible hyperelastic models. Other works such as [64] were interested in more complex behaviors like anisotropy. Similarly, our experiments were only based on simple geometries and more complex geometries should be considered.

We showed the validity of our approach for the beam problem by generating a mesh of the deformed configuration from 2D images and recovering the undeformed configuration. In future work we intend to apply this algorithm to segmented 3D geometries to calculate the undeformed configuration of an organ.

3.6 Appendix

3.6.1 Verification of the direct simulation

The inverse deformation framework is very similar to the traditional direct framework. To assess the numerical precision of the inverse method, we first apply a series of tests to verify

the soundness of the direct approach in which an analytic solution is known. The geometry for every example will remain the same with a unit cube discretized in 216 points.

3.6.2 Shear deformation

Simple shear: Simple shear deformation is a popular benchmark test [149]. The initial geometry is a unit cube with prescribed Dirichlet boundary conditions $\boldsymbol{u}_0 = (y \cdot k, 0, 0)^T$ with y the y-coordinate and k a constant, as illustrated in figure 23.

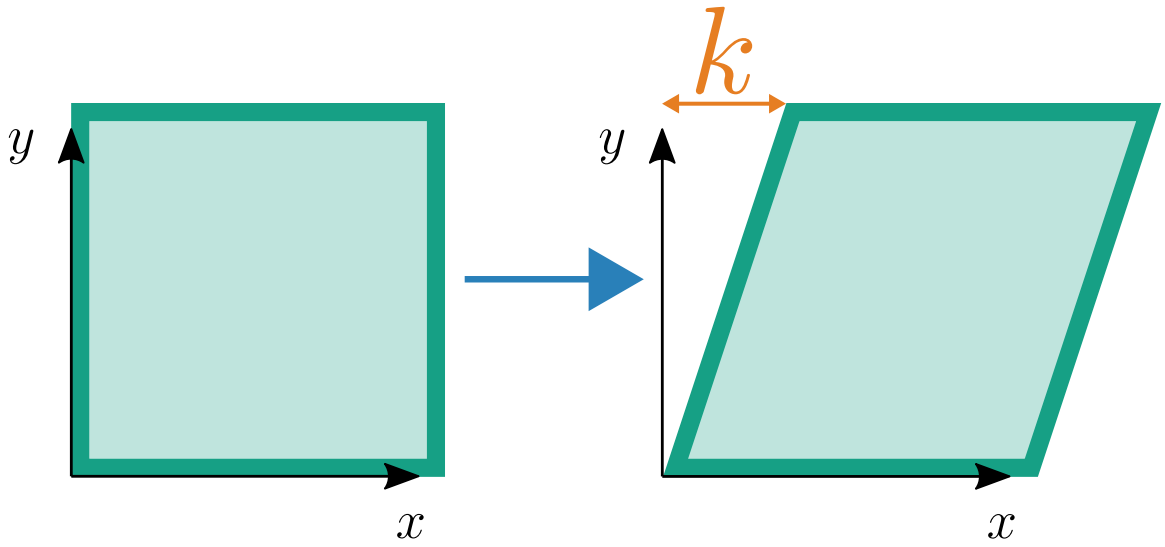

Figure 23: 2D plane cut of a simple shear deformation of a unit cube. An x-displacement of $y \cdot k$ is applied on the boundary while the bottom is subject to a null Dirichlet boundary ($\boldsymbol{u}_0 = (0, 0, 0)^T$ when $y = 0$).

For simple shear deformation, the deformation gradient is equal to

$$\boldsymbol{F} = \nabla_0 \boldsymbol{u} + \boldsymbol{I} = \begin{pmatrix} 1 & k & 0 \\ 0 & 1 & 0 \\ 0 & 0 & 1 \end{pmatrix}. \tag{46}$$

Now, let us consider a cube made of a Mooney-Rivlin material. Following [149], we can obtain the energy density and the components of the Cauchy stress tensor $\boldsymbol{\sigma}$

$$\psi = k^2(C_1 + C_2), \tag{47}$$

$$
\begin{aligned}
\sigma_{00} &= \frac{k^2(2C_2 + 4C_1)}{3}, \\
\sigma_{11} &= -\frac{k^2(4C_2 + 2C_1)}{3}, \\
\sigma_{22} &= \frac{k^2(2C_2 - 2C_1)}{3}, \\
\sigma_{01} &= k(2C_2 + 2C_1), \\
\sigma_{02} &= \sigma_{12} = 0.
\end{aligned}
\tag{48}
$$

The values of ψ and $\boldsymbol{\sigma}$ have been evaluated in our framework with several values of k, degrees of discretization, and constitutive parameters. The relative error (by using the l^2-norm) in strain energy and Cauchy stress tensor, compared to the analytical values, shows the exactness of the direct deformation framework to machine precision (10^{-12} magnitude error).

Generalized shear The generalized shear deformation test is similar to the simple shear deformation [149]. The initial geometry is a unit cube with prescribed Dirichlet boundary conditions $\boldsymbol{u}_0 = (y^2 \cdot k, 0, 0)^T$ with y the y-coordinate and k a constant, as illustrated in figure 24.

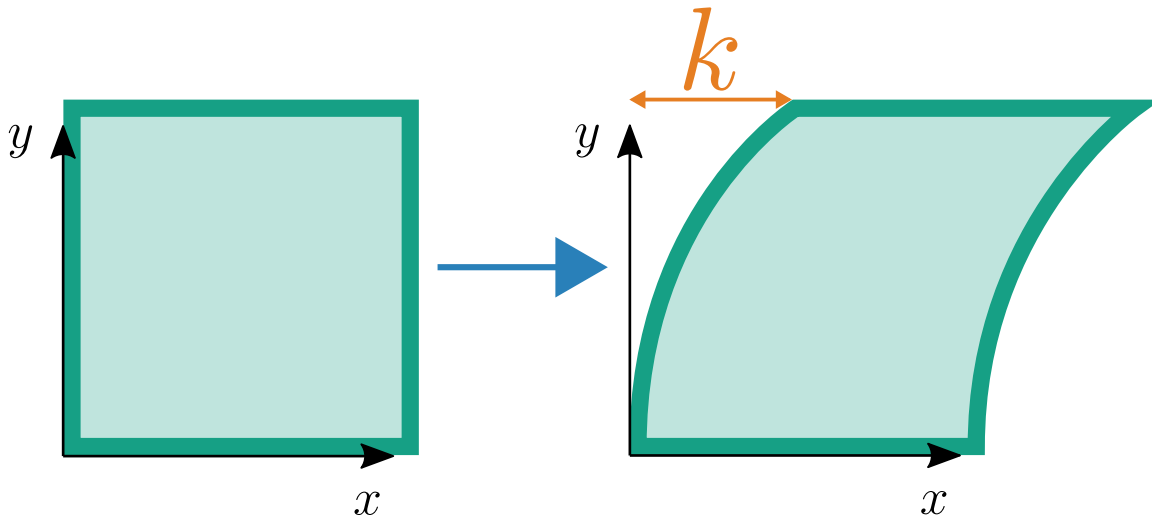

Figure 24: 2D plane cut of a generalized shear deformation of a unit square. An x-displacement of $y^2 \cdot k$ is applied to the boundary of the cube while the bottom is subject to a null Dirichlet boundary ($\boldsymbol{u}_0 = (0, 0, 0)^T$ when $y = 0$).

For generalized shear deformation, the deformation gradient is equal to

$$
\boldsymbol{F} = \begin{pmatrix} 1 & 2ky & 0 \\ 0 & 1 & 0 \\ 0 & 0 & 1 \end{pmatrix}. \tag{49}
$$

In the same manner as in the simple shear deformation, we consider a cube made of a Mooney-Rivlin material and can apply the same methods to find the analytical strain energy density function $\boldsymbol{\psi}$ and the Cauchy stress tensor components $\boldsymbol{\sigma}$

$$\begin{aligned}\psi &= \int_0^1 [C_1(\overline{I_1} - 3) + C_2(\overline{II_1} - 3)] \, \mathrm{dy} \\ &= \int_0^1 4k^2y^2(C_1 + C_2) \, \mathrm{dy} \\ &= \frac{4k^2(C_1 + C_2)}{3},\end{aligned} \tag{50}$$

$$\begin{aligned}\sigma_{00} &= \frac{k^2(8C_2 + 16C_1)}{9}, \\ \sigma_{11} &= -\frac{k^2(16C_2 + 8C_1)}{9}, \\ \sigma_{22} &= \frac{k^2(8C_2 - 8C_1)}{9}, \\ \sigma_{01} &= k(2C_2 + 2C_1), \\ \sigma_{02} &= \sigma_{12} = 0.\end{aligned} \tag{51}$$

We realize the same tests as the simple shear (different k values, mesh precision, and mechanical parameters) and evaluate the identical quantities, ψ and $\boldsymbol{\sigma}$ values. We observed an impact of the mesh on the strain energy and the Cauchy stress. The error quickly decreases on mesh refinement to reach relative errors under 2%.

3.6.3 Verification of the inverse simulation

This section presents a series of tests to verify the consistency of our inverse method with the direct approach. More precisely, we show that the undeformed configuration corresponds to the initial configuration used to deform it. During these tests, we also compare our method to the IGA method presented in section 3.2.4 and evaluate their performance and convergence rates.

3.6.4 Inverse shear deformation

This test is based on the direct shear deformation verification performed in section 3.6.2. We verify that the inverse deformation of the simple shear and the generalized shear is consistent with the direct finite element analysis. The idea is to start the test with the deformed configuration and apply the inverse deformation to verify that the rest-configuration corresponds to the initial geometry of the direct deformation. Since both shear deformations are entirely determined by a displacement field, the inverse deformation consists of applying the opposite displacement field. It is then trivial to claim that the geometry will

be recovered, i.e. a unit cube. However, this test also verifies the deformation gradient, the strain energy, and stress tensors are sound. As explained previously, those measures should be equal in both inverse and direct deformation. We verify these statements numerically in these tests.

Inverse simple shear : For the inverse simple shear deformation, the material points are now shifted by $-k \cdot y$ on the x-axis while the bottom is fixed ($y = 0$). As illustrated in figure 25.

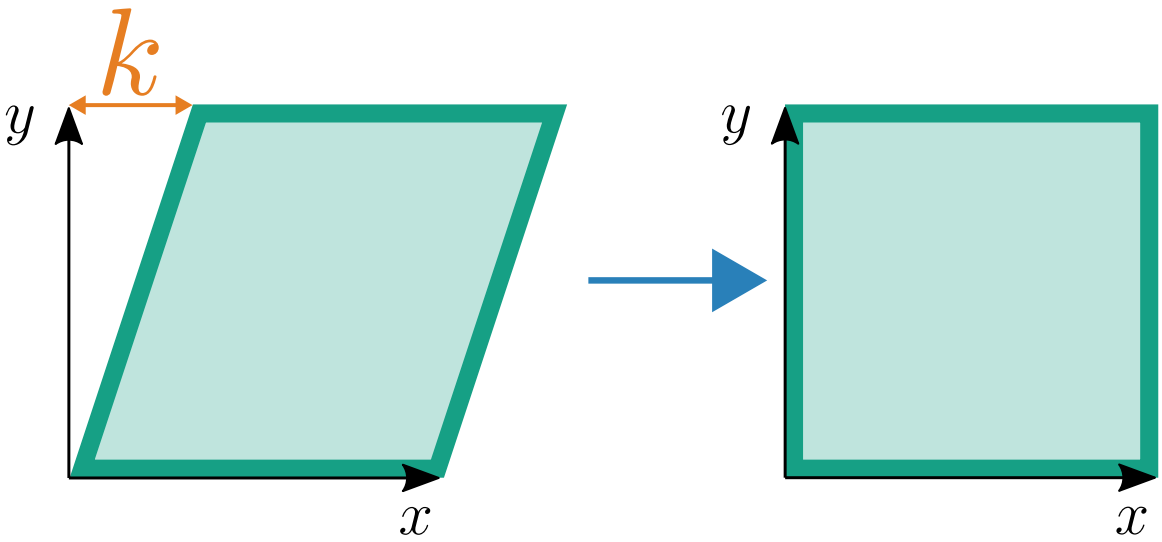

Figure 25: 2D plane cut of an inverse simple shear deformation of a unit cube. An x-displacement of $-y \cdot k$ is applied on the boundary while the bottom is subject to a null Dirichlet boundary ($\boldsymbol{u}_0 = (0, 0, 0)^T$ when $y = 0$).

We calculate the deformation gradient $\boldsymbol{F}$ which is equal to the deformation gradient in equation 46, as expected

$$\nabla \boldsymbol{u'} + \boldsymbol{I} = \begin{pmatrix} 1 & -k & 0 \\ 0 & 1 & 0 \\ 0 & 0 & 1 \end{pmatrix}, \tag{52}$$

$$\boldsymbol{F} = (\nabla \boldsymbol{u'} + \boldsymbol{I})^{-1} = \begin{pmatrix} 1 & k & 0 \\ 0 & 1 & 0 \\ 0 & 0 & 1 \end{pmatrix}. \tag{53}$$

Therefore, the strain energy, which is usually defined depending on $\boldsymbol{F}$, is equal to the strain energy in equation 47, and the stress tensor of equation 48 remains valid. Since the deformation is homogeneous (constant deformation gradient), our quadratic finite element method is able to reproduce the analytical solution down to machine precision.

Inverse generalized shear: Similarly, the inverse version of the generalized shear deformation leads to the same deformation gradient tensor (equation 49), then to the same strain energy density function (equation 50). The relative error is evaluated with different discretizations of the initial mesh but the same parameters set and we obtain with high precision the initial geometry.

References

[1] J.E. Adkins. "A reciprocal plane property of the finite plan strain equations". In: *Journal of the Mechanics Physics of Solid* 6.4 (1958), pp. 267–275 (page 50).

[5] Martin S. Alnæs et al. "Unified Form Language: A Domain-Specific Language for Weak Formulations of Partial Differential Equations". In: *ACM Trans. Math. Softw.* 40.2 (2014). ISSN: 0098-3500. DOI: 10.1145/2566630. URL: https://doi.org/10.1145/2566630 (pages 55, 82).

[12] Satish Balay et al. *PETSc Web page*. https://petsc.org/. 2022. URL: https://petsc.org/ (page 56).

[22] J Bols et al. "A computational method to assess the in vivo stresses and unloaded configuration of patient-specific blood vessels". In: *Journal of Computational and Applied Mathematics* 246 (2013), pp. 10–17. ISSN: 0377-0427. DOI: 10.1016/j.cam.2012.10.034. URL: http://dx.doi.org/10.1016/j.cam.2012.10.034 (page 50).

[32] Donald E. Carlson and T. Shield. "Inverse deformation results for elastic materials". In: *Zeitschrift für angewandte Mathematik und Physik ZAMP* 20.2 (1969), pp. 261–263. ISSN: 00442275. DOI: 10.1007/BF01595564 (page 50).

[33] M M Carroll and F J Rooney. "Implications of Shield ' s inverse deformation theorem for compressible finite elasticity". In: *Zeitschrift für angewandte Mathematik und Physik ZAMP* 56 (2005), pp. 1048–1060. DOI: 10.1007/s00033-005-2023-0 (page 50).

[40] Xiang Chen et al. "An asymptotic numerical method for inverse elastic shape design". In: *ACM Transactions on Graphics* 33.4 (2014). ISSN: 15577333. DOI: 10.1145/2601097.2601189 (page 51).

[52] M. A. Crisfield. *Non-Linear Finite Element Analysis of Solids and Structures: Advanced Topics*. 1st. USA: John Wiley & Sons, Inc., 1997. ISBN: 047195649X (page 54).

[64] Victor Fachinotti and Alberto Cardona. "Design of compliant mechacanisms that exactly fit a desired shape". In: *Mecánica Computacional* 28 (2009), pp. 3191–3205 (pages 50, 51, 67).

[65] Victor D. Fachinotti, Alberto Cardona, and Philippe Jetteur. "Finite element modelling of inverse design problems in large deformations anisotropic hyperelasticity". In: *International Journal For Numerical Methods In Engineering* October 2007 (2008), pp. 894–910. DOI: 10.1002/nme (page 49).

[69] François Faure et al. "SOFA: A Multi-Model Framework for Interactive Physical Simulation". In: *Soft Tissue Biomechanical Modeling for Computer Assisted Surgery*. Ed. by Yohan Payan. Berlin, Heidelberg: Springer Berlin Heidelberg, 2012, pp. 283–321. ISBN: 978-3-642-29014-5. DOI: 10.1007/8415_2012_125. URL: https://doi.org/10.1007/8415_2012_125 (pages 37, 64, 130).

[73] Antonio E. Forte et al. "A composite hydrogel for brain tissue phantoms". In: *Materials and Design* 112 (2016), pp. 227–238. ISSN: 18734197. DOI: 10.1016/j.matdes.2016.09.063. URL: http://dx.doi.org/10.1016/j.matdes.2016.09.063 (page 61).

[74] Leopoldo P. Franca and Thomas J.R. Hughes. "Two classes of mixed finite element methods". In: *Computer Methods in Applied Mechanics and Engineering* 69.1 (1988), pp. 89–129. ISSN: 0045-7825. DOI: https://doi.org/10.1016/0045-7825(88)90168-5. URL: https://www.sciencedirect.com/science/article/pii/0045782588901685 (page 55).

[85] Sanjay Govindjee and Paul A Mihalic. "Computational methods for inverse deformations in quasi-incompressible finite elasticity". In: *International Journal For Numerical Methods In Engineering* 43.5 (1998), pp. 821–838 (page 50).

[86] Sanjay Govindjee and Paul A Mihalic. "Computational methods for inverse finite elastostatics". In: *Computer Methods In Applied Mechanics And Engineering* 136.96 (1996) (page 50).

[114] M. Koishi and S. Govindjee. "Inverse design methodology of a tire". In: *Tire Science and Technology* 29.3 (2001), pp. 155–170. ISSN: 00908657. DOI: 10.2346/1.2135236 (page 49).

[116] Aravindh Krishnamoorthy and Deepak Menon. "Matrix inversion using Cholesky decomposition". In: *2013 Signal Processing: Algorithms, Architectures, Arrangements, and Applications (SPA)*. 2013, pp. 70–72 (page 64).

[123] Chang Kye Lee et al. "Strain smoothing for compressible and nearly-incompressible finite elasticity". In: *Computers and Structures* 182.February (2017), pp. 540–555. ISSN: 00457949. DOI: 10.1016/j.compstruc.2016.05.004. URL: http://dx.doi.org/10.1016/j.compstruc.2016.05.004 (pages 51, 57).

[128] A. Logg, K.A. Mardal, and G. Wells. *Automated Solution of Differential Equations by the Finite Element Method: The FEniCS Book*. Lecture Notes in Computational Science and Engineering. Springer Berlin Heidelberg, 2012. ISBN: 9783642230998. URL: https://books.google.lu/books?id=ASWN_VRr1NQC (page 55).

[129] Anders Logg and Garth N. Wells. "DOLFIN: Automated Finite Element Computing". In: *ACM Trans. Math. Softw.* 37.2 (2010). ISSN: 0098-3500. DOI: 10.1145/1731022.1731030. URL: https://doi.org/10.1145/1731022.1731030 (page 56).

[133] Jia Lu, Xianlian Zhou, and Madhavan L Raghavan. "Inverse elastostatic stress analysis in pre-deformed biological structures : Demonstration using abdominal aortic aneurysms". In: *Journal of Biomechanics* 40.3 (2007), pp. 693–696. DOI: 10.1016/j.jbiomech.2006.01.015 (page 49).

[134] Mickaël Ly et al. "Inverse elastic shell design with contact and friction". In: *SIGGRAPH Asia 2018 Technical Papers, SIGGRAPH Asia 2018* 37.6 (2018). ISSN: 15577368. DOI: 10.1145/3272127.3275036 (page 51).

[135] Alnaes M. et al. "The FEniCS project version 1.5". In: *Archive of Numerical Software 3* (2015). DOI: doi:10.11588/ans.2015.100.20553 (pages 51, 55).

[139] Stéphanie Marchesseau et al. "Fast porous visco-hyperelastic soft tissue model for surgery simulation: Application to liver surgery". In: *Progress in Biophysics and Molecular Biology* 103.2 (2010). Special Issue on Biomechanical Modelling of Soft Tissue Motion, pp. 185–196. ISSN: 0079-6107. DOI: https://doi.org/10.1016/j.pbiomolbio.2010.09.005. URL: https://www.sciencedirect.com/science/article/pii/S0079610710000738 (pages 64, 78).

[143] Arnaud Mazier et al. "Supplementary material for Inverse deformation analysis: an experimental and numerical assessment using the FEniCS Project". In: (Feb. 2021). DOI: 10.6084/m9.figshare.14035793.v1. URL: https://figshare.com/articles/software/Supplementary_material_for_Inverse_deformation_analysis_an_experimental_and_numerical_assessment_using_the_FEniCS_Project/14035793 (pages 56, 57, 60, 91).

[149] L. Angela Mihai and Alain Goriely. "Numerical simulation of shear and the Poynting effects by the finite element method: An application of the generalised empirical inequalities in non-linear elasticity". In: *International Journal of Non-Linear Mechanics* 49.November 2017 (2013), pp. 1–14. ISSN: 00207462. DOI: 10.1016/j.ijnonlinmec.2012.09.001 (pages 51, 57, 68, 69).

[152] Anna Mîra et al. "A biomechanical breast model evaluated with respect to MRI data collected in three different positions". In: *Clinical Biomechanics* 60 (2018), pp. 191–199. DOI: 10.1016/j.clinbiomech.2018.10.020 (pages 49, 51, 117, 119, 129–131, 135, 142, 143).

[154] M. Mooney. "A Theory of Large Elastic Deformation". In: *Journal of Applied Physics* 11.9 (1940), pp. 582–592. DOI: 10.1063/1.1712836. eprint: https://doi.org/10.1063/1.1712836. URL: https://doi.org/10.1063/1.1712836 (pages 54, 81).

[166] R.W. Ogden. "Non-linear elastic deformations". In: *Engineering Analysis* 1.2 (1984), p. 119. ISSN: 0264-682X. DOI: https://doi.org/10.1016/0264-682X(84)90061-3. URL: https://www.sciencedirect.com/science/article/pii/0264682X84900613 (page 54).

[176] M. L. Raghavan, Baoshun Ma, and Mark F. Fillinger. "Non-invasive determination of zero-pressure geometry of arterial aneurysms". In: *Annals of Biomedical Engineering* 34.9 (2006), pp. 1414–1419. ISSN: 00906964. DOI: 10.1007/s10439-006-9115-7 (page 49).

[187] Manuel K. Rausch, Martin Genet, and Jay D. Humphrey. "An augmented iterative method for identifying a stress-free reference configuration in image-based biomechanical modeling". In: *Journal of Biomechanics* 58 (2017), pp. 227–231. ISSN: 18732380. DOI: 10.1016/j.jbiomech.2017.04.021 (page 67).

[190] R. S. Rivlin. "Large elastic deformations of isotropic materials. IV. Further developments of the general theory". In: *Philosophical Transactions of the Royal Society of London. Series A, Mathematical and Physical Sciences* 241.835 (1948), pp. 379–397 (page 54).

[199] Richard T. Schield. "Inverse deformation results in finite elasticity". In: *Zeitschrift für angewandte Mathematik und Physik ZAMP* 18.4 (1967), pp. 490–500. ISSN: 00442275. DOI: 10.1007/BF01601719 (page 50).

[202] M Sellier. "An iterative method for the inverse elasto-static problem". In: *Journal of Fluids and Structures* 27.8 (2011), pp. 1461–1470. ISSN: 0889-9746. DOI: 10.1016/j.jfluidstructs.2011.08.002. URL: http://dx.doi.org/10.1016/j.jfluidstructs.2011.08.002 (pages 50, 51, 53, 56, 67).

[232] Takahiro Yamada. "Finite element procedure of initial shape determination for hyperelasticity". In: *Structural Engineering and Mechanics* 6.2 (1998), pp. 173–183. ISSN: 12254568. DOI: 10.12989/sem.1998.6.2.173 (page 50).

[237] X. Zhou and J Lu. "Estimation of vascular open configuration using finite element inverse elastostatic method". In: *Engineering with Computers* 25.49 (2009). DOI: doi.org/10.1007/s00366-008-0104-3 (page 49).

4 SOniCS: Develop intuition on biomechanical systems through interactive error controlled simulations [5]

Abstract

We describe the SOniCS (SOFA + FEniCS) plugin to help develop intuitive understanding of complex biomechanics systems. This new approach allows the user to experiment with model choices easily and quickly without requiring in-depth expertise. Constitutive models can be modified by one line of code only. This ease in building new models makes SOniCS ideal to develop surrogate, reduced order models and to train machine learning algorithms for enabling real-time patient-specific simulations. SOniCS is thus not only a tool that facilitates the development of surgical training simulations but also, and perhaps more importantly, paves the way to increase the intuition of users or otherwise non-intuitive behaviors of (bio)mechanical systems. The plugin uses new developments of the FEniCSx project enabling automatic generation with FFCx of finite element tensors such as the local residual vector and Jacobian matrix. We verify our approach with numerical simulations such as manufactured solutions, cantilever beams, and benchmarks provided by FEBio. We reach machine precision accuracy and demonstrate the use of the plugin for a real-time haptic simulation involving a surgical tool controlled by the user in contact with a hyperelastic liver. We include complete examples showing the use of our plugin for simulations involving Saint Venant-Kirchhoff, Neo-Hookean, Mooney-Rivlin, and Holzapfel Ogden anisotropic models as supplementary material.

4.1 Introduction

Designing efficient finite element (FE) simulation software is a challenging task. Indeed, as FEM is a vast field, numerous pieces of software emerged to fill different gaps. For instance, commercial software such as Abaqus [207] or Ansys [53] focus on user-friendly GUIs (Graphical User Interface) guiding the user from pre-processing to post-processing. This has the advantage of allowing users to perform complex simulations with a relatively basic theoretical knowledge of FE. Meanwhile, other pieces of software focused on specific domains such as Gmsh [80] for FE meshing, Paraview [2] for FE visualization, OpenFoam [106] for CFD (Computational Fluid Dynamic) simulations, OpenXFEM [24] for extended finite elements [105], collocation methods [102], meshfree methods [161], multiscale problems [214], or material point methods (MPM) [205]. This historical perspective explains the countless FE solvers which makes an exhaustive state-of-the-art review quasi-impossible. Before selecting one piece of FE software, user should consider the benefits and disadvantages associated with each (i.e., meshing, parallel support, solvers, coding language, and visualization). However, generally, simplicity of use and the ability to easily test modelling hypotheses appears like the most important considerations in selecting such a computational tool.

In the medical simulation context, several specific aspects have to be considered.

[5] Reproduced from: A. Mazier, S. El Hadramy, J-N. Brunet, J.S. Hale, S. Cotin, S.P.A. Bordas, SOniCS: Develop intuition on biomechanical systems through interactive error controlled simulations, pre-print submitted, `https://doi.org/10.48550/arXiv.2208.11676`.

- The material model complexity. Contrary to engineering materials such as steel or copper, the mechanical properties of living organs were only recently quantified [81, 172] (early 90s against 1700 for copper) and show immense variability [151]. Various models have been proposed, e.g., anisotropic [25, 63, 72, 175, 236], hyperelastic [38, 100, 140, 150, 234], viscoelastic [61, 89, 139, 221], or poroelastic [15, 31, 51, 120, 188, 204, 208] to accurately depict their complex mechanical behaviors. Indeed, predicting the deformations of bio-materials can only be achieved through complex material models (sometimes even multi-scale), which are rarely implemented in commercial software. One major difficulty of this implementation remains the differentiation of highly nonlinear equations. Indeed, predicting the deformations of such materials can only be achieved through complex material models, rarely implemented in commercial software. One major difficulty of this implementation remains the linearization of highly nonlinear equations. For instance, hyperelasticity equations can be written as a minimization of a tensorial function. In most cases, this minimization is solved using gradient-descent algorithms requiring the first and second derivatives of the functional. Therefore, obtaining such high-order nonlinear derivatives is not straightforward and can be prone to manual errors.

- The complexity of the simulation. In addition to the complexity of the material model, the simulation setup itself can be problematic. For instance, the material parameters are patient-specific and require data-driven or inference methods [91, 220]. The simulations can also (partially) involve unknown boundary conditions [213], contact with other organs [50, 148], or surgical tools [48, 126]. The problem can also require multi-physics models (such as FSI [21, 23] (Fluid-Structure Interactions)) or incompressibility [142, 228], where classical displacement-based finite elements are prone to locking.

- The error control and uncertainty of the solution. When dealing with biomechanical simulations, several uncertainties always arise from the material parameters, loads, geometry, or boundary conditions. This is mainly due to the difficulty in estimating the mechanical properties through ex-vivo methods or the topology of biological tissues using medical imaging. Similarly, error control and mesh adaptivity are necessary to ensure homogeneous convergence of the solution over the domain and that the mesh is optimal given a quantity of interest [3]. Therefore, quantifying the uncertainty or controlling the error on quantities of interests often requires making a very large number of simulations [183, 185] which is incompatible with surgical timing [94, 95]. Meanwhile, those approaches could be functional in clinical settings by using accelerated simulations [30] to build surrogate models or/and machine learning models for faster solutions of those highly non-linear parametric problems.

- The real-time aspect. In addition to the previous point, for clinical environments, the run time of the numerical simulation is crucial. When performing an operation, the surgeon cannot, in general, spend minutes waiting for the model predictions. Eventually, this aspect is also applicable to artificial intelligence. Indeed, in order to build

an efficient machine learning model, a significant amount of data is necessary. Using numerical simulations to create synthetic data is now standard and directly dependent on the simulation time [55, 164]. Consequently, the run-time of the simulation can be considered a principal feature of biomechanics simulations, and indeed, of any non-intuitive non-linear problems subject to significant uncertainties in loading, boundary and initial conditions, and parameters. Nowadays, gaming engines such as Unity3D [145] or Unreal Engine [198] offer real-time animation where physics-based algorithms can be included [46, 218, 224].

- The interaction with the user. In a surgical simulation setting, external variables can impact the simulation during the execution. For example, the exact movement of the surgeon's tool influences the simulation at run-time. Thus, the parameters of the simulation must be tuned, "live", to integrate interactions between the user and the simulation [163, 230].

- The visual rendering. Depending on the research field, visualization can play a critical role in the understanding of the results. For instance, in the computer graphics community, photo-realistic visualization is one of the main objectives [82, 138]. Contrastingly, in the mechanical engineering culture, visualization is a manner of extracting and understanding quantitatively a solution or data set (i.e., stress or displacement fields). For medical simulations, an optimal solution must combine both the accuracy of the results and photo-realistic rendering reflecting the clinical ground truth all within clinical time frames [88].

According to the state-of-the-art, SOFA [70] (Simulation Open Framework Architecture) appears to be a suitable compromise. Indeed, SOFA employs efficient rendering while providing the possibility to interact in real-time with the running simulation. One can note that real-time computing is only possible depending on the complexity of the problem. Indeed, using excessive numbers of degrees of freedom (DOFs) or solving a highly nonlinear problem cannot result in a real-time simulation (without using model order reduction [41, 83, 84] or machine learning [55]). SOFA can also manage complex simulations through an efficient implementation of contact [**Duriez2004**, **Courtecuisse2010**, **Courtecuisse2011**], for example, or enabling multi-physics coupling. Therefore, only a few material models and elements are available. A similar issue is observed for material models where numerous implementations only focused on a 3-dimensional isotropic behavior. Therefore, coding a new material model or element in SOFA requires advanced C++ skills that may discourage individuals from using the software.

To alleviate the problem of complex material models, FEniCS [4] seems like an appropriate solution. Indeed, FEniCS may not possess all of SOFA's features, but definitely overcomes SOFA's capabilities for material model complexity. With FEniCS, the user can generate any material model, regardless of the element's geometry or interpolation. Plus, it authorizes an export of the pertinent finite element tensors in C code to be efficiently plugged into SOFA. The benefits of the synergy are considerable. By using SOFA's interactivity and real-time features, the user can easily prototype a real-time simulation. Indeed,

by modifying "live" various boundary conditions, geometries, or topologies, the user can effortlessly and rapidly verify modeling hypotheses for a specific problem. Combined with the specificities of FEniCS, the user can additionally smoothly prototype complex material models for modeling elaborate scenarios. Such feature has already been used by coupling FEniCS and Acegen but with different objectives [124]. To the authors' knowledge, this paper is the first to use FEniCS code generation capabilities for such an endeavor and is the first coupling between FEniCS and SOFA.

This paper has the following outline. We will first briefly introduce SOFA and FEniCS, highlighting the relative advantages and design choices in each. Section 4.2 will detail the plugin functionalities and a short tutorial for importing a Saint Venant-Kirchhoff model from FEniCS in SOFA. Then, section 4.3 will focus on confirming our implementation for various numerical tests. We will use a manufactured solution in 4.3.1 as validation and compare our solutions for a cantilever beam problem with SOFA in 4.3.2. The last test consists in implementing a new material model (Mooney-Rivlin) in SOFA and benchmarking it with FEBio [137] in 4.3.3. Finally, in the last section 4.4, we will use our plugin in a complex haptic simulation that cannot be implemented in FEniCS, using a custom material model inexistent in SOFA.

4.1.1 SOFA

SOFA was created in 2007 by a joint effort from Inria, CNRS, USTL, UJF, and MGH. This piece of software aims to provide an efficient framework dedicated to research, prototyping, and the development of physics-based simulations. It is an open-source library distributed under the LGPL license, hosted on GitHub at `https://github.com/sofa-framework/sofa`, and developed by an international community. SOFA is modular. Users can create public or private plugins to include additional features.

SOFA is a C++ library, including Python wrappers for a user-friendly prototyping interface. It was originally designed for deformable solid mechanics but has been extended to various domains such as robotics, registration, fluid simulations, model-order reduction, and haptic simulations [**Courtecuisse2010-2**, 58, 59]. SOFA exhibits many attractive features, but among them, the combination of multi-model representations and mappings differentiate it from other software.

Multi-model representation: Most classical FE software uses an identical discretization for the whole model. Consequently, if one user wants to refine the mesh along a contact surface, the FE mesh will undergo the same refinement in the contact region. It can induce slow simulations for solving the FE system while the user was initially only interested in the contact part. Conversely, utilizing a multi-model representation approach, users can split the principal model into three distinct sub-models: deformation, collision, and visual. Thus, the user can decide to have high fidelity deformations with flawed contact detection

while maintaining a fine rendering, or vice-versa. Similarly, an object can be made of several deformation models. For example, one can model a muscle by the interaction of FE 3D tetrahedra for the volume and 1D beams for modeling ligaments, using 2 different solvers.

Mappings: In SOFA, the "mappings" are responsible for the communication between the different models. The models have parent-child relationships constructing a hierarchy (and a DOF hierarchy by extension). It enables propagating the positions, velocities, accelerations, and forces across the different models. For example, if the contact model calculates a force, it is mapped on the deformation model that will communicate back the computed displacement.

Finally, by combining the multi-model representation with the mappings, SOFA can build complex real-time simulations with high fidelity rendering. In addition to a scenegraph structure and visitors (responsible for going through the model hierarchy) implementation, it can account for interactivity with the users.

Despite the advantages provided by SOFA, some drawbacks have to be acknowledged. First, in terms of solid mechanics simulations, only a few elements and material models are available. Indeed, SOFA only proposes Lagrange linear elements, and the geometries are limited to segments, triangles, quadrangles, tetrahedra, and hexahedra. The following material models are coded: Boyce and Aruda [8], Costa [47], isotropic and anisotropic Hookean, Mooney Rivlin (2 invariants) [154], classical and stabilized Neo-Hookean, Ogden [165], Saint Venant-Kirchhoff, and Veronda Westman [223]. Despite a reasonable number of mechanical models, a few of them are actually implemented for each element type. Secondly, the benefits provided by the mappings can also turn out to be a disadvantage when it comes to implementation. Indeed, the structure of the mappings is usually complex for unexperimented C++ users, and the mechanical tensors such as the Cauchy-Green or Piola-Kirchhoff are rarely computed. The two previous drawbacks are associated to the same flaw: the strong coupling between the material models and the topology of the element assumed within SOFA's architecture. This coupling implies that changing an element's topology or interpolation will involve a new mapping or the rewriting of the material model, even in the case of a similar material model.

4.1.2 The modular mechanics plugin (Caribou)

The initial goal of the plugin (called Caribou at the time of writing, `https://github.com/mimesis-inria/caribou`) was to quickly implement new shape functions and their derivatives for different Immersed-Boundary and meshless domain discretization while keeping the compatibility with the existing SOFA surgical simulations [29]. Besides, the plugin enabled to effortlessly implement different volumetric quadrature schemes and several hyperelastic material models. Hence, the software design had to be generic enough to combine all the previous requirements. It also had to be efficient enough to avoid the creation of a bottleneck that would prevent the biomechanical model from meeting its computational speed requirement. Hence, the plugin was made as an extension to SOFA, bringing a redesigned software architecture.

In the plugin, the authors implemented a compile-time polymorphism design using generic C++ template programming. The idea is to write the code as close as possible to equations found in traditional FE books. Then, the C++ compiler optimizes the set of operations executed during the simulation while keeping an object-oriented code. In this design, the "Element" concept was created as a generic computational class that would be inherited by all element types. Similarly to OpenXFEM++ [24], it provides a flexible implementation to add interpolation and quadrature numerical procedures quickly. Since standard isoparametric elements have a number of nodes, quadrature points, and shape functions already known at compile-time, most modern compilers will be able to aggressively inline the code to optimize the computation.

Finally, the plugin allows the creation of additional material models by simply defining three methods per material: the strain energy density function, the second Piola-Kirchhoff stress tensor function, and its derivative functions. These three functions are evaluated at a given integration point automatically provided by the plugin. This design delivers an undeniable advantage: writing a new material model is now independent of the topology and integration scheme. However, it comes with a non-negligible cost. The author of the new material model has to manually differentiate the strain energy twice and write it in C++. This manual intervention is error prone and can quickly become a substantial drawback for complex materials.

4.1.3 FEniCS

The FEniCS Project (FEniCS) [4] is a collection of tools for the automated solution of partial differential equations using the finite element method. Like SOFA, the FEniCS components are distributed under open-source licenses (LGPL v3 or later, and MIT) and development is hosted on GitHub at `https://github.com/fenics`.

A distinguishing feature of FEniCS is the ability to allow the user to write variational of weak formulations of finite element methods in a high-level Python-based domain specific language (DSL), the Unified Form Language (UFL) [5]. Subsequently, that high-level description can be compiled/transformed using the FEniCS Form Compiler (FFC) [112] into low-level and high-performance kernels. These kernels can calculate the corresponding local finite element tensor for a given cell in the mesh. UFL is also used by other finite element solvers with independently developed automatic code generation capabilities, notably Firedrake [186] and Dune [16]. Compared with SOFA, FEniCS is limited in scope; its primary focus is the specification and solution of partial differential equations via the finite element method, leaving difficult problems like mesh generation, post-processing and visualisation to leading third-party packages such as Gmsh [80] and Paraview [2].

In the context of implementing finite element models of hyperelastic materials, this automatic approach has a number of advantages over the traditional route used by most finite element codes (including, to some extent, SOFA); differentiating analytical expressions for the residual (first derivative) and Jacobian (second derivative) of the energy functional for the hyperelastic model, picking a suitable finite element basis and then hand-coding the corresponding finite element kernels in a low-level language (C, Fortran, C++) for

performance. Specifically:

1. The symbolic residual and Jacobian can be derived automatically using the symbolic differentiation capabilities of UFL. By contrast taking these derivatives by hand can be tedious and error-prone.

2. The compilation of the UFL description of the problem by FFC into the associated low level kernels is entirely automated. Again, this step is often time consuming and difficult to perform manually.

3. Because of the high-level description of the problem it is possible to experiment quickly with different concrete finite element formulations (material models, basis functions, element topology etc.) without manually modifying low-level kernel code.

The potential of this high-level approach for solid mechanics were recognised early on in the development of FEniCS, with two chapters in the FEniCS Book [157, 240] promoting this direction. Since then, FEniCS has been used in a large number of publications on the topic of hyperelastic large-deformation elasticity e.g. [14, 162, 171, 174, 227].

Recently the FEniCS Project has undergone a major redevelopment, resulting in the new FEniCSx components; DOLFINx (the finite element problem solving environment, replacing DOLFIN), FFCx (the FEniCSx Form Compiler, replacing FFC) and Basix [200] (a finite element basis function tabulator, replacing FIAT [111]). UFL is largely unchanged from the version used in the old FEniCS components and Firedrake.

In this work we do not use DOLFINx. DOLFINx contains the basic finite element data structures and algorithms (e.g. meshes, function spaces, assembly, interfacing with linear algebra data structures in e.g. PETSc []) and therefore there is a significant overlap with the functionality already available in SOFA. Directly interfacing DOLFINx and SOFA at the Application Programming Interface (API) level would be a significant technical challenge due to the substantial differences in their internal data structures. Dedicated weak coupling libraries such as PreCICE [191] could be an interesting alternative to API coupling, but it is not a path that we explore in this work.

Instead, the approach taken by SOniCS is to only use UFL and FFCx (which in turn depends on Basix) to convert the high-level description of the finite element problem into low-level C code, which are then called using SOFA's existing C++ finite element data structures and algorithms. Compared with coupling DOLFINx and SOFA directly, our approach creates a relatively light compile-time coupling between FEniCS (specifically, the generated C code) and SOFA (a large complex C++ code with many dependencies). Consequently, no additional runtime dependencies required for SOFA. This methodology will be familiar to users of the DOLFINx C++ inteface where C finite element kernels are generated in a first step using UFL and FFCx and are then integrated into the DOLFINx solver in a second step through a standard compile/include/link approach. Without going into excessive detail, two changes in the redeveloped FEniCSx components have made SOniCS significantly easier to realise:

1. Basix and FFCx have full support for Serendipity finite elements of arbitrary polynomial order following the construction of Arnold and Awanou [7]. Serendipity elements are used in SOFA and there was a desire to continue supporting Serendipity basis function due to their lower number of degrees of freedom per cell and generally lower number of local computations compared with standard tensor-product Lagrange elements. We remark that despite the widespread use of Serendipity elements in many solvers, they can only obtain optimal order convergence on affinely-mapped meshes, see e.g. [6] for more details.

2. FFCx outputs C99 compliant code according to the UFCx interface, which is specified as a C header file included with FFCx. This is in contrast with FFC, which outputs C++03 compliant code conforming to an interface specified with a C++ header file. This switch makes it significantly easier to call FFCx generated kernels from libraries with a C Foreign Function Interface (FFI) such as Python and Julia, or any language which can easily call functions with a C ABI (e.g. Fortran). Although SOFA is a C++ libraries and could certainly call C++ generated kernels, the C interface is simpler to use, consisting only of structs containing basic native data types and functions.

4.2 SOniCS

In this section, we present more in-depth the SOniCS (SOFA + FEniCS). The plugin is available on a development branch in GitHub `https://github.com/mimesis-inria/caribou/tree/FeniCS-features` and will soon be merged into the main branch. We first introduce the procedure for defining the material model, the element geometry, and the quadrature rule or degree using the UFL (Python) syntax. For simplicity, we only focused on a Saint Venant-Kirchhoff model. But the method can be generalized to all element types following the pipeline shown in figure 26. Secondly, we explain the methodology for converting the UFL script into efficient C kernels. Finally, we show the interface between the SOniCS plugin and SOFA, stating the conceptual and coding differences. For simplicity and as the modular mechanics plugin's name (Caribou) might change, we use the name SOFA to denote the combination of SOFA and the modular mechanics plugin.

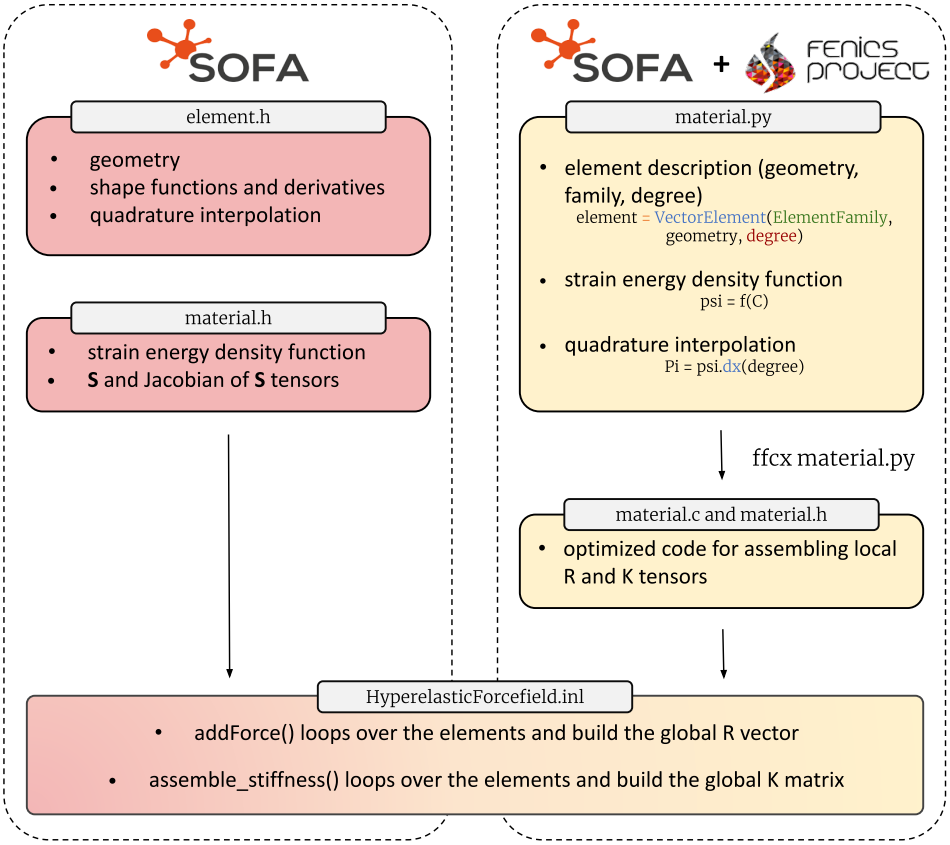

Figure 26: Description of the SOniCS pipeline (on the right) and differences with SOFA(on the left). In SOFA, each element has to be defined, embedding its geometry, shape functions (including derivatives), and the quadrature scheme and degree. In SOniCS, it has been replaced by two Python lines of code for describing the element and its quadrature. The same benefit goes for the material model description. In SOFA, each material has to be created in a separated file stating its strain energy, derivating by the hand the second Piola Kirchhoff tensor (S) and its Jacobian. It was replaced in SOniCS by only defining the strain energy of the desired material model in UFL. The derivative of the strain energy will then be automatically calculated using the FFCX module. Finally, both plugins share the same Forcefield methods for assembling the global residual vector ($\boldsymbol{R}$) and stiffness matrix ($\boldsymbol{K}$).

4.2.1 UFL: from FE model to Python code

The first step is to define the FE model using the UFL syntax in a Python script. As an example, in listing 1, we describe the 3D simplest hyperelastic model and element: Saint

Venant-Kirchhoff with linear Lagrange finite elements on tetrahedra. In the context of hyperelastic simulations, we will exclusively describe features that users could be interested in customizing.

```
# material.py
from ufl import (Coefficient, Constant, Identity,
TestFunction, TrialFunction, inner, ds,
VectorElement, derivative, dx, grad,
tetrahedron, tr, variable)

# Function spaces
cell = tetrahedron
d = cell.geometric_dimension()
element = VectorElement("Lagrange", cell, 1)

# Trial and test functions
du = TrialFunction(element)  # Incremental displacement
v = TestFunction(element)  # Test function

# Functions
u = Coefficient(element)  # Displacement from previous iteration
B = Coefficient(element)   # Body forces
B = Coefficient(element)   # Traction forces

# Kinematics
I = Identity(d)  # Identity tensor
F = variable(I + grad(u))  # Deformation gradient
C = variable(F.T * F)  # Right Cauchy-Green tensor
E = variable(0.5 * (C - I))  # Green-Lagrange tensor

# Elasticity parameters
young = Constant(cell)
poisson = Constant(cell)
mu = young / (2 * (1 + poisson))
lmbda = young * poisson / ((1 + poisson) * (1 - 2 * poisson))

# Stored strain energy density (compressible Neo-Hookean model)
psi = (lmbda / 2) * tr(E) ** 2 + mu * tr(E * E)

# Total potential energy
Pi = psi * dx(degree=1) - inner(B, u) * dx(degree=1) - inner(T, u) * ds(
    degree=1)

# First variation of Pi (directional derivative about u in the direction of
    v)
F = derivative(Pi, u, v)

# Compute Jacobian of F
J = derivative(F, u, du)

# Export forms
```

```
46 forms = [F, J, Pi]
```

Listing 1: Python code example (`material.py`) of a Saint Venant-Kirchhoff material model using Lagrange linear tetrahedron.

Element: After importing the necessary packages, we can define the element geometry. In listing 1, on line 10, we used a linear Lagrange tetrahedron. The user can easily modify different parameters of the element, such as the geometry, the family type, or the interpolation degree. For example, by only changing line 10 to

```
element = VectorElement("Serendipity", hexahedron, 2)
```

the element is now a quadratic Serendipity hexahedron. Note that `VectorElement` creates by default a function space of vector field equal to the spatial dimension. A complete list of the element available in the Basix documentation [200].

Material model: By definition, boundary value problems for hyperelastic media can be expressed as minimization problems. For a domain $\Omega \subset R^3$, the goal is to find the displacement field $\boldsymbol{u} : \Omega \to R^3$ that minimizes the total potential energy Π. The potential energy is given by

$$\Pi(\boldsymbol{u}) = \int_\Omega \psi(\boldsymbol{u})\,\mathrm{d}x - \int_\Omega \boldsymbol{B}\cdot\boldsymbol{u}\,\mathrm{d}x - \int_{\partial\Omega} \boldsymbol{T}\cdot\boldsymbol{u}\,\mathrm{d}s, \tag{54}$$

where ψ is the elastic stored energy density, $\boldsymbol{B}$ is a body force (per unit reference volume), and $\boldsymbol{T}$ is a traction force (per unit reference area) prescribed on a boundary $\partial\Omega$ (of measure $\mathrm{d}s$) of the domain Ω (of measure $\mathrm{d}x$).

In listing 1, at line 37, we define the strain energy of a Saint Venant-Kirchhoff material model as:

$$\psi = \frac{\lambda}{2}\mathrm{tr}(\boldsymbol{E})^2 + \mu\mathrm{tr}(\boldsymbol{E}^2), \tag{55}$$

where λ and μ are Lamé material constants while $\boldsymbol{E}$ is the Green Lagrange strain tensor defined as $\frac{1}{2}(\boldsymbol{C}-\boldsymbol{I})$ where $\boldsymbol{I}$ is the identity matrix and $\boldsymbol{C}$ the right Cauchy-Green tensor $\boldsymbol{C} = \boldsymbol{F}^T\boldsymbol{F} = (\nabla\boldsymbol{u}+\boldsymbol{I})^T(\nabla\boldsymbol{u}+\boldsymbol{I})$. Therefore, we observe that tensor $\boldsymbol{E}$ is expressed with respect to the displacement $\boldsymbol{u}$, which is the unknown displacement field. Moreover, λ and μ are a function of the Young's modulus and of Poisson's ratio that are assumed to be known constants.

If the user would like to change the material model for Neo-Hookean with the strain energy density

$$\psi = \frac{\mu}{2}(I_C - 3) - \mu\ln(J) + \frac{\lambda}{2}\ln(J)^2. \tag{56}$$

It would only require in replacing line 31 with:

```
psi = (mu / 2) * (Ic - 3) - mu * ln(J) + (lmbda / 2) * (ln(J)) ** 2
```

in addition to previously defining the corresponding kinematics variables $J = \det(\boldsymbol{F})$ and $I_C = \mathrm{tr}(\boldsymbol{C})$.

```
J = det(F)
I_C = tr(C)
```

Quadrature rule: In listing 1, at line 37, when calculating the total potential energy it is also possible to choose the quadrature rule and the degree. In our example, we selected a quadrature degree of 1, triggering by default the Zienkiewicz and Taylor scheme [238] for tetrahedra. Hence, the user could also choose to use a Gauss-Jacobi quadrature of degree 2 [182] by replacing line 37 with:

```
Pi = psi * dx(degree=2, scheme="Gauss-Jacobi")  - inner(B, u) * dx(degree=2,
     scheme="Gauss-Jacobi") - inner(T, u) * ds(degree=2, scheme="Gauss-
    Jacobi")
```

.

4.2.2 FFCx: from Python code to efficient C kernels

In the particular case of static hyperelastic simulations, we solve the following non-linear system of equation

$$\boldsymbol{K}(\boldsymbol{u}) \cdot \mathrm{d}\boldsymbol{u} = \boldsymbol{R}(\boldsymbol{u}) - f(\boldsymbol{u}). \tag{57}$$

The $\boldsymbol{R}$ tensor is called the residual vector and is defined as the Gâteaux derivative of the total potential energy Π with respect to change in the displacement $\boldsymbol{u}$ in direction $\boldsymbol{v}$

$$\boldsymbol{R} = \frac{\mathrm{d}\Pi(\boldsymbol{u} + \epsilon\boldsymbol{v})}{\mathrm{d}\epsilon}|_{\epsilon=0}. \tag{58}$$

The tensor $\boldsymbol{K}$ is the Jacobian (also called stiffness in the context of mechanics) matrix and corresponds to the derivative of $\boldsymbol{R}$

$$\boldsymbol{K} = \frac{\mathrm{d}\boldsymbol{R}(\boldsymbol{u} + \epsilon\mathrm{d}\boldsymbol{u})}{\mathrm{d}\epsilon}|_{\epsilon=0}. \tag{59}$$

Solving the non linear system in equation 57 can be achieved using the Newton-Raphson algorithm that will iteratively solve a set of linear systems, assuming an initial guess $\boldsymbol{u}_n$

$$\boldsymbol{u}_{n+1} = \boldsymbol{u}_n - d\boldsymbol{u}. \tag{60}$$

The two tensors can be derived symbolically and exported using the UFL syntax with the function `derivative`, as shown at lines 40 and 43 in listing 1. A simple call to `ffcx` will create a .c and .h files containing the code for generating the local $\boldsymbol{R}$ and $\boldsymbol{K}$ tensors.

```
$ ffcx material.py
```

4.2.3 Integration in SOniCS

In SOFA, the definitions of the residual and stiffness tensors are carried out within a C++ file, `HyperelasticForcefield.cpp`. Each material model is in a separate file. So far, only Saint Venant-Kirchhoff and Neo-Hookean models have been implemented. The users can easily access those functionalities through Python wrappers:

```
node.addObject("SaintVenantKirchhoffMaterial", young_modulus=E,
    poisson_ratio=nu)
node.addObject('HyperelasticForcefield')
```

Listing 2: Python definition of a hyperealstic forcefield in SOFA using a Saint Venant-Kirchhoff material model.

The `HyperelasticForcefield` contains several functions, but we are particularly focusing on two of them. The `addForce` and `assemble_stiffness` functions are assembling the global residual and stiffness tensors respectively. Algorithm 2 details the `addForce` function, while algorithm 3 presents our reimplementation of the procedure. We did not detail the `assemble_stiffness` as it involves the exact same differences between the two implementations.

Algorithm 2 SOFA addForce function. The addForce function is in charge of assembling the global residual vector.

for `element in elements` **do**
  $X \leftarrow$ `element.positions` ▷ return the current positions of the element
  $R_{\text{global}} \leftarrow 0$ ▷ zero the global residual vector of dimension (DOFs $\times 3$)
  $R_{\text{local}} \leftarrow 0$ ▷ zero the local residual vector of dimension (element DOFs $\times 3$)
  for `quadrature in quadratures` **do**
    $\det J \leftarrow \det($`quadrature.nodes`$)$ ▷ return the Jacobian of the quadrature nodes
    $\mathrm{d}N \leftarrow$ `quadrature.nodes.shape_functions_derivatives` ▷ return the derivatives of the shape functions of the quadrature nodes
    $w \leftarrow$ `quadrature.nodes.weights` ▷ return the weights of the quadrature nodes
    $F \leftarrow X^T \cdot \mathrm{d}N$
    $J \leftarrow \det(F)$
    $C \leftarrow F^T \cdot F$
    $S \leftarrow \mathrm{f}(C,$ `MaterialParameters`$)$ ▷ return the second Piola-Kirchhoff depending on the material parameters and kinematics tensors
    for `i in range(0, NumberOfNodesPerElement)` **do**
      $\mathrm{d}x \leftarrow \mathrm{d}N[$`i`$]^T$
      $R_{local}[i] \leftarrow (\det J \cdot w) \cdot F \cdot S \cdot \mathrm{d}x$ ▷ allocate the result in the local residual vector
    end for
  end for
  for `i in range(0, NumberOfNodesPerElement)` **do**
    $R_{\texttt{global}}[\texttt{global}(i)] \leftarrow R_{\text{global}}[\texttt{global}(i)] - R_{\text{local}}[i]$ ▷ i indicates the element node index while `global`(i) denotes the global node index
  end for
end for

The structure is similar but we can still observe a few differences.

- The new implementation of algorithm 3 is more concise and involves less visible ten-

Algorithm 3 SOniCS addForce function. The addForce function is in charge of assembling the global residual vector.

1: **for** `element in elements` **do**
2: $X \leftarrow$ `element.positions` ▷ return the current positions of the element
3: $X_0 \leftarrow$ `element.rest_positions` ▷ return the initial positions of the element
4: $B \leftarrow$ `gravity` ▷ return the body forces
5: $T \leftarrow$ `element.forces` ▷ return the traction forces applied on the element
6: $u \leftarrow X - X_0$
7: $R_{\texttt{global}} \leftarrow 0$ ▷ zero the global residual vector of dimension (DOFs $\times 3$)
8: $R_{\texttt{local}} \leftarrow 0$ ▷ zero the local boundary conditions residual vector of dimension (element DOFs $\times 3$)
9: $R^{\texttt{bc}}_{\texttt{local}} \leftarrow 0$ ▷ zero the local residual vector of dimension (element DOFs $\times 3$)
10: `constants` $\leftarrow$ `MaterialParameters` ▷ return the material parameters
11: $R_{\texttt{local}} \leftarrow \texttt{tabulate\_tensor}(R_{\texttt{local}}, u, B, \texttt{constants}, X_0)$
12: $R^{\texttt{bc}}_{\texttt{local}} \leftarrow \texttt{tabulate\_tensor}(R_{\texttt{local}}, u, T, \texttt{constants}, X_0)$
13: **for** `i in range(0, NumberOfNodesPerElement)` **do**
14: $R_{\texttt{global}}[\texttt{global}(i)] \leftarrow R_{\texttt{global}}[\texttt{global}(i)] - (R_{\texttt{local}}[i] + R^{\texttt{bc}}_{\texttt{local}}[i])$ ▷ i indicates the element node index while $\texttt{global}(i)$ denotes the global node index
15: **end for**
16: **end for**

sorial operations because all those operations are efficiently hard coded in the C file provided by FFCx. For example, in algorithm 2, lines 5 to 17 were replaced in the new algorithm 3 by solely line 11.

- Algorithm 3 needs to have access to the initial position of the object and to the displacement vector. This was indeed not needed in the previous implementation since the modular mechanics plugin takes advantage of writing the deformation gradient only based on the current nodal coordinates $\boldsymbol{x}$:

$$\boldsymbol{F} = \boldsymbol{I} + \nabla_{\Omega_0}\boldsymbol{u} = \boldsymbol{I} + \nabla_{\Omega_0}(\boldsymbol{x} - \boldsymbol{x_0}) = \nabla_{\Omega_0}\boldsymbol{x}. \tag{61}$$

  ∇_{Ω_0} and $\boldsymbol{x_0}$ respectively denote the gradient and the nodal coordinates in the initial configuration, thus saving one extra vector operation.

- In the SOFA implementation, the boundary conditions and body forces are treated in separate files. In the new implementation of the Forcefield 2, the boundary conditions and body forces are now directly carried out in the Forcefield on lines 11 and 12. It avoids calling another function to loop again through every element of the object, thus speeding up the assembly of the residual vector.

Based on this new implementation, we created a new forcefield `HyperelasticForcefield_FEniCS` as close as possible to the existing syntax of `HyperelasticForcefield`. We also needed to tune

the existing material definition to replace unnecessary calculations and allow us to read the corresponding .c file.

```
node.addObject("FEniCS_Material", material="SaintVenantKirchhoff",
    young_modulus=E, poisson_ratio=nu)
node.addObject('HyperelasticForcefield_FEniCS')
```

Listing 3: Python definition of a hyperelastic forcefield in SOniCS using a Saint Venant-Kirchhoff material model.

Finally, the last hurdle was the element definitions. Indeed, SOFA and FEniCS do not use the same vertices, edges, and facets ordering (as shown in figure 27). To avoid any conflict with the existing users of SOFA and solve the ordering issue, we proposed rearranging the topology indices, edges, and vertices and create new elements. It ensured an accurate integration over the elements (especially for quadratic Serendipity integrating over the edges) and preserved an appropriate visualization. Those elements have been interfaced with the existing topology named `CaribouTopology`.

```
node.addObject('CaribouTopology', name='topology', template="Hexahedron",
    indices=mesh.cells_dict['hexahedron'])

node.addObject('CaribouTopology', name='topology', template="
    Hexahedron_FEniCS", indices=mesh.cells_dict['hexahedron'][:, [4, 5, 0,
    1, 7, 6, 3, 2]])
```

Listing 4: Python definition of hexahedron topology in SOFA and SOniCS.

(a) FFCx/Basix. (b) SOFA.

Figure 27: Local numbering of element vertices and edges in both FEniCS and SOFA

4.3 Numerical examples

In this section we describe three numerical examples used for the validation of our SOniCS implementation. Every simulations described in this section can be reproduced and are available on our GitHub page [143] (`https://github.com/Ziemnono/SOniCS_validation`). We use the same domain description for each example while varying the boundary conditions and material parameters of each simulation.

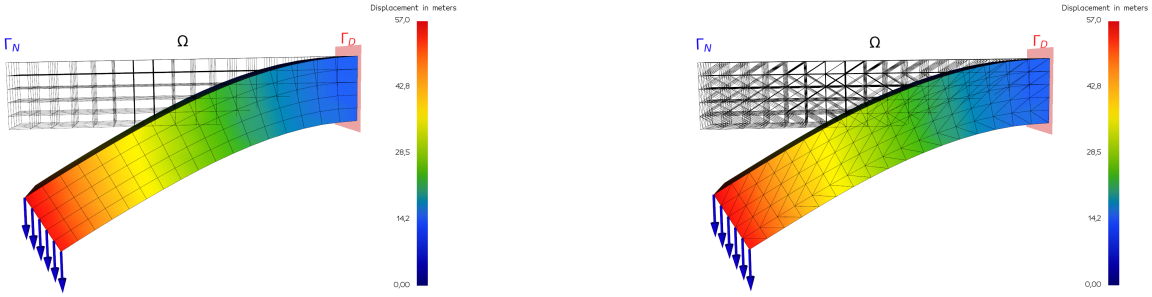

(a) Hexahedral elements.

(b) Tetrahedral elements.

Figure 28: Cantilever beam domain discretization and displacement field. Ω is a domain represented by a squared-section beam of dimensions $80 \times 15 \times 15\text{m}^3$, considered fixed on the right side ($\boldsymbol{u} = 0$ on Γ_D) while Neumann boundary conditions are applied on the left side (Γ_N).

Let Ω be a domain represented by a squared-section beam of dimensions $80 \times 15 \times 15\text{m}^3$, considered fixed on the right side ($\boldsymbol{u} = 0$ on Γ_D) while Neumann boundary conditions are applied on the left side (Γ_N), as shown in figure 28a and 28b.

Ω was discretized using two different geometrical elements using linear and quadratic interpolations. P1 and P2 elements stand for linear or quadratic tetrahedra, while Q1 and Q2 denote linear and quadratic hexahedra.

To solve each hyperlastic formulation described in equation 57 we used an identical implementation of the classical Newton Raphson (NR) solver for SOniCS, SOFA and FEBio. The solver had the following parameters: a maximum of 25 iterations with a residual and displacement tolerance of 10^{-10}. In order to compare the running time of the two implementations, we, therefore, introduced the mean NR iteration time. We defined the NR iteration time as the duration for assembling and factorizing the system matrix, solving and propagating the unknown increment, updating, and computing the force and displacement residual. After checking that the same number of iterations have been achieved, we averaged the total time over the number of iterations needed for the solver convergence. All calculations were performed using an Intel® Core™ i5-6300HQ CPU @ 2.30GHz × 4 processor with a 16GiB memory and a NV117 / Mesa Intel® HD Graphics 530 (SKL GT2) graphics card.

We evaluated the soundness of the SOniCS solution using SOFA, FEBio or a manufactured solution as the reference solution and computed the Euclidean relative L^2 error for the displacement and strain fields [164].

$$L^2_u(\boldsymbol{u}, \boldsymbol{v}) = \frac{||\boldsymbol{u} - \boldsymbol{v}||_2}{||\boldsymbol{v}||_2}, \tag{62}$$

$$L^2_E(\boldsymbol{u}, \boldsymbol{v}) = \frac{||\boldsymbol{E_u} - \boldsymbol{E_v}||_2}{||\boldsymbol{E_v}||_2}, \tag{63}$$

where $\boldsymbol{u}$ and $\boldsymbol{v}$ are the calculated displacement vectors for SOniCS and the reference implementation, respectively, $||\bullet||$ the Euclidean norm, and $\boldsymbol{E_u}$ the Green-Lagrange strain tensor of the displacement $\boldsymbol{u}$.

In this section, we first compare our solution with an analytical one: the manufactured solution. Then, we consider a clamped cantilever beam subject to Neumann boundary conditions and compare its deformation with the SOFA solution. Finally, using the same cantilever beam, we implemented a Mooney Rivlin model (uncoded in SOFA) using SOniCS and compared the solution with FEBio.

4.3.1 Manufactured solution

Aiming at code verification, the method of the manufactured solution consists in choosing an exact solution to the problem as an analytical expression [39]. The chosen analytical expression is then inserted into the Partial Differential Equation (PDE) under consideration to find the conditions that lead to this solution. In general, the manufactured chosen solution is expressed in simple primitive functions like sin(), exp(), tanh(), etc... In the context of hyperelastic equations, we considered the following manufactured solution for the displacement

$$\boldsymbol{u}(x,y,z) = \begin{bmatrix} 10^{-2}\cdot z\cdot e^{x} \\ 10^{-2}\cdot z\cdot e^{y} \\ 10^{-2}\cdot z\cdot e^{z} \end{bmatrix} \text{on}\,\Omega. \tag{64}$$

Starting from the above chosen displacement and using continuum mechanics laws, the relative analytical forces are applied as Neumann boundary conditions and deduced as follows

$$\boldsymbol{F} = \boldsymbol{I_d} + \text{grad}(\boldsymbol{u}), \tag{65}$$

$$\boldsymbol{P} = \frac{\partial W}{\partial \boldsymbol{F}}, \tag{66}$$

$$\boldsymbol{f} = -\nabla\cdot\boldsymbol{P}\,\text{on}\,\Gamma_N. \tag{67}$$

Where $\boldsymbol{F}$ is the deformation gradient, $\boldsymbol{I_d}$ is the identity matrix of dimension d, $\boldsymbol{P}$ is the first Piola-Kirchhoff stress tensor and W is the strain energy density depending on the material model constitutive law. We used a Saint Venant-Kirchhoff material (55) with a Young's Modulus of 3 kPa and a Poisson's ratio of 0.3, the computation of this solution was performed using Python Sympy package [147].

In this experiment, we generated 8 and 6 discretizations of P1 and P2 elements, respectively, with a decreasing element size in both scenarios. For each discretization, we applied the relative analytical forces deduced from the manufactured solution (64) and used SOniCS Saint Venant-Kirchhoff material implementation with the same parameters as Sympy's to fill the domain. The displacements obtained were compared to the chosen analytical solution in equation (64) for each discretization. The results are presented in figure 29, the error metrics are the relative errors presented in equations 62 and 63.

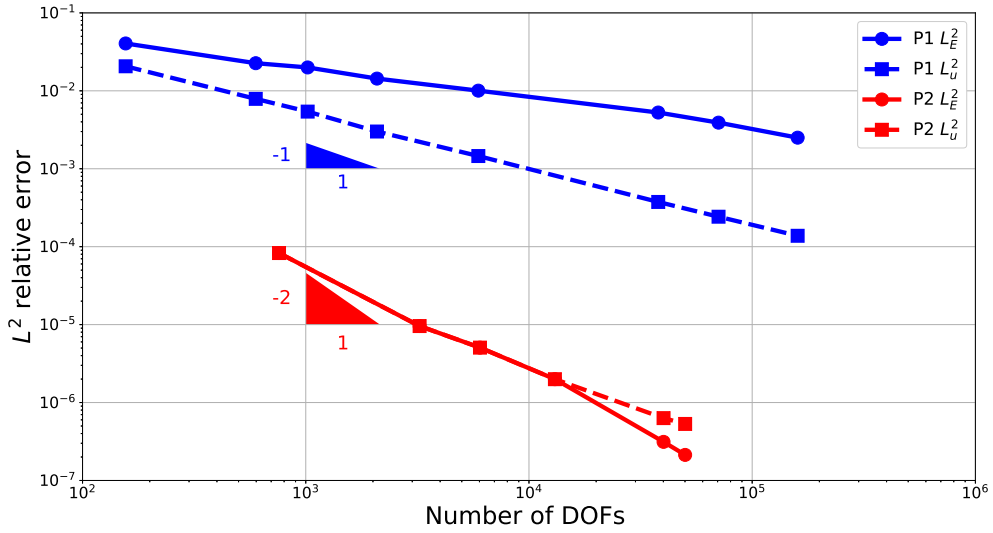

Figure 29: Plot of the mesh convergence analysis of the manufactured solution. The L^2 errors (L_u^2 for displacement and L_E^2 for strain) between the analytical and the SOniCS simulation is calculated for different number of Degrees Of Freedoms (DOFs) with fixed parameters (E=3 kPa and ν=0.3) for P1 linear tetrahedra (blue) and P2 quadratic tetrahedra (red) elements.

4.3.2 Benchmark with SOFA

The cantilever beam deflection is a classical mechanical test case, as you can smoothly refine the mesh due to the simplicity of the geometry or modify its boundary conditions to fit real-life experiments. In this context, the beam was still clamped on the right side (natural Dirichlet condition on Γ_D) while Neumann boundary conditions were applied on the left side (Γ_N). To compare our SOniCS implementation, we model the deformation of the beam with two hyperelastic material models: Saint Venant-Kirchhoff and Neo-Hookean. We fixed the mechanical parameters and the Neumann boundary conditions equal to -10 Pa in the y direction, until reaching sufficient large deformations with the same parameters as before: $E = 3$ kPa and $\nu = 0.3$.

This study aims at comparing the finite element solutions provided by SOniCS and SOFA under the same constraints in terms of computational and running time performances. To do so, we computed the relative L^2 error for the displacement and strain fields ($L_u^2(\boldsymbol{u}_{\texttt{SOniCS}}, \boldsymbol{u}_{\texttt{SOFA}})$ and $L_E^2(\boldsymbol{u}_{\texttt{SOniCS}}, \boldsymbol{u}_{\texttt{SOFA}})$)between the SOniCS solution using SOFA as the reference solution.

The results obtained are presented in tables 4 and 5 for Saint Venant-Kirchhoff and Neo-Hookean materials, respectively.

Saint Venant-Kirchhoff material model					
Element	Number of DOFs	SOniCS mean NR iteration time (s)	SOFA mean NR iteration time (s)	$L^2_u(\boldsymbol{u}_{\texttt{SOniCS}}, \boldsymbol{u}_{\texttt{SOFA}})$	$L^2_E(\boldsymbol{u}_{\texttt{SOniCS}}, \boldsymbol{u}_{\texttt{SOFA}})$
P1	10935	0.387	0.438	4.10e-14	2.32e-16
P2	12705	0.810	0.808	3.49e-14	8.18e-15
Q1	10935	0.449	0.464	6.19e-13	3.76e-16
Q2	11772	0.839	0.942	3.81e-13	23.68e-14

Table 4: Relative error for displacement ($L^2_u(\boldsymbol{u}_{\texttt{SOniCS}}, \boldsymbol{u}_{\texttt{SOFA}})$) and strain ($L^2_E(\boldsymbol{u}_{\texttt{SOniCS}}, \boldsymbol{u}_{\texttt{SOFA}})$) defined in equations 62 and 63 and mean NR (Newton-Raphson) iteration time between SOniCS and SOFA for different element geometries and interpolation schemes using Saint Venant-Kirchhoff material model. P1 and P2 elements stand for linear or quadratic tetrahedra, while Q1 and Q2 denote linear and quadratic hexahedra.

Neo-Hookean material model					
Element	Number of DOFs	SOniCS mean NR iteration time (s)	SOFA mean NR iteration time (s)	$L^2_u(\boldsymbol{u}_{\texttt{SOniCS}}, \boldsymbol{u}_{\texttt{SOFA}})$	$L^2_E(\boldsymbol{u}_{\texttt{SOniCS}}, \boldsymbol{u}_{\texttt{SOFA}})$
P1	10935	0.391	0.428	2.17e-14	7.78e-14
P2	12705	0.826	0.852	1.40e-14	2.18e-20
Q1	10935	0.471	0.478	4.92e-13	5.77e-16
Q2	11772	0.826	0.864	1.64e-13	2.17e-14

Table 5: Relative error for displacement ($L^2_u(\boldsymbol{u}_{\texttt{SOniCS}}, \boldsymbol{u}_{\texttt{SOFA}})$) and strain ($L^2_E(\boldsymbol{u}_{\texttt{SOniCS}}, \boldsymbol{u}_{\texttt{SOFA}})$) defined in equations 62 and 63 and mean NR (Newton-Raphson) iteration time between SOniCS and SOFA for different element geometries and interpolation schemes using Neo-Hookean material model. P1 and P2 elements stand for linear or quadratic tetrahedra, while Q1 and Q2 denote linear and quadratic hexahedra.

4.3.3 Benchmark with FEBio

FEBio is a open-source finite element package specifically designed for biomechanical applications. It offers modeling scenarios, a wide range of constitutive material models, and boundary conditions relevant to numerous research areas in biomechanics. In this section, FEBio was used to compute the same scenarios as in section 4.3.2 to evaluate the trustworthiness of SOniCS. A more advanced constitutive material model, Mooney Rivlin, was introduced for this purpose

$$\psi = C_{01}\left(\overline{\mathrm{I}_C} - 3\right) + C_{10}\left(\overline{\mathrm{II}_C} - 3\right) + \frac{K}{2}\ln(J). \tag{68}$$

Where C_{01}, C_{10}, and K are the material constants in addition to the modified invariants $\overline{\mathrm{I}_C} = J^{-\frac{2}{3}}\,\mathrm{I}_C$, $\overline{\mathrm{II}_C} = J^{-\frac{4}{3}}\,\mathrm{II}_C$ defined based on the classic invariants $\mathrm{I}_{\boldsymbol{C}} = \mathrm{tr}(\mathbf{C})$, $\mathrm{II}_{\boldsymbol{C}} = \frac{1}{2}\left((\mathrm{tr}(\mathbf{C}))^2 - \mathrm{tr}\left(\mathbf{C}^2\right)\right)$. In order to obtain sufficiently large deformations, we chose the following material parameters: $C_{01} = 2000\,\mathrm{Pa}$, $C_{10} = 100\,\mathrm{Pa}$, and $K = 1000\,\mathrm{Pa}$.

Tables 6, 7, 8 show the results obtained for Saint Venant-Kirchhoff, Neo-Hookean and Mooney Rivlin material models and considering the four discretizations implemented so far in SOniCS. The error evaluation is still based on the mean relative error defined in equation 62 using FEBio as the reference while using a Newton Raphson solver with the same characteristics in both cases.

Saint Venant-Kirchhoff material model					
Element	Number of DOFs	SOniCS mean NR iteration time (s)	FEBio mean NR iteration time (s)	$L^2_u(\boldsymbol{u}_{\texttt{SOniCS}}, \boldsymbol{u}_{\texttt{FEBio}})$	$L^2_E(\boldsymbol{u}_{\texttt{SOniCS}}, \boldsymbol{u}_{\texttt{FEBio}})$
P1	10935	0.387	0.401	6.01e-10	4.23e-7
P2	12705	0.810	0.991	0.08	0.117
Q1	10935	0.449	0.508	4.19e-10	2.96e-6
Q2	11772	0.839	0.102	0.13	0.189

Table 6: Relative error for displacement ($L^2_u(\boldsymbol{u}_{\texttt{SOniCS}}, \boldsymbol{u}_{\texttt{FEBio}})$) and strain ($L^2_E(\boldsymbol{u}_{\texttt{SOniCS}}, \boldsymbol{u}_{\texttt{FEBio}})$) defined in equations 62 and 63 and mean NR (Newton-Raphson) iteration time between SOniCS and FEBio for different element geometries and interpolation schemes using Saint Venant-Kirchhoff material model. P1 and P2 elements stand for linear or quadratic tetrahedra, while Q1 and Q2 denote linear and quadratic hexahedra.

4.4 Hozapfel and Ogden anisotropic material model coupled with haptic simulation

In the context of numerical surgical simulations, a robot haptic feedback has been shown to be a consistent tool for drastically improving user-interactions and opening up countless

Neo-Hookean material model					
Element	Number of DOFs	SOniCS mean NR iteration time (s)	FEBio mean NR iteration time (s)	$L_u^2(\boldsymbol{u}_{\texttt{SOniCS}}, \boldsymbol{u}_{\texttt{FEBio}})$	$L_E^2(\boldsymbol{u}_{\texttt{SOniCS}}, \boldsymbol{u}_{\texttt{FEBio}})$
P1	10935	0.391	0.458	6.53e-10	7.33e-7
P2	12705	0.826	0.101	1.5e-2	3.16e-2
Q1	10935	0.471	0.523	8.08e-10	1.02e-6
Q2	11772	0.826	0.908	0.09	0.13

Table 7: Relative error for displacement ($L_u^2(\boldsymbol{u}_{\texttt{SOniCS}}, \boldsymbol{u}_{\texttt{FEBio}})$) and strain ($L_E^2(\boldsymbol{u}_{\texttt{SOniCS}}, \boldsymbol{u}_{\texttt{FEBio}})$) defined in equations 62 and 63 and mean NR (Newton-Raphson) iteration time between SOniCS and FEBio for different element geometries and interpolation schemes using Neo-Hookean material model. P1 and P2 elements stand for linear or quadratic tetrahedra, while Q1 and Q2 denote linear and quadratic hexahedra.

Mooney Rivlin material model					
Element	Number of DOFs	SOniCS mean NR iteration time (s)	FEBio mean NR iteration time (s)	$L_u^2(\boldsymbol{u}_{\texttt{SOniCS}}, \boldsymbol{u}_{\texttt{FEBio}})$	$L_E^2(\boldsymbol{u}_{\texttt{SOniCS}}, \boldsymbol{u}_{\texttt{FEBio}})$
P1	10935	0.662	0.804	2.49e-9	6.81-8
P2	12705	0.102	0.112	9.97e-3	8.28e-2
Q1	10935	0.818	0.910	10.92	14.71
Q2	11772	0.101	0.125	4.23e-2	1.229e-1

Table 8: Relative error for displacement ($L_u^2(\boldsymbol{u}_{\texttt{SOniCS}}, \boldsymbol{u}_{\texttt{FEBio}})$) and strain ($L_E^2(\boldsymbol{u}_{\texttt{SOniCS}}, \boldsymbol{u}_{\texttt{FEBio}})$) defined in equations 62 and 63 and mean NR (Newton-Raphson) iteration time between SOniCS and FEBio for different element geometries and interpolation schemes using Mooney Rivlin material model. P1 and P2 elements stand for linear or quadratic tetrahedra, while Q1 and Q2 denote linear and quadratic hexahedra. The large errors obtained for Q1 elements are further discussed in section 4.5.

applications. Among them, haptic devices have mainly been used as a training tool for surgeons. Indeed prior to surgery, under the assumption of known geometry and mechanical properties of the patient's organ, a surgeon would be able to plan and better choose between specific surgical paths/approaches. In this paper, we used the 3D Systems Touch Haptic Device robot coupled with the SOFA plugin Geomagic to allow interactions between the instrument and the simulations. For this hypothetical simulation, we virtually simulate the contact between a surgical tool and a liver during surgery. The liver was described by an anisotropic Holzapfel Ogden model [98, 173], with an existing FEniCS implementation [95] validated using the manufactured solution. Therefore, to assess the soundness of our implementation, we conducted a mesh convergence analysis on a beam and liver meshes provided in figure 30. We prescribed natural Dirichlet boundary conditions on one side and Neumann boundary conditions on the other side to obtain noticeable deformations. Such material could be described using the following strain energy density function

$$\psi = \psi_{\text{iso}}\left(\boldsymbol{F}\right) + \psi_{\text{vol}}(J). \tag{69}$$

ψ_{iso} and ψ_{vol} are the isochoric and volumetric part of the strain energy density function respectively. The volumetric part can be evaluated as a function of the bulk modulus κ of the material and J

$$\psi_{\text{vol}}\left(J\right) = \frac{\kappa}{4}(J^2 - 1 - 2\ln(J)), \tag{70}$$

$$\begin{aligned}\psi_{\text{iso}}\left(\boldsymbol{F}\right) = \frac{a}{2b}\exp\left[b\left(\mathrm{I}_1 - 3\right)\right] + \sum_{i=f,s}\frac{a_i}{2b_i}\exp\left[b_i\left(\mathrm{I}_{4i} - 1\right)^2\right] + \\ \frac{a_{\text{fs}}}{2b_{\text{fs}}}\left(\exp\left[b_{\text{fs}}\mathrm{I}_{8\text{fs}}^2\right] - 1\right),\end{aligned} \tag{71}$$

with

$$\mathrm{I}_{4f} = \boldsymbol{f_0}\cdot\boldsymbol{C}\cdot\boldsymbol{f_0},\ \mathrm{I}_{4s} = \boldsymbol{s_0}\cdot\boldsymbol{C}\cdot\boldsymbol{s_0},\ \text{and}\ \mathrm{I}_{8\text{fs}} = \boldsymbol{f_0}\cdot\boldsymbol{C}\cdot\boldsymbol{s_0}. \tag{72}$$

The transversely isotropic behavior can be obtained by removing the parameters a_{fs}, b_{fs}, a_s and b_s, while the isotropic behavior is obtained by also suppressing the two parameters a_f and b_f. This kind of model is frequently used to model orthotropic materials (e.g. muscle with fibers or tendons). Vectors $\boldsymbol{f_0}$, $\boldsymbol{s_0}$ are the unit base vectors normal to the planes of symmetry. For our application, we selected the following material properties allowing to obtain sufficient deformation of the objects: $\kappa = 10^2\,\text{MPa}, a = 1.10^2\,\text{kPa}, b = 5\,\text{Pa}, a_f = 16\,\text{kPa}, b_f = 12.8\,\text{Pa}, a_s = 18\,\text{kPa}, b_s = 10\,\text{Pa}, a_{fs} = 9\,\text{kPa}, b_{fs} = 12$ Pa.

The instrument is assumed to be a rigid body kinematically constrained by the haptic device position at each time step. The contact forces generated by the collision between the instrument and the liver are calculated using frictional contact and an implicit Euler scheme to solve the dynamic system [49]. Finally, the contact forces are transmitted back to the user's hand through the haptic device. The result is a simulation running at 100 FPS (Frames Per Seconds) on average displayed in figure 31. A full video of the interaction with

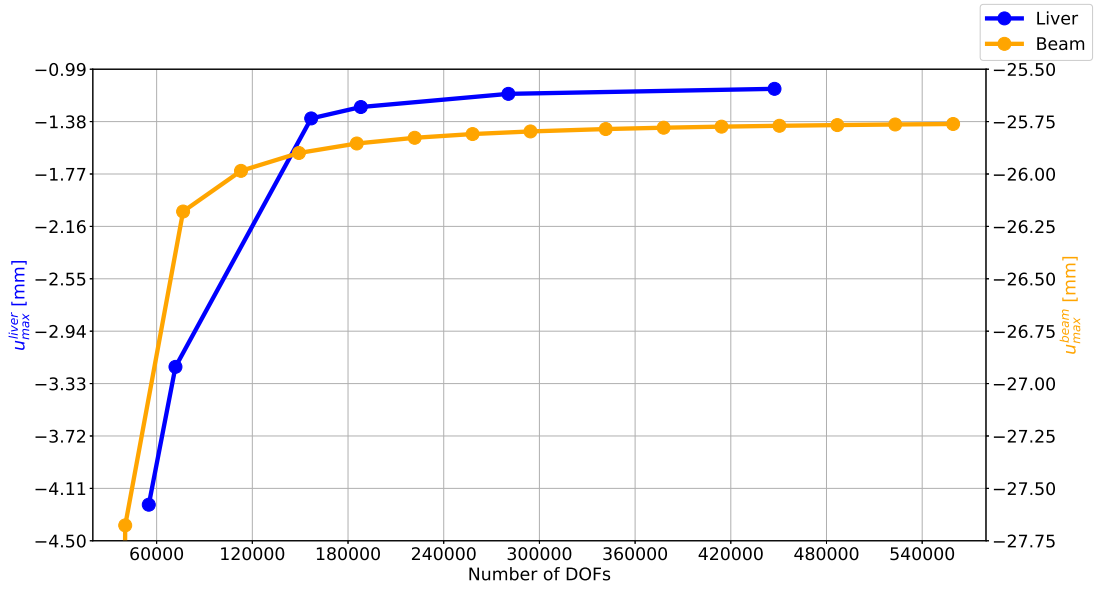

Figure 30: Plot of the mesh convergence analysis applied to a beam and liver using the Hozapfel and Ogden anisotropic material models with the parameters $\kappa = 10^2\,\text{MPa}, a = 1.10^2\,\text{kPa}, b = 5\,\text{Pa}, a_f = 16\,\text{kPa}, b_f = 12.8\,\text{Pa}, a_s = 18\,\text{kPa}, b_s = 10\,\text{Pa}, a_{fs} = 9\,\text{kPa}, b_{fs} = 12\,\text{Pa}$. The maximum displacement of a beam $u^{\texttt{beam}}_{\texttt{max}}$ and liver $u^{\texttt{liver}}_{\texttt{max}}$ meshes are respectively computed in orange and blue for different mesh size increasing the number of Degrees of Freedom (DOFs).

the haptic device is available in the Supplementary Materials. The real-time performance has been obtained by using a small number of DOFs (543). A higher number of DOFs could be used once a GPU implementation is available.

4.5 Discussion

We show that the SOniCS plugin is an efficient implementation of material models for hyperelastic simulations and enables the user to develop an intuitive understanding of the impact of modelling choices on the accuracy and reliability of the predictions. We first demonstrated a convergence study for Saint Venant-Kirchhoff material using P1 and P2 elements with the manufactured solution in section 4.3.1. Indeed, as expected, by refining the mesh, the L^2 relative errors for strain and displacement fields almost follow the theoretical slopes when increasing the number of DOFs (on a log-log plot), showing the stability of our method.

Then, from section 4.3.2, two main results are noteworthy from tables 4 and 5. First, the relative errors of the displacement and strain between SOniCS and SOFA, for both material models, is close to machine precision for P1, P2, Q1, and Q2 discretizations.

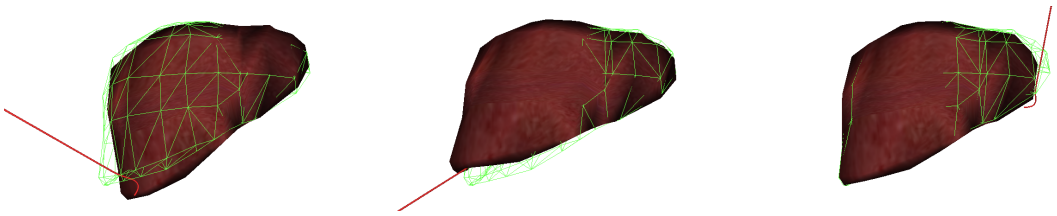

Figure 31: Three different deformation states of a liver in contact with a surgical tool connected to a haptic device. The surgical tool (in red) is guided by the user through the 3D Systems Touch Haptic Device to deform the liver from the initial configuration (green wire-frame) to a deformed state (textured). The liver is modeled using the Holzapfel Ogden anisotropic material with the following parameters $\kappa = 10^2\,\text{MPa}, a = 1.10^2\,\text{kPa}, b = 5\,\text{Pa}, a_f = 16\,\text{kPa}, b_f = 12.8\,\text{Pa}, a_s = 18\,\text{kPa}, b_s = 10\,\text{Pa}, a_{fs} = 9\,\text{kPa}, b_{fs} = 12$ Pa. The maximum displacement of a beam $u_{\texttt{max}}^{\texttt{beam}}$ and liver $u_{\texttt{max}}^{\texttt{liver}}$. In the case of contact detection, the contact forces are transmitted to the user through the haptic device. A video of the simulation is available as supplementary materials.

Secondly, the last comment concerns the mean NR iteration time. We observe that the SOniCS implementation is slightly faster than SOFA for any elements using Saint Venant-Kirchhoff or Neo-Hookean material model. The reason for this difference is the need for SOFA to compute the shape functions and derivatives, then calculate the local residual and Jacobian using multiple tensor operations. Conversely, SOniCS has all those operations efficiently hard-coded in C kernels, thus performing faster than SOFA.

We compared the SOniCS and FEBio simulations for several material models: Saint Venant-Kirchhoff, Neo-Hookean, and Mooney-Rivlin in section 4.3.3. For P1 elements, the errors are close to machine precision for all 3 models. For P2 and Q2 elements, the 3 models display similar errors that still represent a minor error (less than 0.08 and 0.1, respectively) which is of same magnitude between SOFA and FEBio, as well as FEniCS and FEBio. The reasons for those minor errors could be the difference in the implementation of the elements or in the choice of solver parameters. For Q1 elements, we reached an accuracy near machine precision for Saint Venant-Kirchhoff and Neo-Hookean. However, the relative error for displacement rose close to 11 for the Mooney-Rivlin model, while similar behavior is observed for the relative strain errors. To further understand this divergence, we included a third open-source software AceGen. AceGen similarly uses an automatic code generation package for the symbolic generation of new finite elements. The cantilever beam scenario presented in section 4.3.3 was reproduced using AceGen under the same conditions and with an identical Q1 discretization of the domain. Using the same metric as defined in equation 62, the results are the following: $L_u^2(\boldsymbol{u}_{\texttt{SOniCS}}, \boldsymbol{u}_{\texttt{Acegen}}) = 3.33$ and $L_u^2(\boldsymbol{u}_{\texttt{FEBio}}, \boldsymbol{u}_{\texttt{Acegen}}) = 14.19$. Even if SOniCS and Acegen showed similar results, a more in-depth study would be needed to confirm the soundness of our solution. Despite using a finer mesh the error was slightly lower but still noticeable. Eventually, FEBio has shown difficulty in converging with trivial parameter sets or when increasing the number of DOFs.

Thus, as shown in tables 6,7, and 8, on average, SOniCS is solving the equation system faster than FEBio. Several reasons could explain those differences, such as the number of quadrature points used, the implementation of the Newton-Raphson scheme, or the solver parameters.

Finally, we showed the capabilities of the SOniCS plugin in simulating complex material models such as the Holzapfel Ogden anisotropic model coupled with a haptic device in section 4.4. The material model was effortlessly implemented for several elements (P1, P2, Q1, and Q2) without needing any manual derivation or coding. A manufactured solution was used in [95] to validate the FEniCS implementation, while figure 30 demonstrates a convergence of the solution for a beam and liver shape using the SOniCS implementation. Therefore, the absence of analytical solutions or experimental data only proves the convergence to a numerical solution that is not necessarily a ground truth. The final result is a real-time simulator functional for surgeons' training or any other biomechanics simulation replicating the behavior of a liver in contact with a surgical tool.

4.6 Conclusion and outlook

We performed several numerical experiments to develop intuitive understanding of new material models in SOFA using the SOniCS plugin. First, we validated the most common hyperelastic material models: Saint Venant-Kirchhoff and Neo-Hookean using a manufactured solution. Then, utilizing FEBio as a reference, we verified our implementation of a Mooney-Rivlin material model using P1, P2, Q1, and Q2 elements. The final application employed a haptic device to interact with an anisotropic Holzapfel Ogden liver model in real-time.

The study used our SOniCS plugin to generate optimized C code for complex material models compatible with SOFA. On one side, we benefited from FEniCS automatic differentiation and code generation capabilities to bypass the difficulties of deriving and implementing the consistent Jacobian in SOFA. On the user side, we implemented compatible and user-friendly SOFA Forcefields to use the FEniCS C kernels. A SOFA user can now easily define a new material model by specifying its strain energy function, element geometry or family and the quadrature scheme and degree only in Python. We made the open-source code and all data and test cases available as supplementary material.

In future work, we intend to apply the SOniCS plugin for solving more complex mechanical phenomena. For example, mixed formulations for solving incompressible materials, viscous or plastic effects, and multi-material systems. In this paper, we only utilized the plugin for solving hyperelasticity equations, but it would be interesting to tackle multiphysics problems such as thermomechanics or magnetomechanics. An interesting future work could be to investigate the effectiveness of the SOniCS plugin for complex material real-time simulations with surrogate and machine learning models in SOFA. Further, the next step would be to quantify the uncertainty of biomechanical simulations in SOFA via the SOniCS plugin. We only used Lagrangian P1, P2, Q1, and Q2 elements while more geometries such as prisms could be relevant for the SOFA and FEniCS community. Finally, our validation only focused on the deformation field of the structures, while a more in-depth

study would also enable us to validate an analytical stress field.

Some work remains to improve user-friendliness of our package. Indeed, even if writing the Python file describing the material model and generating the associated C file is mostly effortless and automated, some steps are still manual. Indeed, the `FEniCS_Material` C++ class must have knowledge of every new C file created at compile time. Hence, for the moment, the user still has to manually specify two C++ functions in the code and recompile the whole plugin. Even if this step is manageable, it still requires diving into the C++ code, which can discourage a few users. Meanwhile, to mitigate this effect, actions have been taken by providing detailed documentation and tutorials for this crucial step. In addition, future works aim at improving this stage by directly providing the path of the C file in the Python code to trigger just-in-time compilation for new materials.

References

[2] J. Ahrens, Berk Geveci, and Charles Law. "ParaView: An End-User Tool for Large Data Visualization". In: *Visualization Handbook* (Jan. 2005) (pages 77, 82).

[3] Jérémie Allard, Hadrien Courtecuisse, and François Faure. "Chapter 21 - Implicit FEM Solver on GPU for Interactive Deformation Simulation". In: *GPU Computing Gems Jade Edition*. Ed. by Wen mei W. Hwu. Applications of GPU Computing Series. Boston: Morgan Kaufmann, 2012, pp. 281–294. ISBN: 978-0-12-385963-1. DOI: https://doi.org/10.1016/B978-0-12-385963-1.00021-6. URL: https://www.sciencedirect.com/science/article/pii/B9780123859631000216 (page 78).

[4] M. S. Alnaes et al. "The FEniCS Project Version 1.5". In: *Archive of Numerical Software* 3 (2015). DOI: 10.11588/ans.2015.100.20553 (pages 79, 82).

[5] Martin S. Alnæs et al. "Unified Form Language: A Domain-Specific Language for Weak Formulations of Partial Differential Equations". In: *ACM Trans. Math. Softw.* 40.2 (2014). ISSN: 0098-3500. DOI: 10.1145/2566630. URL: https://doi.org/10.1145/2566630 (pages 55, 82).

[6] Todd Arbogast, Zhen Tao, and Chuning Wang. "Direct serendipity and mixed finite elements on convex quadrilaterals". en. In: *Numerische Mathematik* 150.4 (Apr. 2022), pp. 929–974. ISSN: 0945-3245. DOI: 10.1007/s00211-022-01274-3. URL: https://doi.org/10.1007/s00211-022-01274-3 (visited on 07/05/2022) (page 84).

[7] Douglas N. Arnold and Gerard Awanou. "The Serendipity Family of Finite Elements". en. In: *Foundations of Computational Mathematics* 11.3 (June 2011), pp. 337–344. ISSN: 1615-3383. DOI: 10.1007/s10208-011-9087-3. URL: https://doi.org/10.1007/s10208-011-9087-3 (visited on 07/05/2022) (page 84).

[8] Ellen M. Arruda and Mary C. Boyce. "A three-dimensional constitutive model for the large stretch behavior of rubber elastic materials". In: *Journal of the Mechanics and Physics of Solids* 41.2 (1993), pp. 389–412. ISSN: 0022-5096. DOI: https://doi.org/10.1016/0022-5096(93)90013-6. URL: https://www.sciencedirect.com/science/article/pii/0022509693900136 (page 81).

[14] Davide Baroli, Alfio Quarteroni, and Ricardo Ruiz-Baier. "Convergence of a stabilized discontinuous Galerkin method for incompressible nonlinear elasticity". In: *Advances in Computational Mathematics* 39.2 (Dec. 2012), pp. 425–443. DOI: 10.1007/s10444-012-9286-8. URL: https://doi.org/10.1007/s10444-012-9286-8 (page 83).

[15] Olga Barrera. "A unified modelling and simulation for coupled anomalous transport in porous media and its finite element implementation". In: *Computational Mechanics* 68 (Dec. 2021). DOI: 10.1007/s00466-021-02067-5 (page 78).

[16] Peter Bastian et al. "The Dune framework: Basic concepts and recent developments". en. In: *Computers & Mathematics with Applications*. Development and Application of Open-source Software for Problems with Numerical PDEs 81 (Jan. 2021), pp. 75–112. ISSN: 0898-1221. DOI: 10.1016/j.camwa.2020.06.007. URL: https://www.sciencedirect.com/science/article/pii/S089812212030256X (visited on 06/01/2022) (page 82).

[21] Daniele Bianchi et al. "A FSI computational framework for vascular physiopathology: A novel flow-tissue multiscale strategy". In: *Medical Engineering & Physics* 47 (2017), pp. 25–37. ISSN: 1350-4533. DOI: https://doi.org/10.1016/j.medengphy.2017.06.028. URL: https://www.sciencedirect.com/science/article/pii/S1350453317301674 (page 78).

[23] Iman Borazjani. "Fluid–structure interaction, immersed boundary-finite element method simulations of bio-prosthetic heart valves". In: *Computer Methods in Applied Mechanics and Engineering* 257 (2013), pp. 103–116. ISSN: 0045-7825. DOI: https://doi.org/10.1016/j.cma.2013.01.010. URL: https://www.sciencedirect.com/science/article/pii/S0045782513000212 (page 78).

[24] Stéphane Bordas et al. "An extended finite element library". In: *International Journal for Numerical Methods in Engineering* 2 (Jan. 2006), pp. 1–33 (pages 77, 82).

[25] G. Boyer et al. "Assessment of the in-plane biomechanical properties of human skin using a finite element model updating approach combined with an optical full-field measurement on a new tensile device". In: *Journal of the Mechanical Behavior of Biomedical Materials* 27 (2013), pp. 273–282. ISSN: 1751-6161. DOI: https://doi.org/10.1016/j.jmbbm.2013.05.024. URL: https://www.sciencedirect.com/science/article/pii/S1751616113001951 (page 78).

[29] Jean-Nicolas Brunet. "Exploring new numerical methods for the simulation of soft tissue deformations in surgery assistance". Theses. 4 Rue Blaise Pascal: Université de Strasbourg, Nov. 2020. URL: https://hal.inria.fr/tel-03130643 (page 81).

[30] Huu Phuoc Bui et al. "Real-Time Error Control for Surgical Simulation". In: *IEEE Transactions on Biomedical Engineering* 65.3 (2018), pp. 596–607. DOI: 10.1109/TBME.2017.2695587 (page 78).

[31] Raphael Bulle et al. "The Human Meniscus Behaves as a Functionally Graded Fractional Porous Medium under Confined Compression Conditions". In: *Applied Sciences* 11 (Oct. 2021), p. 9405. DOI: 10.3390/app11209405 (page 78).

[38] Gregory Chagnon, Marie Rebouah, and Denis Favier. "Hyperelastic Energy Densities for Soft Biological Tissues: A Review". In: *Journal of Elasticity* 120 (Dec. 2014). DOI: 10.1007/s10659-014-9508-z (page 78).

[39] É. Chamberland, A. Fortin, and M. Fortin. "Comparison of the performance of some finite element discretizations for large deformation elasticity problems". In: *Computers & Structures* 88.11-12 (June 2010), pp. 664–673. DOI: 10.1016/j.compstruc.2010.02.007. URL: https://doi.org/10.1016/j.compstruc.2010.02.007 (page 93).

[41] Francisco Chinesta, Roland Keunings, and Adrien Leygue. *The proper generalized decomposition for advanced numerical simulations. A primer*. Jan. 2014. ISBN: 978-3-319-02864-4. DOI: 10.1007/978-3-319-02865-1 (page 79).

[46] Olivier Comas et al. "Efficient Nonlinear FEM for Soft Tissue Modelling and Its GPU Implementation within the Open Source Framework SOFA". In: Springer. July 2008, pp. 28–39. ISBN: 978-3-540-70520-8. DOI: 10.1007/978-3-540-70521-5_4 (page 79).

[47] K. D. Costa, J. W. Holmes, and A. D. Mcculloch. "Modelling cardiac mechanical properties in three dimensions". In: *Philosophical Transactions of the Royal Society of London. Series A: Mathematical, Physical and Engineering Sciences* 359.1783 (June 2001). Ed. by P. Kohl, D. Noble, and P. J. Hunter, pp. 1233–1250. DOI: 10.1098/rsta.2001.0828. URL: https://doi.org/10.1098/rsta.2001.0828 (page 81).

[48] S. Cotin, H. Delingette, and N. Ayache. "Real-time elastic deformations of soft tissues for surgery simulation". In: *IEEE Transactions on Visualization and Computer Graphics* 5.1 (1999), pp. 62–73. DOI: 10.1109/2945.764872 (page 78).

[49] Hadrien Courtecuisse et al. "Real-time simulation of contact and cutting of heterogeneous soft-tissues". In: *Medical image analysis* 18 (Dec. 2013), pp. 394–410. DOI: 10.1016/j.media.2013.11.001 (page 98).

[50] Hadrien Courtecuisse et al. "Real-time simulation of contact and cutting of heterogeneous soft-tissues". In: *Medical Image Analysis* 18.2 (2014), pp. 394–410. ISSN: 1361-8415. DOI: https://doi.org/10.1016/j.media.2013.11.001. URL: https://www.sciencedirect.com/science/article/pii/S1361841513001692 (page 78).

[51] Stephen C. Cowin. "Bone poroelasticity". In: *Journal of Biomechanics* 32.3 (1999), pp. 217–238. ISSN: 0021-9290. DOI: https://doi.org/10.1016/S0021-9290(98)00161-4. URL: https://www.sciencedirect.com/science/article/pii/S0021929098001614 (page 78).

[53] Gabriel J. DeSalvo and John A. Swanson. *ANSYS engineering analysis system users manual*. English. Houston, Pa.: Swanson Analysis Systems, 1985 (page 77).

[55] Saurabh Deshpande, Jakub Lengiewicz, and Stéphane P.A. Bordas. "Probabilistic deep learning for real-time large deformation simulations". In: *Computer Methods in Applied Mechanics and Engineering* 398 (2022), p. 115307. ISSN: 0045-7825. DOI: https://doi.org/10.1016/j.cma.2022.115307. URL: https://www.sciencedirect.com/science/article/pii/S004578252200411X (page 79).

[58] C. Duriez et al. "Realistic haptic rendering of interacting deformable objects in virtual environments". In: *IEEE Transactions on Visualization and Computer Graphics* 12.1 (2006), pp. 36–47. DOI: 10.1109/TVCG.2006.13 (page 80).

[59] Christian Duriez. "Control of elastic soft robots based on real-time finite element method". In: *2013 IEEE International Conference on Robotics and Automation*. 2013 IEEE International Conference on Robotics and Automation. 2013, pp. 3982–3987. DOI: 10.1109/ICRA.2013.6631138 (page 80).

[61] Wolfgang Ehlers and Bernd Markert. "A Linear Viscoelastic Biphasic Model for Soft Tissues Based on the Theory of Porous Media". In: *Journal of biomechanical engineering* 123 (Nov. 2001), pp. 418–24. DOI: 10.1115/1.1388292 (page 78).

[63] A. Elouneg et al. "An open-source FEniCS-based framework for hyperelastic parameter estimation from noisy full-field data: Application to heterogeneous soft tissues". In: *Computers & Structures* 255 (2021), p. 106620. ISSN: 0045-7949. DOI: https://doi.org/10.1016/j.compstruc.2021.106620. URL: https://www.sciencedirect.com/science/article/pii/S0045794921001425 (pages 78, 118).

[70] François Faure et al. "SOFA: A Multi-Model Framework for Interactive Physical Simulation". In: *Soft Tissue Biomechanical Modeling for Computer Assisted Surgery*. Ed. by Yohan Payan. Vol. 11. Studies in Mechanobiology, Tissue Engineering and Biomaterials. Springer, June 2012, pp. 283–321. DOI: 10.1007/8415_2012_125. URL: https://hal.inria.fr/hal-00681539 (pages 79, 144).

[72] Cormac Flynn, Andrew Taberner, and Poul Nielsen. "Mechanical characterisation of in vivo human skin using a 3D force-sensitive micro-robot and finite element analysis". In: *Biomechanics and modeling in mechanobiology* 10 (Feb. 2011), pp. 27–38. DOI: 10.1007/s10237-010-0216-8 (page 78).

[80] C. Geuzaine and J.-F. Remacle. "Gmsh: a three-dimensional finite element mesh generator with built-in pre- and post-processing facilities". In: *International Journal for Numerical Methods in Engineering* 79 (2009), pp. 1309–1331. DOI: 10.1002/nme.2579 (pages 77, 82, 127).

[81] Chester H. Gibbons. "History of Testing Machines for Materials". In: *Transactions of the Newcomen Society* 15.1 (1934), pp. 169–184. DOI: 10.1179/tns.1934.011. eprint: https://doi.org/10.1179/tns.1934.011. URL: https://doi.org/10.1179/tns.1934.011 (page 78).

[82] Benjamin Gilles et al. "Frame-Based Elastic Models". In: *ACM Trans. Graph.* 30.2 (Apr. 2011). ISSN: 0730-0301. DOI: 10.1145/1944846.1944855. URL: https://doi.org/10.1145/1944846.1944855 (page 79).

[83] Olivier Goury and Christian Duriez. "Fast, Generic, and Reliable Control and Simulation of Soft Robots Using Model Order Reduction". In: *IEEE Transactions on Robotics* 34.6 (2018), pp. 1565–1576. DOI: 10.1109/TRO.2018.2861900 (page 79).

[84] Olivier Goury et al. "Automatised selection of load paths to construct reduced-order models in computational damage micromechanics: from dissipation-driven random selection to Bayesian optimization". In: *Computational Mechanics* 58 (Aug. 2016). DOI: 10.1007/s00466-016-1290-2 (page 79).

[88] Guanhui Guo, Yanni Zou, and Peter X. Liu. "A new rendering algorithm based on multi-space for living soft tissue". In: *Computers & Graphics* 98 (2021), pp. 242–254. ISSN: 0097-8493. DOI: https://doi.org/10.1016/j.cag.2021.06.003. URL: https://www.sciencedirect.com/science/article/pii/S0097849321001187 (page 79).

[89] Rami M. Haj-Ali and Anastasia H. Muliana. "Numerical finite element formulation of the Schapery non-linear viscoelastic material model". In: *International Journal for Numerical Methods in Engineering* 59.1 (2004), pp. 25–45. DOI: https://doi.org/10.1002/nme.861. eprint: https://onlinelibrary.wiley.com/doi/pdf/10.1002/nme.861. URL: https://onlinelibrary.wiley.com/doi/abs/10.1002/nme.861 (page 78).

[91] Lianghao Han et al. "Development of patient-specific biomechanical models for predicting large breast deformation". In: *Physics in medicine and biology* 57 (Dec. 2011), pp. 455–72. DOI: 10.1088/0031-9155/57/2/455 (pages 78, 115, 116, 118).

[94] Paul Hauseux, Jack S. Hale, and Stéphane P.A. Bordas. "Accelerating Monte Carlo estimation with derivatives of high-level finite element models". In: *Computer Methods in Applied Mechanics and Engineering* 318 (2017), pp. 917–936. ISSN: 0045-7825. DOI: https://doi.org/10.1016/j.cma.2017.01.041. URL: https://www.sciencedirect.com/science/article/pii/S0045782516313470 (page 78).

[95] Paul Hauseux et al. "Quantifying the uncertainty in a hyperelastic soft tissue model with stochastic parameters". In: *Applied Mathematical Modelling* 62 (2018), pp. 86–102. ISSN: 0307-904X. DOI: https://doi.org/10.1016/j.apm.2018.04.021. URL: https://www.sciencedirect.com/science/article/pii/S0307904X18302063 (pages 78, 98, 101).

[98] Gerhard A. Holzapfel and Ray W. Ogden. "Constitutive modelling of passive myocardium: a structurally based framework for material characterization". In: *Philosophical Transactions of the Royal Society A: Mathematical, Physical and Engineering Sciences* 367.1902 (Sept. 2009), pp. 3445–3475. DOI: 10.1098/rsta.2009.0091. URL: https://doi.org/10.1098/rsta.2009.0091 (page 98).

[100] Mikhail Itskov. "A generalized orthotropic hyperelastic material model with application to incompressible shells". In: *International Journal for Numerical Methods in Engineering* 50.8 (2001), pp. 1777–1799. DOI: https://doi.org/10.1002/nme.86. eprint: https://onlinelibrary.wiley.com/doi/pdf/10.1002/nme.86. URL: https://onlinelibrary.wiley.com/doi/abs/10.1002/nme.86 (page 78).

[102] Thibault Jacquemin and Stéphane P. A. Bordas. "A unified algorithm for the selection of collocation stencils for convex, concave, and singular problems". In: *International Journal for Numerical Methods in Engineering* 122.16 (2021), pp. 4292–4312. DOI: https://doi.org/10.1002/nme.6703. eprint: https://onlinelibrary.wiley.com/doi/pdf/10.1002/nme.6703. URL: https://onlinelibrary.wiley.com/doi/abs/10.1002/nme.6703 (page 77).

[105] Chintan Jansari et al. "Adaptive smoothed stable extended finite element method for weak discontinuities for finite elasticity". In: *European Journal of Mechanics - A/Solids* 78 (2019), p. 103824. ISSN: 0997-7538. DOI: https://doi.org/10.1016/j.euromechsol.2019.103824. URL: https://www.sciencedirect.com/science/article/pii/S0997753818309288 (pages 77, 142).

[106] Hrvoje Jasak, Ar Jemcov, and United Kingdom. "OpenFOAM: A C++ Library for Complex Physics Simulations". In: *International Workshop on Coupled Methods in Numerical Dynamics, IUC* (2007), pp. 1–20 (page 77).

[111] Robert C. Kirby. "Algorithm 839: FIAT, a New Paradigm for Computing Finite Element Basis Functions". In: *ACM Trans. Math. Softw.* 30.4 (Dec. 2004), pp. 502–516. ISSN: 0098-3500. DOI: 10.1145/1039813.1039820. URL: http://doi.acm.org/10.1145/1039813.1039820 (visited on 01/31/2018) (page 83).

[112] Robert C. Kirby and Anders Logg. "A Compiler for Variational Forms". In: *ACM Trans. Math. Softw.* 32.3 (Sept. 2006), pp. 417–444. ISSN: 0098-3500. DOI: 10.1145/1163641.1163644. URL: http://doi.acm.org/10.1145/1163641.1163644 (visited on 01/31/2018) (page 82).

[120] T. Lavigne et al. "Société de Biomécanique Young Investigator Award 2021: Numerical investigation of the time-dependent stress–strain mechanical behaviour of skeletal muscle tissue in the context of pressure ulcer prevention". In: *Clinical Biomechanics* 93 (2022), p. 105592. ISSN: 0268-0033. DOI: https://doi.org/10.1016/j.clinbiomech.2022.105592. URL: https://www.sciencedirect.com/science/article/pii/S0268003322000225 (page 78).

[124] Jakub Lengiewicz et al. "Interfacing AceGEN and FEniCS for advanced constitutive models". In: *Proceedings of FEniCS 2021, online, 22–26 March*. Ed. by Igor Baratta et al. 2021, p. 474. DOI: 10.6084/m9.figshare.14495463. URL: http://mscroggs.github.io/fenics2021/talks/lengiewicz.html (page 80).

[126] Yi-Je Lim et al. "Soft tissue deformation and cutting simulation for the multimodal surgery training". In: *19th IEEE Symposium on Computer-Based Medical Systems (CBMS'06)*. 19th IEEE Symposium on Computer-Based Medical Systems. 2006, pp. 635–640 (page 78).

[137] Steve Maas et al. "FEBio: Finite Elements for Biomechanics". In: *Journal of biomechanical engineering* 134 (Jan. 2012), p. 011005. DOI: 10.1115/1.4005694 (page 80).

[138] Richard Malgat et al. "Multifarious Hierarchies of Mechanical Models for Artist Assigned Levels-of-Detail". In: *Proceedings of the 14th ACM SIGGRAPH / Eurographics Symposium on Computer Animation*. SCA '15. Association for Computing Machinery. New York, NY, USA, 2015, 27–36. ISBN: 9781450334969. DOI: 10.1145/2786784.2786800. URL: https://doi.org/10.1145/2786784.2786800 (page 79).

[139] Stéphanie Marchesseau et al. "Fast porous visco-hyperelastic soft tissue model for surgery simulation: Application to liver surgery". In: *Progress in Biophysics and Molecular Biology* 103.2 (2010). Special Issue on Biomechanical Modelling of Soft Tissue Motion, pp. 185–196. ISSN: 0079-6107. DOI: https://doi.org/10.1016/j.pbiomolbio.2010.09.005. URL: https://www.sciencedirect.com/science/article/pii/S0079610710000738 (pages 64, 78).

[140] P. A. L. S. Martins, R. M. Natal Jorge, and A. J. M. Ferreira. "A Comparative Study of Several Material Models for Prediction of Hyperelastic Properties: Application to Silicone-Rubber and Soft Tissues". In: *Strain* 42.3 (2006), pp. 135–147. DOI: https://doi.org/10.1111/j.1475-1305.2006.00257.x. eprint: https://onlinelibrary.wiley.com/doi/pdf/10.1111/j.1475-1305.2006.00257.x. URL: https://onlinelibrary.wiley.com/doi/abs/10.1111/j.1475-1305.2006.00257.x (page 78).

[142] Arnaud Mazier et al. "Inverse deformation analysis: an experimental and numerical assessment using the FEniCS Project". In: *Engineering with Computers* (Feb. 2022). DOI: 10.1007/s00366-021-01597-z (page 78).

[143] Arnaud Mazier et al. "Supplementary material for Inverse deformation analysis: an experimental and numerical assessment using the FEniCS Project". In: (Feb. 2021). DOI: 10.6084/m9.figshare.14035793.v1. URL: https://figshare.com/articles/software/Supplementary_material_for_Inverse_deformation_analysis_an_experimental_and_numerical_assessment_using_the_FEniCS_Project/14035793 (pages 56, 57, 60, 91).

[145] Michelle Menard. *Game Development with Unity*. 1st. Boston, MA, USA: Course Technology Press, 2011. ISBN: 9781435456587 (page 79).

[147] Aaron Meurer et al. "SymPy: symbolic computing in Python". In: *PeerJ Computer Science* 3 (Jan. 2017), e103. ISSN: 2376-5992. DOI: 10.7717/peerj-cs.103. URL: https://doi.org/10.7717/peerj-cs.103 (page 93).

[148] Valentina Miguez Pacheco, Larry Hench, and Aldo Boccaccini. "Bioactive glasses beyond bone and teeth: Emerging applications in contact with soft tissues". In: *Acta Biomaterialia* 13 (Nov. 2014). DOI: 10.1016/j.actbio.2014.11.004 (page 78).

[150] L. Angela Mihai et al. "A comparison of hyperelastic constitutive models applicable to brain and fat tissues". In: *Journal of The Royal Society Interface* 12 (Sept. 2015), pp. 1–12. DOI: 10.1098/rsif.2015.0486 (page 78).

[151] L. Angela Mihai et al. "A family of hyperelastic models for human brain tissue". In: *Journal of the Mechanics and Physics of Solids* 106 (2017), pp. 60–79. ISSN: 0022-5096. DOI: https://doi.org/10.1016/j.jmps.2017.05.015. URL: https://www.sciencedirect.com/science/article/pii/S0022509617302703 (page 78).

[154] M. Mooney. "A Theory of Large Elastic Deformation". In: *Journal of Applied Physics* 11.9 (1940), pp. 582–592. DOI: 10.1063/1.1712836. eprint: https://doi.org/10.1063/1.1712836. URL: https://doi.org/10.1063/1.1712836 (pages 54, 81).

[157] Harish Narayanan. "A computational framework for nonlinear elasticity". en. In: *Automated Solution of Differential Equations by the Finite Element Method*. Ed. by Anders Logg, Kent-Andre Mardal, and Garth Wells. Lecture Notes in Computational Science and Engineering 84. Springer Berlin Heidelberg, 2012, pp. 525–541. ISBN: 978-3-642-23098-1 978-3-642-23099-8. URL: http://link.springer.com/chapter/10.1007/978-3-642-23099-8_27 (visited on 03/10/2015) (page 83).

[161] Vinh Phu Nguyen et al. "Meshless methods: A review and computer implementation aspects". In: *Mathematics and Computers in Simulation* 79.3 (2008), pp. 763–813. ISSN: 0378-4754. DOI: https://doi.org/10.1016/j.matcom.2008.01.003. URL: https://www.sciencedirect.com/science/article/pii/S0378475408000062 (page 77).

[162] Vien Minh Nguyen-Thanh, Xiaoying Zhuang, and Timon Rabczuk. "A deep energy method for finite deformation hyperelasticity". In: *European Journal of Mechanics - A/Solids* (Oct. 2019), p. 103874. DOI: 10.1016/j.euromechsol.2019.103874 (page 83).

[163] Siamak Niroomandi et al. "Real Time Simulation of Biological Soft Tissues : A PGD Approach". In: *International journal for numerical methods in biomedical engineering* 29 (May 2013). DOI: 10.1002/cnm.2544 (page 79).

[164] Alban Odot, Ryadh Haferssas, and Stephane Cotin. "DeepPhysics: A physics aware deep learning framework for real-time simulation". In: *International Journal for Numerical Methods in Engineering* 123.10 (2022), pp. 2381–2398. DOI: https://doi.org/10.1002/nme.6943. eprint: https://onlinelibrary.wiley.com/doi/pdf/10.1002/nme.6943. URL: https://onlinelibrary.wiley.com/doi/abs/10.1002/nme.6943 (pages 79, 92).

[165] R.W. Ogden. "Large deformation isotropic elasticity – on the correlation of theory and experiment for incompressible rubberlike solids". In: *Proceedings of the Royal Society of London. A. Mathematical and Physical Sciences* 326.1567 (Feb. 1972), pp. 565–584. DOI: 10.1098/rspa.1972.0026. URL: https://doi.org/10.1098/rspa.1972.0026 (page 81).

[171] Cécile Patte, Martin Genet, and Dominique Chapelle. "A quasi-static poromechanical model of the lungs". In: *Biomechanics and Modeling in Mechanobiology* 21.2 (Jan. 2022), pp. 527–551. DOI: 10.1007/s10237-021-01547-0. URL: https://doi.org/10.1007/s10237-021-01547-0 (page 83).

[172] Yohan Payan. *Biomechanics of Living Organs*. 2017. DOI: 10.1016/c2015-0-00832-2 (page 78).

[173] S. Pezzuto, D. Ambrosi, and A. Quarteroni. "An orthotropic active–strain model for the myocardium mechanics and its numerical approximation". In: *European Journal of Mechanics - A/Solids* 48 (Nov. 2014), pp. 83–96. DOI: 10.1016/j.euromechsol.2014.03.006. URL: https://doi.org/10.1016/j.euromechsol.2014.03.006 (page 98).

[174] V. Phunpeng and P.M. Baiz. "Mixed finite element formulations for strain-gradient elasticity problems using the FEniCS environment". In: *Finite Elements in Analysis and Design* 96 (2015), pp. 23–40. DOI: 10.1016/j.finel.2014.11.002. URL: https://app.dimensions.ai/details/publication/pub.1009763899 (page 83).

[175] Guillaume Picinbono, Hervé Delingette, and Nicholas Ayache. "Non-linear anisotropic elasticity for real-time surgery simulation". In: *Graphical Models* 65.5 (2003). Special Issue on SMI 2002, pp. 305–321. ISSN: 1524-0703. DOI: https://doi.org/10.1016/S1524-0703(03)00045-6. URL: https://www.sciencedirect.com/science/article/pii/S1524070303000456 (page 78).

[182] Anthony Ralston and Philip Rabinowitz. "A First Course in Numerical Analysis (2nd ed.)" In: *A First Course in Numerical Analysis (Second Edition)*. Second Edition. New York: Dover Publications, 2001, p. i. ISBN: 978-0-486-41454-6 (page 88).

[183] H. Rappel et al. "A Tutorial on Bayesian Inference to Identify Material Parameters in Solid Mechanics". In: *Archives of Computational Methods in Engineering* 27 (Jan. 2019). DOI: 10.1007/s11831-018-09311-x (page 78).

[185] H. Rappel et al. "Identifying elastoplastic parameters with Bayes' theorem considering output error, input error and model uncertainty". In: *Probabilistic Engineering Mechanics* 55 (2019), pp. 28–41. ISSN: 0266-8920. DOI: https://doi.org/10.1016/j.probengmech.2018.08.004. URL: https://www.sciencedirect.com/science/article/pii/S0266892018300547 (page 78).

[186] Florian Rathgeber et al. "Firedrake: Automating the Finite Element Method by Composing Abstractions". In: *ACM Transactions on Mathematical Software (TOMS)* 43.3 (Dec. 2016), 24:1–24:27. ISSN: 0098-3500. DOI: 10.1145/2998441. URL: https://doi.org/10.1145/2998441 (visited on 01/20/2020) (page 82).

[188] Scott I. Heath Richardson et al. "A poroelastic immersed finite element framework for modelling cardiac perfusion and fluid–structure interaction". In: *International Journal for Numerical Methods in Biomedical Engineering* 37.5 (2021), e3446. DOI: https://doi.org/10.1002/cnm.3446. eprint: https://onlinelibrary.wiley.com/doi/pdf/10.1002/cnm.3446. URL: https://onlinelibrary.wiley.com/doi/abs/10.1002/cnm.3446 (page 78).

[191] Benjamin Rodenberg et al. "FEniCS–preCICE: Coupling FEniCS to other simulation software". en. In: *SoftwareX* 16 (Dec. 2021), p. 100807. ISSN: 2352-7110. DOI: 10.1016/j.softx.2021.100807. URL: https://www.sciencedirect.com/science/article/pii/S2352711021001072 (visited on 07/05/2022) (page 83).

[198] Andrew Sanders. *An Introduction to Unreal Engine 4*. USA: A. K. Peters, Ltd., 2016. ISBN: 1498765092 (page 79).

[200] M. W. Scroggs et al. "Basix: a runtime finite element basis evaluation library". submitted to Journal of Open Source Software. 2022 (pages 83, 87).

[204] Bruce R. Simon. "Multiphase Poroelastic Finite Element Models for Soft Tissue Structures". In: *Applied Mechanics Reviews* 45.6 (June 1992), pp. 191–218. ISSN: 0003-6900. DOI: 10.1115/1.3121397. eprint: https://asmedigitalcollection.asme.org/appliedmechanicsreviews/article-pdf/45/6/191/5436442/191_1.pdf. URL: https://doi.org/10.1115/1.3121397 (page 78).

[205] Sina Sinaie et al. "Programming the material point method in Julia". In: *Advances in Engineering Software* 105 (Jan. 2017). DOI: 10.1016/j.advengsoft.2017.01.008 (page 77).

[207] Michael Smith. *ABAQUS/Standard User's Manual, Version 6.9*. English. United States: Dassault Systèmes Simulia Corp, 2009 (page 77).

[208] Ian Stokes et al. "Limitation of Finite Element Analysis of Poroelastic Behavior of Biological Tissues Undergoing Rapid Loading". In: *Annals of biomedical engineering* 38 (Mar. 2010), pp. 1780–8. DOI: 10.1007/s10439-010-9938-0 (page 78).

[213] Eleonora Tagliabue et al. "Intra-operative Update of Boundary Conditions for Patient-Specific Surgical Simulation". In: *Medical Image Computing and Computer Assisted Intervention – MICCAI 2021* (2021). Ed. by Marleen de Bruijne et al., pp. 373–382 (page 78).

[214] Hossein Talebi et al. "A computational library for multiscale modeling of material failure". In: *Computational Mechanics* 53.5 (Dec. 2013), pp. 1047–1071. DOI: 10.1007/s00466-013-0948-2. URL: https://doi.org/10.1007/s00466-013-0948-2 (page 77).

[218] Giuseppe Turini et al. "Software Framework for VR-Enabled Transcatheter Valve Implantation in Unity". In: nternational Conference on Augmented Reality, Virtual Reality and Computer Graphics. July 2019, pp. 376–384. ISBN: 978-3-030-25964-8. DOI: 10.1007/978-3-030-25965-5_28 (page 79).

[220] Stephane Urcun et al. "Cortex tissue relaxation and slow to medium load rates dependency can be captured by a two-phase flow poroelastic model". In: *Journal of the Mechanical Behavior of Biomedical Materials* 126 (Nov. 2021), p. 104952. DOI: 10.1016/j.jmbbm.2021.104952 (page 78).

[221] Stéphane Urcun et al. "Digital twinning of Cellular Capsule Technology: Emerging outcomes from the perspective of porous media mechanics". In: *PLOS ONE* 16.7 (July 2021), pp. 1–30. DOI: 10.1371/journal.pone.0254512. URL: https://doi.org/10.1371/journal.pone.0254512 (page 78).

[223] D.R. Veronda and R.A. Westmann. "Mechanical characterization of skin—Finite deformations". In: *Journal of Biomechanics* 3.1 (1970), pp. 111–124. ISSN: 0021-9290. DOI: https://doi.org/10.1016/0021-9290(70)90055-2. URL: https://www.sciencedirect.com/science/article/pii/0021929070900552 (page 81).

[224] Mickeal Verschoor, Daniel Lobo, and Miguel A. Otaduy. "Soft Hand Simulation for Smooth and Robust Natural Interaction". In: *2018 IEEE Conference on Virtual Reality and 3D User Interfaces (VR)*. IEEE Conference on Virtual Reality and 3D User Interfaces (VR). 2018, pp. 183–190. DOI: 10.1109/VR.2018.8447555 (page 79).

[227] Jared A. Weis, Michael I. Miga, and Thomas E. Yankeelov. "Three-dimensional image-based mechanical modeling for predicting the response of breast cancer to neoadjuvant therapy". In: *Computer Methods in Applied Mechanics and Engineering* 314 (2017). Special Issue on Biological Systems Dedicated to William S. Klug, pp. 494–512. ISSN: 0045-7825. DOI: https://doi.org/10.1016/j.cma.2016.08.024. URL: https://www.sciencedirect.com/science/article/pii/S0045782516310167 (page 83).

[228] Jeffrey A. Weiss, Bradley N. Maker, and Sanjay Govindjee. "Finite element implementation of incompressible, transversely isotropic hyperelasticity". In: *Computer Methods in Applied Mechanics and Engineering* 135.1 (1996), pp. 107–128. ISSN: 0045-7825. DOI: https://doi.org/10.1016/0045-7825(96)01035-3. URL: https://www.sciencedirect.com/science/article/pii/0045782596010353 (page 78).

[230] Jun Wu, Rüdiger Westermann, and Christian Dick. "Real-Time Haptic cutting of high-resolution soft tissues". In: *Studies in health technology and informatics* 196 (Apr. 2014), pp. 469–75. DOI: 10.3233/978-1-61499-375-9-469 (page 79).

[234] Milad Zeraatpisheh, Stephane P.A. Bordas, and Lars A.A. Beex. "Bayesian model uncertainty quantification for hyperelastic soft tissue models". In: *Data-Centric Engineering* 2 (2021), e9. DOI: 10.1017/dce.2021.9 (page 78).

[236] J. Zhou and Y. C. Fung. "The degree of nonlinearity and anisotropy of blood vessel elasticity". In: *Proceedings of the National Academy of Sciences* 94.26 (1997), pp. 14255–14260. DOI: 10.1073/pnas.94.26.14255. eprint: https://www.pnas.org/doi/pdf/10.1073/pnas.94.26.14255. URL: https://www.pnas.org/doi/abs/10.1073/pnas.94.26.14255 (page 78).

[238] O.C. Zienkiewicz, R.L. Taylor, and David Fox. "The Finite Element Method for Solid and Structural Mechanics". In: *The Finite Element Method for Solid and Structural Mechanics (Seventh Edition)*. Seventh Edition. Oxford: Butterworth-Heinemann, 2014, p. i. ISBN: 978-1-85617-634-7. DOI: https://doi.org/10.1016/B978-

1-85617-634-7.00016-8. URL: https://www.sciencedirect.com/science/article/pii/B9781856176347000168 (page 88).

[240] Kristian B. Ølgaard and Garth N. Wells. "Applications in solid mechanics". en. In: *Automated Solution of Differential Equations by the Finite Element Method: The FEniCS Book*. Ed. by Anders Logg, Kent-Andre Mardal, and Garth Wells. Lecture Notes in Computational Science and Engineering. Berlin, Heidelberg: Springer, 2012, pp. 505–524. ISBN: 978-3-642-23099-8. DOI: 10.1007/978-3-642-23099-8_26. URL: https://doi.org/10.1007/978-3-642-23099-8_26 (visited on 07/04/2022) (page 83).

5 Breast simulations pipeline: from medical imaging to patient-specific simulations

5.1 Introduction

In breast surgical practice, images are acquired in the prone configuration whereas the surgery is done in the supine position. In this chapter, we are interested in using the Finite Element Method (FEM) to simulate the motion and, thus the tumor movement from one stance to another, hence predicting the displacement and final position of the tumor. The FEM relies on using a model that should mimic as well as possible the movement of the breast. The model behavior is driven by the rheological parameters of the breast, which can significantly modify the final breast shape. Hence, the breast parameters are most of the time impossible to measure in-vivo and can evolve in time depending on many biological factors within the patient's body. The goal of this chapter is to present a numerical pipeline to simulate the change of stance between the imaging to the surgical configuration. We will first present the different steps to obtain a patient-specific FEM model from medical images (MRI). Then, we will detail the different existing breast models, stating our modeling choices for creating a new model. Then, we will introduce our new and intuitive breast model allowing to simulate quickly the change of stance. Finally, we will detail our optimization procedure, only based on a surface scan of the patient to infer the patient-specific material properties and estimate of where the tumor is now located.

5.2 Breast numerical models: a state-of-the-art

Over the past decades, biomechanical breast models have been extensively studied for different medical applications. From surgical training or pre-operative planning to image registration or material parameter estimation. Several of those studies relied on the finite element theory. The model complexity varies from one application to another. Indeed, before selecting a model, a careful reflection has to be accomplished about the number of anatomical structures and the complexity (fidelity) carried out to describe its behavior.

As an example, [42, 91, 180, 193, 197, 210] tackled non-rigid registration from uncompressed data to mammogram. By assuming a linear elastic model combined with natural Dirichlet boundary conditions without calculating the undeformed configuration, the authors successfully mapped the mammogram deformations. Therefore, such a model could be convenient for describing compression efforts but might not be suitable for large deformations occurring in the change from prone to supine configuration.

In the mammogram FEM simulations domain, intensive work has been carried out [10, 127, 153, 195]. The studies showed different aims, such as the paddle's optimal design by minimizing the stress constraints generated on the breast. Notably, [153] discovered that a Gent model was more suitable for compression-like behavior, instead of Neo-Hookean.

In the context of breast preoperative surgical planning, extensive work has been investigated. Those studies mainly differ from FEM mammograms as they involve a larger spectrum of deformations requiring different needs. For instance, when simulating the gravity

direction change from prone to supine, the breast totally changes shape from a hemisphere to an almost flat object [79, 178, 180]. Consequently, a specific need is to reach a fair accuracy compared with the clinical data, which could only be achieved through careful tuning of the mechanical and anatomical breast properties. In this context, patient-specific models should include personalized boundary conditions, material models, and anatomical structures.

In the following non-exhaustive state-of-the-art, we will chronologically detail a few models that display common intersections with our application. Even if the technique or metrics differ, they can still be used as a comparison for our study.

- Over the past 15 years, [178–181] developed a series of models for various contexts, including breast biomechanics for multi-modal image analysis or breast tissue mechanical model under gravity loading. The study used two patient-specific FEM from MR images of the prone gravity-loaded configurations. These personalized models were used to predict the unloaded and supine gravity-loaded configurations and compared to MR images acquired for these states. The unloaded states were predicted with surface Root Mean Square errors of 4.2 mm and 4.1 mm for the two volunteers, while the supine gravity-loaded states were predicted with RMS errors of 8.4 mm and 7.7 mm. The study used a Neo-Hookean model with $c_1 = 0.08\,\text{kPa}$ and $0.15\,\text{kPa}$, respectively, while using fixed boundary conditions on the inner breast.

- [35] described a method to determine breast mechanical properties. They showed that the stress-free state of an object can be approximated by submerging it in a liquid of a similar density. An intensity-based non-rigid image registration algorithm is used to establish point-by-point correspondence between MR images in prone and supine configurations. A FEM of the breast was constructed from the submerged images, and the deformation to prone was simulated by imposing the nodal displacement found previously. The study assumed a Neo-Hookean material model with an initial shear moduli of fibroglandular and adipose tissue of $0.4\,\text{kPa}$ and $0.3\,\text{kPa}$, respectively. The mean target registration error for 8 landmarks was $1.0\,\text{mm}$ for the left breast and $1.6\,\text{mm}$ for the right breast.

- [90, 91] proposed a nonlinear biomechanical model-based image registration method with a simultaneous optimization procedure for both the material parameters of breast tissues and the direction of the gravitational force. FEM was used to estimate a physically plausible deformation of the pectoral muscle and the deformation of breast tissues due to gravity loading. Then, nonrigid intensity-based image registration was employed to recover the remaining deformation that FE analyses did not capture due to the approximations of models and the uncertainties of external forces and constraints. The registration resulted in prone and supine MR images for five patients, achieving the best registration performance on 45 fiducial markers of 8.44 ± 5.5 mm. The Neo-Hookean model was used, describing 4 phases with an average shear modulus: fat ($5.16\,\text{kPa}$), glandular ($2.96\,\text{kPa}$), skin ($3.63\,\text{kPa}$), muscle ($4.16\,\text{kPa}$), and frictionless sliding for the boundary conditions with the pectoral.

- [62] presented biomechanical modeling with a surface registration algorithm to optimize the material parameters and perform a regularised surface alignment to atone for contact with the MR coil. The algorithm was evaluated for the prone-to-supine case using prone MRI and the skin outline of supine Computed Tomography (CT) scans for 3 patients. The optical 3D surface scan was used as a registration target and the nipple distances after alignment between the transformed MRI and the surface were 10.1 mm and 6.3 mm respectively. The breast was approximated using a skin membrane model, adipose, and fibroglandular tissues using a Neo-Hookean model. The boundary conditions are natural Dirichlet on the inner side of the breast.

- [152] developed a breast FEM, including adipose and glandular tissues, muscle, skin, suspensory ligaments, and pectoral fascias. Modeling the tissues using the Neo-Hookean material models, the stress-free breast geometry and subject-specific constitutive models are optimized using MR images. The breast geometry in three breast configurations (prone, supine, supine-tilted) was computed using the breast stress-free geometry with the estimated set of equivalent Young's modulus ($E^r_{\text{breast}} = 0.3\,\text{kPa}, E^l_{\text{breast}} = 0.2\,\text{kPa}, E_{\text{skin}} = 4\,\text{kPa}, E_{\text{fascia}} = 120\,\text{kPa}, E_{\text{ligaments}} = 120\,\text{kPa}, E_{\text{muscle}} = 10\,\text{kPa}$). The Hausdorff distance between estimated and measured breast geometries for prone, supine, and supine tilted configurations is equal to 2.17 mm, 1.72 mm, and 5.90 mm respectively. Sliding boundary conditions were applied including the constraint of the ligament.

- [11, 76] developed an automated breast image analysis workflow to assist clinicians during breast cancer detection and treatment procedures. They designed a fully automated pipeline from image segmentation using Convolutional Neural Networks (CNN) to simulation using population-based statistical analysis and visualization. A Neo-Hookean model was used with Young's modulus varying between 0.25 and 0.3 kPa. The whole process of visualizing the supine simulated configuration from prone takes about an hour per patient. The study showed a Residual Mean Square Error of 5 mm with a maximal distance of 9.3 mm. Sliding boundary conditions were used to demonstrate the importance of the pectoral shape due to arm rotations during the pose change.

In all previous models, few studies attempted simulating the tumor movements, and few communicated the run-time of the simulation. Hence, it makes it difficult to assess the possible applications of the previous studies to breast surgery planning. Among the different models, different choices were made for modeling the breast and organs of interest. Following a short state-of-the-art on the various modeling hypotheses and mechanical properties of such organs.

Muscle

The muscle depicts a complex geometry and mechanical behavior. It is non-linearity, anisotropic, incompressible, and depends on the contractile activity. Hence, to reproduce

the complexity of the muscle behavior, material models such as Hill [113] or Feldman's lambda [158] have been developed, considering the variation of elasticity dependent on the muscle state. For breast biomechanical modeling, the muscle is combined with the thoracic cage and is frequently considered rigid breast support.

Glandular and adipose tissues

Breast, like most soft tissues, are assumed to be incompressible (due to their high water concentration), non-linear, anisotropic, and viscous. Therefore, viscous effects could be neglected in a static simulation, such as breast-conserving surgery, as they only occur in time-dependent situations. In the case of breast simulations, optimal values of the Poisson's ratio range from 0.45 to 0.499 to ensure incompressibility [215]. Several studies demonstrated that breast composition experiences significant changes during a woman's life, especially if the breast develops malignant conditions. Among the reviewed literature, the breast Young's modulus ranges between 0.1 kPa to 271.8 kPa, composing a large gap. Such a significant difference in measurements can be explained by several factors like physical condition, age, the period in the menstrual cycle of the patients, or the experimental set-up itself [91, 132]. Similarly, differences between estimated mechanical properties using the FE method are noticed dues to the variability of modeling techniques [60, 196]. For example, improper speculations on breast mechanics can substantially affect the assessed parameters. Among them, overconstrained boundary conditions such as natural Dirichlet might significantly impact soft material behavior. Conversely, authorizing too much freedom in the boundary conditions (sliding only) of the breast over the chest wall can lead to stiff material properties.

Skin

The skin is subject to nonlinear and anisotropic behavior due to collagen fibers, and mechanical properties are still investigated [63]. Hence, few were interested in estimating the in-vivo skin properties by ultrasound [212] or suction testing [28]. Several studies have shown the importance of considering the skin in biomechanical breast modeling. [212] published a complete study about breast skin of a diverse cohort, estimating the Young modulus in 16 different breast regions. The results are an elastic modulus of 334 ± 88 kPa on average, with an enormous variation in the radial direction. The mechanical properties of the skin are stiffer in the lateral region followed by the superior, inferior, and medial zone with the softest behavior. In several breast simulations, the anisotropic behavior of the skin is generally bypassed for an isotropic, hyperelastic, and incompressible. Through FEM a wide spectrum of Young moduli have been identified ranging from 7.4 kPa [90] to 58.4 kPa [96].

Ligaments

In addition to the complex structure of the breast, the surrounding ligaments are also describing a complicated behavior. Among them, the deep cranial, medial, lateral, and inframammary ligaments are responsible for the solid attachment of the breast to the pectoral [144]. They are well documented, but few mechanical trials were made [201]. On the FEM field, those ligaments are usually represented as a natural Dirichlet boundary condition [11, 87, 170, 179]. In [152], the authors employed a Neo-Hookean material model to describe the behavior, leading to consistent results. Similarly, Cooper's ligaments constituting the support matrix were identified as collagen fibers for surgery purposes but with little mechanical testing. [79] used a spring-mass model to describe the ligaments improving the FEM solution stability of the prone-supine simulation. A first approximation of the elastic modulus of Cooper's ligaments was provided by [78]. By extrapolating known ligamentous structures in the human body, [78] found a range of 80 and 400 MPa. More recently, mechanical properties of Cooper's ligament were identified on 28 breast cadaver samples using uniaxial testing [27]. The results showed a distribution of Young's modulus values that ranges between 1 and 10 MPa, with a mode at 3.00 MPa.

5.3 From medical images to finite element model

5.3.1 Data acquisition

Our study is an observational, retrospective study carried out by the gynecological surgery department of the Centre Hospitalier Universitaire (CHU) of Montpellier. The patients were selected from the "Programme de Médicalisation des Systèmes d'Information" (PMSI) database. All patients who had undergone conservative surgical treatment for subclinical breast cancer between September 2016 and June 2017 were selected. Inclusion was based on medical records with rigorous verification of eligibility criteria and is reported in table 9.

Table 9: Inclusion and exclusion criterion to participate to the study.

Inclusion criterion	Exclusion criterion
Histologically proven breast cancer	Minor or under guardianship
Major	Justifying a neo-adjuvant treatment
Single tumor	
Breast MRI	
Preoperative and per-operative 3D surface scan	
Had a breast conservative surgery	
Did not object to the use of the data	

The age of the patients varied between 47 to 69 years, and the surgeon manually mea-

sured their breast size from 36A to 42C in US/UK bra sizing [235] with significant morphological differences. The lesions (tumor) ranged from 8 to 20mm, with an average of 12. Anatomopathological examination of the surgical specimen revealed invasive ductal carcinoma (IDC) for every patient.

Similarly to section 2.2.1, we obtained consent from the 7 patients for the study and a favorable opinion from the "Comité Local d'éthique Recherche". It has been precisely obtained on the 07/16/2017 under the label 2017_CLER-MTP_07-04. The study was declared in the registry of the CNIL (MR003) under the name of the "Centre Hospitalier Universitaire" (CHU) of Montpellier and registered on the ClinicalTrials website `https://www.clinicaltrials.gov/ct2/show/study/NCT03214419`.

Every patient had MRI in prone configuration (following the procedure explained in section 1.5, namely, in the prone position, breasts hanging, arms abducted above the head.) and a surface scan in the intra-operative (supine) position. We recall such pipeline in figure 32 copied from section . It is important to note that the MRIs are not specific to this study. They are performed routinely as part of the preoperative workup for each patient. Through discussions with a few surgeons, it has been observed that the preoperative workup can change from one country to another or one hospital to another.

5.3.2 Image segmentation

Following the MRI (axial section, T2 injected sequence), a sequence of 2D grey-scale images is obtained, showing the different organs of the patient. On each slice, segmentation has to be performed to extract each organ's geometry separately. Segmentation consists of isolating a pattern in an image by texture, edge, or color, for example. For our application, we want to segment the 3D image to isolate the mammary gland, the adipose tissues, the pectoralis major and minor muscle, the skin, and the tumor. Segmentation is a tedious task requiring expertise and knowledge of the anatomy to segment. We used the open-source software 3D Slicer [71] to perform our segmentations. It already offers multiple automatic, semi-automatic, and manual tools to achieve segmentations. It is also furnished with numerous open-source plugins that can facilitate the segmentation depending on the imaging procedure and format. In our case, the MRI format is a standard medical format called a .mhd file combined with a .raw file. The images' grey levels and voxels are stored in the .raw file, while the .mhd indicates machine parameters such as the contrast, voltage, or filters used.

The MRI acquisition is displayed as three collections of images representing three different points of view on the patient (see figure 34). These views correspond to the anatomical planes, with the axial plane, sagittal plane, and coronal plane depicted in figure 33. The 3D reconstruction algorithms, such as marching cubes [131], are usually automatically used to reconstruct and export a 3D mesh, describing the external surface of the organ. A large panel of techniques exists to identify and isolate patterns on images. Among them, automatic methods such as machine learning algorithms using Convolutional Neural Networks (CNN) can rapidly segment organs of interests [155, 226]. Unfortunately, those algorithms are mostly trained for a specific segmentation with a precise image format that did not

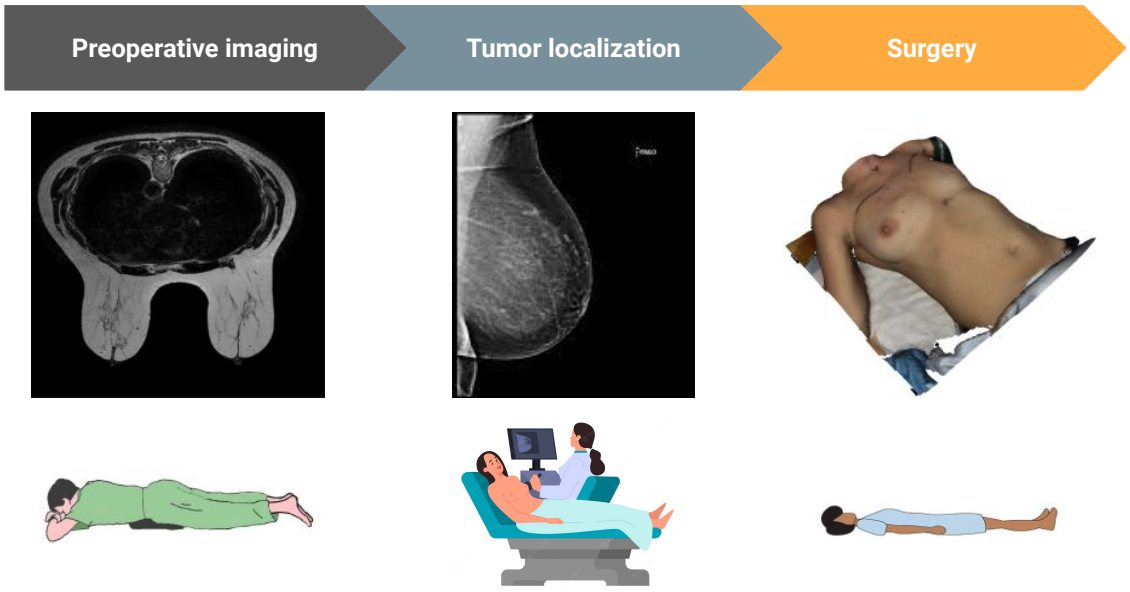

Figure 32: Breast-conserving surgery clinical pipeline. Starting from the left, the identification and evaluation of the tumor occur using an MRI in prone configuration. It allows to naturally expend the breast to evaluate the shape, position, and any relevant information helping the diagnosis. On the right side, the end of the pipeline is represented by a 3D surface acquisition of the patient. In the intra-operative configuration (supine), the surgeon will operate to remove the tumor without any medical imaging guidance. One problem remains, forecasting the tumor position after such a large movement of the breast from the imaging to the surgical configuration. To improve the surgeon's precision, in the middle of the image, an additional step is needed for locating the tumor. The position of the tumor is marked in another new configuration using ultrasound imaging for spotting the tumor and using a Radioguided Occult Lesion Localization (ROLL) or metallic harpoon. The goal of this thesis is to remove this extra step by proposing numerical methods capable of predicting the tumor localization from the imaging to the intra-operative configuration.

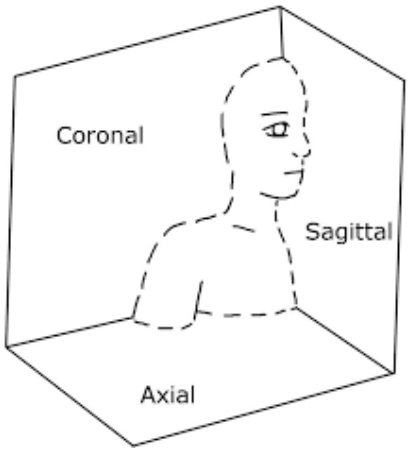

Figure 33: The three medical planes: axial, coronal, and sagittal. Image extracted from "Building a user interface with MATLAB GUIDE for MRI data volumes in Imiomics" from A. Larson, `http://uu.diva-portal.org/smash/get/diva2:1257377/FULLTEXT01.pdf`.

match our needs. Another option would have been to create our own machine learning algorithm. Sadly, the amount of data required to train such a network is not compatible with our database size. In this study, we will mainly focus on the thresholding and growing region methods. Indeed, we mostly privileged those two methods for our segmentation, as they demonstrated to be the most efficient and rapid. Given the contrast product used before the MRI, the acquisitions were detailed and contrasted, making the two following methods straightforward and effective.

Threshold

Thresholding is one of the most utilized techniques in segmentation due to the easy implementation and principle. On a greyscale image, as it is the case in MRI acquisitions, it is possible to represent the image as a function $s(x, y)$ where (x, y) are the coordinates in the image and $s(x, y)$ the value of the pixel at the given coordinate. Basically, the threshold method consists in choosing two values T_1 and T_2 such that

$$p(x, y) = \begin{cases} 1 & \text{if } T_1 < s(x, y) < T_2 \\ 0 & \text{else} \end{cases} \tag{73}$$

where $s(x, y)$ represents the region we want to isolate.

A principal drawback of this method is the requirement of having an image which is well nuanced in colors with sufficiently delimited regions. As shown in figure 34, this was not the case in most of our segmentation, resulting in an incomplete segmentation. As we can see, the MRI image has acceptable blur and color distribution. But different regions of interest can have similar grey level intensities color such as the adipose and the sternum's

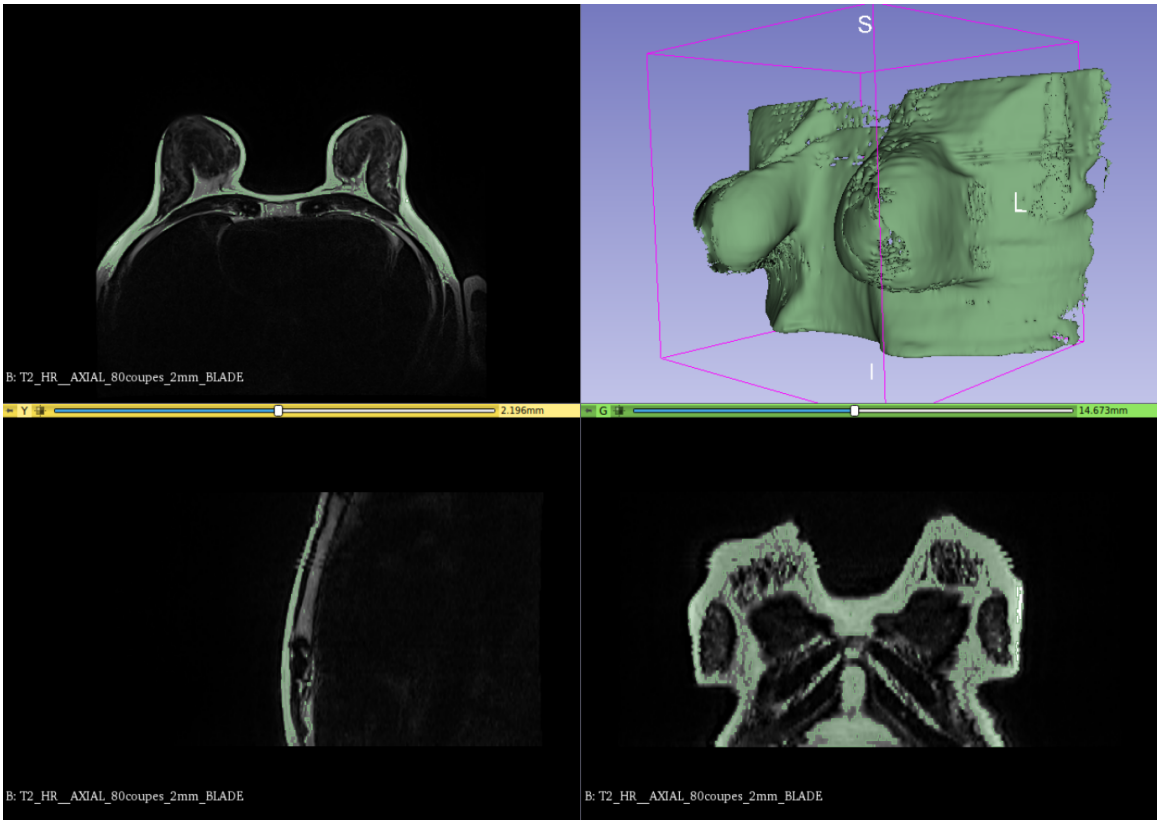

Figure 34: View in 3D Slicer of the MRI acquisition of a patient in prone configuration. The slices of the MRI can be seen in three different views: axial in the top left corner, coronal in the lower right corner, and sagittal in the lower left corner. In each view, a part of the skin is segmented (in green) and the reconstructed surface mesh can be seen in the top right corner.

cartilage, making the use of thresholding methods challenging. Thresholding was the first safe choice, but the growing region method had to be used as a complementary approach.

Growing region

The growing region method relies on the development of seeds [168]. A seed is a pixel or a pixel set, that can be manually or automatically placed. When running the algorithm, the seeds spread to the surrounding pixels based on the characteristics of those pixels, the grey level intensity for example. Each seed will therefore grow into a specific region defined by its own pattern. To be more explicit, we consider a simple case where only one region needs to be segmented. We call $S(x, y)$ the map of the seeds' position, meaning $S(x, y) = 1$ if the pixel at coordinates (x, y) is a seed. Then we choose a predicate P and we construct

recursively our region by updating S such that

$$S(x, y) = 1 \,\text{if}\, T(x, y) = \text{True and } (x, y) \,\text{is a neighbor of a seed in}\, S. \tag{74}$$

This algorithm proved to be efficient, even in complex cases. Despite the contrast liquid injected into the patient before the screening, the MRI acquisition still lacked contrast, and many regions were difficult to distinguish. By using 3D Slicer, we inserted precise seeds for different organs and obtained an admissible segmentation, drastically reducing manual editing. We encountered one specific case where the algorithm failed when one image was overly blurry. It appeared to be one of the known limitations of the growing region algorithm [233] and manual modifications are needed. In figure 35, we can see on the left the original image with the seeds we manually added. We observe that some regions are difficult to arbitrate visually, and a threshold wouldn't have given a satisfactory result. On the right image, we display the outcome of the growth region algorithm, which generates a fair delimitation of our regions. The result is not perfect but can be enhanced either by adding more seeds or by manual editing.

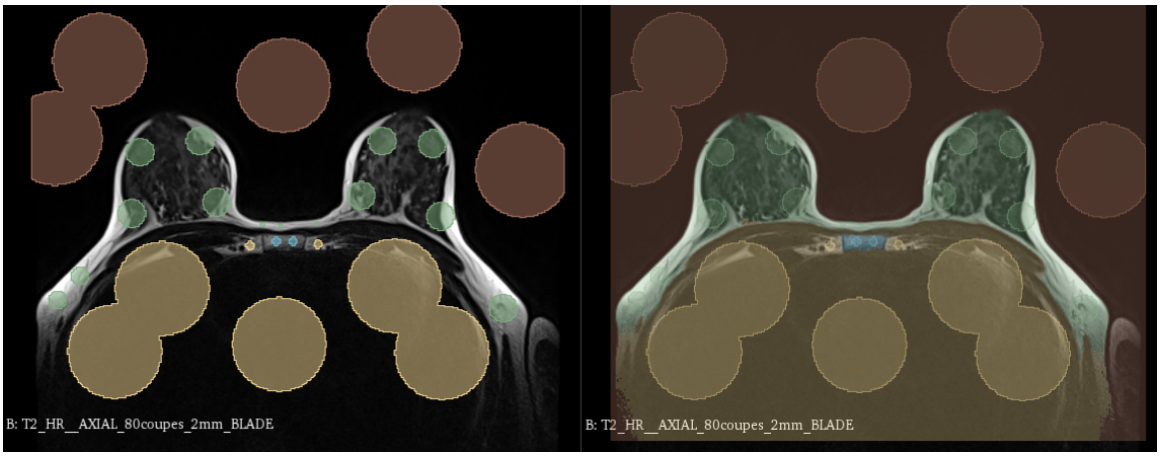

Figure 35: Application of the growth region algorithm on the MRI acquisition of a patient in the prone position (Axial Plane). The red color stands for the void, the green is the breast, the yellow is the muscle, and, the blue is the sternum. On the left, we show the seeds that were placed (small circles), and on the right, the regions are colored by the growth region algorithm.

5.3.3 Mesh registration

Image registration is the process of geometrically aligning one image with another. It is frequently used for aligning different points of view in medical imaging devices or post-treatment analysis [167]. Image registration has been widely transferred to mesh registration for motion capture or medical applications [141]. The registration is needed to compare the simulation result (predicting the surgical stance from the imaging one) and the surface

acquisition of the patient in surgical configuration (ground truth). The main point (and most time-consuming) of the registration is to search for each point in the source mesh (the surface acquisition) and the closest point in the target mesh (the segmented skin). Once the nearest point is found, constraints are applied to the system to minimize the distance between the two meshes. In the case of rigid registration, it amounts to finding the best rotation and translation to fit the closest pairs of points.

The search for closest points is accomplished by constructing a KD-Tree (K stands for any digit and D means Dimensional) and then performing a nearest neighbor search in the data structure. KD-Tree was first introduced by Jon Louis Bentley in 1975 [17] and has been widely used in the nearest-neighbor search algorithm, as they have an average complexity of $\mathcal{O}(n \log n)$ (the worst complexity being $\mathcal{O}(n)$). They proved to be particularly efficient when dealing with a high number of points (to give a better idea, we have around 50 000 points in the surface acquisition). A KD-Tree is built from the distribution of points in a K-dimensional space. The space is recursively split in half along each axis until obtaining an equivalent number of points in each split section. The recursion ends when a tree depth threshold is reached, or when each section contains only one point, as shown in figure 36. A separation forms a node in the tree, splitting into two branches. The final element of a branch (either a point or a section) is called a leaf. The search is accomplished by choosing a query point P, and going down all trees until finding the section where the point P is. The minimum distance between P and each other point in the section is computed and saved. Then, the tree is traveled backward. But from there, instead of computing the distance between each point, the algorithm computes the distance between P and the other sections and subsections. If the distance to the section is higher than the minimum distance computed previously, then this section and all linked subsections are ignored by the algorithm. Else, we search for the closest point in this section and save the minimal distance. The algorithm continues until all sections have been searched or ignored. This closest point search could also be used for various cases, such as contact implementations, where the nearest neighbor on the other mesh is required.

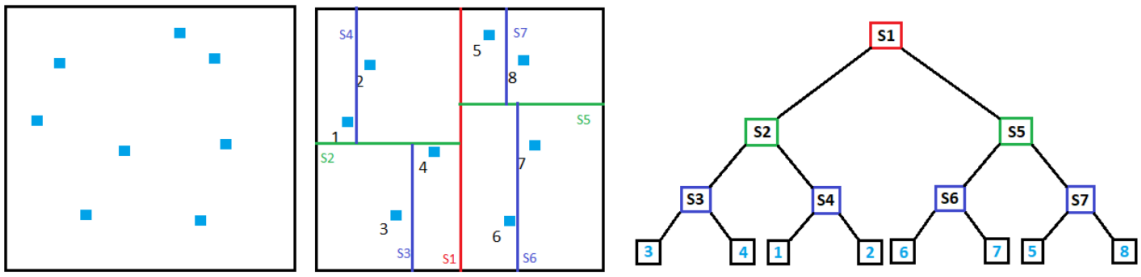

Figure 36: Construction of a KD-Tree in a 2-dimensional space. On the left is the initial distribution of the points where we see the different splits made by the algorithm. On the right is a graphical representation of the spatial separation and associated KD-Tree.

In section 2, we previously have seen a more complicated registration case where the

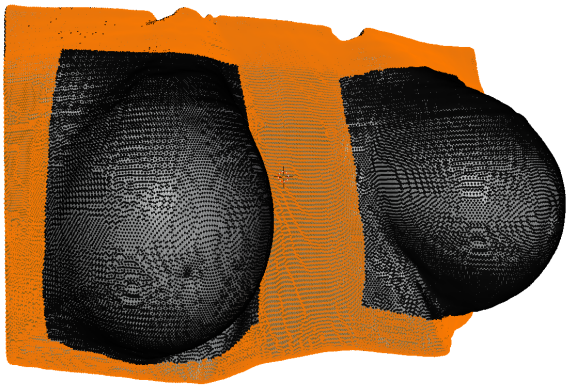

Figure 37: Mesh of the skin of the segmented breast with the Region Of Interest (ROI) selected for the partial registration .

source was a deformable model described by equation 25.

For this case, as the surface acquisition is a static object, thus a rigid body registration is required. Hence, we are looking for the optimal rotation and translation, enabling us to minimize the distance between the surface acquisition and the segmented skin. One hurdle is the geometrical difference between the meshes. Indeed, initially, registration is utilized to fit the surface of two similar shapes. In this singular case, the breasts do not have the same shape in the two acquisitions, as they were screened with different gravity orientations resulting in a large breast deformation. To solve this issue, we used a partial registration by selecting a Region Of Interest (ROI) while favoring the matching of relevant anatomical landmarks such as the upper, middle, and lower sternum. The chosen ROI is the exterior surface of the segmented skin with the exclusion of the breast skin to only focus on the sternal and external skin as shown in figure 37. The result of the partial registration is displayed in figure 38.

5.3.4 Finite element mesh

One vital requirement of FEM is the description of the volume of the object. Hence, the breast has to be discretized in 3D volume elements. Several different topologies are possible such as hexahedra, prisms, pyramids, etc... Among the topologies, the most classical elements are the continuum linear Lagrangian tetrahedra. They are widely spread as they are, in most cases, the most efficient topology for discretizing any shape and the most implemented in FEM packages. A classical method to generate a 3D mesh of a volume based on a 3D surface mesh is to use the Delauney 3D algorithm [99]. Unfortunately, the resolution of the 3D mesh (number of 3D elements of volume generated) depends on the resolution of the 3D surface mesh. In our case, we used the marching cube algorithm to obtain the mesh of the skin (based on the MRI) resulted in a mesh of more than 308 000 triangles, which will lead to a 3D mesh of more than 1 billion volume elements. The number of DOFs obtained

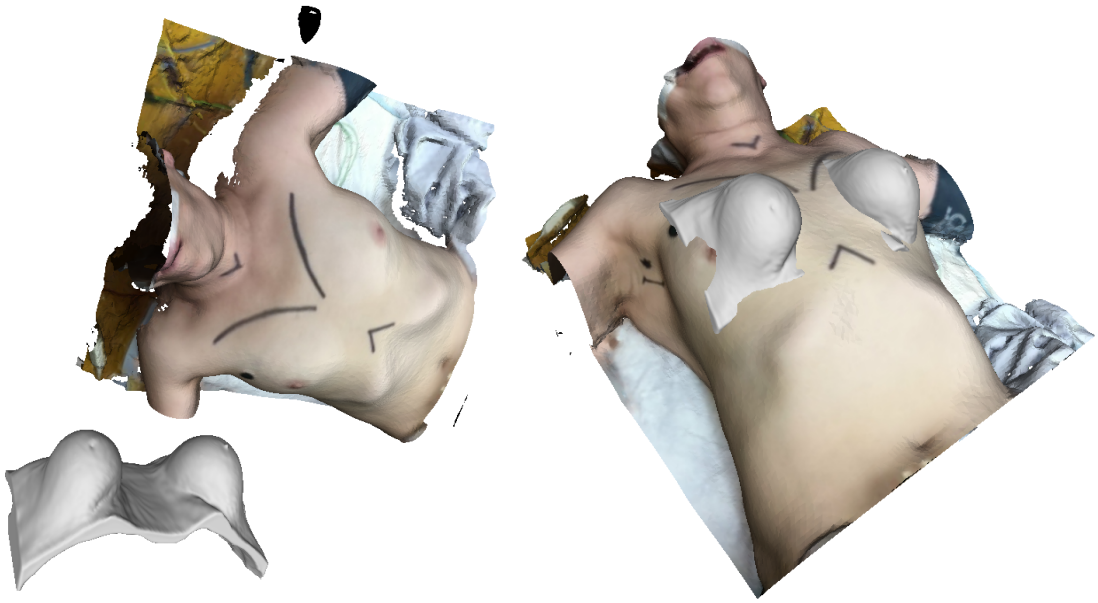

(a) (b)

Figure 38: The segmented skin corresponds to the uncolored mesh while the textured one corresponds to the surface acquisition. (a) Surface acquisition position before registration. (b) Surface acquisition position after registration.

will be too extensive to solve the physical equations under surgical time using the classical FEM. One solution is to coarsen the original mesh of the skin, to obtain fewer tetrahedra as an output of the Delauney algorithm. One major drawback of this method is the accuracy loss compared with the original shape. Thus, we used the software InstantMesh [103] to decimate and coarsen the original skin mesh, while trying to preserve boundaries as much as possible. The result is shown in figure 39 and allowed to pass from 308 844 triangles to only 2040. Finally, we used the software Gmsh [80] to generate the volumic mesh made of 3025 tetrahedra displayed in figure 40.

5.4 A novel breast model

The breast model we developed rests upon:

- A rigid pectoral muscle described by the domain Ω_{muscle}. As we do not intend to deform the pectoral muscle, we only extracted the surface in contact with the breast. This hypothesis has been also chosen if a few other studies [34, 35, 62]. Hence, in several others, the pectoral is essential for the simulation and will strongly influence the final breast shape [76]. But for the scope of this research in making a model as simple as it could be, having a rigid pectoral will drastically limit the complexity of the problem.

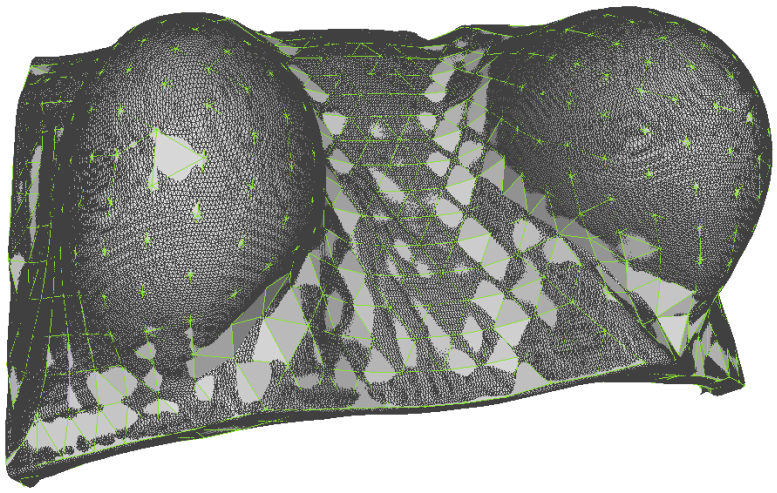

Figure 39: 3D surface mesh of the breast skin after segmentation and reconstruction in wireframe grey (308 844 triangles). 3D surface mesh of the breast skin after coarsening using the InstantMesh software in wireframe green (2.040 triangles) while preserving boundaries.

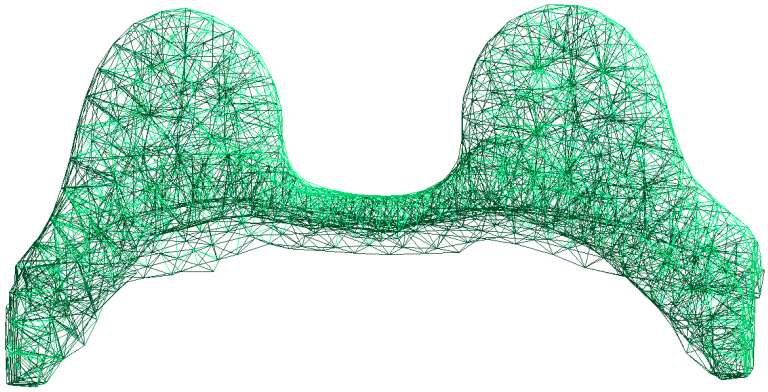

Figure 40: 3D volumic mesh of the breast using the software Gmsh resulting in 3025 tetrahedra.

- A FEM model of the breast volume. The breast domain is denoted by Ω_{breast} while the domain boundaries are indicated by Γ_{breast}. The domain Γ_{breast} is subdivided into 3 sub-domains $\Gamma = \Gamma_{\text{inner}} \cup \Gamma_{\text{skin}} \cup \Gamma_{\text{ligament}}$. In this model, we assume having a single material to represent the glandular and adipose tissues. This hypothesis is quite common in the litterature [34, 35, 152]. Despite a known non-linear anisotropic heterogeneous behavior, we chose to model the breast using an isotropic Hooke's law coupled with corotational strains [160]. A heterogeneous model could have handled more complex behavior and maybe better represent the breast behavior by using more parameters, hence, increasing the uncertainty on those. Similarly, a non-linear material model could have expanded the deformation space but at the cost of solving a more complex system, increasing the computational cost. Finally, anisotropy would have allowed favoring a deformation direction at the cost of adding extra parameters that are not extensively studied in the literature.

$$\begin{aligned} -\nabla \cdot \boldsymbol{\sigma} &= \boldsymbol{f} \text{ in } \Omega_{\text{breast}}, \\ \boldsymbol{\sigma} &= \lambda \operatorname{tr}(\boldsymbol{\varepsilon}) \boldsymbol{I} + 2\mu\boldsymbol{\varepsilon} \\ \boldsymbol{J} &= \boldsymbol{R}_{qr} \cdot \boldsymbol{\varepsilon} \\ \boldsymbol{\varepsilon} = \boldsymbol{R}_{qr}^{-1} \boldsymbol{J} &= \begin{bmatrix} 1+\varepsilon_{xx} & 2\varepsilon_{xy} & 2\varepsilon_{xz} \\ 0 & 1+\varepsilon_{yy} & 2\varepsilon_{yz} \\ 0 & 0 & 1+\varepsilon_{zz} \end{bmatrix} \end{aligned} \tag{75}$$

  Where $\boldsymbol{\sigma}$ is the stress tensor, $\boldsymbol{f}$ is the body force per unit of volume, μ and λ are Lame elasticity parameters for the material in Ω_{right}, $\boldsymbol{I}$ is the identity tensor, tr is the trace operator on a tensor, $\boldsymbol{J}$ is the displacement matrix decomposed with the QR method in order to extract separately a rigid rotation $\boldsymbol{R}_{qr}$ and the deformation matrix ϵ made of the different values $\boldsymbol{\varepsilon}$.

- A FEM model of the skin on Γ_{skin} is only made of triangles. In the same manner, we use the same set of equations for the Ω_{skin} domain but with different Lame elasticity parameters. The Lame coefficients can be expressed with the Young's Modulus (E): $\lambda = \frac{E\nu}{(1+\nu)(1-2\nu)}$ and Poisson's ratio (ν): $\nu = \frac{E}{2(1+\nu)}$. A perfectly incompressible isotropic material deformed elastically at small strains would have a Poisson's ratio of exactly 0.5. This hypothesis has been vastly used for breast simulations, especially for breast compression simulations. In this study, to avoid additional numerical complexity during the optimization, we assumed that the breast was nearly incompressible, meaning that $\nu_{\text{breast}} = \nu_{\text{skin}} = 0.45$, while E_{breast} and E_{skin} will be optimized in the next section.

- A 1D ligament constraining the breast movement. In addition to the pectoral, [144] describes a deep ligament between the inside part of the breast boundaries and the pectoral muscle (figure 47). For each DOF of the ligament (belonging to Γ_{ligament}), we used the ICP to find the closest point on the domain Ω_{muscle}. Hence, we prescribed for each DOFs a constraint violation where the intensity of the forces by $\lambda = -\frac{1}{c}(\boldsymbol{x} - d\boldsymbol{v})$.

Where $\boldsymbol{x}$ and $\boldsymbol{v}$ are the positions and velocities of the DOFs, c and d are, respectively, the compliance and damping ratio. The damping ratio is fixed to 0 and the compliance to $1E^{-}8$ m/N, enforcing a strong attachment between the DOFs and the pectoral.

- Sliding boundary conditions to reproduce the sliding behavior of the breast on the pectoral. The contact between the breast and the pectoral has been poorly studied. Hence, it is difficult to obtain physical quantities from the literature, such as friction coefficients. Even if available, the contact computation would negatively impact the run-time and stability of our simulation. To imitate the contact between the pectoral and the breast, we used the ICP to find the closest point from the breast inside (Γ_{inner}) to the pectoral muscle (Γ_{muscle}). Once the correspondence is established, we used a compliant formulation described in [217] to mimic in a computationally stable manner the sliding between the 2 surfaces.

  To summarize, the model uses Hooke's law with a corotational strain formulation for the breast (including the adipose and glandular tissues) and the skin. We used the identical Poisson's ratios for the breast and skin of $\nu_{\text{breast}} = \nu_{\text{skin}} = 0.45$, and Young's moduli of each phase E_{breast} and E_{skin} have to be optimized. The ligaments are rigidly attached between the inner part of the breast and the rigid pectoral with considerable compliance of $1E^{-8}$ m/N to stimulate the deep attachment of the ligament. Finally, a compliant formulation is used to ensure the sliding of the inner breast on the pectoral muscle.

5.5 Simulation pipeline

We chose the Simulation Open Framework Architecture (SOFA [69]) to perform our simulations. SOFA allows for running real-time rendered simulations, which is one objective of our work. In addition, several features were already implemented, such as the ICP or the stable constraints and the corotational strain [160, 217]. We followed the same simulation pipeline as [152], described in figure 41. Namely, the theoretical undeformed configuration is obtained using the inverse method described in chapter 3 by applying gravity in the opposite direction to the sagging breast in the prone configuration. Afterwards, gravity is again applied to estimate the final intra-operative pose. The estimation is compared with the measured intra-operative configuration obtained with a surface acquisition device (assumed to be the gold standard). The comparison is made by calculating the Mean Absolute Error (MAE) described in section 2.4 on the breast surface. If the MAE is superior to the threshold, the pipeline is run again, choosing a different set of mechanical parameters. Otherwise, the estimated supine configuration is close enough to the patient's intra-operative pose.

Two differences can be noted compared with [152]. First, [152] simulated the imaging configuration from the intra-operative one, while we simulated the opposite path. Secondly, [152] computed the difference between the simulated and measured prone configuration to optimize the simulation from stress-free to imaging configuration. We chose a different approach. After evaluating the difference between the simulated and ground truth intra-operative pose, we restart the complete pipeline from the imaging to the intra-operative

estimation. It allows us to optimize the material parameters $[E_{\text{breast}}, E_{\text{skin}}]$ on the complete pipeline and to adjust the stress-free/undeformed configuration.

The simulation (including the 2 simulations, namely, from the prone to undeformed stance and from the undeformed to the supine configuration) takes less than 20 s.

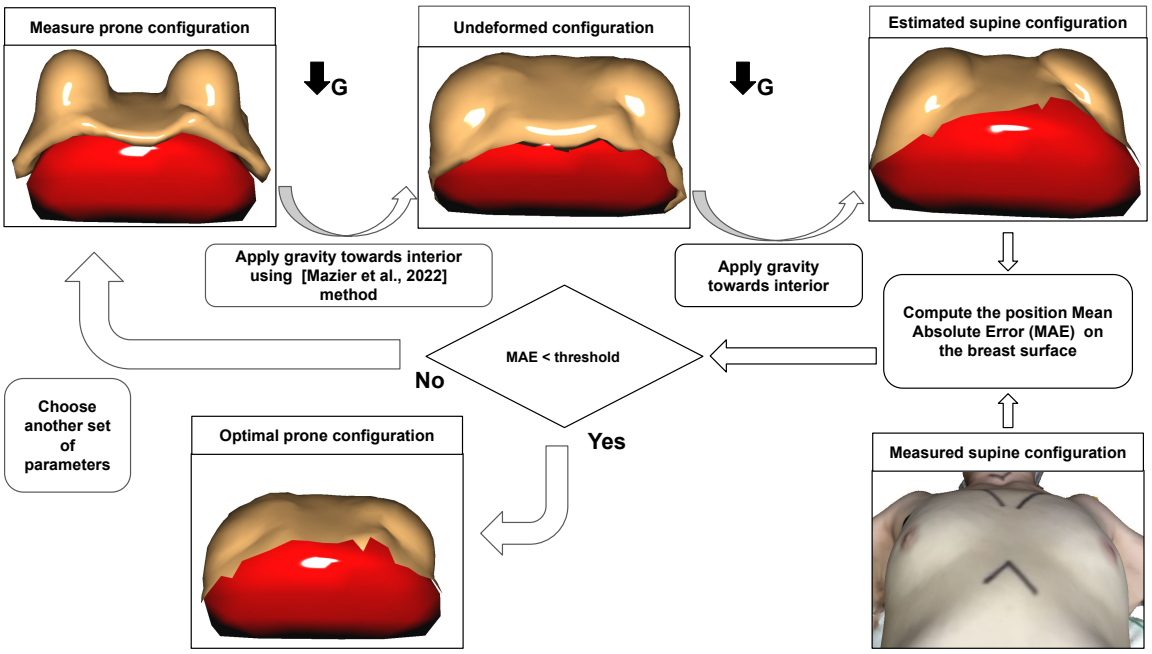

Figure 41: Simulation pipeline for estimating the patient-specific intra-operative (supine) configuration. The pipeline starts on the top left corner, the measured prone configuration geometry is obtained from the MRI by segmentation and 3D reconstruction. Then, the theoretical undeformed configuration is obtained using the inverse method described in section 3 by applying gravity in the opposite direction of the sagging breast. Afterward, gravity is again applied to estimate the final intra-operative pose. The estimation is compared with the measured intra-operative configuration obtained with a surface acquisition device (assumed to be the gold standard). The comparison is made by calculating the Mean Absolute Error (MAE) described in section 2.4 on the breast surface. If the MAE is superior to the threshold, the pipeline is run again, choosing a different set of mechanical parameters. Otherwise, the estimated supine configuration is close enough to the patient's intra-operative pose. Image inspired from [152].

5.6 Optimization

Classical gradient-descent methods are commonly used for optimization. However, they require access to the derivative of the cost function with respect to the (mechanical) parameters. With SOFA, this derivative is not yet available, but extensive work is currently done

to achieve this goal. Conversely to gradient-descent optimizers, derivatives-free optimizers have been vastly used to overcome multi-local solutions. In the category of derivative-free optimizers, among the graphic community, the Nelder-Mead [159] method has been prevalent for large-scale problems. More recently, statistical optimizers, such as the Covariance Matrix Adaptation Evolution Strategy (CMA-ES) have proven to be also reliable. In this study, even if a fair comparison is difficult, we will investigate and compare the 2 methods to observe which one gives the best results for this specific optimization.

Nelder-Mead

The Nelder-Mead method is a nonlinear optimization algorithm using a numerical heuristic method that seeks to minimize a continuous function in a multidimensional space [159]. Also called the downhill simplex method, the algorithm exploits the concept of simplex, which is a polytope of N+1 vertices in an N-dimensional space. Initially starting from a simplex, it undergoes simple transformations during iterations: it deforms, moves, and reduces progressively until its vertices approach a point where the function is locally minimal.

Let f be a function defined on a space of dimension N. Algorithm 4 starts by defining a non-degenerate simplex (generalization of triangles or tetrahedra to arbitrary dimensions) chosen in this space. By successive iterations, the process consists in determining the point of the simplex where the function is maximal for replacing it by the reflection (the symmetrical) of this point with respect to the barycentre of the N remaining points. If the value of the function at this new point is less than all the other values taken at the other points, the simplex is stretched in that direction. Otherwise, if the value of the function at this new point is better than the second worst but worse than the best, we keep this value and start again. Otherwise, it is assumed that the local shape of the function is a valley, and the simplex is contracted on itself. If this still does not give a better point, the simplex is reduced by a homothety centered on the point of the simplex where the function is minimal.

This method has several benefits, such as the unnecessity of evaluating the function derivatives, a simple implementation, efficiency for non-derivative function, a geometric interpretation, and the assurance of obtaining a decreasing series of values. Drawbacks include the difficulty of converging when the definition domain of the function is complex or the minimum is located close to the boundaries. Additionally, it requires an arbitrary initial simplex that can slow down the algorithm if poorly chosen or leads to a performance reduction when the dimension space expands (improved by [77]). Finally, the solution obtained by the method is not necessarily a global optimum.

Covariance Matrix Adaptation Evolution Strategy (CMA-ES)

In the category of statistical optimizers, the Covariance Matrix Adaptation Evolution Strategy (CMA-ES) is an attractive option for non-linear, non-convex black-box optimization problems in the continuous domain. Especially if classical search methods, e.g., quasi-Newton methods (BFGS) and/or conjugate gradient methods, fail due to a non-convex

Algorithm 4 Nelder-Mead algorithm. The criterion is usually a tolerance between 2 iterations on the function to minimize $f(x_r)$ or the value x_r itself. Standard values are $\lambda = 1, \gamma = 2, \rho = 0.5, \sigma = 0.5$

$S^0 \leftarrow S^{\text{ini}} = \{x_1, x_2, ..., x_{N+1}\}$ ▷ S^{ini} is an initial simplex of dimension $N+1$ $\{x_1, x_2, ..., x_{N+1}\}$
while criterion is not **do**
    sort($f(S^0)$) ▷ ascending sort of the values of f evaluated on the simplex $f(x_1) \leq f(x_2) \leq ... \leq f(x_{N+1})$
    $x_0 \leftarrow$ center(S_0) ▷ compute the barycentre x_0 based on the inital simplex (excluding the last value (x_{N+1}))
    $x_r \leftarrow x_0 + \alpha(x_0 - x_{N+1})$
    if $f(x_1) \leq f(x_r) \leq f(x_N)$ **then**
        $x_{N+1} \leftarrow x_r$
    end if
    if $f(x_r) < f(x_1)$ **then**
        $x_e \leftarrow x_0 + \gamma(x_r - x_0)$
        if $f(x_e) \leq f(x_r)$ **then**
            $x_{N+1} \leftarrow x_e$
        else
            $x_{N+1} \leftarrow x_r$
        end if
    end if
    if $f(x_r) \geq f(x_N)$ **then**
        $x_c \leftarrow x_0 + \rho(x_{N+1} - x_0)$
        if $f(x_c) < f(x_{N+1})$ **then**
            $x_{N+1} \leftarrow x_c$
        else
            $x_i \leftarrow x_1 + \sigma(x_i - x_1)$
        end if
    end if
end while

or rugged search landscape (e.g., sharp bends, discontinuities, outliers, noise, and local optima). The CMA-ES method was created in 1965 and made popular in 2005 [9].

Similar to quasi-Newton methods, the CMA-ES is a second-order approach to estimating a positive definite matrix in an iterative procedure (more precisely: a covariance matrix, i.e., on convex-quadratic functions, closely related to the inverse Hessian). Unlike quasi-Newton methods, CMA-ES does not use or approach gradients and does not assume or even require their existence. This makes the algorithm applicable to non-smooth and even non-continuous problems. It is a reliable and competitive evolutionary algorithm for local and global optimization.

CMA-ES employs an evolutionary strategies using a set of μ parents to produce λ children. To produce each child, ρ parents are recombined. Once produced, the children are mutated, usually by adding a random variable following a normal distribution. The selection step can be applied either only to the children or to the set of children and parents. The algorithm relies on the adaptation, during the iterations, of the variance-covariance matrix of the multi-normal distribution used for the mutation. The complete methodology of the algorithm and its subtleties are explained [92].

The application of CMA-ES does not require tedious parameter tuning. In fact, the choice of internal strategy parameters is considered part of the design of the algorithm. For the application of CMA-ES, an initial solution, an initial standard deviation, and possibly the end criteria (e.g., a function tolerance) are the only parameters defined by the user.

In this optimization, the cost function is the MAE between the estimated and observed prone position, previously defined in section 2.4. To have a general idea of the cost function distribution, we ran 2000 simulations using an uniform distribution for E_{breast} and E_{skin} to plot a heatmap of the objective function shown in figure 42. Several observations can be made from the figure. First, we observe a region where the MAE is smoothly decreasing if the values of E_{breast} is decreasing from 2 to almost 0 kPa and E_{skin} also decreases from 500 to 100 kPa. Secondly, an optimal region seems to appear for values between 0.1 to 0.5 kPa for E_{breast} and from 20 to 40 kPa. Then, we observe critical areas, especially on the bottom left corner ($E_{\text{breast}} < 0.2$ and $E_{\text{skin}} < 20$ kPa) and the bottom right corner ($E_{\text{breast}} > 1.2$ and $E_{\text{skin}} < 30$ kPa) which corresponds to the limits of the admissible values for elastic parameters. Finally, a last area comprised between 120 to 50 kPa for E_{skin} and 0.6 to 1.25 kPa for $E_{\text{breast}}$is problematic and holds several local minima.

In figure 43, we performed a first optimization using an initial guess close to the optimal solutions. For both optimizers, we set the initial guess to $[E_{\text{breast}}, E_{\text{skin}}] = [0.3, 75]$ kPa. For the CMA-ES optimizer, we used a variance of $[\sigma_{\text{breast}}, \sigma_{\text{skin}}] = [0.1, 50]$ kPa and stop the algorithm when reaching a MAE prior to 4.2 mm. For the Nelder-Mead optimizer, the stopping criterion was fixed to an MAE difference of $1E^{-}3$ mm between two consecutive iterations. The results are satisfactory for the CMA-ES algorithm that succeeded in converging in 13 iterations, exploring a wide parameter space. Conversely, the Nelder-Mead algorithm stopped after 10 iterations and did not reach a suitable MAE. Despite choosing different convergence criteria, we did not succeed in obtaining better results for the Nelder-Mead algorithm. Several explanations are possible. First, the initial simplex was maybe

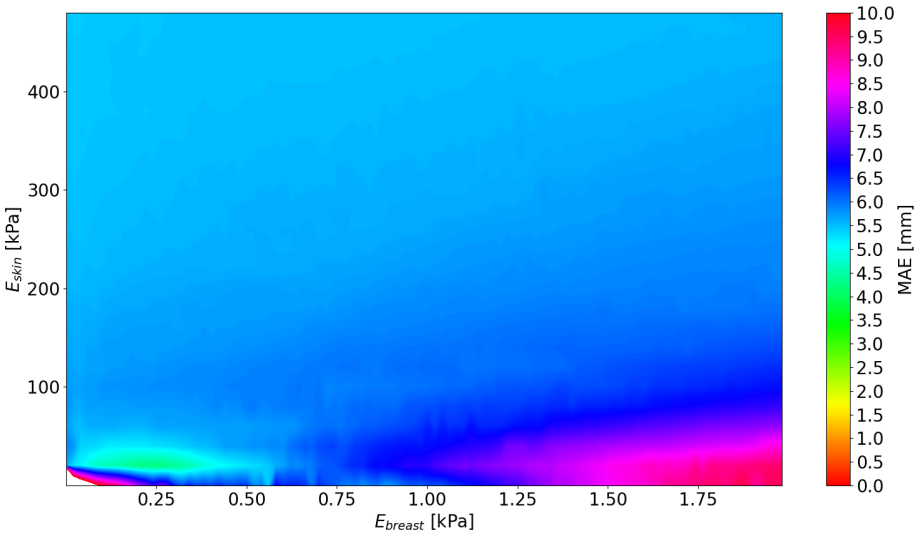

Figure 42: Plot of the cost function (MAE) when using an uniform distribution of 2500 values for E_{breast} and E_{skin}.

inadequately chosen, and the algorithm could not explore further. Another hypothesis could be that the algorithm got trapped in a local minimum (valley), as is usually the case for gradient-descent algorithms.

Hence in the rest of the study, we will only consider the CMA-ES optimizer. In table 10, we summarize the different initial conditions and variance, the different values minimizing the MAE found by the optimizer, and the number of iterations needed. Due to the statistical nature of the algorithm, an average of the output has been performed for ten sequences.

We can observe the following points:

- The optimized values of $E_{\text{breast}}^{\text{optimized}}$, $E_{\text{skin}}^{\text{optimized}}$ are consistent with the literature. For the breast elasticity, similarly to [152], we obtain a value between 0.26 and 0.35 kPa, belonging to the inferior range of the breast Young's modulus state-of-the-art [0.3 kPa: 6 kPa]. For the skin elasticity, we obtain a wide range of optimized Yong's modulus between 20.50 and 30.83 kPa. According to the literature, the range of skin Young's modulus is [7.4 kPa: 58.4 kPa], placing our optimized value in the middle range.

- By trying different initial values and variances, we are testing the sensibility of the CMA-ES algorithm to the initial conditions. Indeed, most gradient-descent optimizers do not support an initialization distant from the optimized solutions or stop in local minima. In this application, CMA-ES seems to converge to several optimal configurations depending on the initial values and standard deviation of the parameters. Indeed, between the two first rows of table 10, we kept the same initial parameters

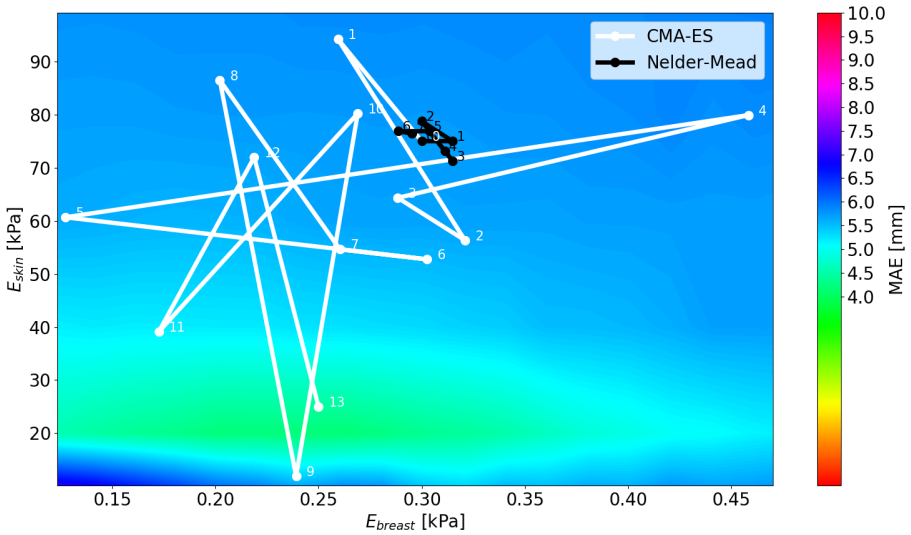

Figure 43: Result of the first optimization by choosing an initial guess close to the optimal solutions. The path described by the Nelder-Mead algorithm is drawn in black while the path used by CMA-ES is drawn in white color. For both optimizers, we set the initial guess to $[E^{\text{initial}}_{\text{breast}}, E^{\text{initial}}_{\text{skin}}] = [0.3, 75]$ kPa. For the CMA-ES optimizer, we used an initial variance of $[\sigma^{\text{initial}}_{\text{breast}}, \sigma^{\text{initial}}_{\text{skin}}] = [0.1, 50]$ kPa and stop the algorithm when reaching a MAE prior to 4.2 mm. For the Nelder-Mead optimizer, the stopping criterion was fixed to an MAE difference of $1E^{-}3$ mm between two consecutive iterations.

close to the optimized parameters but increased the initial standard deviation. The results of choosing more significant initial standard deviations are an increase in the number of iterations (twice in this case), stiffer optimized parameters, and a decrease of 0.1 mm of the MAE. Obtaining a larger number of iterations is expected as expanding the initial standard deviation values results in increasing the search domain, hence, demanding more time to converge. However, expanding the search domain enabled obtaining a lower MAE value. It indicates that limited initial standard deviation values restrict the search space, hence, ignoring possible better solutions.

On the third row of table 10, we drastically increased the initial values of the mechanical properties. Firstly, it leads to an expected severe increase in the number of iterations (101 compared to 15 or 30). Secondly, we obtain similar values of the MAE but, again, diverse values of the optimized parameters. It indicates that multiple combinations of parameters can lead to comparable error measures. The influence of the rheological parameters will be studied deeper in the section 5.7.

- We did not succeed in obtaining an MAE lower than 4 mm, as displayed in table 10.

$E_{\text{breast}}^{\text{initial}}$	$E_{\text{skin}}^{\text{initial}}$	$\sigma_{\text{breast}}^{\text{initial}}$	$\sigma_{\text{skin}}^{\text{initial}}$	$E_{\text{breast}}^{\text{optimized}}$	$E_{\text{skin}}^{\text{optimized}}$	MAE [mm]	# iterations
0.3	75	0.1	50	0.26	20.50	4.17	15
0.3	75	0.3	100	0.32	22.72	4.00	30
1.5	120	1.5	100	0.35	30.83	4.02	101

Table 10: CMA-ES optimization of E_{breast} and E_{skin} to minimize the Mean Absolute Error (MAE). Different initial values of the parameters ($E_{\text{breast}}^{\text{initial}}$, $E_{\text{skin}}^{\text{initial}}$) in [kPa] and standard deviations ($\sigma_{\text{breast}}^{\text{initial}}$, $\sigma_{\text{skin}}^{\text{initial}}$) in [kPa] have been selected. The results averaged over 10 sequences are the optimized Young moduli of the breast and skin $E_{\text{breast}}^{\text{optimized}}$, $E_{\text{skin}}^{\text{optimized}}$ in [kPa] and the number of iterations (# iterations) minimizing the MAE in [mm].

The error is acceptable and comparable with the literature. However, we expect that more complex material laws such as Mooney-Rivlin or Neo-Hooke materials could decrease the MAE by better fitting the surface acquisition. This would indicate that the corotational strain is maybe not sufficient to model such large deformations, and a more classical deformation measure may be more suitable. Finally, we used a simplified and coarsen mesh but choosing a finer mesh might have led to better results (at the cost of a higher computation time).

5.7 Sensitivity analysis

In the previous section, we have shown that we were able to find suitable values for E_{breast} and E_{skin} to minimize the error between the estimated and measured supine configuration. Hence, we want to quantify the influence of the mechanical properties on the final breast shape. Consequently, we used Monte Carlo (MC) simulations which use a stochastic distribution to understand the parameters' influence.

Without any prior information on the two parameters E_{breast} and E_{skin}, we assumed that they were both following a normal distribution with a mean value $\overline{E}$ and standard deviation σ:

$$E_{\text{breast}} \sim N(\overline{E_{\text{breast}}}, \sigma_{\text{breast}}^2),$$
$$E_{\text{skin}} \sim N(\overline{E_{\text{skin}}}, \sigma_{\text{skin}}^2).$$

We chose $\overline{E_{\text{breast}}} = 0.32$ and $\overline{E_{\text{skin}}} = 23$ kPa as they are close to the optimal solution found previously. To slightly perturb the parameters, we chose the following standard deviations $\sigma_{\text{breast}}^2 = 0.4$ and $\sigma_{\text{skin}}^2 = 40$. The standard variations are big enough to allow large variations of the parameter space. We drew 1000 samples of each parameter and ran the simulation with the stochastic parameter sets.

The results obtained are shown in figures 45 and 46. In figure 45, we observe what seems to be a smooth surface without any jumps and a drop of the MAE close to the

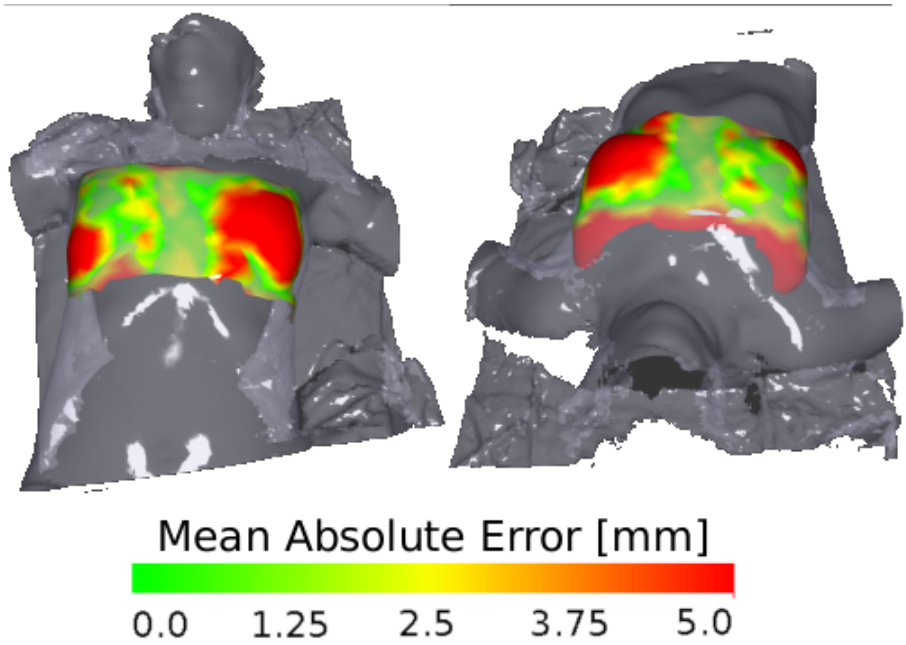

Figure 44: Numerical simulations results for the optimized parameters $E_{\text{breast}}^{\text{optimized}} = 0.32$ kPa and $E_{\text{skin}}^{\text{optimized}} = 22.72$ kPa. The colorbar is displaying the absolute distance error between the estimated and measured (in grey) prone configuration.

optimal zone identified previously. Unfortunately, as shown in the last section, several local minima surround this optimal zone. It likely indicates that a gradient-based optimizer would probably have been an inadequate tool encouraging the choice of the CMA-ES optimizer. As shown in figures 45 and 46, the mechanical parameters have a strong impact on the resulting shape of the breast. Indeed, by taking extremes values of our normal distributions e.g. $E_{\text{breast}} = 0.8$ kPa and $E_{\text{skin}} = 80$ kPa, the MAE is equal to 6.56 mm approximately 2.5 mm off the optimal MAE.

A conclusion from the sensitivity analysis is that after running 1000 MC simulations with the distributions $E_{\text{breast}} \sim N(0.32, 0.4)$ kPa and $E_{\text{skin}} \sim N(23, 40)$ kPa we obtain a Gaussian distribution of mean 5.70 mm and a standard deviation of 0.48 mm. The mean is higher than the MAE found by optimizing the parameters, but as we settled the mean of the parameter's distributions slightly off the optimal values, this result appears ordinary. Hence, the standard deviation of the MAE distribution indicates that a respective error of $\pm$ 40 kPA or $\pm$ 0.4 kPA for the stiffness of the skin and breast could have a 68 % of chance of creating an error less than 0.48 mm. Thus, the parameter identification allows to a decrease the MAE to the maximum but a slight error on the parameters will still lead to an acceptable MAE (as long as degenerated parameters are not selected).

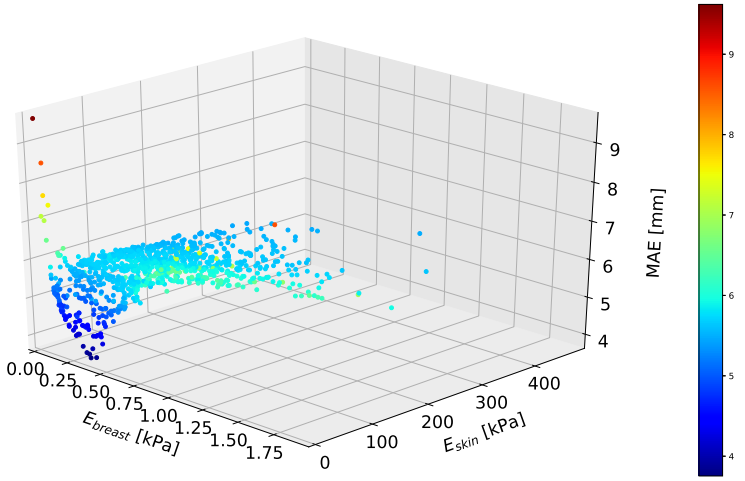

Figure 45: 3D plot of the MAE with 1000 MC simulations. The 2000 parameters were sampled from the following normal distributions: $E_{\text{breast}} \sim N(0.32, 0.4)\,\text{kPa}$, $E_{\text{skin}} \sim N(23, 40)\,\text{kPa}$.

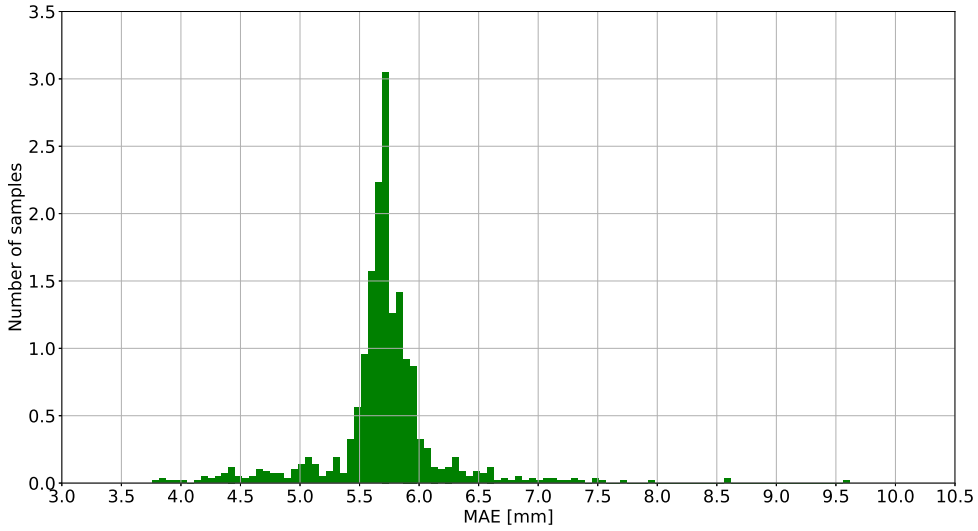

Figure 46: MAE statistics of the 1000 MC simulations obtained from figure 45.

5.8 Influence of the circum-mammary ligament

We previously showed that the breast shape was slightly sensitive to the rheological parameters of the model. In this section, we briefly study the influence of the circum-mammary ligament on the simulation. This ligament is described in [144] and described as a deep attach between the breast and the pectoral muscle. To do so, we fixed the optimal mechanical properties and only changed the thickness and position of the ligaments, as shown in figure 47.

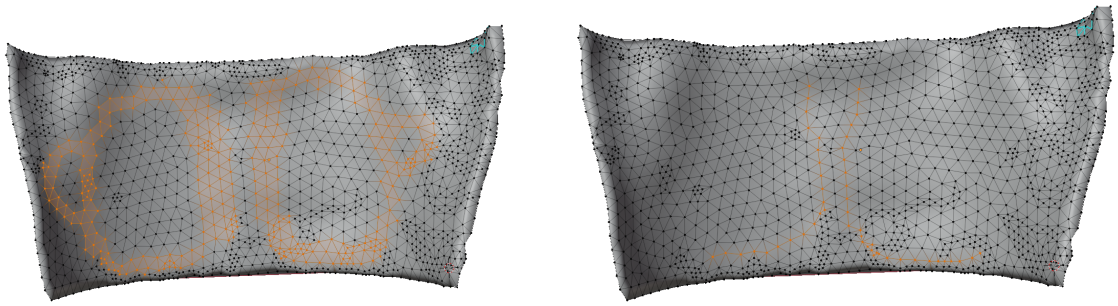

(a) (b)

Figure 47: Nodes of the inner breast side defining the infra-mammary ligament geometry (in orange). (a) Full ligament as described in [144]. (b) Thinner ligament.

The effects of the ligaments on the simulation are shown in figure 48. For the ligament in the configuration described in [144] (figure 47a), we obtain the same results as mentioned in section 5.6. On the contrary, in figure 47b, the ligament is thinner without describing a full circle sustaining the inner breast. In figure 48b, by choosing the same material properties used in the simulation 47a, the effect of the ligament is strongly remarkable. We first observe a higher MAE, especially close to the sternal region and breasts. Indeed, as the ligament is not constraining the breast as strongly as before (almost fixed to the sternum), the breasts can freely move away from the sternum causing too large deformations on the sides. Quantitatively, the MAE is bigger for the thin ligament with a value of 8.24 mm compared with a MAE of 4.00 mm for the full ligament.

One conclusion could be drawn from this experiment. The infra-mammary ligament shape could be as important as the material properties of the breast. This opens a question about the shape or topological optimization of the ligament. Unfortunately, this information is not currently available with classical MRIs and a finer resolution would be needed to extract the real geometry.

5.9 Future work and outlook

For future work, we utilized the complete geometry for the simulation by including the mammary gland and the tumor segmented in the prone configuration. As we only optimize the surface (skin), we could technically optimize the mechanical properties of the gland

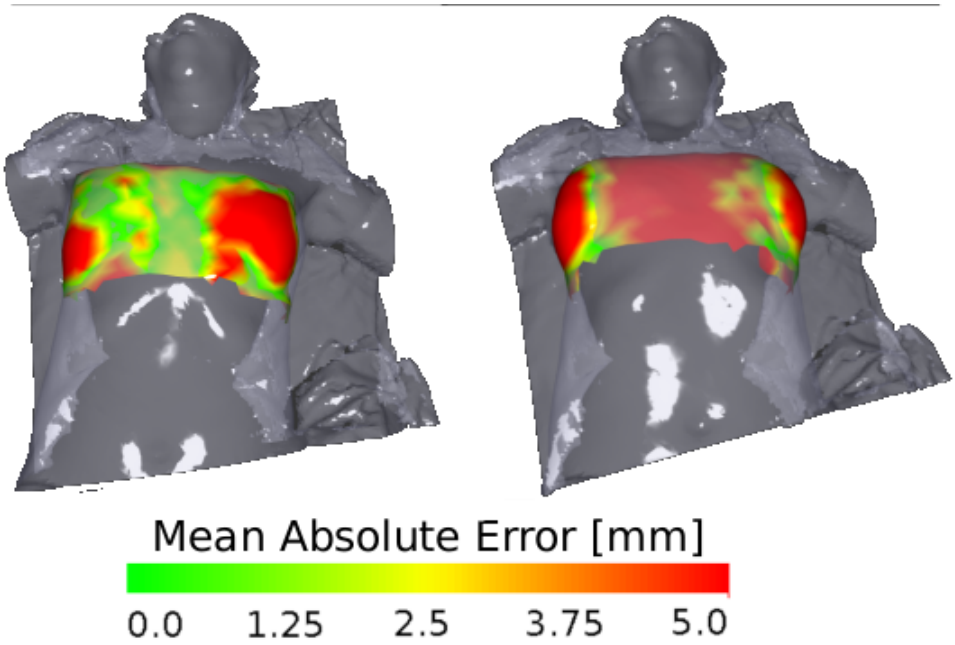

Figure 48: Simulation from the prone to the supine configuration with optimized mechanical properties. On the left, the simulation result with the full ligament design (corresponding to figure 47a). On the right, the simulation result with the thinner ligament design (corresponding to figure 47b).

and tumor, but this could lead to unrealistic values. As a first approximation, we used mechanical parameters found in the literature for simulating the gland and tumor behavior. As shown in figure 49, we can estimate the intra-operative configuration with the previously optimized parameters and predict the tumor position.

Despite reaching the convergence of the simulation, it is impossible to validate the tumor position with the current dataset. Indeed, surface acquisitions only allow measuring the displacement occurring on the skin. To validate the estimated position of the tumor, volumic imaging, such as MRI is needed for validation (and/or optimization). Therefore, this imaging procedure is not clinically relevant for surgeons, and another investigation is required to validate our model.

This study is still in its early stages, and more validation or improvement steps could be implemented. For the validation steps, a mesh convergence analysis could quantify the compromise between computation time and accuracy. Additionally, only two optimizers were tried with the common specificity of gradient-free, and Nelder-Mead might have been improved by choosing a better initial simplex. Therefore, we focused on using CMA-ES which allowed an efficient optimization without tuning any specific parameters. A deeper study could investigate the efficiency of gradient-descent algorithms or other gradient-free methods. Indeed, for the moment, the optimizer is slow to converge (especially if initial

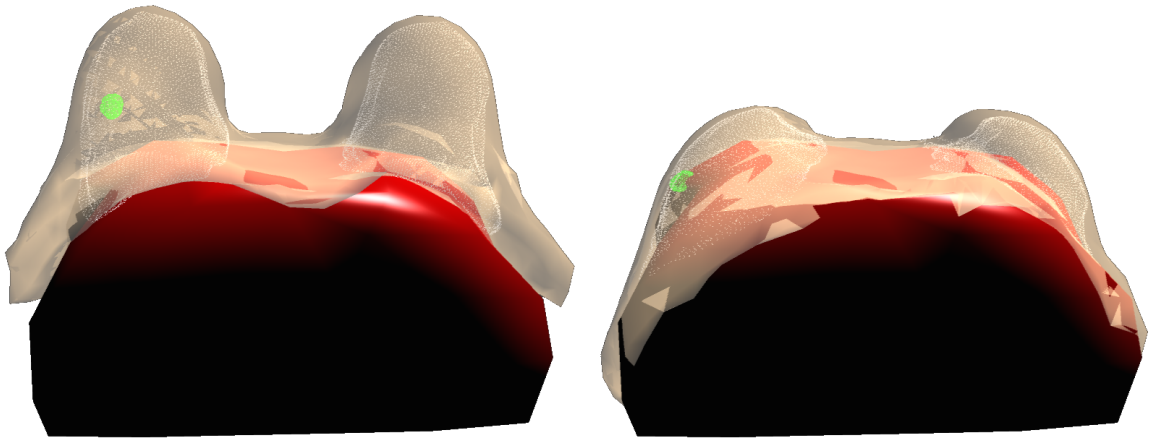

(a) (b)

Figure 49: Complete simulation including the skin and the adipose tissues (in yellow transparent), the mammary gland (white dots), and the tumor (green dots). (a) Imaging configuration of the patient (prone). (b) Estimated intra-operative configuration (supine).

parameters are distant from the optimal ones), making practical usage of the software problematic. Further, as shown in figure 44, compared with the right breast, the MAE is lower on the left breast. This indicates that choosing different material properties for the left and right breast (as in [152]) could be relevant. In addition, we designed the breast using a linear elasticity model to describe the stress-strain relation. As far as concerned, the co-rotational model allowed sufficient deformations to reach the supine configuration. However, more complex material models such as Mooney-Rivlin or Yeoh could be tested to (maybe) increase the deformation space to predict an accurate stress field. Thanks to our contribution in section 4, this could be implemented effortlessly and enable different interpolation schemes and degrees. Plus, the muscle was assumed to be a rigid body, even if stiffer than the breast, is still highly deformable. Indeed, neglecting the deformation of the muscle during the repositioning of the volunteer (as demonstrated in [76]) and the possible misalignments during the rigid registration process may impact the estimates in prone and supine tilted breast configurations. Finally, our choice of using FEM is also questionable while other methods such as cutFEM [66] or IGA [105] (IsoGeometric Analysis) could alleviate the meshing problem of complex geometries such as the organs composing the breast

5.10 Conclusion

In this last section, we presented a complete pipeline, starting from the image to an optimized, patient-specific breast model. We first demonstrate the manual process to obtain the patient's biomechanical model from the MRI in the prone pose. Then, using the CMA-ES

optimizers, we were able to retrieve the personalized mechanical properties of the patient's breast. Hence, we studied the sensibility of the optimizer to the initial parameters and the rheological properties. Finally, the last study demonstrated the importance of the infra-mammary ligament in the simulation process. We were finally able to include the mammary gland and tumor in the simulation but cannot evaluate the accuracy of our prediction due to a lack of data.

The final results are an MAE of 4.00 mm for the mechanical parameters $E_{\text{breast}} = 0.32$ kPa and $E_{\text{skin}} = 22.72$ kPa. The mechanical parameters are congruent with the literature found in [76, 152]. The simulation (including finding the undeformed and prone configuration) takes less than 20 s. The CMA-ES optimizer converges on average between 15 to 100 iterations depending on the choice of initial parameters for a total time between 5 to 30 mins. The final MAE is slightly superior to the one found by [152], but to our knowledge, our model is the fastest to converge to such low MAE. Therefore, depending on the final application, a compromise between accuracy (thus complexity of the model) and time has to be found.

6 Conclusion

In this thesis, we have addressed the problem of patient-specific simulations for breast-conserving surgery purposes. Specifically, we were interested in developing a complete pipeline beginning from the medical imaging in the prone configuration to the tumor movement prediction in the supine stance. Most importantly, the numerical model had to produce an accurate and patient-specific three-dimensional virtual representation of the breast deformations for the medical team. It includes an intuitive interface to visualize the final position of the tumor. The model also had to render stable solutions within a time frame that meets the requirements of a clinical environment. Finally, the model was designed in an effort of minimizing the next development effort and ensure minimum involvement from the medical staff.

We began our work with a thorough review of breast anatomy and cancer characteristics. This allowed not only the understanding of the causes of breast cancer but also identifying the several main organs involved in the simulation. Then, we provided the basic theoretical knowledge of hyperelasticity principles and established the finite element method popular in a wide range of biomechanics applications. We quickly realized that implementing quasi-real-time and interactive models was inconceivable with most of the software currently available. These tools were just inadequate for our application, requiring the intra-operative data to be injected into the simulation process to assess the prediction error. Those design constraints drove us to utilize the open-source software SOFA [70], perfect for filling the different objectives.

In this work, we first proposed to tackle a subproblem of breast-conserving surgery: patient-specific preoperative surgical drawings that are a common foundation for any surgery. To map the personalized patterns, we first created a template model embedding the surgical designs of a specific surgery (breast-conserving surgery in this case). To that extent, we used rigging and skinning methods to atone for articulated movements of the patients sustained by blendshapes basis to address the intra-patient variability. Through a registration process using the ICP, we were able to map the surgical patterns in less than 3 s with a precision comparable to the state-of-the-art breast-conserving surgery on 7 patients in two completely different poses. Tested by surgeons, our application could become the future pedagogic tool for training junior surgeons with preoperative surgical drawings.

In the breast-conserving surgery pipeline, we quickly noticed an essential missing element. When the imaging is acquired, gravity acts on the breast, responsible for the sagging shape observed in the MRI antennae. Therefore, in the intraoperative configuration, gravity operates in the opposite direction. This motivated the investigation of the undeformed configuration corresponding to the posture in-between prone and supine after the removal of gravity. After inquiry, we did not find any tool to perform this simulation. Hence, using the FEniCS project, we implemented an open-source code to obtain the undeformed configuration with the sole condition of describing the problem (deformed geometry, material model and properties, boundary conditions). We demonstrated the use of our code on benchmark cases and experimental data with a highly deformable PDMS beam. The

code can sustain any complex material model and is publicly available, demonstrating an incompressible hyperelastic mixed formulation[6].

One requirement for accurately simulating soft tissues is to use advanced material models that best describe the behavior. We quickly noticed a lack of hyperelastic material models and finite element topologies in SOFA. Additionally, implementing a novel material law involved excavating into the source code (in C++) and using tensorial derivation to obtain the local residual vector and stiffness matrix for every element topology. We chose to create the SOniCS[7] plugin to address this issue. By only describing the strain density energy function using the FEniCS UFL language, the element topology, and the interpolation scheme and degree, the user can simply generate a C code compatible with SOFA. After properly benchmarking our implementation with SOFA and FEBio using manufactured solutions and cantilever beams example. We demonstrated the full capabilities of our plugin using an 8 invariant anisotropic HO model for a surgical haptic simulation.

Finally, we assembled all the previous compositions to solve the core problem of this thesis. We created from the medical images a pipeline for manually segmenting and creating the patient-specific breast model. Using our custom implementation to find the undeformed configuration, we were able to predict the intra-operative state with the finite element method. We used the registration method developed in the preoperative drawing application to measure the error between our prediction and the clinical data. Based on this metric (Mean Absolute Error), we optimized the mechanical properties of the model to fit the patient's surface acquisition.

Overall, despite a slow optimization process, the simulation can converge in less than 20 s with an accuracy comparable to the state-of-the-art. The latest results showed the possibility of predicting the tumor position based on routine clinical imaging, only using a surface acquisition in the intra-operative configuration. Nevertheless, the accuracy of the tumor position is still to be assessed with an adequate dataset.

Future work

Throughout this work, manual operations still have to be accomplished, such as tissue segmentation or establishing the finite element model. One aim of this work would be to propose a fully automated pipeline comparable to [76]. Therefore, more knowledge is needed, especially in automatic segmentation through deep learning methods. Despite acceptable results, we exclusively validated our simulations on one patient, and a more specific cohort would be necessary to assess the capabilities of our application. Still, during the validation process, we were able to estimate the final position of the tumor but impossible to validate with only surface acquisitions. A more thoroughgoing dataset involving MRIs in prone configuration would be necessary. Therefore, acquiring data in this specific stance is not part of the clinical routine and could be challenging to acquire. The optimization method employed showed good performance despite a slow convergence while extensive work has to

[6] `https://github.com/Ziemnono/fenics-inverseFEM`

[7] `https://github.com/mimesis-inria/caribou/tree/FeniCS-features`

be carried out to improve the convergence rapidity and create a practical application in a clinical setting. Finally, despite the prediction of the tumor position, further investigation has to be carried out to empower the surgeon's intuition. Augmented reality is the key to such an opening, while extensive work has already been initiated to broadcast SOFA in a Virtual Reality setting. One future aim would likely be to witness if our applications can be transferred to such futuristic technology. Finally, the surface acquisition is a static mesh and could be replaced by a dynamic acquisition to capture the patient's movements during the surgery with a real-time registration and optimization process.

References

[1] J.E. Adkins. "A reciprocal plane property of the finite plan strain equations". In: *Journal of the Mechanics Physics of Solid* 6.4 (1958), pp. 267–275 (page 50).

[2] J. Ahrens, Berk Geveci, and Charles Law. "ParaView: An End-User Tool for Large Data Visualization". In: *Visualization Handbook* (Jan. 2005) (pages 77, 82).

[3] Jérémie Allard, Hadrien Courtecuisse, and François Faure. "Chapter 21 - Implicit FEM Solver on GPU for Interactive Deformation Simulation". In: *GPU Computing Gems Jade Edition*. Ed. by Wen mei W. Hwu. Applications of GPU Computing Series. Boston: Morgan Kaufmann, 2012, pp. 281–294. ISBN: 978-0-12-385963-1. DOI: https://doi.org/10.1016/B978-0-12-385963-1.00021-6. URL: https://www.sciencedirect.com/science/article/pii/B9780123859631000216 (page 78).

[4] M. S. Alnaes et al. "The FEniCS Project Version 1.5". In: *Archive of Numerical Software* 3 (2015). DOI: 10.11588/ans.2015.100.20553 (pages 79, 82).

[5] Martin S. Alnæs et al. "Unified Form Language: A Domain-Specific Language for Weak Formulations of Partial Differential Equations". In: *ACM Trans. Math. Softw.* 40.2 (2014). ISSN: 0098-3500. DOI: 10.1145/2566630. URL: https://doi.org/10.1145/2566630 (pages 55, 82).

[6] Todd Arbogast, Zhen Tao, and Chuning Wang. "Direct serendipity and mixed finite elements on convex quadrilaterals". en. In: *Numerische Mathematik* 150.4 (Apr. 2022), pp. 929–974. ISSN: 0945-3245. DOI: 10.1007/s00211-022-01274-3. URL: https://doi.org/10.1007/s00211-022-01274-3 (visited on 07/05/2022) (page 84).

[7] Douglas N. Arnold and Gerard Awanou. "The Serendipity Family of Finite Elements". en. In: *Foundations of Computational Mathematics* 11.3 (June 2011), pp. 337–344. ISSN: 1615-3383. DOI: 10.1007/s10208-011-9087-3. URL: https://doi.org/10.1007/s10208-011-9087-3 (visited on 07/05/2022) (page 84).

[8] Ellen M. Arruda and Mary C. Boyce. "A three-dimensional constitutive model for the large stretch behavior of rubber elastic materials". In: *Journal of the Mechanics and Physics of Solids* 41.2 (1993), pp. 389–412. ISSN: 0022-5096. DOI: https://doi.org/10.1016/0022-5096(93)90013-6. URL: https://www.sciencedirect.com/science/article/pii/0022509693900136 (page 81).

[9] A. Auger and N. Hansen. "A restart CMA evolution strategy with increasing population size". In: *2005 IEEE Congress on Evolutionary Computation*. Vol. 2. 2005, 1769–1776 Vol. 2. DOI: 10.1109/CEC.2005.1554902 (page 134).

[10] Rebecca Axelsson et al. "Finite element model of mechanical imaging of the breast". In: *Journal of Medical Imaging* 9.3 (2022), p. 033502. DOI: 10.1117/1.JMI.9.3.033502. URL: https://doi.org/10.1117/1.JMI.9.3.033502 (page 115).

[11] Thiranja Babarenda Gamage et al. "Modelling Prone to Supine Breast Deformation Under Gravity Loading Using Heterogeneous Finite Element Models". In: Jan. 2012. ISBN: 978-1-4614-3171-8. DOI: 10.1007/978-1-4614-3172-5_5 (pages 117, 119).

[12] Satish Balay et al. *PETSc Web page*. https://petsc.org/. 2022. URL: https://petsc.org/ (page 56).

[13] Ilya Baran and Jovan Popovi. "Automatic rigging and animation of 3D characters". In: *ACM Transactions on Graphics* 26.3 (2007). DOI: 10.1145/1275808.1276467 (page 32).

[14] Davide Baroli, Alfio Quarteroni, and Ricardo Ruiz-Baier. "Convergence of a stabilized discontinuous Galerkin method for incompressible nonlinear elasticity". In: *Advances in Computational Mathematics* 39.2 (Dec. 2012), pp. 425–443. DOI: 10.1007/s10444-012-9286-8. URL: https://doi.org/10.1007/s10444-012-9286-8 (page 83).

[15] Olga Barrera. "A unified modelling and simulation for coupled anomalous transport in porous media and its finite element implementation". In: *Computational Mechanics* 68 (Dec. 2021). DOI: 10.1007/s00466-021-02067-5 (page 78).

[16] Peter Bastian et al. "The Dune framework: Basic concepts and recent developments". en. In: *Computers & Mathematics with Applications*. Development and Application of Open-source Software for Problems with Numerical PDEs 81 (Jan. 2021), pp. 75–112. ISSN: 0898-1221. DOI: 10.1016/j.camwa.2020.06.007. URL: https://www.sciencedirect.com/science/article/pii/S089812212030256X (visited on 06/01/2022) (page 82).

[17] Jon Louis Bentley. "Multidimensional Binary Search Trees Used for Associative Searching". In: *Commun. ACM* 18.9 (Sept. 1975), 509–517. ISSN: 0001-0782. DOI: 10.1145/361002.361007. URL: https://doi.org/10.1145/361002.361007 (page 125).

[18] Paul J Besl and Neil D Mckay. "A Method for Registration of 3-D Shapes". In: *IEEE Transactions on Pattern Analysis and Machine Intelligence* 14.2 (1992), pp. 239–256. DOI: 10.1109/34.121791 (page 37).

[19] S Bessa, Pedro H Carvalho, and P Oliveira. "Registration of Breast MRI and 3D Scan Data Based on Surface Matching". In: *In Proceedings of the IEEE 16th International Symposium on Biomedical Imaging* (2019). DOI: 10.1109/ISBI.2019.8759306 (pages 32, 43).

[20] Sílvia Bessa et al. "3D digital breast cancer models with multimodal fusion algorithms". In: *The Breast* 49 (2020), pp. 281–290. ISSN: 15323080. DOI: 10.1016/j.breast.2019.12.016 (page 32).

[21] Daniele Bianchi et al. "A FSI computational framework for vascular physiopathology: A novel flow-tissue multiscale strategy". In: *Medical Engineering & Physics* 47 (2017), pp. 25–37. ISSN: 1350-4533. DOI: https://doi.org/10.1016/j.medengphy.2017.06.028. URL: https://www.sciencedirect.com/science/article/pii/S1350453317301674 (page 78).

[22] J Bols et al. "A computational method to assess the in vivo stresses and unloaded configuration of patient-specific blood vessels". In: *Journal of Computational and Applied Mathematics* 246 (2013), pp. 10–17. ISSN: 0377-0427. DOI: 10.1016/j.cam.2012.10.034. URL: http://dx.doi.org/10.1016/j.cam.2012.10.034 (page 50).

[23] Iman Borazjani. "Fluid–structure interaction, immersed boundary-finite element method simulations of bio-prosthetic heart valves". In: *Computer Methods in Applied Mechanics and Engineering* 257 (2013), pp. 103–116. ISSN: 0045-7825. DOI: https://doi.org/10.1016/j.cma.2013.01.010. URL: https://www.sciencedirect.com/science/article/pii/S0045782513000212 (page 78).

[24] Stéphane Bordas et al. "An extended finite element library". In: *International Journal for Numerical Methods in Engineering* 2 (Jan. 2006), pp. 1–33 (pages 77, 82).

[25] G. Boyer et al. "Assessment of the in-plane biomechanical properties of human skin using a finite element model updating approach combined with an optical full-field measurement on a new tensile device". In: *Journal of the Mechanical Behavior of Biomedical Materials* 27 (2013), pp. 273–282. ISSN: 1751-6161. DOI: https://doi.org/10.1016/j.jmbbm.2013.05.024. URL: https://www.sciencedirect.com/science/article/pii/S1751616113001951 (page 78).

[26] "Breast cancer and hormone-replacement therapy in the Million Women Study". In: *The Lancet* 362.9382 (2003), pp. 419–427. ISSN: 0140-6736. DOI: https://doi.org/10.1016/S0140-6736(03)14065-2. URL: https://www.sciencedirect.com/science/article/pii/S0140673603140652 (page 10).

[27] N. Briot et al. "Experimental characterisation and modelling of breast Cooper's ligaments". In: *Biomechanics and Modeling in Mechanobiology* 21.4 (Apr. 2022), pp. 1157–1168. DOI: 10.1007/s10237-022-01582-5. URL: https://doi.org/10.1007/s10237-022-01582-5 (page 119).

[28] N. Briot et al. "In vivo measurement of breast tissues stiffness using a light aspiration device". In: *Clinical Biomechanics* (2022), p. 105743. ISSN: 0268-0033. DOI: https://doi.org/10.1016/j.clinbiomech.2022.105743. URL: https://www.sciencedirect.com/science/article/pii/S0268003322001735 (page 118).

[29] Jean-Nicolas Brunet. "Exploring new numerical methods for the simulation of soft tissue deformations in surgery assistance". Theses. 4 Rue Blaise Pascal: Université de Strasbourg, Nov. 2020. URL: https://hal.inria.fr/tel-03130643 (page 81).

[30] Huu Phuoc Bui et al. "Real-Time Error Control for Surgical Simulation". In: *IEEE Transactions on Biomedical Engineering* 65.3 (2018), pp. 596–607. DOI: 10.1109/TBME.2017.2695587 (page 78).

[31] Raphael Bulle et al. "The Human Meniscus Behaves as a Functionally Graded Fractional Porous Medium under Confined Compression Conditions". In: *Applied Sciences* 11 (Oct. 2021), p. 9405. DOI: 10.3390/app11209405 (page 78).

[32] Donald E. Carlson and T. Shield. "Inverse deformation results for elastic materials". In: *Zeitschrift für angewandte Mathematik und Physik ZAMP* 20.2 (1969), pp. 261–263. ISSN: 00442275. DOI: 10.1007/BF01595564 (page 50).

[33] M M Carroll and F J Rooney. "Implications of Shield ' s inverse deformation theorem for compressible finite elasticity". In: *Zeitschrift für angewandte Mathematik und Physik ZAMP* 56 (2005), pp. 1048–1060. DOI: 10.1007/s00033-005-2023-0 (page 50).

[34] Tim Carter et al. "Application of Biomechanical Modelling to Image-Guided Breast Surgery". In: Feb. 2012, pp. 71–94. ISBN: 978-3-642-29013-8. DOI: 10.1007/8415_2012_128 (pages 127, 129).

[35] Timothy J. Carter, Christine Tanner, and David J. Hawkes. "Determining material properties of the breast for image-guided surgery". In: *Medical Imaging 2009: Visualization, Image-Guided Procedures, and Modeling*. Ed. by Michael I. Miga and Kenneth H. Wong. Vol. 7261. International Society for Optics and Photonics. SPIE, 2009, p. 726124. DOI: 10.1117/12.810092. URL: https://doi.org/10.1117/12.810092 (pages 116, 127, 129).

[36] Dan Casas and Miguel A Otaduy. "Learning Nonlinear Soft-Tissue Dynamics for Interactive Avatars". In: *In Proceedings of the ACM on Computer Graphics and Interactive Techniques* (2018). DOI: 10.1145/3203187 (page 32).

[37] Michael P. Chae et al. "Breast volumetric analysis for aesthetic planning in breast reconstruction: A literature review of techniques". In: *Gland Surgery* 5.2 (2016), pp. 212–226. ISSN: 22278575. DOI: 10.3978/j.issn.2227-684X.2015.10.03 (page 32).

[38] Gregory Chagnon, Marie Rebouah, and Denis Favier. "Hyperelastic Energy Densities for Soft Biological Tissues: A Review". In: *Journal of Elasticity* 120 (Dec. 2014). DOI: 10.1007/s10659-014-9508-z (page 78).

[39] É. Chamberland, A. Fortin, and M. Fortin. "Comparison of the performance of some finite element discretizations for large deformation elasticity problems". In: *Computers & Structures* 88.11-12 (June 2010), pp. 664–673. DOI: 10.1016/j.compstruc.2010.02.007. URL: https://doi.org/10.1016/j.compstruc.2010.02.007 (page 93).

[40] Xiang Chen et al. "An asymptotic numerical method for inverse elastic shape design". In: *ACM Transactions on Graphics* 33.4 (2014). ISSN: 15577333. DOI: 10.1145/2601097.2601189 (page 51).

[41] Francisco Chinesta, Roland Keunings, and Adrien Leygue. *The proper generalized decomposition for advanced numerical simulations. A primer*. Jan. 2014. ISBN: 978-3-319-02864-4. DOI: 10.1007/978-3-319-02865-1 (page 79).

[42] Jae-Hoon Chung et al. "Modelling Mammographic Compression of the Breast". In: *Medical Image Computing and Computer-Assisted Intervention – MICCAI 2008*. Ed. by Dimitris Metaxas et al. Berlin, Heidelberg: Springer Berlin Heidelberg, 2008, pp. 758–765. ISBN: 978-3-540-85990-1 (page 115).

[43] Matteo Cianchetti et al. "Biomedical applications of soft robotics". In: *Nature Reviews Materials* 3.6 (May 2018), pp. 143–153. DOI: 10.1038/s41578-018-0022-y. URL: https://doi.org/10.1038/s41578-018-0022-y (page 2).

[44] W.L. Claeys et al. "Consumption of raw or heated milk from different species: An evaluation of the nutritional and potential health benefits". In: *Food Control* 42 (2014), pp. 188–201. ISSN: 0956-7135. DOI: https://doi.org/10.1016/j.foodcont.2014.01.045. URL: https://www.sciencedirect.com/science/article/pii/S0956713514000607 (page 11).

[45] Françoise Clavel-Chapelon. "Cumulative number of menstrual cycles and breast cancer risk: results from the E3N cohort study of French women." In: *Cancer Causes and Control* 13.9 (Nov. 2002), pp. 831–8. URL: https://www.hal.inserm.fr/inserm-00136439 (page 10).

[46] Olivier Comas et al. "Efficient Nonlinear FEM for Soft Tissue Modelling and Its GPU Implementation within the Open Source Framework SOFA". In: Springer. July 2008, pp. 28–39. ISBN: 978-3-540-70520-8. DOI: 10.1007/978-3-540-70521-5_4 (page 79).

[47] K. D. Costa, J. W. Holmes, and A. D. Mcculloch. "Modelling cardiac mechanical properties in three dimensions". In: *Philosophical Transactions of the Royal Society of London. Series A: Mathematical, Physical and Engineering Sciences* 359.1783 (June 2001). Ed. by P. Kohl, D. Noble, and P. J. Hunter, pp. 1233–1250. DOI: 10.1098/rsta.2001.0828. URL: https://doi.org/10.1098/rsta.2001.0828 (page 81).

[48] S. Cotin, H. Delingette, and N. Ayache. "Real-time elastic deformations of soft tissues for surgery simulation". In: *IEEE Transactions on Visualization and Computer Graphics* 5.1 (1999), pp. 62–73. DOI: 10.1109/2945.764872 (page 78).

[49] Hadrien Courtecuisse et al. "Real-time simulation of contact and cutting of heterogeneous soft-tissues". In: *Medical image analysis* 18 (Dec. 2013), pp. 394–410. DOI: 10.1016/j.media.2013.11.001 (page 98).

[50] Hadrien Courtecuisse et al. "Real-time simulation of contact and cutting of heterogeneous soft-tissues". In: *Medical Image Analysis* 18.2 (2014), pp. 394–410. ISSN: 1361-8415. DOI: https://doi.org/10.1016/j.media.2013.11.001. URL: https://www.sciencedirect.com/science/article/pii/S1361841513001692 (page 78).

[51] Stephen C. Cowin. "Bone poroelasticity". In: *Journal of Biomechanics* 32.3 (1999), pp. 217–238. ISSN: 0021-9290. DOI: https://doi.org/10.1016/S0021-9290(98)00161-4. URL: https://www.sciencedirect.com/science/article/pii/S0021929098001614 (page 78).

[52] M. A. Crisfield. *Non-Linear Finite Element Analysis of Solids and Structures: Advanced Topics*. 1st. USA: John Wiley & Sons, Inc., 1997. ISBN: 047195649X (page 54).

[53] Gabriel J. DeSalvo and John A. Swanson. *ANSYS engineering analysis system users manual*. English. Houston, Pa.: Swanson Analysis Systems, 1985 (page 77).

[54] Carol E DeSantis et al. "Breast Cancer Statistics , 2019". In: *American Cancer Society Journal* 69.6 (2019), pp. 438–451. DOI: 10.3322/caac.21583 (page 31).

[55] Saurabh Deshpande, Jakub Lengiewicz, and Stéphane P.A. Bordas. "Probabilistic deep learning for real-time large deformation simulations". In: *Computer Methods in Applied Mechanics and Engineering* 398 (2022), p. 115307. ISSN: 0045-7825. DOI: https://doi.org/10.1016/j.cma.2022.115307. URL: https://www.sciencedirect.com/science/article/pii/S004578252200411X (page 79).

[56] Evanthia Diamanti-Kandarakis et al. "Endocrine-Disrupting Chemicals: An Endocrine Society Scientific Statement". In: *Endocrine Reviews* 30.4 (June 2009), pp. 293–342. ISSN: 0163-769X. DOI: 10.1210/er.2009-0002. eprint: https://academic.oup.com/edrv/article-pdf/30/4/293/10334449/edrv0293.pdf. URL: https://doi.org/10.1210/er.2009-0002 (page 10).

[57] Martha Duraes et al. "Surgery of nonpalpable breast cancer: First step to a virtual per-operative localization? First step to virtual breast cancer localization". In: *The Breast Journal* 25.5 (2019), pp. 874–879. DOI: doi.org/10.1111/tbj.13379. eprint: https://onlinelibrary.wiley.com/doi/pdf/10.1111/tbj.13379. URL: https://onlinelibrary.wiley.com/doi/abs/10.1111/tbj.13379 (page 31).

[58] C. Duriez et al. "Realistic haptic rendering of interacting deformable objects in virtual environments". In: *IEEE Transactions on Visualization and Computer Graphics* 12.1 (2006), pp. 36–47. DOI: 10.1109/TVCG.2006.13 (page 80).

[59] Christian Duriez. "Control of elastic soft robots based on real-time finite element method". In: *2013 IEEE International Conference on Robotics and Automation*. 2013 IEEE International Conference on Robotics and Automation. 2013, pp. 3982–3987. DOI: 10.1109/ICRA.2013.6631138 (page 80).

[60] Maximilian Eder et al. "Comparison of Different Material Models to Simulate 3-D Breast Deformations Using Finite Element Analysis". In: *Annals of biomedical engineering* 42 (Dec. 2013). DOI: 10.1007/s10439-013-0962-8 (page 118).

[61] Wolfgang Ehlers and Bernd Markert. "A Linear Viscoelastic Biphasic Model for Soft Tissues Based on the Theory of Porous Media". In: *Journal of biomechanical engineering* 123 (Nov. 2001), pp. 418–24. DOI: 10.1115/1.1388292 (page 78).

[62] Björn Eiben et al. "Surface driven biomechanical breast image registration". In: *In Proceedings of SPIE Medical Imaging* (2016). ISSN: 16057422. DOI: 10.1117/12.2216728 (pages 32, 117, 127).

[63] A. Elouneg et al. "An open-source FEniCS-based framework for hyperelastic parameter estimation from noisy full-field data: Application to heterogeneous soft tissues". In: *Computers & Structures* 255 (2021), p. 106620. ISSN: 0045-7949. DOI: https://doi.org/10.1016/j.compstruc.2021.106620. URL: https://www.sciencedirect.com/science/article/pii/S0045794921001425 (pages 78, 118).

[64] Victor Fachinotti and Alberto Cardona. "Design of compliant mechacanisms that exactly fit a desired shape". In: *Mecánica Computacional* 28 (2009), pp. 3191–3205 (pages 50, 51, 67).

[65] Victor D. Fachinotti, Alberto Cardona, and Philippe Jetteur. "Finite element modelling of inverse design problems in large deformations anisotropic hyperelasticity". In: *International Journal For Numerical Methods In Engineering* October 2007 (2008), pp. 894–910. DOI: 10.1002/nme (page 49).

[66] Sofia Farina et al. "A cut finite element method for spatially resolved energy metabolism models in complex neuro-cell morphologies with minimal remeshing". In: *Advanced Modeling and Simulation in Engineering Sciences* 8.1 (Mar. 2021). DOI: 10.1186/s40323-021-00191-8. URL: https://doi.org/10.1186/s40323-021-00191-8 (page 142).

[67] Giovanni Maria Farinella et al. "Objective Outcome Evaluation of Breast Surgery". In: *In Proceedings of Medical Image Computing and Computer-Assisted Intervention – MICCAI 2006: 9th International Conference* (2006). DOI: 10.1007/11866565_95 (pages 37, 40).

[68] Jessica M. Faupel-Badger et al. "Postpartum Remodeling, Lactation, and Breast Cancer Risk: Summary of a National Cancer Institute–Sponsored Workshop". In: *JNCI: Journal of the National Cancer Institute* 105.3 (Dec. 2012), pp. 166–174. ISSN: 0027-8874. DOI: 10.1093/jnci/djs505. eprint: https://academic.oup.com/jnci/article-pdf/105/3/166/17985592/djs505.pdf. URL: https://doi.org/10.1093/jnci/djs505 (page 10).

[69] François Faure et al. "SOFA: A Multi-Model Framework for Interactive Physical Simulation". In: *Soft Tissue Biomechanical Modeling for Computer Assisted Surgery*. Ed. by Yohan Payan. Berlin, Heidelberg: Springer Berlin Heidelberg, 2012, pp. 283–321. ISBN: 978-3-642-29014-5. DOI: 10.1007/8415_2012_125. URL: https://doi.org/10.1007/8415_2012_125 (pages 37, 64, 130).

[70] François Faure et al. "SOFA: A Multi-Model Framework for Interactive Physical Simulation". In: *Soft Tissue Biomechanical Modeling for Computer Assisted Surgery*. Ed. by Yohan Payan. Vol. 11. Studies in Mechanobiology, Tissue Engineering and Biomaterials. Springer, June 2012, pp. 283–321. DOI: 10.1007/8415_2012_125. URL: https://hal.inria.fr/hal-00681539 (pages 79, 144).

[71] Andriy Fedorov et al. "3D Slicer as an image computing platform for the Quantitative Imaging Network". In: *Magnetic Resonance Imaging* 30.9 (2012). Quantitative Imaging in Cancer, pp. 1323–1341. ISSN: 0730-725X. DOI: https://doi.org/10.1016/j.mri.2012.05.001. URL: https://www.sciencedirect.com/science/article/pii/S0730725X12001816 (page 120).

[72] Cormac Flynn, Andrew Taberner, and Poul Nielsen. "Mechanical characterisation of in vivo human skin using a 3D force-sensitive micro-robot and finite element analysis". In: *Biomechanics and modeling in mechanobiology* 10 (Feb. 2011), pp. 27–38. DOI: 10.1007/s10237-010-0216-8 (page 78).

[73] Antonio E. Forte et al. "A composite hydrogel for brain tissue phantoms". In: *Materials and Design* 112 (2016), pp. 227–238. ISSN: 18734197. DOI: 10.1016/j.matdes.2016.09.063. URL: http://dx.doi.org/10.1016/j.matdes.2016.09.063 (page 61).

[74] Leopoldo P. Franca and Thomas J.R. Hughes. "Two classes of mixed finite element methods". In: *Computer Methods in Applied Mechanics and Engineering* 69.1 (1988), pp. 89–129. ISSN: 0045-7825. DOI: https://doi.org/10.1016/0045-7825(88)90168-5. URL: https://www.sciencedirect.com/science/article/pii/0045782588901685 (page 55).

[75] Sarah M. Friedewald et al. "Breast Cancer Screening Using Tomosynthesis in Combination With Digital Mammography". In: *JAMA* 311.24 (June 2014), pp. 2499–2507. ISSN: 0098-7484. DOI: 10.1001/jama.2014.6095. eprint: https://jamanetwork.com/journals/jama/articlepdf/1883018/joi140069.pdf. URL: https://doi.org/10.1001/jama.2014.6095 (page 20).

[76] Thiranja Prasad Babarenda Gamage et al. "An automated computational biomechanics workflow for improving breast cancer diagnosis and treatment". In: *Interface Focus* 9.4 (June 2019), p. 20190034. DOI: 10.1098/rsfs.2019.0034. URL: https://doi.org/10.1098/rsfs.2019.0034 (pages 117, 127, 142, 143, 145).

[77] Fuchang Gao and Lixing Han. "Implementing the Nelder-Mead simplex algorithm with adaptive parameters". In: *Computational Optimization and Applications* 51 (May 2012), pp. 259–277. DOI: 10.1007/s10589-010-9329-3 (page 132).

[78] Amit Gefen and Benny Dilmoney. "Mechanics of the normal woman's breast". In: *Technology and health care : official journal of the European Society for Engineering and Medicine* 15 (Feb. 2007), pp. 259–71. DOI: 10.3233/THC-2007-15404 (page 119).

[79] Joachim Georgii et al. "Simulation and Visualization to Support Breast Surgery Planning". In: *Breast Imaging*. Ed. by Anders Tingberg, Kristina Lång, and Pontus Timberg. Cham: Springer International Publishing, 2016, pp. 257–264. ISBN: 978-3-319-41546-8 (pages 116, 119).

[80] C. Geuzaine and J.-F. Remacle. "Gmsh: a three-dimensional finite element mesh generator with built-in pre- and post-processing facilities". In: *International Journal for Numerical Methods in Engineering* 79 (2009), pp. 1309–1331. DOI: 10.1002/nme.2579 (pages 77, 82, 127).

[81] Chester H. Gibbons. "History of Testing Machines for Materials". In: *Transactions of the Newcomen Society* 15.1 (1934), pp. 169–184. DOI: 10.1179/tns.1934.011. eprint: https://doi.org/10.1179/tns.1934.011. URL: https://doi.org/10.1179/tns.1934.011 (page 78).

[82] Benjamin Gilles et al. "Frame-Based Elastic Models". In: *ACM Trans. Graph.* 30.2 (Apr. 2011). ISSN: 0730-0301. DOI: 10.1145/1944846.1944855. URL: https://doi.org/10.1145/1944846.1944855 (page 79).

[83] Olivier Goury and Christian Duriez. "Fast, Generic, and Reliable Control and Simulation of Soft Robots Using Model Order Reduction". In: *IEEE Transactions on Robotics* 34.6 (2018), pp. 1565–1576. DOI: 10.1109/TRO.2018.2861900 (page 79).

[84] Olivier Goury et al. "Automatised selection of load paths to construct reduced-order models in computational damage micromechanics: from dissipation-driven random selection to Bayesian optimization". In: *Computational Mechanics* 58 (Aug. 2016). DOI: 10.1007/s00466-016-1290-2 (page 79).

[85] Sanjay Govindjee and Paul A Mihalic. "Computational methods for inverse deformations in quasi-incompressible finite elasticity". In: *International Journal For Numerical Methods In Engineering* 43.5 (1998), pp. 821–838 (page 50).

[86] Sanjay Govindjee and Paul A Mihalic. "Computational methods for inverse finite elastostatics". In: *Computer Methods In Applied Mechanics And Engineering* 136.96 (1996) (page 50).

[87] Rebekah H Griesenauer et al. "Breast tissue stiffness estimation for surgical guidance using gravity-induced excitation". In: *Physics in Medicine and Biology* 62.12 (May 2017), pp. 4756–4776. DOI: 10.1088/1361-6560/aa700a. URL: https://doi.org/10.1088/1361-6560/aa700a (page 119).

[88] Guanhui Guo, Yanni Zou, and Peter X. Liu. "A new rendering algorithm based on multi-space for living soft tissue". In: *Computers & Graphics* 98 (2021), pp. 242–254. ISSN: 0097-8493. DOI: https://doi.org/10.1016/j.cag.2021.06.003. URL: https://www.sciencedirect.com/science/article/pii/S0097849321001187 (page 79).

[89] Rami M. Haj-Ali and Anastasia H. Muliana. "Numerical finite element formulation of the Schapery non-linear viscoelastic material model". In: *International Journal for Numerical Methods in Engineering* 59.1 (2004), pp. 25–45. DOI: https://doi.org/10.1002/nme.861. eprint: https://onlinelibrary.wiley.com/doi/pdf/10.1002/nme.861. URL: https://onlinelibrary.wiley.com/doi/abs/10.1002/nme.861 (page 78).

[90] Lianghao Han et al. "A Nonlinear Biomechanical Model Based Registration Method for Aligning Prone and Supine MR Breast Images". In: *IEEE Transactions on Medical Imaging* 33.3 (2014), pp. 682–694. DOI: 10.1109/TMI.2013.2294539 (pages 116, 118).

[91] Lianghao Han et al. "Development of patient-specific biomechanical models for predicting large breast deformation". In: *Physics in medicine and biology* 57 (Dec. 2011), pp. 455–72. DOI: 10.1088/0031-9155/57/2/455 (pages 78, 115, 116, 118).

[92] Nikolaus Hansen. "The CMA Evolution Strategy: A Tutorial". In: *ArXiv* (2016), pp. 1–39. DOI: https://hal.inria.fr/hal-01297037 (page 134).

[93] Charles R. Harris et al. "Array programming with NumPy". In: *Nature* 585.7825 (Sept. 2020), pp. 357–362. DOI: 10.1038/s41586-020-2649-2. URL: https://doi.org/10.1038/s41586-020-2649-2 (page 38).

[94] Paul Hauseux, Jack S. Hale, and Stéphane P.A. Bordas. "Accelerating Monte Carlo estimation with derivatives of high-level finite element models". In: *Computer Methods in Applied Mechanics and Engineering* 318 (2017), pp. 917–936. ISSN: 0045-7825. DOI: https://doi.org/10.1016/j.cma.2017.01.041. URL: https://www.sciencedirect.com/science/article/pii/S0045782516313470 (page 78).

[95] Paul Hauseux et al. "Quantifying the uncertainty in a hyperelastic soft tissue model with stochastic parameters". In: *Applied Mathematical Modelling* 62 (2018), pp. 86–102. ISSN: 0307-904X. DOI: https://doi.org/10.1016/j.apm.2018.04.021. URL: https://www.sciencedirect.com/science/article/pii/S0307904X18302063 (pages 78, 98, 101).

[96] F.M. Hendriks et al. "The relative contributions of different skin layers to the mechanical behavior of human skin in vivo using suction experiments". In: *Medical Engineering & Physics* 28.3 (2006), pp. 259–266. ISSN: 1350-4533. DOI: https://doi.org/10.1016/j.medengphy.2005.07.001. URL: https://www.sciencedirect.com/science/article/pii/S1350453305001451 (page 118).

[97] Nikolas Hesse et al. "Learning and Tracking the 3D Body Shape of Freely Moving Infants from RGB-D sequences". In: *IEEE Transactions on Pattern Analysis and Machine Intelligence* (2019), pp. 1–12. DOI: 10.1109/TPAMI.2019.2917908 (page 32).

[98] Gerhard A. Holzapfel and Ray W. Ogden. "Constitutive modelling of passive myocardium: a structurally based framework for material characterization". In: *Philosophical Transactions of the Royal Society A: Mathematical, Physical and Engineering Sciences* 367.1902 (Sept. 2009), pp. 3445–3475. DOI: 10.1098/rsta.2009.0091. URL: https://doi.org/10.1098/rsta.2009.0091 (page 98).

[99] Yasushi Ito. "Delaunay Triangulation". In: *Encyclopedia of Applied and Computational Mathematics*. Ed. by Björn Engquist. Berlin, Heidelberg: Springer Berlin Heidelberg, 2015, pp. 332–334. ISBN: 978-3-540-70529-1. DOI: 10.1007/978-3-540-70529-1_314. URL: https://doi.org/10.1007/978-3-540-70529-1_314 (page 126).

[100] Mikhail Itskov. "A generalized orthotropic hyperelastic material model with application to incompressible shells". In: *International Journal for Numerical Methods in Engineering* 50.8 (2001), pp. 1777–1799. DOI: https://doi.org/10.1002/nme.86. eprint: https://onlinelibrary.wiley.com/doi/pdf/10.1002/nme.86. URL: https://onlinelibrary.wiley.com/doi/abs/10.1002/nme.86 (page 78).

[101] Alec Jacobson and Olga Sorkine. "Stretchable and Twistable Bones for Skeletal Shape Deformation". In: *ACM Transactions on Graphics* 30.6 (2011), pp. 1–8. ISSN: 15577368. DOI: 10.1145/2070781.2024199 (page 32).

[102] Thibault Jacquemin and Stéphane P. A. Bordas. "A unified algorithm for the selection of collocation stencils for convex, concave, and singular problems". In: *International Journal for Numerical Methods in Engineering* 122.16 (2021), pp. 4292–4312. DOI: https://doi.org/10.1002/nme.6703. eprint: https://onlinelibrary.wiley.com/doi/pdf/10.1002/nme.6703. URL: https://onlinelibrary.wiley.com/doi/abs/10.1002/nme.6703 (page 77).

[103] Wenzel Jakob et al. "Instant Field-Aligned Meshes". In: *ACM Trans. Graph.* 34.6 (Oct. 2015). ISSN: 0730-0301. DOI: 10.1145/2816795.2818078. URL: https://doi.org/10.1145/2816795.2818078 (page 127).

[104] Doug L James and Christopher D Twigg. "Skinning Mesh Animations". In: *ACM Transactions on Graphics* 1.212 (2005), pp. 399–407. DOI: 10.1145/1073204.1073206 (page 32).

[105] Chintan Jansari et al. "Adaptive smoothed stable extended finite element method for weak discontinuities for finite elasticity". In: *European Journal of Mechanics - A/Solids* 78 (2019), p. 103824. ISSN: 0997-7538. DOI: https://doi.org/10.1016/j.euromechsol.2019.103824. URL: https://www.sciencedirect.com/science/article/pii/S0997753818309288 (pages 77, 142).

[106] Hrvoje Jasak, Ar Jemcov, and United Kingdom. "OpenFOAM: A C++ Library for Complex Physics Simulations". In: *International Workshop on Coupled Methods in Numerical Dynamics, IUC* (2007), pp. 1–20 (page 77).

[107] Mohd Javaid et al. "Substantial capabilities of robotics in enhancing industry 4.0 implementation". In: *Cognitive Robotics* 1 (2021), pp. 58–75. ISSN: 2667-2413. DOI: https://doi.org/10.1016/j.cogr.2021.06.001. URL: https://www.sciencedirect.com/science/article/pii/S2667241321000057 (page 2).

[108] Pushkar Joshi et al. "Learning controls for blend shape based realistic facial animation". In: *In Proceedings of 2003 ACM SIGGRAPH/Eurographics Symposium on Computer Animation* (2003). DOI: 10.1145/1198555.1198588 (page 32).

[109] Ladislav Kavan et al. "Geometric skinning with approximate dual quaternion blending". In: *ACM Transactions on Graphics* 27.4 (2008), pp. 1–23. ISSN: 07300301. DOI: 10.1145/1409625.1409627 (page 44).

[110] Youngjun Kim, Kunwoo Lee, and Wontae Kim. "3D virtual simulator for breast plastic surgery". In: *Computer Animation and Virtual Worlds* (2008), pp. 33–47. DOI: 10.1002/cav.237 (page 32).

[111] Robert C. Kirby. "Algorithm 839: FIAT, a New Paradigm for Computing Finite Element Basis Functions". In: *ACM Trans. Math. Softw.* 30.4 (Dec. 2004), pp. 502–516. ISSN: 0098-3500. DOI: 10.1145/1039813.1039820. URL: http://doi.acm.org/10.1145/1039813.1039820 (visited on 01/31/2018) (page 83).

[112] Robert C. Kirby and Anders Logg. "A Compiler for Variational Forms". In: *ACM Trans. Math. Softw.* 32.3 (Sept. 2006), pp. 417–444. ISSN: 0098-3500. DOI: 10.1145/1163641.1163644. URL: http://doi.acm.org/10.1145/1163641.1163644 (visited on 01/31/2018) (page 82).

[113] Christian Kleinbach et al. "Implementation and validation of the extended Hill-type muscle model with robust routing capabilities in LS-DYNA for active human body models". In: *BioMedical Engineering OnLine* 16 (Sept. 2017). DOI: 10.1186/s12938-017-0399-7 (page 118).

[114] M. Koishi and S. Govindjee. "Inverse design methodology of a tire". In: *Tire Science and Technology* 29.3 (2001), pp. 155–170. ISSN: 00908657. DOI: 10.2346/1.2135236 (page 49).

[115] Henrik Albert Kolstad. "Nightshift work and risk of breast cancer and other cancers—a critical review of the epidemiologic evidence". In: *Scandinavian Journal of Work, Environment & Health* 1 (Feb. 2008), pp. 5–22. ISSN: 0355-3140. DOI: 10.5271/sjweh.1194. URL: https://www.sjweh.fi/show_abstract.php?abstract_id=1194 (page 11).

[116] Aravindh Krishnamoorthy and Deepak Menon. "Matrix inversion using Cholesky decomposition". In: *2013 Signal Processing: Algorithms, Architectures, Arrangements, and Applications (SPA)*. 2013, pp. 70–72 (page 64).

[117] R M Lacher et al. "Nonrigid reconstruction of 3D breast surfaces with a low-cost RGBD camera for surgical planning and aesthetic evaluation". In: *Medical Image Analysis* 53 (2019), pp. 11–25. DOI: 10.1016/j.media.2019.01.003 (page 32).

[118] René M Lacher et al. "A comparative study of breast surface reconstruction for aesthetic outcome assessment". In: *In Proceedings of Medical Image Computing and Computer-Assisted Intervention - MICCAI 2017: 20th International Conference,* (2017). ISSN: 16113349. DOI: 10.1007/978-3-319-66185-8_58 (page 32).

[119] Susanna C. Larsson, Nicola Orsini, and Alicja Wolk. "Milk, milk products and lactose intake and ovarian cancer risk: A meta-analysis of epidemiological studies". In: *International Journal of Cancer* 118.2 (2006), pp. 431–441. DOI: https://doi.org/10.1002/ijc.21305. eprint: https://onlinelibrary.wiley.com/doi/pdf/10.1002/ijc.21305. URL: https://onlinelibrary.wiley.com/doi/abs/10.1002/ijc.21305 (page 11).

[120] T. Lavigne et al. "Société de Biomécanique Young Investigator Award 2021: Numerical investigation of the time-dependent stress–strain mechanical behaviour of skeletal muscle tissue in the context of pressure ulcer prevention". In: *Clinical Biomechanics* 93 (2022), p. 105592. ISSN: 0268-0033. DOI: https://doi.org/10.1016/j.clinbiomech.2022.105592. URL: https://www.sciencedirect.com/science/article/pii/S0268003322000225 (page 78).

[121] Binh Huy Le and Zhigang Deng. "Robust and accurate skeletal rigging from mesh sequences". In: *ACM Transactions on Graphics* 33.4 (2014). ISSN: 15577333. DOI: 10.1145/2601097.2601161 (page 32).

[122] Angela W. C. Lee et al. "Breast Image Registration by Combining Finite Elements and Free-Form Deformations". In: *Digital Mammography*. Ed. by Joan Martí et al. Berlin, Heidelberg: Springer Berlin Heidelberg, 2010, pp. 736–743. ISBN: 978-3-642-13666-5 (page 32).

[123] Chang Kye Lee et al. "Strain smoothing for compressible and nearly-incompressible finite elasticity". In: *Computers and Structures* 182.February (2017), pp. 540–555. ISSN: 00457949. DOI: 10.1016/j.compstruc.2016.05.004. URL: http://dx.doi.org/10.1016/j.compstruc.2016.05.004 (pages 51, 57).

[124] Jakub Lengiewicz et al. "Interfacing AceGEN and FEniCS for advanced constitutive models". In: *Proceedings of FEniCS 2021, online, 22–26 March*. Ed. by Igor Baratta et al. 2021, p. 474. DOI: 10.6084/m9.figshare.14495463. URL: http://mscroggs.github.io/fenics2021/talks/lengiewicz.html (page 80).

[125] J P Lewis et al. "Practice and Theory of Blendshape Facial Models". In: *Proceedings of Eurographics 2014 - State of the Art Reports*. 2014. DOI: 10.2312/egst.20141042 (page 32).

[126] Yi-Je Lim et al. "Soft tissue deformation and cutting simulation for the multimodal surgery training". In: *19th IEEE Symposium on Computer-Based Medical Systems (CBMS'06)*. 19th IEEE Symposium on Computer-Based Medical Systems. 2006, pp. 635–640 (page 78).

[127] Yan-Lin Liu et al. "Simulation of breast compression in mammography using finite element analysis: A preliminary study". In: *Radiation Physics and Chemistry* 140 (Jan. 2017). DOI: 10.1016/j.radphyschem.2017.01.017 (page 115).

[128] A. Logg, K.A. Mardal, and G. Wells. *Automated Solution of Differential Equations by the Finite Element Method: The FEniCS Book*. Lecture Notes in Computational Science and Engineering. Springer Berlin Heidelberg, 2012. ISBN: 9783642230998. URL: https://books.google.lu/books?id=ASWN_VRr1NQC (page 55).

[129] Anders Logg and Garth N. Wells. "DOLFIN: Automated Finite Element Computing". In: *ACM Trans. Math. Softw.* 37.2 (2010). ISSN: 0098-3500. DOI: 10.1145/1731022.1731030. URL: https://doi.org/10.1145/1731022.1731030 (page 56).

[130] Matthew Loper et al. "SMPL : A Skinned Multi-Person Linear Model". In: *ACM Transactions on Graphics* 34 (2015), 248:1–248:16. DOI: 10.1145/2816795.2818013 (pages 32, 43).

[131] William E. Lorensen and Harvey E. Cline. "Marching Cubes: A High Resolution 3D Surface Construction Algorithm". In: *Proceedings of the 14th Annual Conference on Computer Graphics and Interactive Techniques*. SIGGRAPH '87. New York, NY, USA: Association for Computing Machinery, 1987, 163–169. ISBN: 0897912276. DOI: 10.1145/37401.37422. URL: https://doi.org/10.1145/37401.37422 (page 120).

[132] Jörn Lorenzen et al. "Menstrual-Cycle Dependence of Breast Parenchyma Elasticity: Estimation With Magnetic Resonance Elastography of Breast Tissue During the Menstrual Cycle". In: *Investigative radiology* 38 (May 2003), pp. 236–40. DOI: 10.1097/01.RLI.0000059544.18910.BD (page 118).

[133] Jia Lu, Xianlian Zhou, and Madhavan L Raghavan. "Inverse elastostatic stress analysis in pre-deformed biological structures : Demonstration using abdominal aortic aneurysms". In: *Journal of Biomechanics* 40.3 (2007), pp. 693–696. DOI: 10.1016/j.jbiomech.2006.01.015 (page 49).

[134] Mickaël Ly et al. "Inverse elastic shell design with contact and friction". In: *SIGGRAPH Asia 2018 Technical Papers, SIGGRAPH Asia 2018* 37.6 (2018). ISSN: 15577368. DOI: 10.1145/3272127.3275036 (page 51).

[135] Alnaes M. et al. "The FEniCS project version 1.5". In: *Archive of Numerical Software 3* (2015). DOI: doi:10.11588/ans.2015.100.20553 (pages 51, 55).

[136] Wan-Chun Ma et al. "A blendshape model that incorporates physical interaction". In: *Computer Animation and Virtual Worlds* 23 (2012), pp. 235–243. DOI: 10.1145/2073304.2073343 (page 32).

[137] Steve Maas et al. "FEBio: Finite Elements for Biomechanics". In: *Journal of biomechanical engineering* 134 (Jan. 2012), p. 011005. DOI: 10.1115/1.4005694 (page 80).

[138] Richard Malgat et al. "Multifarious Hierarchies of Mechanical Models for Artist Assigned Levels-of-Detail". In: *Proceedings of the 14th ACM SIGGRAPH / Eurographics Symposium on Computer Animation*. SCA '15. Association for Computing Machinery. New York, NY, USA, 2015, 27–36. ISBN: 9781450334969. DOI: 10.1145/2786784.2786800. URL: https://doi.org/10.1145/2786784.2786800 (page 79).

[139] Stéphanie Marchesseau et al. "Fast porous visco-hyperelastic soft tissue model for surgery simulation: Application to liver surgery". In: *Progress in Biophysics and Molecular Biology* 103.2 (2010). Special Issue on Biomechanical Modelling of Soft Tissue Motion, pp. 185–196. ISSN: 0079-6107. DOI: https://doi.org/10.1016/j.pbiomolbio.2010.09.005. URL: https://www.sciencedirect.com/science/article/pii/S0079610710000738 (pages 64, 78).

[140] P. A. L. S. Martins, R. M. Natal Jorge, and A. J. M. Ferreira. "A Comparative Study of Several Material Models for Prediction of Hyperelastic Properties: Application to Silicone-Rubber and Soft Tissues". In: *Strain* 42.3 (2006), pp. 135–147. DOI: https://doi.org/10.1111/j.1475-1305.2006.00257.x. eprint: https://onlinelibrary.wiley.com/doi/pdf/10.1111/j.1475-1305.2006.00257.x. URL: https://onlinelibrary.wiley.com/doi/abs/10.1111/j.1475-1305.2006.00257.x (page 78).

[141] Arnaud Mazier et al. "A rigged model of the breast for preoperative surgical planning". In: *Journal of Biomechanics* 128 (2021), p. 110645. ISSN: 0021-9290. DOI: https://doi.org/10.1016/j.jbiomech.2021.110645. URL: https://www.sciencedirect.com/science/article/pii/S0021929021004140 (page 124).

[142] Arnaud Mazier et al. "Inverse deformation analysis: an experimental and numerical assessment using the FEniCS Project". In: *Engineering with Computers* (Feb. 2022). DOI: 10.1007/s00366-021-01597-z (page 78).

[143] Arnaud Mazier et al. "Supplementary material for Inverse deformation analysis: an experimental and numerical assessment using the FEniCS Project". In: (Feb. 2021). DOI: 10.6084/m9.figshare.14035793.v1. URL: https://figshare.com/articles/software/Supplementary_material_for_Inverse_deformation_analysis_an_experimental_and_numerical_assessment_using_the_FEniCS_Project/14035793 (pages 56, 57, 60, 91).

[144] Deirdre E. McGhee and Julie R. Steele. "Breast biomechanics: What do we really know?" In: *Physiology* 35.2 (2020), pp. 144–156. DOI: 10.1152/physiol.00024.2019 (pages 119, 129, 140).

[145] Michelle Menard. *Game Development with Unity*. 1st. Boston, MA, USA: Course Technology Press, 2011. ISBN: 9781435456587 (page 79).

[146] Ray M. Merrill et al. "Cancer risk associated with early and late maternal age at first birth". In: *Gynecologic Oncology* 96.3 (2005), pp. 583–593. ISSN: 0090-8258. DOI: https://doi.org/10.1016/j.ygyno.2004.11.038. URL: https://www.sciencedirect.com/science/article/pii/S0090825804009631 (page 10).

[147] Aaron Meurer et al. "SymPy: symbolic computing in Python". In: *PeerJ Computer Science* 3 (Jan. 2017), e103. ISSN: 2376-5992. DOI: 10.7717/peerj-cs.103. URL: https://doi.org/10.7717/peerj-cs.103 (page 93).

[148] Valentina Miguez Pacheco, Larry Hench, and Aldo Boccaccini. "Bioactive glasses beyond bone and teeth: Emerging applications in contact with soft tissues". In: *Acta Biomaterialia* 13 (Nov. 2014). DOI: 10.1016/j.actbio.2014.11.004 (page 78).

[149] L. Angela Mihai and Alain Goriely. "Numerical simulation of shear and the Poynting effects by the finite element method: An application of the generalised empirical inequalities in non-linear elasticity". In: *International Journal of Non-Linear Mechanics* 49.November 2017 (2013), pp. 1–14. ISSN: 00207462. DOI: 10.1016/j.ijnonlinmec.2012.09.001 (pages 51, 57, 68, 69).

[150] L. Angela Mihai et al. "A comparison of hyperelastic constitutive models applicable to brain and fat tissues". In: *Journal of The Royal Society Interface* 12 (Sept. 2015), pp. 1–12. DOI: 10.1098/rsif.2015.0486 (page 78).

[151] L. Angela Mihai et al. "A family of hyperelastic models for human brain tissue". In: *Journal of the Mechanics and Physics of Solids* 106 (2017), pp. 60–79. ISSN: 0022-5096. DOI: https://doi.org/10.1016/j.jmps.2017.05.015. URL: https://www.sciencedirect.com/science/article/pii/S0022509617302703 (page 78).

[152] Anna Mîra et al. "A biomechanical breast model evaluated with respect to MRI data collected in three different positions". In: *Clinical Biomechanics* 60 (2018), pp. 191–199. DOI: 10.1016/j.clinbiomech.2018.10.020 (pages 49, 51, 117, 119, 129–131, 135, 142, 143).

[153] Anna Mîra et al. "Simulation of breast compression using a new biomechanical model". In: *Medical Imaging 2018: Physics of Medical Imaging*. Ed. by Joseph Y. Lo, Taly Gilat Schmidt, and Guang-Hong Chen. Vol. 10573. International Society for Optics and Photonics. SPIE, 2018, 105735A. DOI: 10.1117/12.2293488. URL: https://doi.org/10.1117/12.2293488 (page 115).

[154] M. Mooney. "A Theory of Large Elastic Deformation". In: *Journal of Applied Physics* 11.9 (1940), pp. 582–592. DOI: 10.1063/1.1712836. eprint: https://doi.org/10.1063/1.1712836. URL: https://doi.org/10.1063/1.1712836 (pages 54, 81).

[155] Noémie Moreau et al. "Automatic Segmentation of Metastatic Breast Cancer Lesions on 18F-FDG PET/CT Longitudinal Acquisitions for Treatment Response Assessment". In: *Cancers* 14.1 (2022). ISSN: 2072-6694. DOI: 10.3390/cancers14010101. URL: https://www.mdpi.com/2072-6694/14/1/101 (page 120).

[156] Nicola Napoli et al. "High Prevalence of Low Vitamin D and Musculoskeletal Complaints in Women with Breast Cancer". In: *The Breast Journal* 16.6 (2010), pp. 609–616. DOI: https://doi.org/10.1111/j.1524-4741.2010.01012.x. eprint: https://onlinelibrary.wiley.com/doi/pdf/10.1111/j.1524-4741.2010.01012.x. URL: https://onlinelibrary.wiley.com/doi/abs/10.1111/j.1524-4741.2010.01012.x (page 11).

[157] Harish Narayanan. "A computational framework for nonlinear elasticity". en. In: *Automated Solution of Differential Equations by the Finite Element Method*. Ed. by Anders Logg, Kent-Andre Mardal, and Garth Wells. Lecture Notes in Computational Science and Engineering 84. Springer Berlin Heidelberg, 2012, pp. 525–541. ISBN: 978-3-642-23098-1 978-3-642-23099-8. URL: http://link.springer.com/chapter/10.1007/978-3-642-23099-8_27 (visited on 03/10/2015) (page 83).

[158] Mohammad Nazari, Pascal Perrier, and Yohan Payan. "A Muscle Model Based on Feldman's Lambda Model: 3D Finite Element Implementation". In: (July 2013) (page 118).

[159] J. A. Nelder and R. Mead. "A Simplex Method for Function Minimization". In: *The Computer Journal* 7.4 (Jan. 1965), pp. 308–313. ISSN: 0010-4620. DOI: 10.1093/comjnl/7.4.308. eprint: https://academic.oup.com/comjnl/article-pdf/7/4/308/1013182/7-4-308.pdf. URL: https://doi.org/10.1093/comjnl/7.4.308 (page 132).

[160] Matthieu Nesme, Yohan Payan, and François Faure. "Efficient, Physically Plausible Finite Elements". In: *Eurographics* (2005), pp. 77–80. DOI: 10.2312/egs.20051028 (pages 129, 130).

[161] Vinh Phu Nguyen et al. "Meshless methods: A review and computer implementation aspects". In: *Mathematics and Computers in Simulation* 79.3 (2008), pp. 763–813. ISSN: 0378-4754. DOI: https://doi.org/10.1016/j.matcom.2008.01.003. URL: https://www.sciencedirect.com/science/article/pii/S0378475408000062 (page 77).

[162] Vien Minh Nguyen-Thanh, Xiaoying Zhuang, and Timon Rabczuk. "A deep energy method for finite deformation hyperelasticity". In: *European Journal of Mechanics - A/Solids* (Oct. 2019), p. 103874. DOI: 10.1016/j.euromechsol.2019.103874 (page 83).

[163] Siamak Niroomandi et al. "Real Time Simulation of Biological Soft Tissues : A PGD Approach". In: *International journal for numerical methods in biomedical engineering* 29 (May 2013). DOI: 10.1002/cnm.2544 (page 79).

[164] Alban Odot, Ryadh Haferssas, and Stephane Cotin. "DeepPhysics: A physics aware deep learning framework for real-time simulation". In: *International Journal for Numerical Methods in Engineering* 123.10 (2022), pp. 2381–2398. DOI: https://doi.org/10.1002/nme.6943. eprint: https://onlinelibrary.wiley.com/doi/pdf/10.1002/nme.6943. URL: https://onlinelibrary.wiley.com/doi/abs/10.1002/nme.6943 (pages 79, 92).

[165] R.W. Ogden. "Large deformation isotropic elasticity – on the correlation of theory and experiment for incompressible rubberlike solids". In: *Proceedings of the Royal Society of London. A. Mathematical and Physical Sciences* 326.1567 (Feb. 1972), pp. 565–584. DOI: 10.1098/rspa.1972.0026. URL: https://doi.org/10.1098/rspa.1972.0026 (page 81).

[166] R.W. Ogden. "Non-linear elastic deformations". In: *Engineering Analysis* 1.2 (1984), p. 119. ISSN: 0264-682X. DOI: https://doi.org/10.1016/0264-682X(84)90061-3. URL: https://www.sciencedirect.com/science/article/pii/0264682X84900613 (page 54).

[167] Francisco Oliveira and Joao Tavares. "Medical image registration: A review". In: *Computer methods in biomechanics and biomedical engineering* 17 (Jan. 2014), pp. 73–93. DOI: 10.1080/10255842.2012.670855 (page 124).

[168] Nikhil R Pal and Sankar K Pal. "A review on image segmentation techniques". In: *Pattern Recognition* 26.9 (1993), pp. 1277–1294. ISSN: 0031-3203. DOI: https://doi.org/10.1016/0031-3203(93)90135-J. URL: https://www.sciencedirect.com/science/article/pii/003132039390135J (page 123).

[169] Frederick I Parke. "Computer generated animation of faces". In: *Proceedings of the ACM annual conference* (1972), pp. 451–457. DOI: 10.1145/800193.569955 (page 32).

[170] Pras Pathmanathan et al. "Predicting Tumor Location by Modeling the Deformation of the Breast". In: *IEEE transactions on bio-medical engineering* 55 (Nov. 2008), pp. 2471–80. DOI: 10.1109/TBME.2008.925714 (page 119).

[171] Cécile Patte, Martin Genet, and Dominique Chapelle. "A quasi-static poromechanical model of the lungs". In: *Biomechanics and Modeling in Mechanobiology* 21.2 (Jan. 2022), pp. 527–551. DOI: 10.1007/s10237-021-01547-0. URL: https://doi.org/10.1007/s10237-021-01547-0 (page 83).

[172] Yohan Payan. *Biomechanics of Living Organs*. 2017. DOI: 10.1016/c2015-0-00832-2 (page 78).

[173] S. Pezzuto, D. Ambrosi, and A. Quarteroni. "An orthotropic active–strain model for the myocardium mechanics and its numerical approximation". In: *European Journal of Mechanics - A/Solids* 48 (Nov. 2014), pp. 83–96. DOI: 10.1016/j.euromechsol.2014.03.006. URL: https://doi.org/10.1016/j.euromechsol.2014.03.006 (page 98).

[174] V. Phunpeng and P.M. Baiz. "Mixed finite element formulations for strain-gradient elasticity problems using the FEniCS environment". In: *Finite Elements in Analysis and Design* 96 (2015), pp. 23–40. DOI: 10.1016/j.finel.2014.11.002. URL: https://app.dimensions.ai/details/publication/pub.1009763899 (page 83).

[175] Guillaume Picinbono, Hervé Delingette, and Nicholas Ayache. "Non-linear anisotropic elasticity for real-time surgery simulation". In: *Graphical Models* 65.5 (2003). Special Issue on SMI 2002, pp. 305–321. ISSN: 1524-0703. DOI: https://doi.org/10.1016/S1524-0703(03)00045-6. URL: https://www.sciencedirect.com/science/article/pii/S1524070303000456 (page 78).

[176] M. L. Raghavan, Baoshun Ma, and Mark F. Fillinger. "Non-invasive determination of zero-pressure geometry of arterial aneurysms". In: *Annals of Biomedical Engineering* 34.9 (2006), pp. 1414–1419. ISSN: 00906964. DOI: 10.1007/s10439-006-9115-7 (page 49).

[177] Ganiyu A Rahman. "Breast conserving therapy: A surgical technique where little can mean more". In: *Journal of Surgical Technique and Case Report* 3.1 (2011), pp. 1–4. ISSN: 20068808. DOI: 10.4103/2006-8808.78459 (page 31).

[178] Vijay Rajagopal. "Modelling Breast Tissue Mechanics Under Gravity Loading". In: (Jan. 2007) (page 116).

[179] Vijay Rajagopal et al. "Creating Individual-specific Biomechanical Models of the Breast for Medical Image Analysis". In: *Academic Radiology* 15.11 (2008), pp. 1425–1436. ISSN: 1076-6332. DOI: https://doi.org/10.1016/j.acra.2008.07.017. URL: https://www.sciencedirect.com/science/article/pii/S1076633208004224 (pages 116, 119).

[180] Vijay Rajagopal et al. "Mapping Microcalcifications Between 2D Mammograms and 3D MRI Using a Biomechanical Model of the Breast". In: Jan. 2010, pp. 17–28. ISBN: 978-1-4419-5873-0. DOI: 10.1007/978-1-4419-5874-7_3 (pages 115, 116).

[181] Vijay Rajagopal et al. "Towards Tracking Breast Cancer Across Medical Images Using Subject-Specific Biomechanical Models". In: *Medical image computing and computer-assisted intervention : MICCAI ... International Conference on Medical Image Computing and Computer-Assisted Intervention* 10 Pt 1 (2007), pp. 651–8 (page 116).

[182] Anthony Ralston and Philip Rabinowitz. "A First Course in Numerical Analysis (2nd ed.)" In: *A First Course in Numerical Analysis (Second Edition)*. Second Edition. New York: Dover Publications, 2001, p. i. ISBN: 978-0-486-41454-6 (page 88).

[183] H. Rappel et al. "A Tutorial on Bayesian Inference to Identify Material Parameters in Solid Mechanics". In: *Archives of Computational Methods in Engineering* 27 (Jan. 2019). DOI: 10.1007/s11831-018-09311-x (page 78).

[184] H. Rappel et al. "A Tutorial on Bayesian Inference to Identify Material Parameters in Solid Mechanics". In: *Archives of Computational Methods in Engineering* 27.2 (2020), pp. 361–385. ISSN: 18861784. DOI: 10.1007/s11831-018-09311-x (page 44).

[185] H. Rappel et al. "Identifying elastoplastic parameters with Bayes' theorem considering output error, input error and model uncertainty". In: *Probabilistic Engineering Mechanics* 55 (2019), pp. 28–41. ISSN: 0266-8920. DOI: https://doi.org/10.1016/j.probengmech.2018.08.004. URL: https://www.sciencedirect.com/science/article/pii/S0266892018300547 (page 78).

[186] Florian Rathgeber et al. "Firedrake: Automating the Finite Element Method by Composing Abstractions". In: *ACM Transactions on Mathematical Software (TOMS)* 43.3 (Dec. 2016), 24:1–24:27. ISSN: 0098-3500. DOI: 10.1145/2998441. URL: https://doi.org/10.1145/2998441 (visited on 01/20/2020) (page 82).

[187] Manuel K. Rausch, Martin Genet, and Jay D. Humphrey. "An augmented iterative method for identifying a stress-free reference configuration in image-based biomechanical modeling". In: *Journal of Biomechanics* 58 (2017), pp. 227–231. ISSN: 18732380. DOI: 10.1016/j.jbiomech.2017.04.021 (page 67).

[188] Scott I. Heath Richardson et al. "A poroelastic immersed finite element framework for modelling cardiac perfusion and fluid–structure interaction". In: *International Journal for Numerical Methods in Biomedical Engineering* 37.5 (2021), e3446. DOI: https://doi.org/10.1002/cnm.3446. eprint: https://onlinelibrary.wiley.com/doi/pdf/10.1002/cnm.3446. URL: https://onlinelibrary.wiley.com/doi/abs/10.1002/cnm.3446 (page 78).

[189] Amy E. Rivere, V. Suzanne Klimberg, and Kirby I. Bland. "32 - Breast Conservation Therapy for Invasive Breast Cancer". In: *The Breast (Fifth Edition)*. Ed. by Kirby I. Bland et al. Fifth Edition. Elsevier, 2018, 462–476.e4. ISBN: 978-0-323-35955-9. DOI: doi.org/10.1016/B978-0-323-35955-9.00032-5. URL: https://www.sciencedirect.com/science/article/pii/B9780323359559000325 (page 31).

[190] R. S. Rivlin. "Large elastic deformations of isotropic materials. IV. Further developments of the general theory". In: *Philosophical Transactions of the Royal Society of London. Series A, Mathematical and Physical Sciences* 241.835 (1948), pp. 379–397 (page 54).

[191] Benjamin Rodenberg et al. "FEniCS–preCICE: Coupling FEniCS to other simulation software". en. In: *SoftwareX* 16 (Dec. 2021), p. 100807. ISSN: 2352-7110. DOI: 10.1016/j.softx.2021.100807. URL: https://www.sciencedirect.com/science/article/pii/S2352711021001072 (visited on 07/05/2022) (page 83).

[192] Stephen L. Rose et al. "Implementation of Breast Tomosynthesis in a Routine Screening Practice: An Observational Study". In: *American Journal of Roentgenology* 200.6 (2013). PMID: 23701081, pp. 1401–1408. DOI: 10.2214/AJR.12.9672. eprint: https://doi.org/10.2214/AJR.12.9672. URL: https://doi.org/10.2214/AJR.12.9672 (page 20).

[193] Nicole Ruiter et al. "Model-based registration of X-ray mammograms and MR images of the female breast". In: vol. 53. Nov. 2004, 3290–3294 Vol. 5. ISBN: 0-7803-8700-7. DOI: 10.1109/NSSMIC.2004.1466392 (page 115).

[194] Guillermo Ruiz et al. "Weighted regularized statistical shape space projection for breast 3D model reconstruction". In: *Medical Image Analysis* 47 (2018), pp. 164–179. DOI: 10.1016/j.media.2018.04.007 (pages 32, 43).

[195] Remi Salmon et al. "Multimodal Imaging of the Breast to Retrieve the Reference State in the Absence of Gravity Using Finite Element Modeling". In: June 2017, pp. 254–263. ISBN: 978-3-319-59396-8. DOI: 10.1007/978-3-319-59397-5_27 (page 115).

[196] Abbas Samani, Judit Zubovits, and Donald Plewes. "Elastic moduli of normal and pathological human breast tissues: An inversion-technique-based investigation of 169 samples". In: *Physics in medicine and biology* 52 (Apr. 2007), pp. 1565–76. DOI: 10.1088/0031-9155/52/6/002 (page 118).

[197] Abbas Samani et al. "Biomechanical 3-D finite element modeling of the human breast for MR/X-ray using MRI data". In: *IEEE transactions on medical imaging* 20 (May 2001), pp. 271–9. DOI: 10.1109/42.921476 (page 115).

[198] Andrew Sanders. *An Introduction to Unreal Engine 4*. USA: A. K. Peters, Ltd., 2016. ISBN: 1498765092 (page 79).

[199] Richard T. Schield. "Inverse deformation results in finite elasticity". In: *Zeitschrift für angewandte Mathematik und Physik ZAMP* 18.4 (1967), pp. 490–500. ISSN: 00442275. DOI: 10.1007/BF01601719 (page 50).

[200] M. W. Scroggs et al. "Basix: a runtime finite element basis evaluation library". submitted to Journal of Open Source Software. 2022 (pages 83, 87).

[201] Brooke R. Seckel, Shawkat A. Sati, and W. Thomas McClellan. "The Inframammary Crease". In: *Breast Augmentation: Principles and Practice*. Ed. by Melvin A. Shiffman. Berlin, Heidelberg: Springer Berlin Heidelberg, 2009, pp. 51–55. ISBN: 978-3-540-78948-2. DOI: 10.1007/978-3-540-78948-2_5. URL: https://doi.org/10.1007/978-3-540-78948-2_5 (page 119).

[202] M Sellier. "An iterative method for the inverse elasto-static problem". In: *Journal of Fluids and Structures* 27.8 (2011), pp. 1461–1470. ISSN: 0889-9746. DOI: 10.1016/j.jfluidstructs.2011.08.002. URL: http://dx.doi.org/10.1016/j.jfluidstructs.2011.08.002 (pages 50, 51, 53, 56, 67).

[203] Myung-Hee Shin et al. "Intake of Dairy Products, Calcium, and Vitamin D and Risk of Breast Cancer". In: *JNCI: Journal of the National Cancer Institute* 94.17 (Sept. 2002), pp. 1301–1310. ISSN: 0027-8874. DOI: 10.1093/jnci/94.17.1301. eprint: https://academic.oup.com/jnci/article-pdf/94/17/1301/9849203/1301.pdf. URL: https://doi.org/10.1093/jnci/94.17.1301 (page 11).

[204] Bruce R. Simon. "Multiphase Poroelastic Finite Element Models for Soft Tissue Structures". In: *Applied Mechanics Reviews* 45.6 (June 1992), pp. 191–218. ISSN: 0003-6900. DOI: 10.1115/1.3121397. eprint: https://asmedigitalcollection.asme.org/appliedmechanicsreviews/article-pdf/45/6/191/5436442/191_1.pdf. URL: https://doi.org/10.1115/1.3121397 (page 78).

[205] Sina Sinaie et al. "Programming the material point method in Julia". In: *Advances in Engineering Software* 105 (Jan. 2017). DOI: 10.1016/j.advengsoft.2017.01.008 (page 77).

[206] Per Skaane et al. "Two-View Digital Breast Tomosynthesis Screening with Synthetically Reconstructed Projection Images: Comparison with Digital Breast Tomosynthesis with Full-Field Digital Mammographic Images". In: *Radiology* 271.3 (2014). PMID: 24484063, pp. 655–663. DOI: 10.1148/radiol.13131391. eprint: https://doi.org/10.1148/radiol.13131391. URL: https://doi.org/10.1148/radiol.13131391 (page 20).

[207] Michael Smith. *ABAQUS/Standard User's Manual, Version 6.9*. English. United States: Dassault Systèmes Simulia Corp, 2009 (page 77).

[208] Ian Stokes et al. "Limitation of Finite Element Analysis of Poroelastic Behavior of Biological Tissues Undergoing Rapid Loading". In: *Annals of biomedical engineering* 38 (Mar. 2010), pp. 1780–8. DOI: 10.1007/s10439-010-9938-0 (page 78).

[209] Alison M. Stuebe et al. "Lactation and Incidence of Premenopausal Breast Cancer: A Longitudinal Study". In: *Archives of Internal Medicine* 169.15 (Aug. 2009), pp. 1364–1371. ISSN: 0003-9926. DOI: 10.1001/archinternmed.2009.231. eprint: https://jamanetwork.com/journals/jamainternalmedicine/articlepdf/1108505/ioi90036_1364_1371.pdf. URL: https://doi.org/10.1001/archinternmed.2009.231 (page 10).

[210] Gregory Sturgeon et al. "Finite-element modeling of compression and gravity on a population of breast phantoms for multi-modality imaging simulation". In: *Med. Phys.* 43 (May 2016), pp. 2207–2217. DOI: 10.1118/1.4945275 (page 115).

[211] Hyuna Sung et al. "Global Cancer Statistics 2020: GLOBOCAN Estimates of Incidence and Mortality Worldwide for 36 Cancers in 185 Countries". In: *CA: A Cancer Journal for Clinicians* 71.3 (2021), pp. 209–249. DOI: https://doi.org/10.3322/caac.21660. eprint: https://acsjournals.onlinelibrary.wiley.com/doi/pdf/10.3322/caac.21660. URL: https://acsjournals.onlinelibrary.wiley.com/doi/abs/10.3322/caac.21660 (page 9).

[212] Alok Sutradhar and Michael Miller. "In vivo measurement of breast skin elasticity and breast skin thickness". In: *Skin research and technology : official journal of International Society for Bioengineering and the Skin (ISBS) [and] International Society for Digital Imaging of Skin (ISDIS) [and] International Society for Skin Imaging (ISSI)* 19 (Aug. 2012). DOI: 10.1111/j.1600-0846.2012.00627.x (page 118).

[213] Eleonora Tagliabue et al. "Intra-operative Update of Boundary Conditions for Patient-Specific Surgical Simulation". In: *Medical Image Computing and Computer Assisted Intervention – MICCAI 2021* (2021). Ed. by Marleen de Bruijne et al., pp. 373–382 (page 78).

[214] Hossein Talebi et al. "A computational library for multiscale modeling of material failure". In: *Computational Mechanics* 53.5 (Dec. 2013), pp. 1047–1071. DOI: 10.1007/s00466-013-0948-2. URL: https://doi.org/10.1007/s00466-013-0948-2 (page 77).

[215] Christine Tanner et al. "Factors influencing the accuracy of biomechanical breast models". In: *Medical physics* 33 (July 2006), pp. 1758–69. DOI: 10.1118/1.2198315 (page 118).

[216] Radoslaw Tarkowski and Marek Rzaca. "Cryosurgery in the treatment of women with breast cancer—a review". In: *Gland Surgery* 3.2 (2014). ISSN: 2227-8575. URL: https://gs.amegroups.com/article/view/3784 (page 23).

[217] Maxime Tournier et al. "Stable Constrained Dynamics". In: *ACM Transactions on Graphics, Association for Computing Machinery, in Proceedings of SIGGRAPH* 34.4 (2015), 132:1–132:10. DOI: 10.1145/2766969 (pages 34, 37, 130).

[218] Giuseppe Turini et al. "Software Framework for VR-Enabled Transcatheter Valve Implantation in Unity". In: nternational Conference on Augmented Reality, Virtual Reality and Computer Graphics. July 2019, pp. 376–384. ISBN: 978-3-030-25964-8. DOI: 10.1007/978-3-030-25965-5_28 (page 79).

[219] Chieh Han John Tzou et al. "Comparison of three-dimensional surface-imaging systems". In: *Journal of Plastic, Reconstructive and Aesthetic Surgery* 67.4 (2014), pp. 489–497. ISSN: 18780539. DOI: 10.1016/j.bjps.2014.01.003 (page 32).

[220] Stephane Urcun et al. "Cortex tissue relaxation and slow to medium load rates dependency can be captured by a two-phase flow poroelastic model". In: *Journal of the Mechanical Behavior of Biomedical Materials* 126 (Nov. 2021), p. 104952. DOI: 10.1016/j.jmbbm.2021.104952 (page 78).

[221] Stéphane Urcun et al. "Digital twinning of Cellular Capsule Technology: Emerging outcomes from the perspective of porous media mechanics". In: *PLOS ONE* 16.7 (July 2021), pp. 1–30. DOI: 10.1371/journal.pone.0254512. URL: https://doi.org/10.1371/journal.pone.0254512 (page 78).

[222] Rodolphe Vaillant et al. "Implicit skinning: Real-time skin deformation with contact modeling". In: *ACM Transactions on Graphics* 32.4 (2013). ISSN: 07300301. DOI: 10.1145/2461912.2461960 (page 44).

[223] D.R. Veronda and R.A. Westmann. "Mechanical characterization of skin—Finite deformations". In: *Journal of Biomechanics* 3.1 (1970), pp. 111–124. ISSN: 0021-9290. DOI: https://doi.org/10.1016/0021-9290(70)90055-2. URL: https://www.sciencedirect.com/science/article/pii/0021929070900552 (page 81).

[224] Mickeal Verschoor, Daniel Lobo, and Miguel A. Otaduy. "Soft Hand Simulation for Smooth and Robust Natural Interaction". In: *2018 IEEE Conference on Virtual Reality and 3D User Interfaces (VR)*. IEEE Conference on Virtual Reality and 3D User Interfaces (VR). 2018, pp. 183–190. DOI: 10.1109/VR.2018.8447555 (page 79).

[225] Pauli Virtanen et al. "SciPy 1.0: Fundamental Algorithms for Scientific Computing in Python". In: *Nature Methods* 17 (2020), pp. 261–272. DOI: 10.1038/s41592-019-0686-2 (page 38).

[226] Wolf-Dieter Vogl et al. "Automatic segmentation and classification of breast lesions through identification of informative multiparametric PET/MRI features". In: *European Radiology Experimental* 3 (2019) (page 120).

[227] Jared A. Weis, Michael I. Miga, and Thomas E. Yankeelov. "Three-dimensional image-based mechanical modeling for predicting the response of breast cancer to neoadjuvant therapy". In: *Computer Methods in Applied Mechanics and Engineering* 314 (2017). Special Issue on Biological Systems Dedicated to William S. Klug, pp. 494–512. ISSN: 0045-7825. DOI: https://doi.org/10.1016/j.cma.2016.08.024. URL: https://www.sciencedirect.com/science/article/pii/S0045782516310167 (page 83).

[228] Jeffrey A. Weiss, Bradley N. Maker, and Sanjay Govindjee. "Finite element implementation of incompressible, transversely isotropic hyperelasticity". In: *Computer Methods in Applied Mechanics and Engineering* 135.1 (1996), pp. 107–128. ISSN: 0045-7825. DOI: https://doi.org/10.1016/0045-7825(96)01035-3. URL: https://www.sciencedirect.com/science/article/pii/0045782596010353 (page 78).

[229] Richard Wooster and Barbara L. Weber. "Breast and Ovarian Cancer". In: *New England Journal of Medicine* 348.23 (2003). PMID: 12788999, pp. 2339–2347. DOI: 10.1056/NEJMra012284. eprint: https://doi.org/10.1056/NEJMra012284. URL: https://doi.org/10.1056/NEJMra012284 (pages 9, 11).

[230] Jun Wu, Rüdiger Westermann, and Christian Dick. "Real-Time Haptic cutting of high-resolution soft tissues". In: *Studies in health technology and informatics* 196 (Apr. 2014), pp. 469–75. DOI: 10.3233/978-1-61499-375-9-469 (page 79).

[231] Fei Xue et al. "Cigarette Smoking and the Incidence of Breast Cancer". In: *Archives of Internal Medicine* 171.2 (Jan. 2011), pp. 125–133. ISSN: 0003-9926. DOI: 10.1001/archinternmed.2010.503. eprint: https://jamanetwork.com/journals/jamainternalmedicine/articlepdf/226457/ioi05123_125_133.pdf. URL: https://doi.org/10.1001/archinternmed.2010.503 (page 11).

[232] Takahiro Yamada. "Finite element procedure of initial shape determination for hyperelasticity". In: *Structural Engineering and Mechanics* 6.2 (1998), pp. 173–183. ISSN: 12254568. DOI: 10.12989/sem.1998.6.2.173 (page 50).

[233] Song Yuheng and Yan Hao. "Image Segmentation Algorithms Overview". In: *CoRR* abs/1707.02051 (2017). arXiv: 1707.02051. URL: http://arxiv.org/abs/1707.02051 (page 124).

[234] Milad Zeraatpisheh, Stephane P.A. Bordas, and Lars A.A. Beex. "Bayesian model uncertainty quantification for hyperelastic soft tissue models". In: *Data-Centric Engineering* 2 (2021), e9. DOI: 10.1017/dce.2021.9 (page 78).

[235] R Zheng, W Yu, and J Fan. "2 - Breast measurement and sizing". In: *Innovation and Technology of Women's Intimate Apparel*. Ed. by W. Yu et al. Woodhead Publishing Series in Textiles. Woodhead Publishing, 2006, pp. 28–58. ISBN: 978-1-84569-046-5. DOI: doi.org/10.1016/B978-1-84569-046-5.50002-1. URL: https://www.sciencedirect.com/science/article/pii/B9781845690465500021 (pages 33, 120).

[236] J. Zhou and Y. C. Fung. "The degree of nonlinearity and anisotropy of blood vessel elasticity". In: *Proceedings of the National Academy of Sciences* 94.26 (1997), pp. 14255–14260. DOI: 10.1073/pnas.94.26.14255. eprint: https://www.pnas.org/doi/pdf/10.1073/pnas.94.26.14255. URL: https://www.pnas.org/doi/abs/10.1073/pnas.94.26.14255 (page 78).

[237] X. Zhou and J Lu. "Estimation of vascular open configuration using finite element inverse elastostatic method". In: *Engineering with Computers* 25.49 (2009). DOI: doi.org/10.1007/s00366-008-0104-3 (page 49).

[238] O.C. Zienkiewicz, R.L. Taylor, and David Fox. "The Finite Element Method for Solid and Structural Mechanics". In: *The Finite Element Method for Solid and Structural Mechanics (Seventh Edition)*. Seventh Edition. Oxford: Butterworth-Heinemann, 2014, p. i. ISBN: 978-1-85617-634-7. DOI: https://doi.org/10.1016/B978-1-85617-634-7.00016-8. URL: https://www.sciencedirect.com/science/article/pii/B9781856176347000168 (page 88).

[239] Margarita L. Zuley et al. "Comparison of Two-dimensional Synthesized Mammograms versus Original Digital Mammograms Alone and in Combination with Tomosynthesis Images". In: *Radiology* 271.3 (2014). PMID: 24475859, pp. 664–671. DOI: 10.1148/radiol.13131530. eprint: https://doi.org/10.1148/radiol.13131530. URL: https://doi.org/10.1148/radiol.13131530 (page 20).

[240] Kristian B. Ølgaard and Garth N. Wells. "Applications in solid mechanics". en. In: *Automated Solution of Differential Equations by the Finite Element Method: The FEniCS Book*. Ed. by Anders Logg, Kent-Andre Mardal, and Garth Wells. Lecture Notes in Computational Science and Engineering. Berlin, Heidelberg: Springer, 2012, pp. 505–524. ISBN: 978-3-642-23099-8. DOI: 10.1007/978-3-642-23099-8_26. URL: https://doi.org/10.1007/978-3-642-23099-8_26 (visited on 07/04/2022) (page 83).